QUANTUM COMPUTING WITH SUPERCONDUCTOR-SEMICONDUCTOR HYBRID SYSTEMS

by

BENJAMIN ELTON HARPT

A dissertation submitted in partial fulfillment of

the requirements of the degree of

DOCTOR OF PHILOSOPHY

(Physics)

at the

UNIVERSITY OF WISCONSIN-MADISON

2024

Date of final oral examination: November 18, 2024

This dissertation is approved by the following members of the Final Oral Committee:
Mark A. Eriksson, Professor, Physics
Mark Friesen, Distinguished Scientist, Physics
Benjamin D. Woods, Assistant Professor, Physics
Paul M. Voyles, Professor, Materials Science & Engineering

Abstract

Quantum computers offer the potential to solve problems beyond the reach of classical computers by harnessing fundamentally different physics. Today, researchers worldwide are racing to develop quantum computers that are both controllable and scalable, utilizing a wide range of hardware approaches to encode quantum information. Superconducting circuits and semiconductor quantum dots are, individually, two of the leading qubit platforms for building solid-state quantum processors; combining the strengths of both materials in hybrid devices opens up new possibilities for quantum computing architectures. This dissertation explores key aspects of superconductor-semiconductor hybrid systems for quantum computing, and is structured in three parts. Part I presents an in-depth overview of silicon quantum-dot qubits, with a focus on experiments investigating crosstalk between exchange-only spin qubits. Part II addresses the integration of these qubits with superconducting resonators for readout and long-range entanglement. Using a quantum-dot device coupled to a vertically integrated resonator, we demonstrate an unconventional electron-photon interaction mechanism and show how it can be utilized for qubit readout and spectroscopy. Finally, Part III examines superconductor-semiconductor hybrid junctions and their qubit applications, detailing the development of superconducting alloys tailored for germanium-based hybrid devices. Together, these findings advance our understanding and introduce new techniques for developing hybrid quantum technologies.

Acknowledgements

Graduate school has been a collaborative effort in every sense, and I owe a profound debt of gratitude to the many individuals who have helped me along the way. Though this space is too brief to name everyone who has had an impact, I hope these words can convey my heartfelt thanks. Your support has been invaluable and deeply appreciated.

I would first like to thank the members of my Thesis Committee for reviewing this dissertation, attending my defense, and asking thoughtful questions: Mark Eriksson, Mark Friesen, Ben Woods, and Paul Voyles.

The past six years of research have been enriched by the mentorship of 'Mark and Mark.' I owe special thanks to Mark Eriksson for being an excellent Ph.D. advisor. While his expertise in quantum dots and cryogenic measurements has been instrumental in developing my skill set, it is the practical lessons—the kind you cannot learn from papers—that have had the greatest impact on me as a scientist. From preparing an engaging talk to navigating project collaborations to responding tactfully to referees during peer review, these lessons have shaped how I approach my work. Mark's sound advice and unwavering optimism have carried me through more challenging days in the lab than I can count, and I aspire to bring even a fraction of those qualities into my future endeavors. The steady guidance of Mark Friesen has also been instrumental in my research journey. Mark is the kind of theorist that every experimentalist hopes to work with—his deep grasp of experiments and clear interpretations of measurement results have been invaluable. He has also mastered the art of the Socratic method, always posing the right questions to help me uncover deeper insights into the data. I am especially grateful for the many hours Mark spent critiquing my writing and figures, which have significantly elevated the quality of our publications.

I have been fortunate to learn from several faculty members and scientists at UW–Madison who have generously shared their expertise. My first project in the Eriksson group involved fabricating devices on the 'Wiggle Well,' a novel heterostructure imagined by Bob Joynt and grown by Don Savage. I will fondly remember Bob's easygoing humor and Don's outsider perspective in our group meetings, where his so-called "dumb questions" often led to important insights. Robert McDermott's extensive knowledge of superconducting qubits and resonators was a constant resource, and his advice greatly benefited my electron-photon coupling experiments. I also learned much from Ben Woods, an expert in superconductor-semiconductor hybrids and Majorana physics (among several other things). It has been a joy to witness his transition from postdoc to professor over the last few years.

I would like to extend my gratitude to our external collaborators, Rusko Ruskov and Charlie Tahan from the Laboratory for Physical Sciences. The story of how we accidentally uncovered longitudinal coupling in our quantum dot-resonator experiments is one for another time, but it is clear that their theoretical insights were crucial to making this discovery possible. I also thank Will Oliver and his team at MIT Lincoln Laboratory for their assistance with packaging the unique flip-chip sample featured in Chapters 5 and 6, as well as Giordano Scappucci of TU Delft for providing the germanium heterostructure used in Chapter 8.

None of my work would have been possible without support from many talented and dedicated staff at UW–Madison. From the NFC and NIAC, I am deeply grateful to Quinn Leonard, Kurt Kupcho, Frank Flack, Julie Morasch, Ming-Wei Lin, Alex Kvit, Ed Gonzales, and Hal Giles for many hours of training and technical assistance. In the Physics Department, I thank Ann Austin for her purchasing wizardry, Dawn Suchomel for her travel coordination, Michelle Holland and Sharon Khan for helping me navigate the graduate program, and Aimee Lefkow for the innumerable ways she keeps the department running. I also want to acknowledge Gabe Bernhardt, whose arrival to the Eriksson group has been a game changer—Gabe's creative engineering and skill at maintaining lab equipment has kept all of our experiments on track.

I would be remiss if I did not express my gratitude to the many students and postdocs from the Eriksson and Friesen groups, who have been not only invaluable scientific collaborators but also great friends. In approximate order of seniority, I thank Evan MacQuarrie, Mario Palma, Brandur Thorgrimsson, José Carlos Abadillo Uriel, Sam Neyens, Ekmel Ercan, JP Dodson, Gabe Jaffe, Leah Tom, Merritt Losert, Michael Wolfe, Justin White, Emily Joseph, Sanghyeok Park, Piotr Marciniec, Avani Vivrekar, Tyler Kovach, Brighton Coe, Jared Benson, Jack Reily, Alysa Rogers, Hudaiba Soomro, Emma Brann, Owen Eskandari, Daniel King, Cate Sturner, Tali Oh, and Patrick Walsh. A special acknowledgment goes to Tom McJunkin and Joelle Corrigan, whose mentorship and collaboration during my early days in the Eriksson group were instrumental in shaping my research skills, and to Nathan Holman, who fabricated the device used in Chapters 5 and 6. I enjoyed many long hours in Chamberlin alongside all of you.

In my final year of graduate school, I had the privilege of interning with Intel's quantum computing research group. This experience not only broadened my perspectives and refined my qubit measurement skills but also opened the door to an exciting job opportunity. My sincere thanks go to the entire quantum team, and especially to Jeanette Roberts, Elliot Connors, and Jolle Corrigan (again!) for mentoring me during my internship project.

Finally, I want to express my heartfelt gratitude to my family and friends for their endless love and support. Returning to my home state of Wisconsin and being close to family has been one of the most gratifying aspects of graduate school. To my parents, thank you for encouraging me and enabling me to follow my passions; to my siblings, thank you for your humor and reminders not to take myself too seriously; and to my girlfriend Mara, thank you for your love and for keeping me sane through the long nights and weekends spent writing this dissertation.

Funding Acknowledgements

I am deeply appreciative of the organizations and agencies that made my graduate research possible. The work described in Chapters 2, 4, 5, and 6 received support from HRL Laboratories. The project detailed in Chapter 3 was funded by Intel. Research in Chapters 7 and 8 was made possible through support from the NSF Quantum Leap Challenge Institute for Hybrid Quantum Architectures and Networks (NSF Award 2016136). Additional acknowledgements are found in Chapters 5 and 6.

Contents

List of Figures

List of Tables

Chapter 1

Introduction: Quantum Computing with Superconductors & Semiconductors

In our increasingly digital world, the influence of classical computers touches nearly every aspect of daily life, from communication and commerce to scientific discovery. In many ways, modern computing owes its existence to quantum mechanics, which was instrumental in enabling the development of the central processing unit. The quantum theory that emerged a century ago—marking what has been called the *first quantum revolution*—unlocked our understanding of semiconductors and ultimately led to the invention of the transistor, the fundamental building block of digital computing. As transistor technology advanced, computer processors grew exponentially in scale and capability, transforming society in profound and irreversible ways.

Despite the vast utility of classical computers, some problems—such as simulating quantum systems or tackling complex optimization tasks—remain beyond the reach of even the most advanced machines. Remarkably, quantum mechanics may once again hold the key to advancing computational technology and overcoming these limitations. Many researchers believe we are at the outset of a *second quantum revolution*, where quantum phenomena serve not merely to improve classical devices, but as the computational medium itself. The

American physicist Richard Feynman articulated this vision in 1982, proposing that quantum systems might simulate other quantum systems far more efficiently than classical computers [1]. From this insight emerged the field of **quantum computing**, which has evolved from a theoretical curiosity into a rapidly advancing area of technology. Today, scientists and engineers are building increasingly sophisticated quantum computers that aim to harness the principles of quantum mechanics to expand the computational frontier.

1.1 Quantum Bits

The starting point for any computation is encoding the information to be processed. In classical computing, information is encoded using binary units called **bits**. Each bit can exist in one of two states: 0 or 1, as depicted on the left side of Fig. 1.1. In quantum computing, information is encoded in fundamental units called quantum bits or **qubits**. Unlike a classical bit, a qubit is a two-level quantum system, which can exist not only in the discrete **logical states** $|0\rangle$ and $|1\rangle$, but also in any superposition of these states, represented by the wavefunction

$$|\psi\rangle = \cos\left(\frac{\theta}{2}\right)|0\rangle + e^{i\phi}\sin\left(\frac{\theta}{2}\right)|1\rangle\,. \tag{1.1}$$

The **Bloch sphere**, shown on the right side of Fig. 1.1, provides an intuitive, geometric representation of a qubit's state. The sphere's north and south poles correspond to the logical states $|0\rangle$ and $|1\rangle$; any other point on its surface represents a unique superposition, defined by the angles θ and ϕ. This representation is particularly useful for visualizing how a qubit's state evolves during computational operations.

The property of superposition gives qubits an exponential advantage in storing information compared to classical bits. While N bits can store N discrete units of information at a time, the same number of qubits can encode 2^N units of information simultaneously. For example, a system of three qubits has an eight-dimensional Hilbert space ($2^3 = 8$), and the

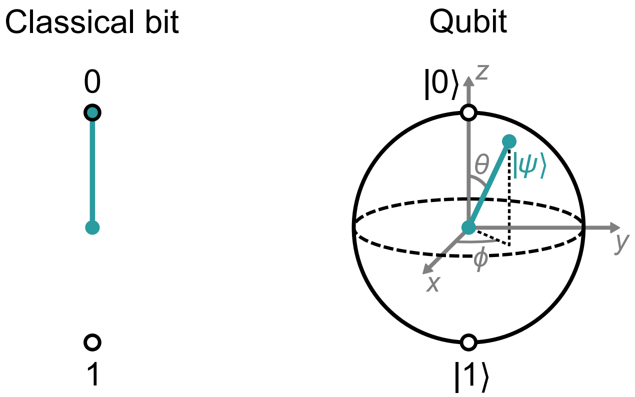

Figure 1.1: A classical bit and a qubit represented on the Bloch sphere. The classical bit can occupy the binary states 0 or 1; the qubit can exist in an arbitrary superposition of the logical basis states $|0\rangle$ and $|1\rangle$.

---

wavefunction required to represent an arbitrary state of the system is

$$\begin{aligned} |\psi\rangle = c_0 |000\rangle + c_1 |001\rangle + c_2 |010\rangle + c_3 |011\rangle \\ + c_4 |100\rangle + c_5 |101\rangle + c_6 |110\rangle + c_7 |111\rangle , \end{aligned} \tag{1.2}$$

where each of the probability amplitudes c_i encodes a unit of information. The ability to represent and process exponentially more information is a central aspect of quantum computing's potential power.

1.2 Quantum Gates & Algorithms

In both classical and quantum computing, complex computational tasks are decomposed into basic operations called logic gates, which are executed by the underlying processor hardware. Classical processors rely on gates like AND, OR, and NOT to manipulate binary bits. In quantum computing, elementary operations on qubits are known as **quantum logic gates**. These gates are assembled into sequences called **quantum circuits**, which can be executed to implement **quantum algorithms**.

Each quantum gate corresponds to a unitary operator that evolves the state of one or more qubits. For example, the **X gate**, also known as the quantum NOT gate, flips the

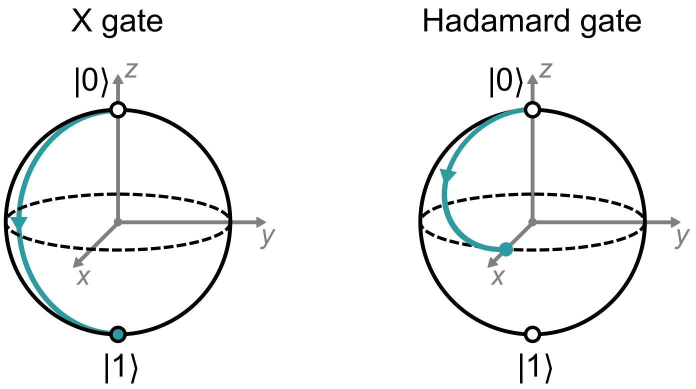

Figure 1.2: X and Hadamard gates represented as rotations on the Bloch sphere.

state of a qubit, transforming $|0\rangle$ into $|1\rangle$ and vice versa. Mathematically, it is represented by the Pauli-x matrix:

$$X = \begin{pmatrix} 0 & 1 \\ 1 & 0 \end{pmatrix}. \tag{1.3}$$

As another example, the **Hadamard gate**, given by

$$H = \frac{1}{\sqrt{2}} \begin{pmatrix} 1 & 1 \\ 1 & -1 \end{pmatrix}, \tag{1.4}$$

is often used to initialize a qubit into an equal superposition of $|0\rangle$ and $|1\rangle$, enabling quantum parallelism. The wavefunction evolution induced by single-qubit gates like these corresponds to rotations around various axes on the Bloch sphere, as illustrated in Fig. 1.2. Two-qubit gates, like the **Controlled-NOT (CNOT) gate**, are used for creating entangled states, which are a key resource in many quantum algorithms.

A quantum computer is said to be **universal** if it can perform any computation that a classical computer can, as well as additional computations that leverage the quantum behavior of qubits [2]. Universal quantum computation requires only a set of basic gates: arbitrary single-qubit gates combined with at least one entangling two-qubit gate, such as CNOT. This minimal set is sufficient to construct any quantum circuit [3, 4].

Quantum algorithms are cleverly designed to exploit the unique properties of quantum mechanics—namely, superposition, interference, and entanglement—to perform certain tasks more efficiently than classical algorithms. For example, **Shor's algorithm** uses quantum circuits to factorize large integers exponentially faster than any known classical method, posing a challenge to conventional cryptographic security [5]. Similarly, **Grover's algorithm** offers a quadratic speed-up for searching unsorted databases, reducing the search time from N steps to $\sqrt{N}$ [6]. Quantum circuits also excel in the simulation of quantum systems, where classical approaches struggle due to exponential complexity [7].

The potential benefits of these specialized quantum algorithms have driven significant interest and investment in the field of quantum computing. However, it is important to recognize that only a few examples of quantum speed-ups are currently known. For the vast majority of computational tasks, quantum computers do not outperform their classical counterparts. It remains an open question whether quantum computers will prove useful in areas such as machine learning and artificial intelligence. For now, the promise of quantum computing is focused on niche applications, and we may not fully understand its capabilities until universal machines are developed, allowing us to empirically test new algorithms and explore their potential.

For additional background reading on the theory of quantum computation, I like N. David Mermin's *Quantum Computer Science* [8].

1.3 Building a Quantum Computer

Thus far, we have discussed qubits and quantum gates in an idealized sense. However, building a real quantum computer requires overcoming significant engineering challenges to translate these concepts into physical hardware. To guide this process, the physicist David DiVincenzo proposed a set of criteria that outline the necessary conditions for constructing a functional quantum computer. The **DiVincenzo criteria** consist of five key requirements [9]:

1. **A well-defined system of qubits:** The hardware must be capable of reliably encod-

ing qubits, ensuring they can exist in a superposition of states $|0\rangle$ and $|1\rangle$.

2. **Initialization capabilities:** The system should be able to prepare qubits in a known initial state, typically $|0\rangle$, with high fidelity.
3. **Long coherence times:** Qubits must maintain coherence long enough to perform meaningful computations. Minimizing decoherence due to environmental noise is critical for accurate quantum operations.
4. **A universal set of quantum gates:** The hardware must support the implementation of arbitrary single-qubit gates and at least one two-qubit entangling gate, enabling universal computation.
5. **Measurement capabilities:** The ability to reliably measure qubits in a given basis, known as **readout**, is essential for extracting the results of a quantum circuit.

While these criteria establish a framework for building quantum computers, they do not specify how to implement them in practice. As a result, researchers have pursued a variety of strikingly different hardware platforms, each with its own unique approach to realizing qubits and gates. Some of the primary platforms being explored today include: superconducting circuits; trapped ions; semiconductor quantum dots; neutral atoms; photonic circuits; and topological superconductors. Each of these approaches has distinct advantages and challenges, making it difficult to predict which—if any—will ultimately succeed in realizing a universal quantum computer.

All platforms face a common challenge: overcoming **decoherence**, where interactions with the environment cause qubits to lose their quantum properties, potentially leaking their encoded quantum information and leading to computational errors. To address this issue and achieve fault tolerance, **quantum error correction** will be a necessary component of any universal quantum computing architecture. Quantum error correction works by encoding logical qubits across multiple physical qubits to detect and correct errors without directly measuring the qubits' states. However, this approach introduces a significant overhead, requiring a large number of additional physical qubits to protect each logical qubit [2, 8]. As a result, **platform scalability** becomes a critical factor; the physical hardware for a universal quantum processor must not only achieve high-fidelity operations, but also support the $10^6 - 10^9$ qubits that may be necessary for implementing error correction codes [10].

1.4 Materials Platforms for Solid-State Quantum Processors

Superconducting circuits and semiconductor quantum dots are two of the leading hardware platforms for quantum computing. The qubits in each implementation share several similarities: both utilize solid-state devices fabricated on chips using nanolithography; both are controlled by high-frequency electrical signals; and both require cryogenic temperatures to minimize thermal noise and preserve coherence. However, the differing materials properties of superconductors and semiconductors confer distinct strengths and weaknesses to each platform.

Superconducting qubits, such as transmons [11, 12], have achieved significant progress in this era of quantum computing development thanks to their fast, high-fidelity single- and two-qubit gates. Their design integrates seamlessly with microwave circuits, enabling efficient readout and non-local coupling between qubits via resonators. The platform's simple control architecture, with relatively few input and output lines, simplifies scaling. Superconducting circuits are constructed from large elements ($\sim$ 100 µm), making them robust against atomic-scale defects; however, their substantial physical footprint presents challenges for high-density integration. Their coherence times, though sufficient for current experiments, remain relatively short, limiting the number of operations before decoherence sets in. Moreover, superconducting qubits require operating temperatures well below 1 K, adding to the cost of cryogenic systems and imposing stringent thermal management demands on both the qubits and control hardware.

Semiconductor qubits are built on the same technology as field-effect transistors, which have driven the exponential growth of classical processors. This makes them compatible with existing semiconductor manufacturing processes, providing a pathway toward mass production and interoperability with CMOS electronics. The high degree of electrical tunability in semiconductors allows precise, *in situ* control over qubit properties. Additionally, semiconductor qubits exhibit long coherence times and are capable of operating at temperatures above 1 K. With an extremely compact footprint ($\sim$ 100 nm), vast numbers of qubits could potentially be packed onto a single chip ($\sim$ 1,000 can fit into a 10 $\mu\mathrm{m}^2$ region [13]). Yet, as with superconducting qubits, physical size can be a double-edged sword: these mesoscopic qubits are susceptible to atomic-scale defects, resulting in performance variability, and establishing qubit connectivity over macroscopic distances remains challenging. Furthermore, these qubits have thus far exhibited lower gate fidelities than their superconducting counterparts, and require more control lines, complicating the wiring needed for scaling up.

What if we could combine the advantages of both materials into a single solid-state platform? **Superconductor-semiconductor hybrid** architectures aim to do just that, leveraging the tunability and integration benefits of semiconductors alongside the incredible properties of superconductors. These hybrid systems create an exciting playground for physicists and engineers alike, offering opportunities for exploring new physics and developing innovative technologies for quantum computing.

1.5 Overview of the Dissertation

This dissertation explores avenues for quantum computing with superconductor-semiconductor hybrids, and is organized into three parts focusing on different aspects of hybrid quantum architectures.

Part I (Chapters 2 and 3) introduces the fundamentals of quantum-dot qubits in silicon, with an emphasis on the operation of exchange-only spin qubits. Experimental investigations of qubit crosstalk provide insights into scaling challenges for quantum-dot systems.

Part II (Chapters 4, 5, and 6) delves into electron-photon coupling in quantum dot-resonator hybrid devices, drawing on techniques from the field of superconducting circuits. We demonstrate an unconventional longitudinal coupling mechanism suitable for readout even when qubit and resonator frequencies are far-detuned.

Part III (Chapters 7 and 8) focuses on superconductor-semiconductor hybrid junctions and their qubit applications. This section includes a detailed analysis of the proximity effect in germanium heterostructures and the design of superconducting alloys for enhanced device performance.

Part I

Quantum-Dot Qubits in Silicon

Chapter 2

Semiconductor Quantum Dots

This chapter serves as a general introduction to semiconductor qubits, covering much of the foundational physics that enables their operation. It opens with a discussion of quantum confinement, outlining how quantum dots—formed by gate-controlled electrostatic fields in silicon heterostructures—are used to isolate and trap individual electrons. The focus then turns to electron transport and occupancy in quantum-dot devices, with an emphasis on experimental techniques for analyzing and controlling the electron population within each dot. Following this, the quantum states available within these systems for encoding information are explored, including the charge, orbital, valley, and spin degrees of freedom. The chapter concludes with an overview of how these concepts are combined to realize quantum-dot qubits, laying the groundwork for more complex qubit architectures presented in subsequent chapters.

2.1 Quantum Confinement

In order to use individual electrons[1] as qubits, it is first necessary to confine and isolate them within a nanoscale system. For this purpose, we employ **quantum dots**, which are

---

[1] While individual holes can also serve as qubits under a similar framework, and this is routinely done, our focus here is on electron qubits.

semiconductor structures that trap conduction-band electrons in all three spatial dimensions, creating discrete, atomic-like energy levels. There are several types of quantum dots formed within different semiconductor nanostructures; these include self-assembled quantum dots [14, 15], colloidal quantum dots [16, 17], vertical quantum dots [18], and molecular quantum dots [19]. For semiconductor qubits, implanted donor atoms [20, 21] or **gate-defined quantum dots**, formed by applying electrostatic fields to trap electrons within one-dimensional nanowires or two-dimensional planar heterostructures [22–24], are typically used. This dissertation focuses specifically on gate-defined quantum dots in two-dimensional semiconductor heterostructures. This highly tunable system provides an ideal stage on which the drama of quantum mechanics can play out.

Early semiconductor qubits were formed using gate-defined quantum dots in GaAs/AlGaAs planar heterostructures [25–28]. However, the use of GaAs-based devices presented significant challenges for qubit coherence and scalability. The electrons trapped in these devices experienced rapid spin dephasing due to magnetic field noise originating from the gallium and arsenide nuclei [29]. Additionally, GaAs is not as compatible with advanced semiconductor manufacturing processing as silicon, making the platform more difficult to scale.

The limitations of GaAs motivated the research community to shift toward silicon-based qubits in the early 2010s [30–37].[2] With approximately 95% of naturally occurring isotopes having zero nuclear spin, silicon offers a more favorable environment for coherent control of electron spins. Moreover, the remaining 5% of spin-1/2 ^{29}Si nuclei can be removed through isotopic purification, enabling spin decoherence times that are four orders of magnitude longer than those in GaAs dots [36, 38, 39]. Silicon heterostructures are also compatible with existing CMOS technology, and they can be processed in modern semiconductor foundries, making them well suited for large-scale qubit integration [40–45].

---

[2] GaAs-based semiconductor qubits are still used today for academic experiments, but they are not considered viable for building large-scale quantum processors.

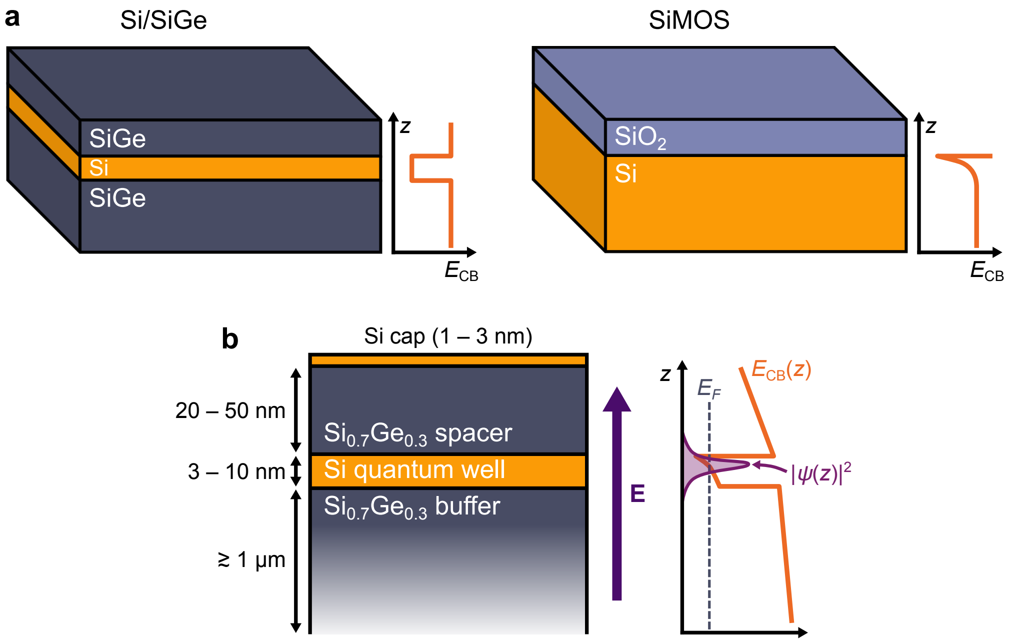

Figure 2.1: Silicon heterostructures for vertical quantum-dot confinement. **(a)** Si/SiGe and SiMOS heterostructures with their conduction-band energy minimum E_{CB} displayed as a function of depth. **(b)** Typical semiconductor stack for Si/SiGe heterostructures. Application of a vertical electric field $\mathbf{E}$ fosters 2DEG accumulation within the quantum well and pulls electronic wavefunctions $\psi(z)$ against the upper Si-SiGe interface.

2.1.1 Vertical Confinement

Figure 2.1(a) illustrates two types of planar silicon heterostructures used to host quantum-dot qubits: Si/SiGe and SiMOS. Both heterostructures are designed to confine electrons in the vertical (z) dimension through conduction band engineering. To illustrate how this works, the conduction-band energy minimum E_{CB} is plotted next to each structure as a function of depth. At sufficiently low temperatures, conduction-band electrons moving through these heterostructures naturally become stuck in the engineered energy minima. In Si/SiGe, the electrons are confined within a thin silicon **quantum well**, while in SiMOS structures, they are trapped at the Si-$\mathrm{SiO_2}$ interface. In this manner, the electrons form a **two-dimensional electron gas (2DEG)**, confined in the vertical direction but free to move laterally.

A convenient way to evaluate the quality of a heterostructure is by measuring its **electron mobility**, a parameter that quantifies how easily electrons can move through a conductor.

Higher mobility indicates fewer scattering events, allowing for more efficient electron transport through the material [46]. One key advantage of the Si/SiGe platform is its significantly higher electron mobility compared to SiMOS heterostructures. This is largely due to the smooth, epitaxial Si-SiGe interfaces in the quantum well, which allow electrons in the 2DEG to travel much farther without scattering [47–49]. In contrast, the rough Si-SiO_2 interface in SiMOS structures leads to more frequent scattering, reducing electron mobility. This reduction in mobility can be problematic for quantum dot control, as excessive disorder sometimes causes spurious dots to form in unintended locations of devices [42]. The quantum-dot devices used in experiments for this dissertation are fabricated on Si/SiGe heterostructures, so our focus will remain on this platform moving forward.

Figure 2.1(b) provides a detailed view of the typical semiconductor stack used for accumulation-mode Si/SiGe quantum-dot qubits [30, 34, 48, 50]. In this structure, a strained silicon quantum well—usually 10 nm thick or less—is sandwiched between two layers of $Si_{0.7}Ge_{0.3}$ alloy. Below the well lies the strain-relaxed SiGe ‘buffer’ layer, which is a micron or more in thickness. This layer plays a critical role in keeping the 2DEG electrons far away from lattice defects that form deeper in the substrate during chemical vapor deposition or molecular beam epitaxy growth. Above the well, a SiGe ‘spacer’ layer is grown thick enough to partially shield the electrons from the influence of charged defects in the device’s gate layers. Finally, a thin silicon ‘cap’ is grown over the heterostructure surface, facilitating device fabrication using standard silicon processing techniques. 2DEGs formed in this materials stack routinely achieve peak mobility values of order $\sim 10^5\ \mathrm{cm}^2/\mathrm{V}\cdot\mathrm{s}$ [34, 43, 46].

The lattice constant of germanium is 4.2% larger than that of silicon. As a result, embedding the silicon quantum well between layers of a relaxed germanium-containing alloy places the well under tensile strain. This strain, together with the smaller band gap of silicon compared to SiGe, creates the conduction band offset in the quantum well, lowering its energy by roughly 160 meV relative to the surrounding SiGe layers [48, 51]. As illustrated in Figure 2.1(b), applying a vertical electric field bends the conduction band near the het-

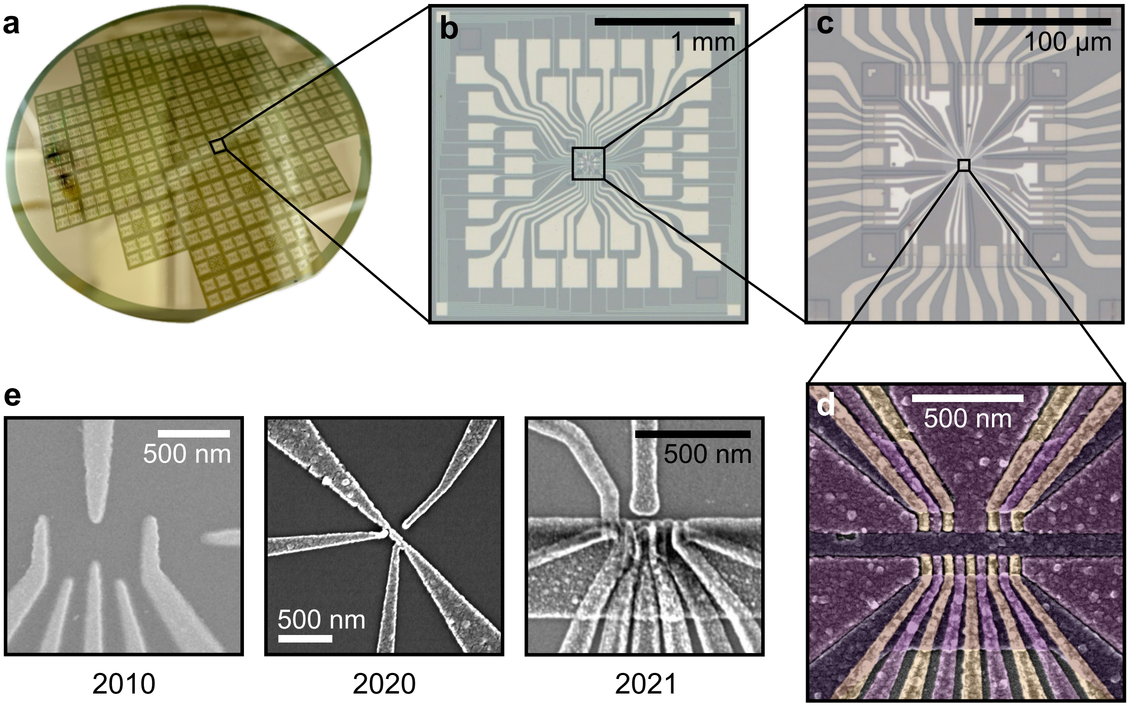

Figure 2.2: Quantum-dot device design and integration. **(a)** A three-inch wafer containing roughly 400 quantum dot and Hall bar dies. **(b,c)** Optical micrographs of a quantum-dot device die, showing bond pads and leads. **(d)** False-color, scanning electron micrograph of quantum-dot device gates. Fabrication credit: Thomas McJunkin and me. **(e)** Scanning electron micrographs of various Eriksson-group devices through the years. Fabrication credit (left to right): Christine Simmons; Justin White and me; and Nathan Holman.

---

erostructure surface. When E_{CB} dips below the Fermi energy E_F, electrons are pulled from doped regions of the substrate into the well, a process known as **accumulation**. The accumulated electrons remain trapped in a triangular potential, with their wavefunctions pulled tightly against the energy barrier at the upper quantum well interface, ensuring strong vertical confinement [52].

2.1.2 Lateral Confinement

With vertical confinement taken care of by the heterostructure, the next step in forming quantum dots is to confine the electrons laterally within the quantum well. This is accom-

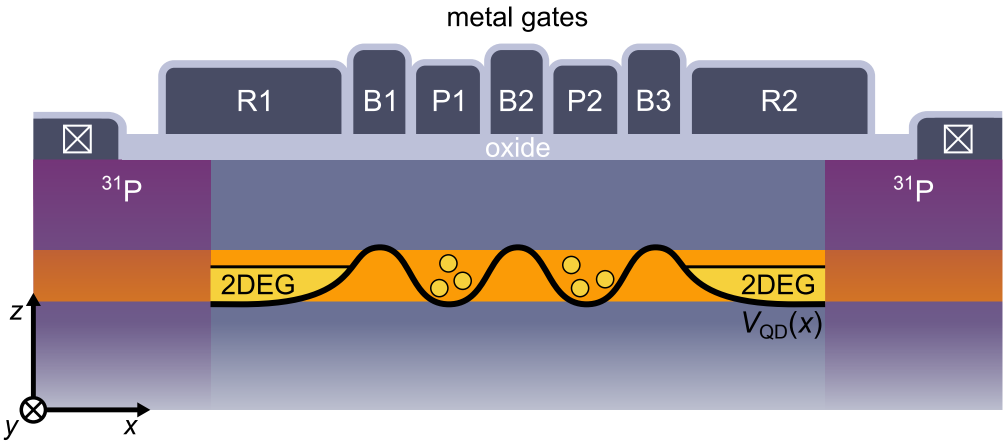

Figure 2.3: Cross-sectional view of a quantum-dot device (not to scale). Electrons are accumulated and confined by applying voltages to the metallic gates, shaping the local energy potential $V_{\mathrm{QD}}(x)$.

plished using metallic **gate electrodes**[3] fabricated above the heterostructure, which apply electrostatic fields to locally accumulate electrons in the active region of the device and corral them into dots of around 20 – 100 nm in size [51]. These same gates will later be used to control the trapped electrons' quantum states. Figures 2.2(a) through (d) display an example quantum-dot device from wafer-scale down to nanoscale. The planar geometry of the Si/SiGe platform offers considerable flexibility in device design, and gate architectures have steadily evolved in sophistication and performance over time with improvements in fabrication technology. Figure 2.2(e) shows examples of devices with different architectures fabricated by members of the Eriksson group over the years.

The leading approach today for creating one-dimensional arrays of quantum dots employs multiple layers of overlapping gates [43, 53–55]. Figure 2.3 illustrates a cross-sectional view of a typical materials stack used in devices with this architecture.[4] To enable current

---

[3] The term 'gate' has an unfortunate double meaning in both classical and quantum information processing: it is used to refer to both *gate electrodes* and *logic gates*. Although this can sometimes cause confusion for newcomers to the field—it certainly did for me—the term's meaning is generally made clear by the context in which it appears.

[4] While Fig. 2.3 depicts a two-dot device, this architecture can be extended by adding additional plunger and barrier gates to create larger arrays. Designing architectures capable of scaling quantum-dot arrays in two dimensions for more complex quantum computing applications is an active area of research [56–60].

flow between the quantum-dot system and external measurement circuits, **ohmic contacts** (labeled by '⊠' symbols in Fig. 2.3) are created by depositing metal over phosphorous-doped regions of the heterostructure. An insulating **gate dielectric**—often a few-nanometer-thick oxide layer—covers the remainder of the heterostructure surface in the active region in order to prevent current leakage to the device gates. The gates themselves sit on top of this dielectric layer. Multiple types of gates with different functions are utilized to accumulate and trap electrons. **Reservoir gates** (R1 and R2) control the **electron reservoirs**, which act as sources and sinks for electrons in the dots. These gates overlap the doped areas, accumulating 2DEG and shepherding it toward the outer edges of the quantum-dot array. **Screening gates** (not shown in Fig. 2.3) are responsible for confining electrons along the y-dimension, defining a one-dimensional channel to host the array. They also screen the dots from stray electric fields. **Plunger gates** (P1 and P2) are positioned directly above each quantum dot. By applying local electrostatic fields, these gates modify the potential energy of individual dots, allowing for precise control of the dot's electron occupancy. Finally, **barrier gates** (B1, B2, and B3) are placed on either side of each plunger. They are used to create tunable electrostatic barriers, confining electrons along the x-dimension and providing control over the rate of electron tunneling between adjacent dots, or between dots and reservoirs. The full collection of gates provides a highly configurable platform for creating and controlling quantum-dot qubits. By adjusting the gate voltages—with reservoir and plunger gates receiving more positive voltages, and screening and barrier gates receiving more negative voltages—it is possible to precisely shape the electrostatic energy landscape experienced by electrons in the quantum well. A line cut of an idealized potential, defining two dots and two reservoirs, is displayed in Fig. 2.3.

In order to form well-behaved quantum dots suitable for qubit operation, a device's gate voltages must be carefully tuned, much like tuning the strings of a guitar before a performance. This is a delicate and time-consuming process, requiring both scientific precision and intuitive skill. Further information on the methods used within the Eriksson group for device fabrication, characterization, and tune-up can be found in recent theses by Thomas McJunkin [51] and J. P. Dodson [61]. Although these aspects of the experimentalist's work are not covered here, they are an essential part of the research endeavor for semiconductor qubits.

2.2 Electron Transport & Occupancy

Harnessing the transport processes by which electrons move through and populate quantum dots plays a foundational role in operating these systems as qubits. In this section, we derive an effective model for understanding electron movement and charge occupancy in quantum-dot devices, starting from a single dot and building toward more complex architectures.

2.2.1 The Single Quantum Dot

While modeling the quantum-mechanical behavior of quantum dots can be a challenging task, it turns out that transport processes are dominated by classical, electrostatic effects, and so we can capture most of the key behavior using a *classical* circuit model. Figure 2.4(a) shows a one-dimensional, electrostatic potential for a quantum dot (QD) coupled to source (S) and drain (D) reservoirs. Electrons can move between the dot and the reservoirs by tunneling through the energy barriers controlled by gates B1 and B2. We can map this system onto an equivalent circuit diagrammed in Fig. 2.4(b), with each tunnel barrier modeled by a capacitor and resistor in parallel, following the approach of Kouwenhoven *et al.* [22].

In our effective circuit model, the quantum dot is treated as a conductive island that can be populated by electrons. Due to the dot's nanoscale dimensions, the confined electrons experience strong Coulomb repulsion, which will give rise to an energy cost associated with adding additional electrons. To derive this behavior, we start by writing the electrostatic

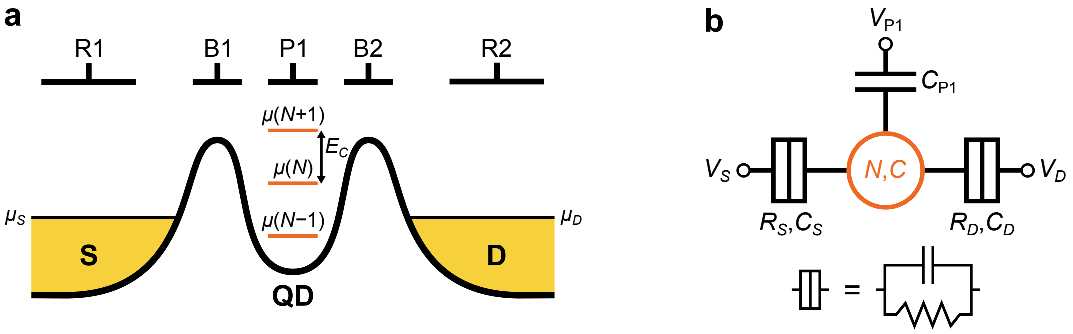

Figure 2.4: Effective circuit model for a single quantum dot. **(a)** One-dimensional potential for a quantum dot (QD) tunnel-coupled to source (S) and drain (D) reservoirs. **(b)** Equivalent circuit schematic for describing electron transport through the system in (a).

potential energy of the dot in terms of its charge Q:

$$U(Q) = \frac{Q^2}{2C}, \tag{2.1}$$

with $C = C_S + C_D + C_{\text{P1}}$ giving the dot's total capacitance with the surrounding circuit elements. The dot's total charge consists of two components: intrinsic charge from the electrons held within, and induced charge from the external voltages applied to the source, drain, and plunger electrodes:

$$Q = -eN + C_S V_S + C_D V_D + C_{\text{P1}} V_{\text{P1}}, \tag{2.2}$$

where e is the elementary charge,[5] and N is the number of electrons in the dot, or the dot's **charge occupancy**. Substituting into Eq. (2.1), the electrostatic energy becomes

$$U(N) = \frac{(-eN + C_S V_S + C_D V_D + C_{\text{P1}} V_{\text{P1}})^2}{2C}. \tag{2.3}$$

A more useful quantity for deriving transport behavior will be the **electrochemical po-**

---

[5] In this dissertation, we will take e to be positive. Thus, the charge of an electron is $-e$.

tential[6] $\mu(N)$, which we define as the energy required to add the N^{th} electron to the dot:

$$\begin{aligned}\mu(N) &\equiv U(N) - U(N-1) \\ &= E_C\left(N - \frac{1}{2}\right) - \frac{E_C}{e}(C_S V_S + C_D V_D + C_{\text{P1}} V_{\text{P1}}).\end{aligned} \tag{2.4}$$

Here, we have introduced the **charging energy** for the dot, $E_C = e^2/C$. We can interpret Eq. (2.4) as describing a 'ladder' of discrete energy levels spaced by E_C,[7] as illustrated in Fig. 2.4(a). By varying the gate voltages, the ladder can be shifted up or down in energy; however, adding another electron to the dot requires a large enough voltage shift to overcome the charging-energy barrier. This discrete energy spacing[8] between different charge occupancies is a defining characteristic of quantum dots.

Coulomb Blockade

The impact of Coulomb repulsion and discrete charge occupancies has a dramatic impact on the quantum dot's transport behavior. Consider what happens if we apply a small source-drain bias between our reservoirs, such that $V_{\text{SD}} = V_S - V_D \neq 0$. We consider the case where $eV_{\text{SD}} < E_C$, and for simplicity, we assume zero temperature. Whenever one of the dot's chemical potential levels lies within the bias window, as depicted in Fig. 2.5(a), it is energetically favorable for current to flow through the system. Electrons will tunnel through the barriers from source to drain, passing one at a time through the dot. A quantum-dot

---

[6] There is a subtle distinction between the *chemical potential*, which refers to the intrinsic energy required to add an electron to the quantum dot, and the *electrochemical potential*, which includes both the chemical potential and the effects of external voltages. Colloquially, it is common to refer to the chemical potential when, in practice, we mean the electrochemical potential. For simplicity, these terms will be used interchangeably throughout this dissertation.

[7] In real quantum dots, the level spacing is not constant as a function of N. Rather, as more electrons are added, their Coulomb repulsion increases the dot's physical size, changing its capacitance C. As a result, E_C typically decreases as the first several electrons are added, before leveling off to a more constant value for $N \gg 1$ [53, 62].

[8] It should be emphasized again that we are working in a classical framework. The discreteness of the energy spectrum has nothing to do with quantum behavior (yet)—it is purely the consequence of Coulomb repulsion and the system containing a small, integer number of electrons.

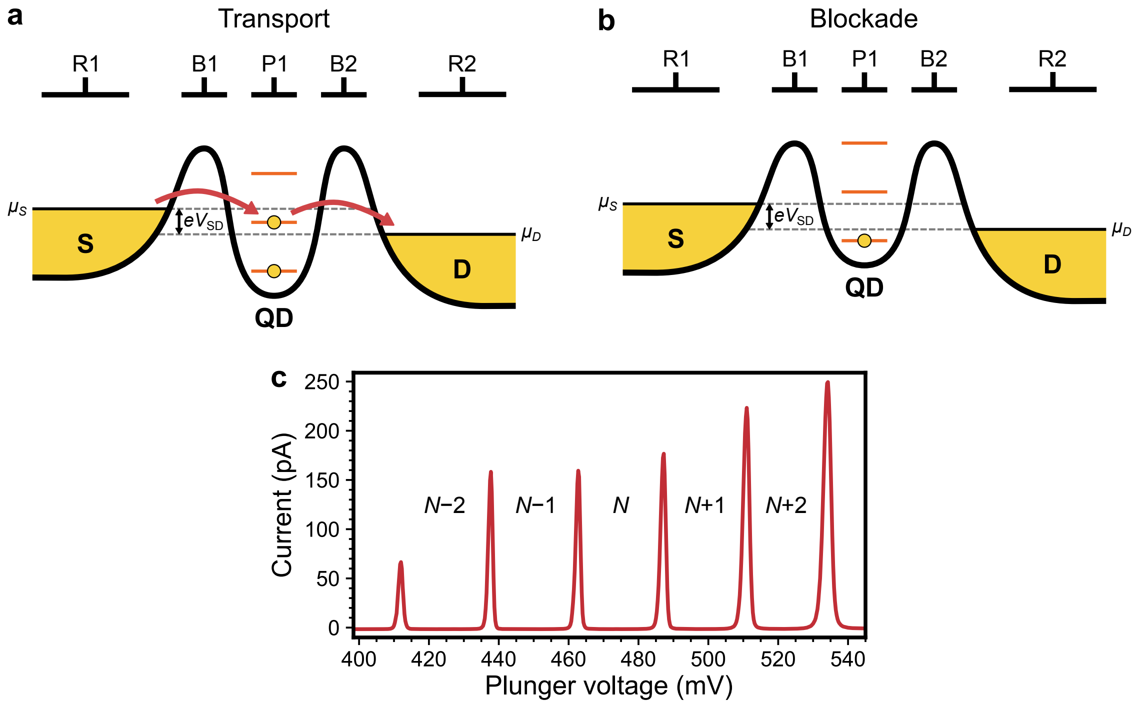

Figure 2.5: Coulomb blockade in a quantum dot. **(a)** Transport through a quantum dot when an energy level aligns with the source-drain bias window. **(b)** Coulomb blockade when no energy levels are inside the bias window. **(c)** Coulomb blockade oscillations measured in a quantum-dot device.

---

device operated in this transport regime is often referred to as a **single-electron transistor (SET)**. In contrast, when none of the chemical potential levels align with the bias window, as in Fig. 2.5(b), transport is *not* energetically allowed, and current flow is blocked. This phenomenon is called **Coulomb blockade**.

In experiments, sweeping a gate voltage will shift the ladder of energy levels, causing the measured current to oscillate periodically between zero and finite values as energy levels pass through the bias window. Figure 2.5(c) shows an example of such a measurement and its characteristic **Coulomb blockade oscillations**. The height of the Coulomb peaks is non-uniform because varying the plunger voltage also modifies the tunnel barriers, which alters the tunnel rates. In the blockade regions between current spikes, the quantum dot has a stable charge occupancy.

Gate Lever Arms

In our theoretical treatment of quantum-dot transport and occupancy, we have used energies and capacitance values to derive the system behavior. In experiments, however, these quantities are often difficult or impossible to measure directly. As experimentalists, we directly control the gate voltages applied, and so it is useful to have a conversion factor between these voltages and the dot's energy. The **lever arm** is the parameter that serves this purpose, converting changes in gate voltage to shifts of the chemical potential. Measuring lever arms is a crucial calibration step for quantum dot experiments. There are several techniques for performing these measurements; one such method is discussed in Section 5.6.4.

We can define the lever arm for a gate i as

$$\alpha_i \equiv \left| \frac{\partial \mu}{\partial V_i} \right| . \tag{2.5}$$

From Eq. (2.4), the plunger gate's lever arm in our single-dot system given by

$$\alpha_{\text{P1}} = \frac{E_C \, C_{\text{P1}}}{e} . \tag{2.6}$$

This lever arm is the one most frequently used in experiments, since the plunger is the primary gate for controlling the dot's chemical potential. However, it is important to remember that in a real device, a quantum dot has a capacitance with *every* gate, and so every gate has its own lever arm.

Quantum-Dot Energy Scales: An Interlude

Before moving on, it will be helpful to pause for a moment and get an idea of the energy scale we are working with in quantum-dot qubit experiments. A quick estimate for the charging energy can be obtained by treating the dot as a metallic disk with a radius R and self-capacitance $C = 8\epsilon_r\epsilon_0 R$ [22]. Using a relative permittivity of $\epsilon_r = 11.7$ for silicon and assuming a 50 nm dot radius, the charging energy is $E_C = e^2/C \approx 4$ meV, which corresponds to an effective temperature of roughly 46 K. In order to form quantum dots with well-defined charge occupancies, the thermal energy of electrons must be kept well below E_C, which explains (to first order) why we must conduct experiments at cryogenic temperatures. We also note that in order to observe Coulomb blockade, the effective tunnel barrier resistances (R_S and R_D in our circuit model) must be greater than the resistance quantum [63].

In reality, E_C is only the largest energy within a hierarchy of quantum-dot energy splittings, so 46 K represents an upper bound for experiments. When we discuss quantum states in Section 2.3, we will encounter energy splittings of less than 100 µeV, or 1 K. Therefore, to confine electrons to specific energy levels and achieve precise control over the quantum state of our qubits, we generally operate at electron temperatures around 50 – 120 mK.[9]

2.2.2 The Double Quantum Dot

The next step in furthering our understanding of charge occupancy is adding a second dot to the system. Figure 2.6(a) shows the electrostatic potential for a **double quantum dot (DQD)**. This system introduces an important new feature to our model: the two dots (QD1 and QD2) are not only coupled to reservoirs, but also to each other. Understanding the DQD is essential for operating quantum-dot qubits. Many qubit encodings are defined by electrons confined in DQDs [24]. Furthermore, it is common practice to analyze large-scale quantum-dot arrays by breaking the system down into pairs of DQDs for simplification.

Figure 2.6(b) shows the equivalent circuit schematic for a DQD. Ignoring other cross

---

[9] Interestingly, in some cases, silicon spin qubits can be operated at much higher temperatures—even exceeding 1 K [64–67]. The ability to run 'hot' semiconductor qubits is intriguing from an engineering standpoint, and could enable the development of processors with less stringent thermal requirements and lower operational costs. However, working at elevated temperatures requires meticulous engineering of the device, qubit encodings, and control scheme to ensure that all relevant energy splittings remain sufficiently large to avoid errors from thermal excitation.

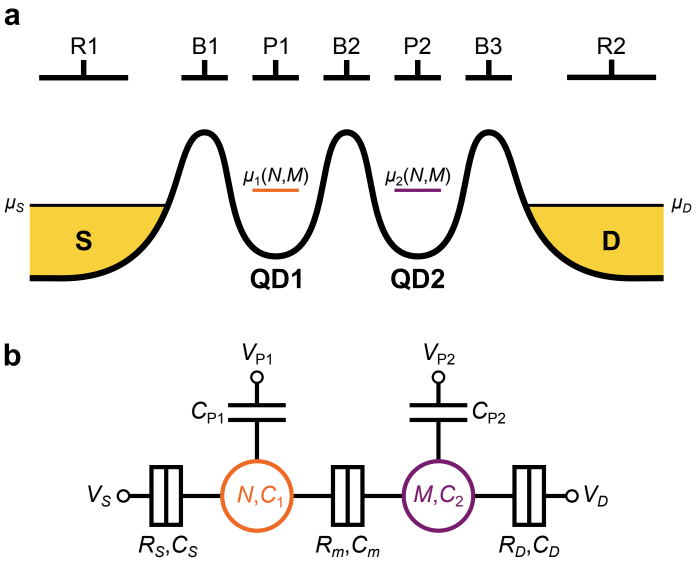

Figure 2.6: Effective circuit model for a DQD. **(a)** One-dimensional potential for two quantum dots (QD1 and QD2) tunnel-coupled to source (S) and drain (D) reservoirs. **(b)** Equivalent circuit schematic for describing electron transport through the system in (a).

capacitances (such as between V_{P1} and V_{P2}, or between V_{P1} and QD2),[10] the dots have a mutual capacitance C_m through the B2 tunnel barrier. Given our discussion of the single quantum dot in the previous section, it is straightforward to extend the circuit analysis to the DQD, following the work of van der Wiel *et al.* [23]. We can write the charging energy for each dot as

$$E_{C1} = \frac{e^2\,C_2}{C_1C_2 - C_m^2}, \qquad E_{C2} = \frac{e^2\,C_1}{C_1C_2 - C_m^2}, \tag{2.7}$$

where $C_1 = C_S + C_{\mathrm{P1}} + C_m +$ and $C_2 = C_D + C_{\mathrm{P2}} + C_m$. We can also compute an electrostatic coupling energy between the dots:

$$E_m = \frac{e^2\,C_m}{C_1C_2 - C_m^2}. \tag{2.8}$$

This quantity describes the energy shift of one dot's chemical potential when an electron is added to the other dot. Using these terms, the chemical potentials for each dot in the DQD

---

[10] This assumption is, of course, an oversimplification. Real devices feature intricate capacitance networks, with numerous capacitances between dots, gates, PCB traces, and ground influencing the overall device behavior.

are given by

$$\begin{aligned} \mu_1(N,M) &= E_{C1}\left(N-\frac{1}{2}\right)+E_mM-\frac{1}{e}(E_{C1}C_{\mathrm{P1}}V_{\mathrm{P1}}+E_mC_{\mathrm{P2}}V_{\mathrm{P2}}), \\ \mu_2(N,M) &= E_{C2}\left(M-\frac{1}{2}\right)+E_mN-\frac{1}{e}(E_mC_{\mathrm{P1}}V_{\mathrm{P1}}+E_{C2}C_{\mathrm{P2}}V_{\mathrm{P2}}), \end{aligned} \tag{2.9}$$

where N is the electron occupancy of QD1, and M is the electron occupancy of QD2. In these expressions, we have disregarded the influence of the source and drain voltages, as quantum-dot qubits are typically operated with fixed reservoir voltages and $V_{\mathrm{SD}} = 0$. Without loss of generality, we can let $V_S = V_D = 0$, and similarly, $\mu_S = \mu_D = 0$.

Just as for the single quantum dot, we can define lever arms for the plunger gates that allow conversion between energy and voltage. However, because of the coupling between the dots, each dot's chemical potential can be shifted by *either* plunger. This introduces the need for a broader set of lever arms. Defining the lever arm between dot i and gate j as

$$\alpha_j^i \equiv \left|\frac{\partial \mu_i}{\partial V_j}\right|, \tag{2.10}$$

the four plunger lever arms for the DQD system are

$$\begin{aligned} \alpha_{\mathrm{P1}}^1 &= \frac{E_{C1}\,C_{\mathrm{P1}}}{e}, & \alpha_{\mathrm{P2}}^1 &= \frac{E_{Cm}\,C_{\mathrm{P2}}}{e}, \\ \alpha_{\mathrm{P1}}^2 &= \frac{E_{Cm}\,C_{\mathrm{P1}}}{e}, & \alpha_{\mathrm{P2}}^2 &= \frac{E_{C2}\,C_{\mathrm{P2}}}{e}. \end{aligned} \tag{2.11}$$

The Charge Stability Diagram

As the chemical potentials of each dot are varied, the energetically favored arrangement of electrons within the system changes. A useful way to visualize these changes is by plotting the equipotentials where the various chemical potentials align. Figure 2.7(a) plots these equipotentials in two dimensions, mapped against the plunger voltages. This type of visualization, known as a **charge stability diagram**, is perhaps the most commonly used method

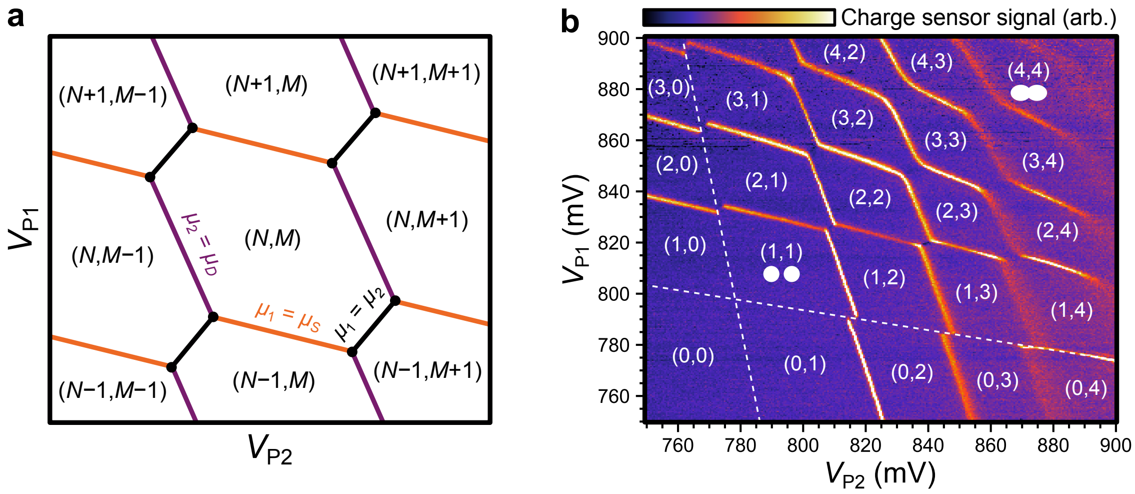

Figure 2.7: DQD charge stability diagrams. **(a)** Charge stability diagram derived by plotting equipotentials where the DQD chemical potentials align as a function of the plunger voltages. Each cell corresponds to a stable charge configuration, and crossing between cells represents an electron transition within the system. **(b)** Experimentally measured charge stability diagram. Charge configurations are indicated for each cell, and transition lines that are not visible have been marked by dashed lines. The dots' approximate shapes in the (1,1) and (4,4) configurations are indicated by white ovals.

---

for analyzing charge occupancy in quantum dots [23].

We can identify two categories of equipotentials in Fig. 2.7(a). First, there are equipotentials where a quantum-dot level aligns with a reservoir potential: $\mu_1 = \mu_S$ (shown in orange), or $\mu_2 = \mu_D$ (shown in purple). We refer to these as **charge transition lines**, as crossing one corresponds to an electron tunneling between QD1 or QD2 and the neighboring reservoir, thereby changing the total number of charges in the DQD by one. Second, there are equipotentials where two quantum-dot levels align: $\mu_1 = \mu_2$ (shown in black). Crossing one of these **polarization lines** represents an *interdot* transition, with an electron hopping from QD1 to QD2, or vice versa. Together, the plotted equipotentials form a honeycomb lattice. Each lattice cell corresponds to a stable **charge configuration** of the DQD, denoted by the notation (N, M). The height and width of the cells are proportional to the dots' charging energies, E_{C1} and E_{C2}, respectively. The slopes of the charge transition lines and the width of the interdot transitions are directly determined by the strength of the interdot coupling E_m. The points where the charge transition and polarization lines meet (marked by black dots) are called **triple points**, as they signify the energy alignment of three different charge configurations (or equivalently, all four chemical potentials).

Figure 2.7(b) presents an experimentally measured charge stability diagram, which shows the distinctive honeycomb pattern expected from theory. The charge transition lines are not measured via transport (since $V_{\mathrm{SD}} = 0$), but by using a device component called a charge sensor—we will discuss this further in later chapters.[11] Looking closely, we can spot a few differences between this plot and the theoretical version in panel (a). First, the charging energies of each dot—reflected in the dimensions of the lattice cells—are not constant with plunger voltage, as we previously noted for the single quantum dot. Second, the charge transition lines exhibit some amount of curvature due to interaction nonlinearities not captured by our classical circuit model. And third, the interdot transitions become wider toward the upper right corner of the plot. This is because increasing the plunger voltages and adding electrons expands the dots' physical sizes, causing them to overlap, and increasing the coupling energy E_m [we indicate this by the white ovals in Fig. 2.7(b)]. In the lower left corner of the stability diagram, we see the (0,0) cell where both dots have been completely emptied of electrons. Reducing the plunger voltages further beyond this region will not lead to additional charge transitions.

Detuning

An important control knob for operating quantum-dot qubits is the **detuning** ε, which parameterizes the 'energy tilt' of a DQD, as depicted in Fig. 2.8(a). Formally, we define the DQD detuning as the difference between the chemical potentials of the dots:

$$\varepsilon \equiv \pm(\mu_1 - \mu_2), \tag{2.12}$$

---

[11] The stability diagram in Fig. 2.7(b) is from the device featured in Chapters 5 and 6. It is measured by using the sample's superconducting resonator for dispersive charge sensing.

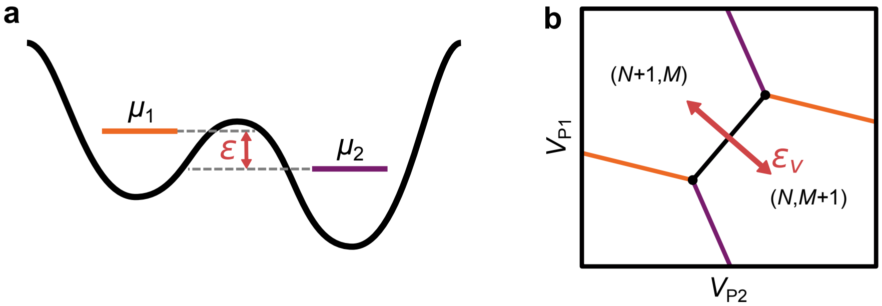

Figure 2.8: DQD detuning. **(a)** One-dimensional DQD potential showing the energy detuning ε between the chemical potentials of the dots. **(b)** Charge stability diagram shown near the $(N+1, M) - (N, M+1)$ interdot transition. The voltage detuning ε_v is measured along the axis perpendicular to the polarization line.

---

where the choice of the leading sign is arbitrary. Using detuning brings a degree of notational simplicity to our expressions—it is usually more convenient to write the Hamiltonian of a DQD-based qubit in terms of ε rather than referencing the individual dot energies.

In charge stability diagrams, the detuning can be measured along an axis perpendicular to the polarization line at an interdot transition, as Fig. 2.8(b) shows. Here, we make a distinction between the *energy* detuning (ε) and the *voltage* detuning,

$$\varepsilon_v = \pm\left(\frac{\mu_1}{\alpha^1_{\mathrm{P1}}} - \frac{\mu_2}{\alpha^2_{\mathrm{P2}}}\right) + \mathrm{const.} \tag{2.13}$$

The polarization line corresponds to the equipotential where $\varepsilon = 0$; as the plunger voltages are swept across this line, it becomes energetically favorable for an electron to tunnel between the two dots. From the stability diagram depiction, it is evident that detuning can be controlled by varying either plunger voltage individually, or both in unison. We can therefore assign lever arms for adjusting the detuning in terms of the single-dot lever arms defined in Eq. (2.11):

$$\begin{aligned} \alpha^{\varepsilon}_{\mathrm{P1}} &\equiv \left|\frac{\partial\varepsilon}{\partial V_{\mathrm{P1}}}\right| = \alpha^1_{\mathrm{P1}} - \alpha^2_{\mathrm{P1}}, \\ \alpha^{\varepsilon}_{\mathrm{P2}} &\equiv \left|\frac{\partial\varepsilon}{\partial V_{\mathrm{P2}}}\right| = \alpha^2_{\mathrm{P2}} - \alpha^1_{\mathrm{P2}}. \end{aligned} \tag{2.14}$$

2.2.3 Crosstalk & Virtual Gates

We have already pointed out that adjusting one of the plunger voltages in the DQD system not only shifts the chemical potential of the dot directly below—it also influences the neighboring dot's energy. This is clearly reflected in the slopes of the charge transition lines on a stability diagram. Looking, for instance, at an orange QD1 transition line in Fig. 2.7(a), we see that it has a negative slope with respect to V_{P2}—indicating that changing V_{P2} alters μ_1. Mathematically, we can emphasize the interdependence of the chemical potentials on the plunger voltages by rewriting Eq. (2.9) using lever arms in Eq. (2.11), obtaining

$$\begin{aligned} \mu_1(N, M; V_{\mathrm{P1}}, V_{\mathrm{P2}}) &= f_1(N, M) - (\alpha^1_{\mathrm{P1}} V_{\mathrm{P1}} + \alpha^1_{\mathrm{P2}} V_{\mathrm{P2}}), \\ \mu_2(N, M; V_{\mathrm{P1}}, V_{\mathrm{P2}}) &= f_2(N, M) - (\alpha^2_{\mathrm{P1}} V_{\mathrm{P1}} + \alpha^2_{\mathrm{P2}} V_{\mathrm{P2}}), \end{aligned} \tag{2.15}$$

where, for notational simplicity, we have introduced the terms $f_1(N, M)$ and $f_2(N, M)$ to quantify the charge occupancy-dependent part of each function.

What we are observing is an example of electrostatic **crosstalk** within the DQD system. In a broader sense, crosstalk refers to unintended interactions within a quantum processor, typically caused when control signals affect more than just the targeted dot or qubit. Capacitive crosstalk between different device components is an unavoidable obstacle when working with quantum processors. If not carefully accounted for in the engineering of devices and control protocols, it can lead to serious errors in qubit operations.

One approach for partially mitigating capacitive crosstalk in quantum-dot devices is the use of **voltage compensation**. This technique adjusts the voltages applied to non-targeted gates to counterbalance the effects of crosstalk. As an example, if the voltage on P2 of the DQD is stepped by an amount δV_{P2}, we can use Eq. (2.15) to apply a compensating adjustment to P1; to hold μ_1 constant, this compensating voltage should be $\delta V_{\mathrm{P1,\,comp}} = \alpha^1_{\mathrm{P2}}\,\delta V_{\mathrm{P2}}$ (assuming that the DQD charge configuration remains fixed). Likewise, in order to keep μ_2 constant when P1 is stepped by δV_{P1}, the compensating voltage applied to P2 is

$\delta V_{\mathrm{P2,\,comp}} = \alpha^2_{\mathrm{P1}}\,\delta V_{\mathrm{P1}}$.

A systematic way to implement voltage compensation in devices is through the use of **virtual gates** [68–70]. This framework creates an abstraction layer over the physical gate voltages within a device, enabling independent control over quantum-dot parameters while offsetting crosstalk. Each virtual plunger gate voltage $u_{\mathrm{P}i}$ is defined by a linear combination of the physical plunger gate voltages[12], which can be efficiently expressed as a matrix equation. For the DQD plunger-voltage compensation scenario we just considered, the virtual plunger gates are defined by

$$\begin{pmatrix} u_{\mathrm{P1}} \\ u_{\mathrm{P2}} \end{pmatrix} = \begin{pmatrix} 1 & \alpha^1_{\mathrm{P2}}/\alpha^1_{\mathrm{P1}} \\ \alpha^2_{\mathrm{P1}}/\alpha^2_{\mathrm{P2}} & 1 \end{pmatrix} \begin{pmatrix} V_{\mathrm{P1}} \\ V_{\mathrm{P2}} \end{pmatrix} = \begin{pmatrix} 1 & \beta^1_{\mathrm{P2}} \\ \beta^2_{\mathrm{P1}} & 1 \end{pmatrix} \begin{pmatrix} V_{\mathrm{P1}} \\ V_{\mathrm{P2}} \end{pmatrix}, \tag{2.16}$$

where the dimensionless parameter $\beta^i_j \equiv \alpha^i_j/\alpha^i_{\mathrm{P}i}$ measures the degree of crosstalk between dot i and gate j. Expressing the chemical potentials in Eq. (2.15) in terms of these virtual voltages makes clear that each virtual plunger provides independent control of its corresponding dot:

$$\begin{aligned} \mu_1(N, M; u_{\mathrm{P1}}, u_{\mathrm{P2}}) &= f_1(N, M) - \alpha^1_{\mathrm{P1}} u_{\mathrm{P1}}, \\ \mu_2(N, M; u_{\mathrm{P1}}, u_{\mathrm{P2}}) &= f_2(N, M) - \alpha^2_{\mathrm{P2}} u_{\mathrm{P2}}. \end{aligned} \tag{2.17}$$

Figure 2.9 compares examples of the same charge stability diagram measured in physical voltage space and virtual voltage space, with panel (a) showing a theoretical depiction, and panel (b) showing measurements by Mills *et al.* [70]. In virtual voltage space, the charge transition lines are nicely straightened out, running perpendicular to their corresponding plunger axes.

What if we wish to extend the virtual gates framework, so that the quantum-dot chemical potentials are held constant when non-plunger gate voltages are varied? This is easily accomplished by expanding the conversion relation in Eq. (2.16) to include additional gates,

---

[12] Since virtual gate voltages are derived from combinations of multiple physical voltages, their values do not correspond to any directly measurable quantity. Therefore, in plots, we will represent virtual voltages using imaginary units, abbreviated by ‘$\tilde{\mathrm{V}}$’

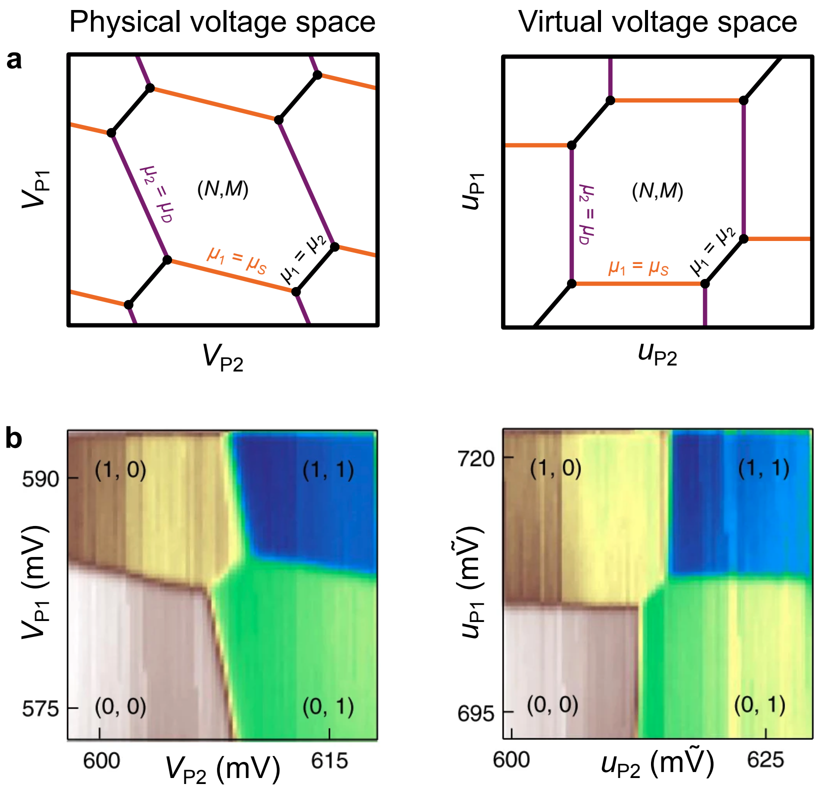

Figure 2.9: Comparison of charge stability diagrams plotted in physical and virtual voltage space: **(a)** theoretical depiction; and **(b)** experimental example, adapted from Ref. [70]. Virtual voltage units are abbreviated by '$\tilde{\text{V}}$.'

---

leveraging the linear relationship between chemical potential and gate voltage. As an example, to compensate the DQD plunger voltages against the entire set of device gates shown in Fig. 2.6(a), the virtual voltages are defined

$$\begin{pmatrix} u_{\text{P1}} \\ u_{\text{P2}} \\ u_{\text{B1}} \\ u_{\text{B2}} \\ u_{\text{B3}} \\ u_{\text{R1}} \\ u_{\text{R2}} \end{pmatrix} = \begin{pmatrix} 1 & \beta^1_{\text{P2}} & \beta^1_{\text{B1}} & \beta^1_{\text{B2}} & \beta^1_{\text{B3}} & \beta^1_{\text{R1}} & \beta^1_{\text{R2}} \\ \beta^2_{\text{P1}} & 1 & \beta^2_{\text{B1}} & \beta^2_{\text{B2}} & \beta^2_{\text{B3}} & \beta^2_{\text{R1}} & \beta^2_{\text{R2}} \\ 0 & 0 & 1 & 0 & 0 & 0 & 0 \\ 0 & 0 & 0 & 1 & 0 & 0 & 0 \\ 0 & 0 & 0 & 0 & 1 & 0 & 0 \\ 0 & 0 & 0 & 0 & 0 & 1 & 0 \\ 0 & 0 & 0 & 0 & 0 & 0 & 1 \end{pmatrix} \begin{pmatrix} V_{\text{P1}} \\ V_{\text{P2}} \\ V_{\text{B1}} \\ V_{\text{B2}} \\ V_{\text{B3}} \\ V_{\text{R1}} \\ V_{\text{R2}} \end{pmatrix}. \tag{2.18}$$

This transformation does not apply any crosstalk compensation to the barrier or reservoir gate voltages (i.e., $u_{\text{B}i} = V_{\text{B}i}$; $u_{\text{R}i} = V_{\text{R}i}$). In principle, barrier gate voltages can be virtualized to provide independent control of the tunnel barriers between dots. However, in this dissertation—and in most experiments—device barrier gates are not virtualized.[13] The methodology above can be further extended to include an arbitrary number of device gates using the general relation

$$\mathbf{u} = \mathbf{X}\mathbf{V}, \tag{2.19}$$

where $\mathbf{u}$ and $\mathbf{V}$ are vectors containing the virtual and physical gate voltages, and $\mathbf{X}$ is a matrix containing the β^i_j coefficients used for conversion. We will refer to $\mathbf{X}$ as the 'crosstalk matrix' going forward, since its elements parameterize the amount of crosstalk between each dot-gate pair in the device.

The virtual gates abstraction offers a massive simplification during quantum-dot experiments, especially for large-scale systems with many device gates. It allows us, as human experimentalists, to think in terms of idealized virtual voltages, avoiding the headache of capacitively coupled physical gates. Meanwhile, with a bit of behind-the-scenes linear algebra, our control computers can easily handle the task of translating virtual voltages into physical voltages, which are then sent to the control instruments. This approach greatly streamlines the process of device tune-up and control pulse programming, making operation more intuitive and efficient.

Implementing virtual gates in a quantum-dot device requires knowledge of the various β^i_j coefficients which populate the device's crosstalk matrix—for a device with many dots and gates, this can involve numerous parameters. Fortunately, due to the device geometry, it is usually not necessary to calibrate every matrix element. Gate-to-dot cross capacitance decreases with distance, and in many cases, the crosstalk from distant gates has negligible impact on the dots. As a result, it is common to assume that $\beta^i_j \approx 0$ for gates beyond the nearest few to any particular dot. For example, in the DQD crosstalk matrix in Eq. (2.18),

---

[13] The primary reason that virtual barrier gates are seldom used is because the tunnel coupling between dots has an *exponential* dependence on barrier voltage [69, 71] Therefore, fully virtualizing the barriers requires modifying Eq. (2.18) to include higher-order terms. The non-linearity makes virtual barrier gates much trickier to calibrate than virtual plungers, and much more susceptible to small calibration errors. For examples of experiments where virtual barrier gates are implemented, refer to Refs. [69, 71, 72].

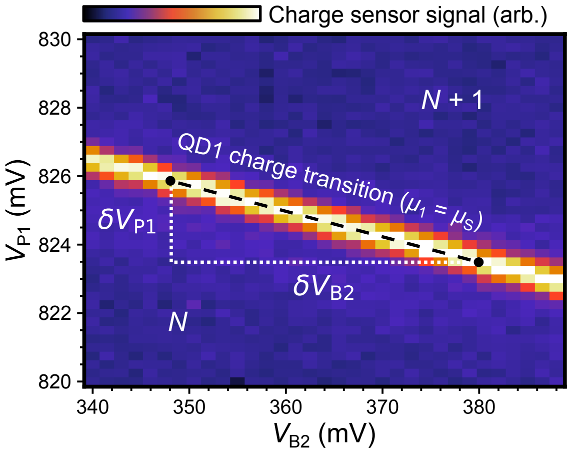

Figure 2.10: Example of a gate-to-dot crosstalk measurement. The dot's plunger gate, P1, is swept through a charge transition line while simultaneously varying a neighboring barrier gate, B2. The crosstalk matrix element β^1_{B2} can be extracted from the slope of the transition line, $(\delta V_{\mathrm{P1}}/\delta V_{\mathrm{B2}})_1$.

one might reasonably assume that $\beta^1_{\mathrm{B3}} \approx 0$, and focus their time on calibrating the more dominant crosstalk matrix elements. The remaining β^i_j coefficients can be extracted from charge transition line slopes measured in two-dimensional gate voltage sweeps. To demonstrate, Fig. 2.10 shows an example of a scan from a DQD, where the plunger P1 and neighboring barrier B2 are swept in the vicinity of a QD1 charge transition line. We denote the slope of the line as $(\delta V_{\mathrm{P1}}/\delta V_{\mathrm{B2}})_1$, with the subscript indicating that the measurement is performed over a QD1 transition. From Eq. (2.10), the B2 lever arm for this dot is

$$\alpha^1_{\mathrm{B2}} = \left|\frac{\partial \mu_1}{\partial V_{\mathrm{B2}}}\right| = \left|\frac{\partial \mu_1}{\partial V_{\mathrm{P1}}}\left(\frac{\delta V_{\mathrm{P1}}}{\delta V_{\mathrm{B2}}}\right)_1\right| = \alpha^1_{\mathrm{P1}}\left|\left(\frac{\delta V_{\mathrm{P1}}}{\delta V_{\mathrm{B2}}}\right)_1\right|, \tag{2.20}$$

thus the crosstalk matrix element β^1_{B2} corresponds to the magnitude of the slope: $\beta^1_{\mathrm{B2}} = |(\delta V_{\mathrm{P1}}/\delta V_{\mathrm{B2}})_1|$. More generally, the matrix element quantifying crosstalk between dot i and gate j is given by

$$\beta^i_j = \left|\left(\frac{\delta V_{\mathrm{P}i}}{\delta V_j}\right)_i\right|, \tag{2.21}$$

This measurement technique can be repeated for multiple gates to efficiently populate the crosstalk matrix, *provided that each dot is tunnel-coupled to a reservoir.* We will revisit the topic of virtual gate calibration in Section 3.3.3.

2.3 Quantum States & Degrees of Freedom

The isolated electrons within a quantum dot are quantum-mechanical objects with discrete states and energy levels. These quantum states can be used to encode and manipulate quantum information. However, the spectrum of states in any quantum dot is shaped by a complex interplay of multiple **quantum degrees of freedom**. We now examine each of these degrees of freedom individually to build up our understanding of the mechanisms underlying semiconductor qubit encodings.

2.3.1 The Charge Degree of Freedom

In the previous section, by treating quantum dots as classical circuit elements, we were able to derive explicit charge configurations, where each dot in the system holds a fixed number of electrons. However, we must keep in mind that electrons possess spatial wavefunctions that may extend beyond the confinement potential of a single quantum dot, venturing into and crossing through classically forbidden zones.

This effect becomes evident if we study a strongly coupled pair of quantum dots containing a single electron. Figure 2.11(a) depicts this DQD system, where the barrier-gate-tunable tunneling rate between the dots is parameterized by the **tunnel coupling** t_c. When the dot energies are detuned such that $|\varepsilon| > t_c$, the electron's wavefunction becomes localized to one dot or the other, and the DQD charge configurations correspond to quantum **charge states**: $|L\rangle \leftrightarrow (1,0)$ and $|R\rangle \leftrightarrow (0,1)$. The DQD system can be described by a two-level Hamiltonian written in the $\{|L\rangle, |R\rangle\}$ basis as [73]

$$\hat{H}_{\text{charge}} = \begin{pmatrix} \varepsilon/2 & t_c \\ t_c & -\varepsilon/2 \end{pmatrix}. \tag{2.22}$$

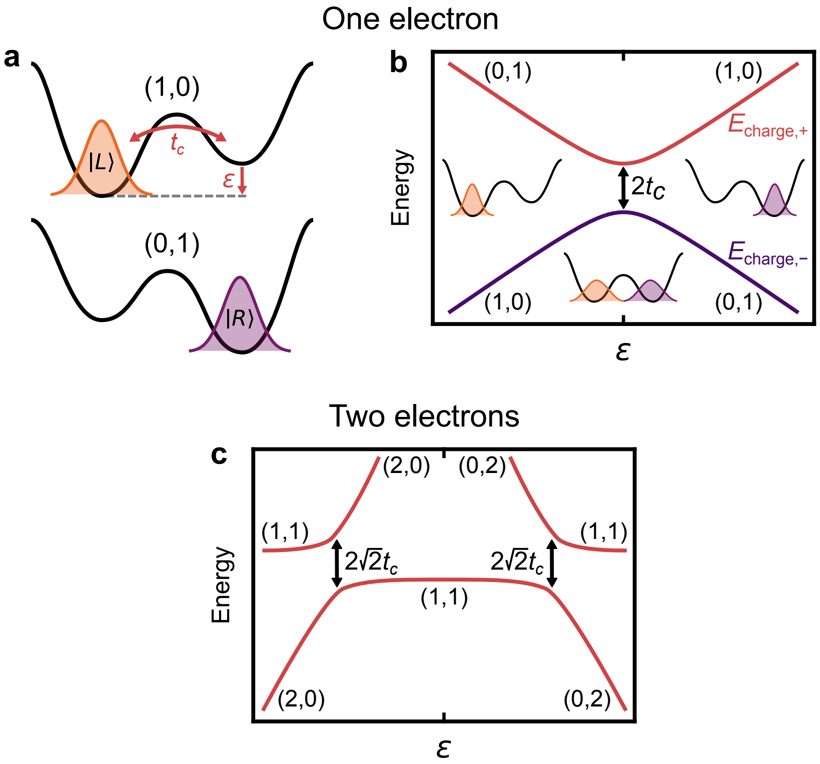

Figure 2.11: Charge states in DQDs. **(a)** Charge state definitions for a one-electron DQD with tunnel coupling t_c. When the dots are detuned, the electron's wavefunction is localized to one dot, and the $(1,0)$ and $(0,1)$ charge configurations map to the quantum charge states $|L\rangle$ and $|R\rangle$. **(b)** Energy spectrum for the system in (a), plotted as a function of DQD detuning ε. An avoided level crossing with energy splitting $2t_c$ occurs at the interdot transition ($\varepsilon = 0$). Electron wavefunctions are illustrated for $\varepsilon < -t_c$, $\varepsilon = 0$, and $\varepsilon > t_c$. **(c)** Energy spectrum for a two-electron DQD, showing avoided level crossings of $2\sqrt{2}t_c$ at the $(2,0)-(1,1)$ and $(1,1)-(0,2)$ interdot transitions.

Diagonalizing this Hamiltonian results in a pair of energy levels,

$$E_{\text{charge},\pm} = \pm\frac{1}{2}\sqrt{\varepsilon^2 + 4t_c^2}, \tag{2.23}$$

which are plotted in Fig. 2.11(b). The corresponding eigenstates are

$$\begin{aligned} |+\rangle &= \cos\left(\frac{\theta}{2}\right)|L\rangle + \sin\left(\frac{\theta}{2}\right)|R\rangle\,, \\ |-\rangle &= \sin\left(\frac{\theta}{2}\right)|L\rangle - \cos\left(\frac{\theta}{2}\right)|R\rangle\,, \end{aligned} \tag{2.24}$$

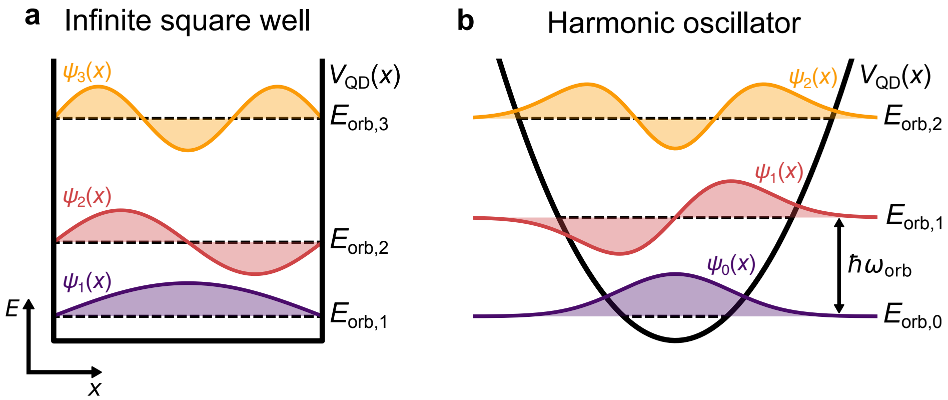

Figure 2.12: Orbital energy levels and wavefunction real parts plotted for a quantum dot, where the one-dimensional confinement potential $V_{\mathrm{QD}}(x)$ is **(a)** an infinite square well potential; and **(b)** a harmonic oscillator potential.

where $\tan\theta = 2t_c/\varepsilon$. This analysis reveals that the charge states become hybridized near the interdot transition, causing the electron's wavefunction to spread across both dots. At $\varepsilon = 0$, the energy levels exhibit an avoided crossing with a gap of $\Delta E_{\mathrm{charge}} = 2t_c$, and the electron is equally likely to be found in either dot when measured.

Figure 2.11(c) shows the energy levels obtained from a similar analysis of a two-electron DQD [24]. In this system, there are three possible charge configurations which can be mapped to quantum charge states: $(2,0)$, $(1,1)$, and $(0,2)$. Once again, we see evidence of charge-state hybridization, with avoided level crossings of $\Delta E_{\mathrm{charge}} = 2\sqrt{2}t_c$ at each interdot transition.[14]

2.3.2 The Orbital Degree of Freedom

Like the 'particle in a box' studied in introductory quantum mechanics courses, an electron in a quantum dot has quantized energy states arising from its nanoscale confinement potential. These **orbital states** correspond to different spatial configurations of the electron's

---

[14] Note that in this two-electron system, the $\varepsilon = 0$ point is chosen to be in the (1,1) charge configuration. It follows that the interdot transitions are at $|\varepsilon| > 0$, as significant detuning is required to overcome Coulomb repulsion so that the $(2,0)$ or $(0,2)$ charge configurations are energetically favored.

wavefunction.[15] The energies and spatial profiles of orbital states are determined by the specific details of a quantum dot's three-dimensional confinement potential. Nevertheless, we can gain useful intuition by considering one-dimensional toy-model potentials.

Perhaps the simplest model is an infinite square well potential, known well to every physicist. For a dot of length L with this type of confinement, the n^{th} orbital energy level is given by

$$E_{\text{orb},n} = \frac{\pi^2 \hbar^2 n^2}{2m^* L^2}, \quad n = 1, 2, 3... \tag{2.25}$$

where $m^* = 0.19 m_e$ represents the effective mass of an electron in silicon. Figure 2.12(a) plots the first three energy levels and wavefunctions for the square-well potential. The orbital energies increase quadratically with n, which is not typical for quantum dots. However, the $E_{\text{orb},n} \propto 1/m^* L^2$ scaling in Eq. (2.25) is a good match to experimental data.

A more accurate confinement potential, frequently used in theoretical modeling of quantum dots, is the harmonic oscillator potential [74,75]. As shown in Fig. 2.12(b), this potential creates evenly spaced orbital levels of

$$E_{\text{orb},n} = \hbar \omega_{\text{orb}} \left(n + \frac{1}{2} \right), \quad n = 0, 1, 2... \tag{2.26}$$

where the 'frequency' ω_{orb} characterizes the strength of the confinement.

An important system parameter for qubit experiments is the **orbital splitting** ΔE_{orb}, which measures the energy splitting between the first two orbital levels in a quantum dot. For a dot size of 50 nm, the harmonic-oscillator model predicts an orbital splitting of $\Delta E_{\text{orb}} = \hbar \omega_{\text{orb}} = 4\hbar / m^* L^2 \approx 0.6$ meV [74]. The square-well model predicts a larger splitting of $\Delta E_{\text{orb}} = E_{\text{orb},2} - E_{\text{orb},1} \approx 2.4$ meV, using Eq. (2.25). Both of these estimates fall within the typical range of orbital splittings measured in Si/SiGe quantum dots [53, 76–78].

---

[15] Quantum dots are sometimes called 'artificial atoms' due to their resemblance to the energy level structure of real atoms.

2.3.3 The Valley Degree of Freedom

Silicon is an indirect-bandgap semiconductor, meaning that the valence-band maximum and conduction-band minimum occur at different points in the Brillouin zone. Figure 2.13(a) shows a one-dimensional plot of the energy dispersion in bulk silicon along the $L - \Gamma - X$ trajectory in the Brillouin zone [see the dotted black lines in panel (b)]. The minimum conduction-band energy, highlighted in orange, is located near the zone boundary at $k_0 \approx 0.85(2\pi/a_{\mathrm{Si}})$, where $a_{\mathrm{Si}} = 0.543$ nm is the silicon lattice constant [34]. This energy minimum, known as a 'valley,' forms a bandgap of about 1.1 eV with the valence band maximum at the Γ ($k = 0$) point.

Due to the Brillouin zone's three-dimensional symmetry, bulk silicon has six energy-degenerate valleys located along the k_x, k_y, and k_z axes, as Fig. 2.13(b) depicts. However, when silicon is subjected to lateral tensile strain in a Si/SiGe heterostructure, the six-fold degeneracy splits into a four-fold plus two-fold degenerate structure. The $k_{\pm x}$ and $k_{\pm y}$ valleys (yellow) in the plane of the applied strain are raised in energy, while the $k_{\pm z}$ valleys (purple) are lowered, creating an energy gap of around 200 meV [47]. Figure 2.13(c) illustrates this effect.

The low-energy $k_{\pm z}$ valleys are the ones that matter for qubit operation (the other four valleys sit well above the system's thermal and confinement energy scales). The degeneracy of these valleys introduces another degree of freedom to the quantum-dot system, concentrating the momentum-space wavefunctions of confined electrons into two distinct **valley states** $|k_{\pm z}\rangle$. The valley-state degeneracy can be broken by interface effects, where different oscillation phases of the $|k_{+z}\rangle$ and $|k_{-z}\rangle$ real-space wavefunctions, together with the abrupt change in potential at the upper quantum-well interface, induce a small **valley splitting** ΔE_{val} [74, 79–81]. Experimentally measured valley splittings in Si/SiGe quantum dots typically fall within the range of $10 - 300$ µeV, and in some cases approach zero, as indicated in Fig. 2.13(c) [53, 77, 82–85]. The lower end of this range is problematic, as it means that even tiny energy fluctuations can cause encoded information to leak between valley states [86–89].

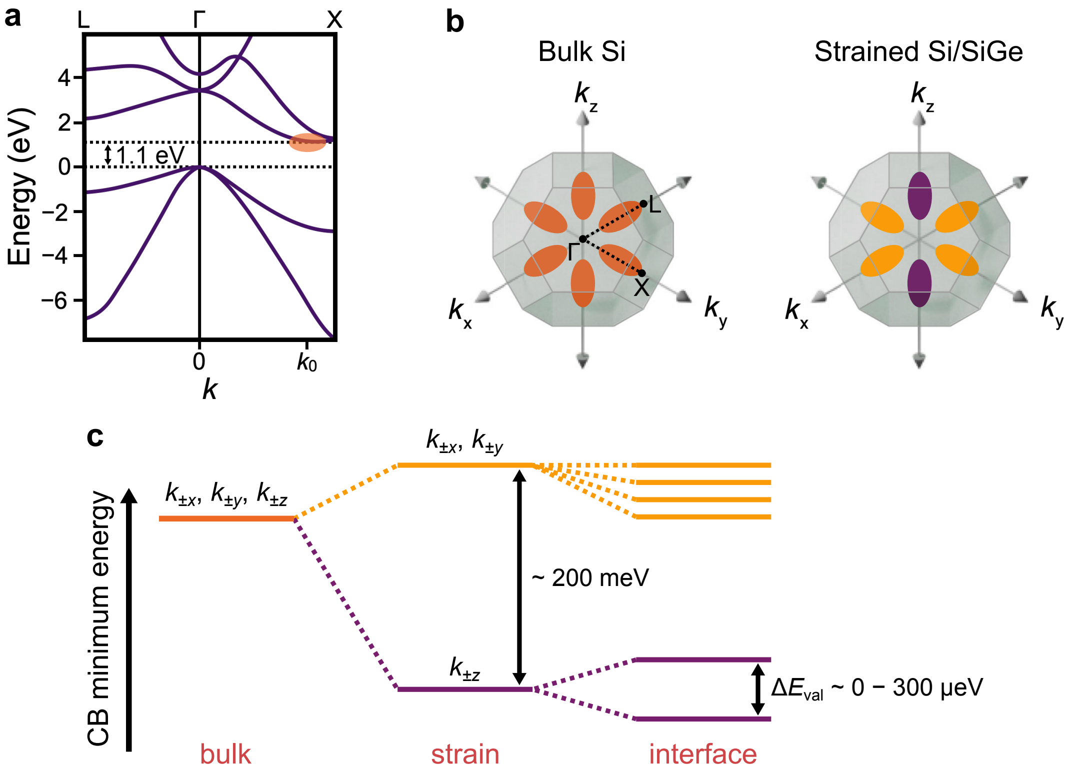

Figure 2.13: Valley states in strained silicon quantum wells. **(a)** Portion of the energy band structure for bulk silicon along symmetric axes of the Brillouin zone. The minimum-energy valley in the conduction band is highlighted at $k = k_0$ near the zone boundary. **(b)** Valley locations for bulk silicon and strained Si/SiGe. In bulk silicon, there are six energy-degenerate valleys (orange); introducing tensile strain lifts the degeneracy between the transverse (yellow) and longitudinal (purple) valleys. **(c)** Energy splitting between valley states in Si/SiGe heterostructures. The six-fold valley degeneracy is broken by strain and interface effects, creating a small valley splitting ΔE_{val} between the $|k_{\pm z}\rangle$ valley states. (b) adapted with permission from Ref. [24]. © 2023 by the American Physical Society.

Equally concerning is the fact that valley splitting is highly sensitive to atomistic details where the confined electrons' wavefunctions overlap with the quantum-well interface, making it a largely uncontrolled variable that can vary significantly between different dots in an array [77, 81, 90–92]. Consequently, valley splitting presents one of the major obstacles to scaling silicon-based quantum-dot qubit architectures. Developing methods to increase and stabilize valley splitting remains a crucial focus of research [78, 92–95].

2.3.4 The Spin Degree of Freedom

The final quantum degree of freedom we consider is spin. The highly coherent spin states of confined electrons are a key resource for semiconductor qubit encodings. Both individual and composite spin states are utilized.

Individual Spins

In the absence of a magnetic field, each energy level in a quantum dot is doubly degenerate with respect to spin, as Fig. 2.14(a) depicts. When a magnetic field is introduced, the spin $\hat{\mathbf{S}}$ of a confined electron interacts with the field via the Zeeman Hamiltonian,

$$\hat{H}_Z = \frac{g\mu_B}{\hbar}\hat{\mathbf{S}} \cdot \mathbf{B}_{\text{eff}}, \tag{2.27}$$

where $g \approx 2$ is the electron g-factor in silicon and $\mu_B = 58$ µeV/T is the Bohr magneton. The effective magnetic field $\mathbf{B}_{\text{eff}}$ can originate from external sources such as cryostat magnets or on-chip micromagnets, as well as from internal hyperfine and spin-orbit interactions [24]. We will ignore the internal factors, which are relatively weak in Si/SiGe, and consider a global, external field $\mathbf{B}_{\text{eff}} = B_0\hat{\mathbf{z}}$. In this case, the interaction simplifies to

$$\hat{H}_Z = \frac{1}{2}g\mu_B B_0 \hat{\sigma}_z. \tag{2.28}$$

The eigenstates, $|\uparrow\rangle$ and $|\downarrow\rangle$, correspond to spin-up and spin-down states along the z-axis. The external field lifts the spin degeneracy and introduces a **Zeeman splitting** $\Delta E_{\text{spin}} = E_\uparrow - E_\downarrow = g\mu_B B_0$, as shown in Fig. 2.14(b). In this manner, the eigenstates of an individual spin can be energetically isolated and used to store and manipulate quantum information.

Interacting Spins

In systems where multiple spins are held in close proximity, their mutual interactions influence the overall energy spectrum. The dominant spin-spin interaction mechanism in quantum

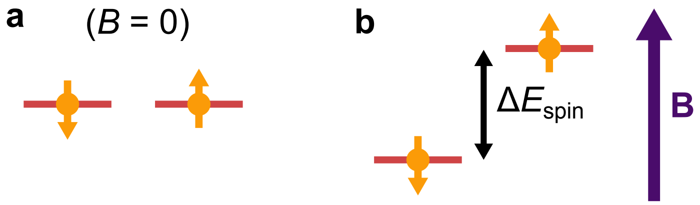

Figure 2.14: The Zeeman effect in quantum dots. **(a)** In the absence of a magnetic field ($B = 0$), quantum-dot energy levels are spin-degenerate. **(b)** Applying an external field $\mathbf{B}$ creates a Zeeman splitting ΔE_{spin} between spin states.

dots is the **exchange interaction**, which emerges from the confluence of the Pauli exclusion principle, Coulomb repulsion, and electron tunneling [24]. To illustrate how this mechanism works in practice, we will examine scenarios involving two confined spins. The spin pair can take one of four composite states: a **singlet** state with total spin $S = 0$, defined as

$$|S\rangle \equiv \frac{1}{\sqrt{2}}\left(|\uparrow\downarrow\rangle - |\downarrow\uparrow\rangle\right); \tag{2.29}$$

and three **triplet** states with $S = 1$, defined as

$$|T_+\rangle \equiv |\uparrow\uparrow\rangle\,, \qquad |T_-\rangle \equiv |\downarrow\downarrow\rangle\,, \qquad |T_0\rangle \equiv \frac{1}{\sqrt{2}}\left(|\uparrow\downarrow\rangle + |\downarrow\uparrow\rangle\right). \tag{2.30}$$

At zero magnetic field, which we assume going forward, the triplet states are degenerate in energy, meaning they are equally probable in describing the system's spin configuration. We will use the shorthand $|T\rangle$ to refer to any state from the triplet set $\{|T_+\rangle\,, |T_-\rangle\,, |T_0\rangle\}$.

Let us first consider the case where the two spins are confined within a single quantum dot, as illustrated in Fig. 2.15(a). To simplify the model, we assume the dot has two energy states,[16] $|g\rangle$ and $|e\rangle$, with an energy separation ΔE in the absence of electronic interactions. The overall wavefunction for the pair of confined electrons, which must be antisymmetric to adhere to Fermi statistics, is formed by the tensor product of their energy and spin states.

---

[16] The nature of these states is unimportant—they could be valley states, orbital states, or a hybridization of the two, depending on the specifics of the heterostructure and whether there are additional electrons occupying lower energy levels within the dot.

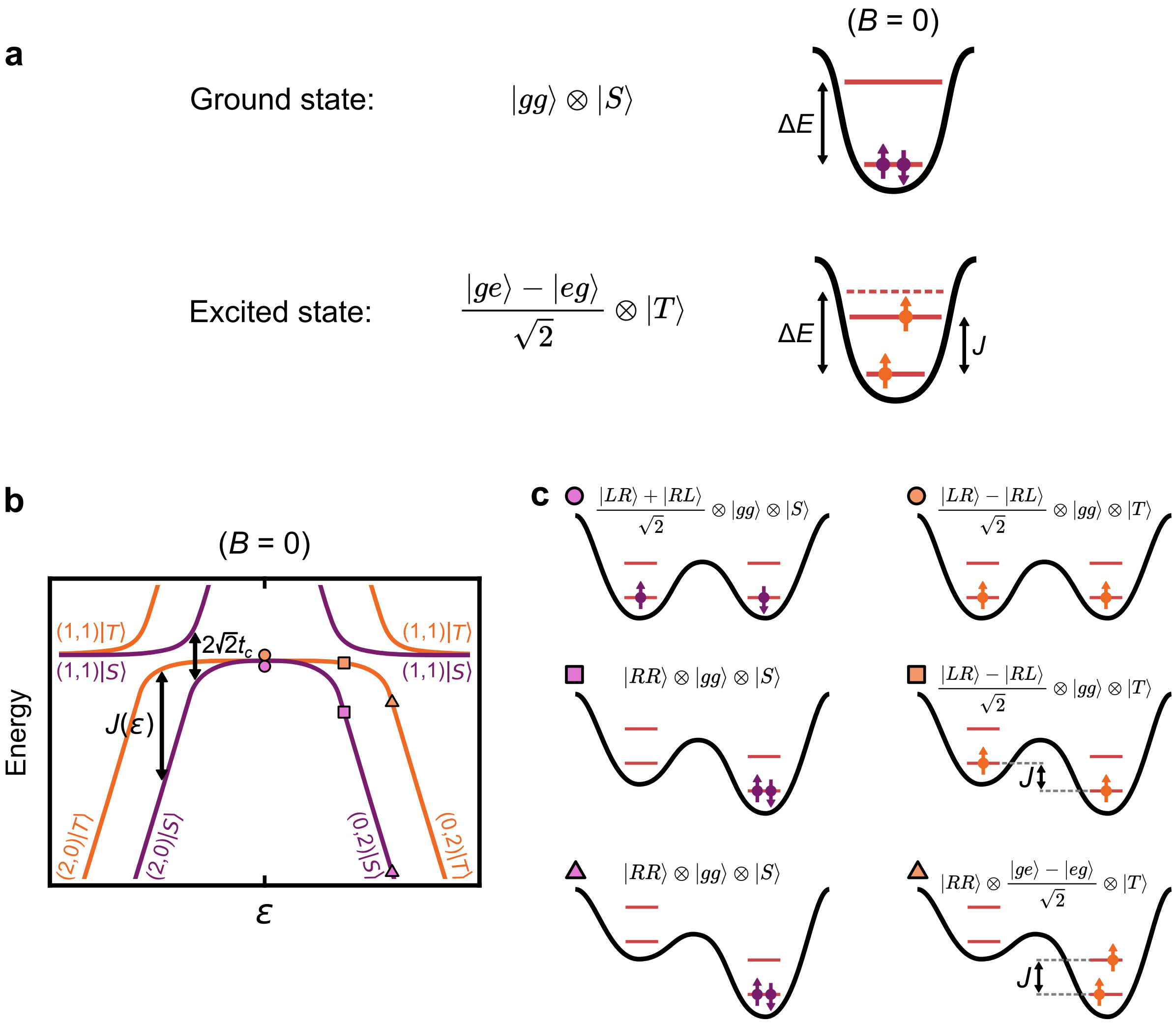

Figure 2.15: Spin-spin exchange coupling in quantum dots. **(a)** Wavefunctions and visualizations of the ground and first-excited states in a quantum dot with two spins. The energy splitting between these states is given by the exchange coupling J. **(b)** Two-electron DQD energy levels as a function of the detuning ε. The exchange coupling $J(\varepsilon)$ measures the splitting between the lowest-energy singlet and triplet states. **(c)** DQD configurations at corresponding marked points in (b). Approximate wavefunctions for each configuration are written, using the single-electron charge states $|L\rangle$ and $|R\rangle$. All panels assume zero magnetic field ($B = 0$). For illustrative purposes, the $|T_+\rangle$ state is used to depict spin-triplet configurations.

In the system's ground state, both electrons occupy the lower-energy state, represented by $|gg\rangle$. Since this state is symmetric with respect to particle exchange, the wavefunction's spin component *must* take on the antisymmetric singlet configuration $|S\rangle$. In order to arrange the spins in a symmetric triplet configuration $|T\rangle$, an electron *must* be promoted to the excited level, allowing the energy state to adopt the antisymmetric form $(|ge\rangle - |eg\rangle)/\sqrt{2}$. The energy difference between the singlet ground state and the triplet excited state is referred to as the **exchange coupling** J.[17] Due to interactions between the electrons, this energy splitting is reduced compared to the bare level spacing (i.e., $J < \Delta E$), as indicated in Fig. 2.15(a) [24]. The magnitude of this suppression is highly sensitive to the dot's confinement, which influences the strength of electron-electron interactions [75, 77, 96].[18]

We can also consider the case where the two spins are confined in a DQD. Figure 2.15(b) plots the energy spectrum for this system as a function of the detuning ε. The effect of the exchange interaction is clearly demonstrated by comparing this plot to Fig. 2.11(c), which does not account for spin. As with the single-dot case, the interaction opens an energy gap $J(\varepsilon)$ between the singlet and triplet configurations. However, in a DQD, the exchange coupling strength can be adjusted by varying the detuning parameter. To understand how this coupling influences the energy-preferred DQD states, we can trace the evolution of the lowest-energy singlet (purple) and triplet (orange) curves as detuning increases. The magnitude of $J(\varepsilon)$ is directly related to the overlap of the electron position wavefunctions. At zero detuning, each electron resides in a different dot with minimal wavefunction overlap, leaving the singlet and triplet states nearly degenerate. As detuning increases, interdot tunneling causes a portion of the left electron's wavefunction to transfer into the right dot, increasing $J(\varepsilon)$. At intermediate detuning, the (0,2) charge configuration becomes favored for the singlet state, while the triplet remains in the (1,1) configuration. Finally, at high detuning, both spin states prefer the (0,2) charge configuration, making the system equivalent to the single-dot case. Here, the wavefunction overlap is maximal, and $J(\varepsilon)$ reaches its peak value. Figure 2.15(c) illustrates the system configurations at various points along the

---

[17] This energy splitting is also called the **singlet-triplet splitting**, and we refer to it by this name in Chapter 6 in the context of three-electron DQDs.

[18] The suppression of the energy splitting is more pronounced in larger dots than in smaller ones because—somewhat counter-intuitively—electron-electron interactions are stronger in big dots. This effect arises from a competition between the Coulomb repulsion energy and the orbital energy: as the dot size increases, the orbital energy decreases faster than the Coulomb energy, amplifying the relative strength of electron-electron interactions [75].

energy curves where the DQD states are closely approximated by charge-spin basis states (the suppression of energy splitting due to electron-electron interactions is not shown in these depictions). With the charge degree of freedom included in the DQD wavefunction, both the spin-singlet and spin-triplet states maintain their antisymmetric exchange character throughout the evolution.

2.4 Bringing It All Together: Quantum-Dot Qubits

We conclude this chapter with a brief, high-level overview of how electrons in quantum dots are used as qubits, bringing together many of the concepts covered so far. The methods for encoding, manipulating, and measuring qubit states are highly varied and nuanced, so we will intentionally keep our discussion broad here, focusing on general principles. A more detailed exploration of certain concepts and techniques is presented in upcoming chapters.

There are at least a dozen proposed qubit encoding schemes based on quantum-dot systems [24]. The most widely studied approaches today involve systems of one to three electrons confined within one to three dots.[19] Each encoding utilizes one or more of the quantum degrees of freedom we discussed to represent information in an effective two-level system. We have already encountered two examples of basic qubit encodings: the **charge qubit**, defined by single-electron DQD charge states [97]; and the **single-spin qubit** (also known as the **Loss-DiVincenzo qubit**), defined by Zeeman-split spin states [98]. Figure 2.16 depicts the logical states for each of these encodings. Additional encodings are discussed in Sections 3.2.1 and 6.5.1.

To implement one- and two-qubit logic gates, qubit states are manipulated using a range of control schemes, which are tailored to the Hamiltonian of the specific encoding. These schemes may involve pulsing, ramping, or resonant ac driving of the plunger and barrier voltages to modulate the chemical potentials, tunnel couplings, and exchange interactions of

---

[19] Sometimes qubits operate with extra ‘valence’ electrons trapped in their dots, which do not contribute toward the qubit’s effective Hilbert space or Hamiltonian.

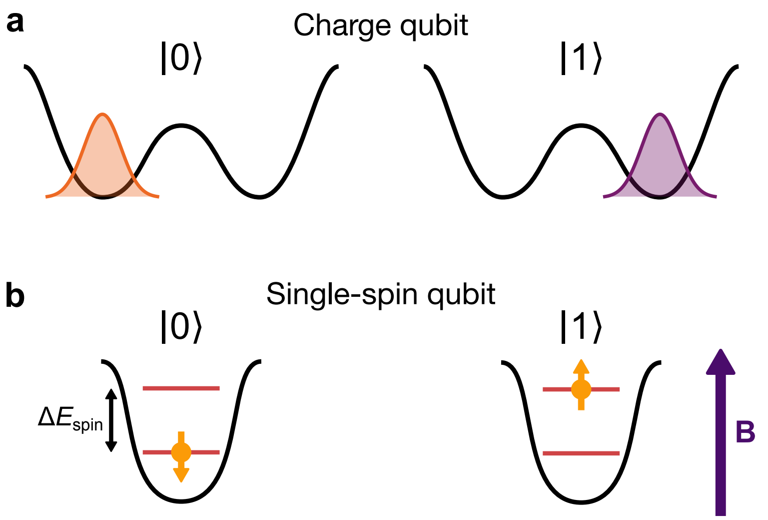

Figure 2.16: Example logical state encodings for **(a)** the charge qubit; and **(b)** the single-spin qubit.

---

quantum dots [27,73,99–103]. Individual spin rotations can be driven by applying a resonant, oscillating magnetic field [104]; they can also be generated by an oscillating electric field, which induces orbital motion of the electron wavefunction within a magnetic field gradient, creating an effective oscillating magnetic field [105].

With few exceptions, quantum state readout in semiconductor qubits relies on the ability to measure the system's charge states, which are easily detected using well-established charge-sensing technologies. Reading out non-charge degrees of freedom (e.g., spin or valley states) is more challenging, as these states do not directly couple to the measurement apparatus. To address this, qubit operation schemes typically convert non-charge-encoded states into measurable charge states just before readout [24]. This can be accomplished through state-dependent tunneling mechanisms, which map the qubit's final state to a distinct quantum-dot charge configuration [106, 107]. This indirect measurement approach facilitates the readout of spin or other quantum information encoded in the qubit.

Decoherence, which leads to the loss of quantum information and hinders the reliable operation of qubits, occurs via two pathways: relaxation and dephasing. **Relaxation** is the process by which a qubit loses energy and returns to its ground state, often due to coupling with acoustic phonons. **Dephasing** is the loss of qubit phase coherence without energy dissipation, and is typically attributed to noise in the nearby electric and magnetic fields [24]. In semiconductor qubits, characteristic dephasing times (T_2) are much shorter than relaxation times (T_1), making dephasing the primary limiter of quantum coherence [108].

Different qubit encodings come with distinct advantages and trade-offs, depending on the quantum degrees of freedom they utilize. For instance, certain encodings might offer enhanced resilience to specific types of noise, reduced control overhead, or greater compatibility with high-temperature (> 1 K) operation. A general theme is that spin states are far more coherent than charge states, since their coupling to the environment is weaker [20,39,108,109]. For this reason, there is a strong focus on leveraging spin for quantum information storage. At present, quantum processor prototypes are quite small, and there is no clear consensus on which encoding scheme will be easiest to scale to hundreds, thousands, or millions of qubits. However, the major industry groups in the field seem to be placing their bets on either single-spin or exchange-only qubits [43,58,110–112]. In the next chapter, we will take an in-depth look at the latter encoding and get the opportunity to see semiconductor qubits in action.

Chapter 3

Coherent Control & Crosstalk in Exchange-Only Spin Qubits

This chapter presents research conducted during an internship with Intel from January to May 2024.

Exchange-only spin qubits are regarded as one of the leading candidate encodings for scalable quantum-dot qubit architectures. The first half of this chapter provides a detailed discussion of how exchange-only qubits work, illustrating how many of the principles introduced in Chapter 2 are applied in practice. The second half of the chapter shifts focus to an investigation of capacitive crosstalk between exchange-only qubits. Our experiments reveal that crosstalk becomes an important factor when neighboring qubits are operated in parallel. Through analysis of exchange fingerprints and randomized benchmarking data, we demonstrate how these crosstalk effects lead to errors in qubit operations, and discuss strategies to mitigate these errors. These findings offer insights into the challenges of scaling exchange-only qubit systems and provide guidance for optimizing their performance in larger, more complex quantum processors.

3.1 Tunnel Falls Device Architecture

Experiments in this chapter are performed using a device from Intel's Tunnel Falls quantum computing research chip, pictured in Fig. 3.1(a). Tunnel Falls is manufactured using extreme ultraviolet lithography and CMOS transistor technology at Intel's D1 fabrication facility in Hillsboro, Oregon [113]. As detailed in Ref. [43], the integration of advanced semiconductor manufacturing processes and high-throughput cryogenic characterization has enabled Intel to achieve high yield and uniformity of devices across a 300 mm wafer.

Figure 3.1(b) displays a scanning electron micrograph of a quantum-dot device from Tunnel Falls. The materials stack for this device, illustrated in Fig. 3.1(c), closely resembles the one outlined in Section 2.1, with a Si/SiGe heterostructure, a high-dielectric constant (high-κ) composite stack, and two layers of overlapping metallic gates. The device gate structure, shown in Fig. 3.1(d), includes plunger, barrier, reservoir, and screening gates. Additional 'flanking' gates assist with 2DEG accumulation in the reservoirs. The gates are electrically isolated from each other by an insulating 'spacer' layer [43].

The device is designed with two channels of quantum-dot gates separated by a center screening gate. The upper channel in Fig. 3.1(c) is used to form a one-dimensional array of up to 12 quantum dots, intended for hosting qubits. The lower channel is equipped with gates for additional dots that are dedicated to charge sensing and qubit readout.

3.1.1 Charge Sensing Scheme

Charge sensing is implemented by quantum dots acting as SETs (as described in Section 2.2.1). One of the four integrated SET charge sensors is highlighted by the dashed box in Fig. 3.1(c). As depicted in the effective circuit schematic in Fig. 3.2(a), each SET is capacitively coupled to nearby dots in the qubit array and functions as a sensitive electrometer, detecting changes in their charge occupancies. For optimal charge sensing, the SET's plunger gate voltage V_{SET} is tuned to the steep flank of a Coulomb blockade oscillation peak,

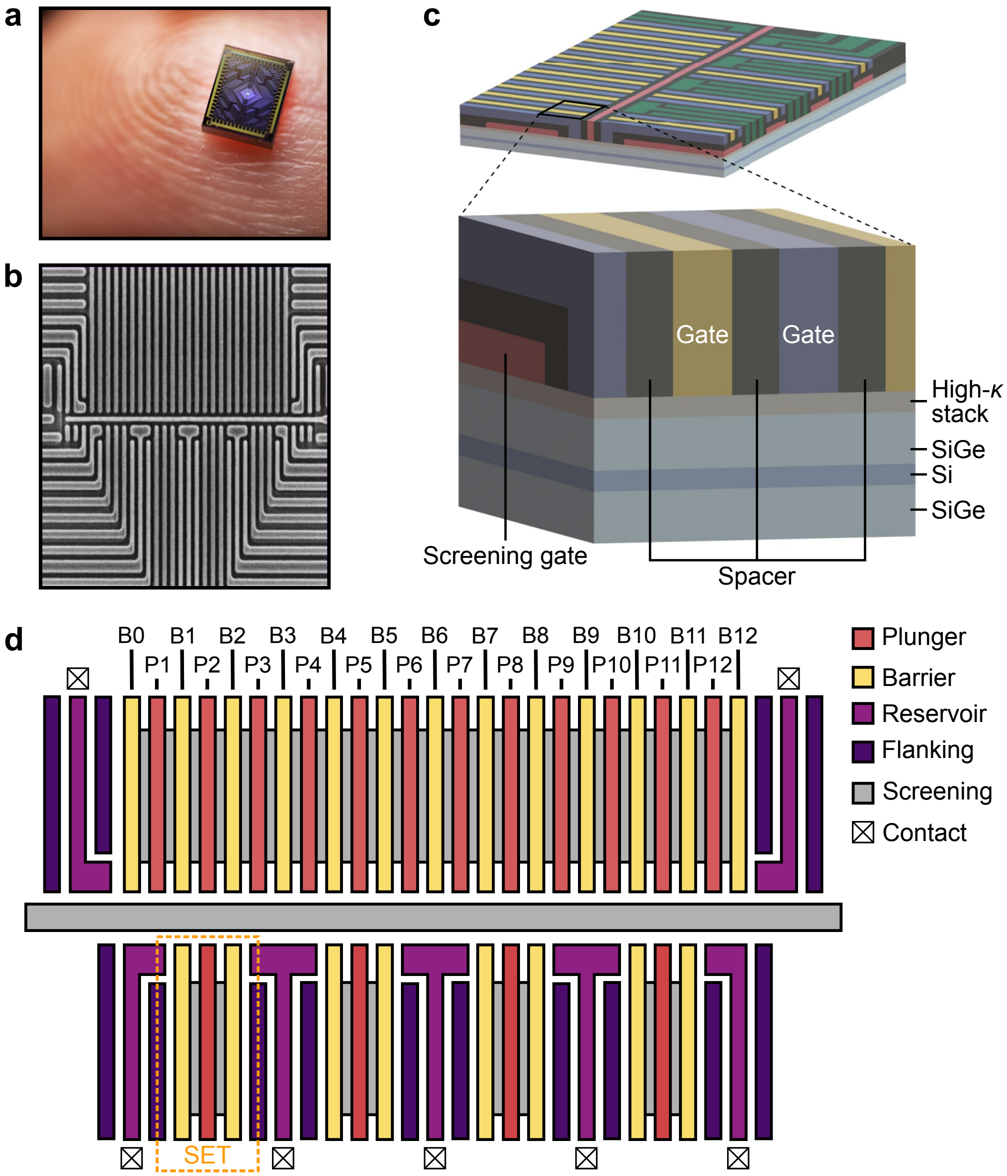

Figure 3.1: Intel's Tunnel Falls quantum chip. **(a)** Photo showing a Tunnel Falls chip on a human finger to demonstrate its scale. **(b)** Scanning electron micrograph of a 12-quantum-dot device on Tunnel Falls. **(c)** Cross-sectional view of the device materials stack. **(d)** Device gate structure with qubit plunger and barrier gates labeled. A dashed box highlights one of four SET charge sensors. Reservoir connections to Ohmic contacts are indicated by '⊠' symbols. (a) and (b) reprinted from Ref. [113]. (c) adapted from Ref. [43].

---

indicated by the vertical dashed line in Fig. 3.2(b). Any changes in the charge configuration of the qubit dots modify the SET's electrostatic environment, which in turn alters the current flowing through it [114]. For example, Fig. 3.2(b) illustrates an interdot transition from $(N+1, M, L)$ to $(N, M+1, L)$ which shifts the SET's Coulomb peak toward higher gate

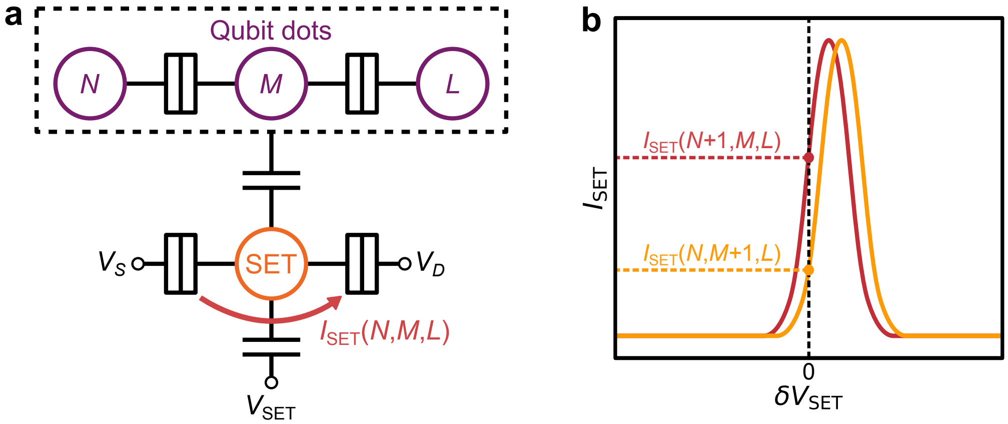

Figure 3.2: SET charge sensing scheme. **(a)** Equivalent circuit model for an SET capacitively coupled to three nearby dots in the qubit array. The current $I_{\mathrm{SET}}(N, M, L)$ is sensitive to the charge configuration within the qubit dots. **(b)** Comparison of SET Coulomb peaks for different charge configurations in the qubit array. By tuning the SET gate voltage V_{SET} to the peak's flank, a sharp change in current is measured during charge transitions.

voltage. As a result, the current I_{SET} sharply decreases from the red to the orange dashed line. By using frequency-multiplexed lock-in techniques to monitor the currents of all SET charge sensors, charge state transitions across the qubit array can be detected.

3.2 The Exchange-Only Qubit

The **exchange-only qubit** is, in several aspects, a quirky qubit. Proposed by DiVincenzo *et al.* in 2000 [115], it utilizes three electron spins distributed across three adjacent quantum dots. This setup comes at a cost, requiring more resources than other one- and two-dot spin qubit encodings, and reducing the number of qubits in an array—a Tunnel Falls device, for example, can accomodate 12 single-spin qubits, but only four exchange-only qubits. Nonetheless, as we will see, the exchange-only design offers key advantages for scalable qubit control, making it an attractive option for large-scale quantum computing implementations.

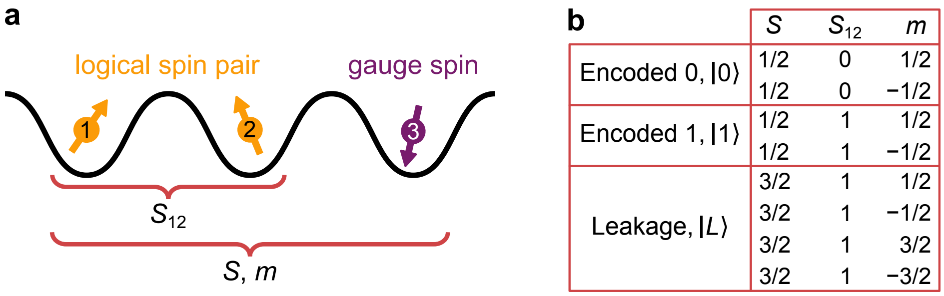

	S	S_{12}	m
Encoded 0, $\lvert 0\rangle$	1/2	0	1/2
	1/2	0	−1/2
Encoded 1, $\lvert 1\rangle$	1/2	1	1/2
	1/2	1	−1/2
Leakage, $\lvert L\rangle$	3/2	1	1/2
	3/2	1	−1/2
	3/2	1	3/2
	3/2	1	−3/2

Figure 3.3: Three-spin encoding for the exchange-only qubit. **(a)** Exchange-only qubit comprising three spins in a triple quantum dot. Spins 1 and 2 form the logical spin pair, with spin 3 being the gauge spin. **(b)** Three-electron states in the coupled spin basis, defined by the spin quantum numbers S, m, and S_{12} denoted in (a). (b) adapted from Ref. [103]. Reproduced with permission from Springer Nature.

3.2.1 Qubit Encoding

Figure 3.3(a) depicts an archetypal exchange-only qubit as a linear, triple-dot array in the (1,1,1) charge configuration; the confined electrons are indexed 1, 2, and 3. The combined Hilbert space $\mathcal{H}$ for the three spin-1/2 electrons is eight-dimensional ($2^3 = 8$). Using angular momentum addition rules, it can be decomposed into three subspaces $\mathcal{H}_S$ of total spin S:

$$\mathcal{H} = \mathcal{H}_{1/2} \otimes \mathcal{H}_{1/2} \otimes \mathcal{H}_{1/2} = \mathcal{H}_{1/2} \oplus \mathcal{H}_{1/2} \oplus \mathcal{H}_{3/2}, \tag{3.1}$$

with two degenerate $S = 1/2$ subspaces (each two-dimensional) and one $S = 3/2$ subspace (four-dimensional) [24]. Here, the symbols $\otimes$ and $\oplus$ denote tensor product and direct sum operations on vector spaces, respectively. The basis states within each subspace can be further classified in terms of the spin quantum numbers $|S, S_{12}, m\rangle$, where m is the total spin projection (along an arbitrary axis) and S_{12} is the combined spin of electrons 1 and 2. Figure 3.3(b) tabulates the quantum numbers of all eight basis states [103].

The logical qubit states are encoded within the $S = 1/2$ subspaces.[1] In this computational subsystem[2], the two spin states with $S_{12} = 0$ map to $|0\rangle$, while the two with $S_{12} = 1$ map to $|1\rangle$. Explicitly, we define the four logical states in the coupled-spin basis as

$$\begin{aligned} |0_+\rangle &\equiv \left|\frac{1}{2}, 0, \frac{1}{2}\right\rangle, \qquad & |1_+\rangle &\equiv \left|\frac{1}{2}, 1, \frac{1}{2}\right\rangle, \\ |0_-\rangle &\equiv \left|\frac{1}{2}, 0, -\frac{1}{2}\right\rangle, \qquad & |1_-\rangle &\equiv \left|\frac{1}{2}, 1, -\frac{1}{2}\right\rangle, \end{aligned} \tag{3.2}$$

with ± subscripts corresponding to the value of $m = \pm 1/2$. An alternative way to conceptualize the exchange-only encoding is to transform these logical states to a different basis using Clebsch-Gordan coefficients [117]:

$$\begin{aligned} |0_+\rangle &= |S\rangle\,|{\uparrow}\rangle, \qquad & |1_+\rangle &= \sqrt{\frac{2}{3}}\,|T_+\rangle\,|{\downarrow}\rangle - \sqrt{\frac{1}{3}}\,|T_0\rangle\,|{\uparrow}\rangle, \\ |0_-\rangle &= |S\rangle\,|{\downarrow}\rangle, \qquad & |1_-\rangle &= \sqrt{\frac{2}{3}}\,|T_-\rangle\,|{\uparrow}\rangle - \sqrt{\frac{1}{3}}\,|T_0\rangle\,|{\downarrow}\rangle. \end{aligned} \tag{3.3}$$

In this basis, the first ket represents the configuration of spins 1 and 2. We will refer to these spins collectively as the **logical spin pair**, since the qubit's logical state is uniquely determined by whether the pair is in a singlet ($S_{12} = 0$) or triplet ($S_{12} = 1$) configuration. The second ket gives the orientation of spin 3, which is sometimes called the **gauge spin**.[3]

Notice that the quantum number m—or equivalently, the projection of the gauge spin—does not influence the logical state mapping. Therefore, although the logical states have duplicate representations within the $S = 1/2$ computational subsystem, there is no need to

---

[1] The $S = 1/2$ subsystem is chosen for its insensitivity to global magnetic field fluctuations. While such fluctuations can induce spin flips, the logical states in the logical states in Eq. (3.3) are defined such that a *global* perturbation—felt equally by all three spins—will not cause leakage out of the subsystem [115,116]. For this reason, the exchange-only qubit's computational subsystem is sometimes called a 'decoherence-free subsystem.' This is a terrible misnomer; although the qubit is protected from global field noise, it is in no way immune to other sources of decoherence, as we will observe later in the chapter.

[2] The term *subsystem* refers to the combined structure of the two $S = 1/2$ *subspaces*.

[3] In a linear quantum-dot array, the gauge spin can be positioned on either side of the logical spin pair—the spatial orientation is irrelevant.

distinguish between '+' and '−' states.[4] As such, we can treat the entire subsystem as an effective two-state system for qubit operations. The effective logical states are referred to as **encoded 0** ($|0\rangle \equiv \{|0_+\rangle, |0_-\rangle\}$) and **encoded 1** ($|1\rangle \equiv \{|1_+\rangle, |1_-\rangle\}$) moving forward [103].

The states outside the exchange-only encoding with $S = 3/2$ are **leakage states**, collectively denoted as $|L\rangle$. These states do not participate in the encoding of quantum information, and any leakage of the qubit state into this subsystem results in computational error.

3.2.2 Initialization & Readout

Reading out the exchange-only qubit requires measurement of the logical spin pair. The gauge spin—which has no effect on the logical state—can be ignored. This scenario lends itself well to a readout implementation based on **Pauli spin blockade (PSB)** [103,107,118]. This spin-transport phenomenon can be observed in two-electron DQDs. If the energy levels in each dot are properly aligned, such as in Fig. 3.4(a), a scenario exists where interdot tunneling is permitted only when the electron spins form a singlet; when the spins are in a triplet configuration, tunneling between the dots is energetically blocked [119].

To illustrate how PSB is utilized to determine the exchange-only qubit's state, we focus exclusively on the DQD hosting the logical spin pair, leaving the gauge spin's dot inactive during the readout sequence. When the qubit is ready to be measured, the DQD's plunger voltages are pulsed into the yellow-shaded region of the charge stability diagram shown in Fig. 3.4(b), crossing the polarization line from the $(1, 1)$ cell into $(0, 2)$.[5] This voltage window corresponds to the shaded sector of the energy dispersion diagram in Fig. 3.4(c), where the DQD levels are in the PSB arrangement. The system is maintained in this regime for a calibrated time interval (e.g., a few microseconds). If the logical spin pair is projected into

---

[4] More specifically, this is the case when operating without an external magnetic field—relevant for experiments in this chapter—where '+' and '−' states are energetically degenerate.

[5] PSB readout can also be implemented at the $(1, 1) - (2, 0)$ interdot transition. Our choice to focus on $(1, 1) - (0, 2)$ here is arbitrary.

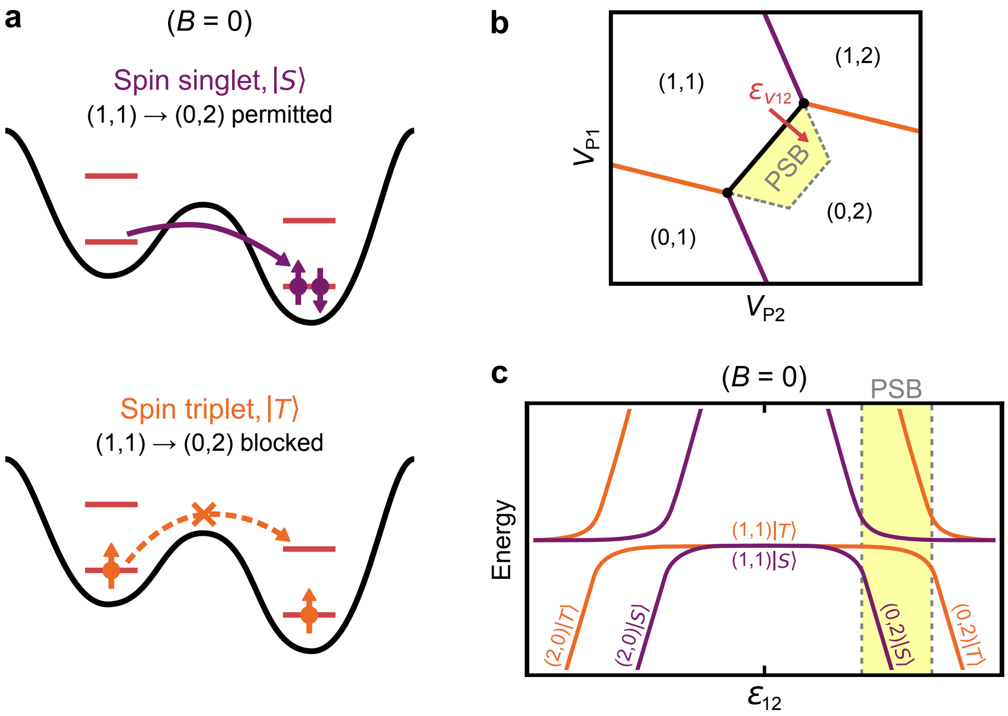

Figure 3.4: PSB readout scheme. **(a)** PSB in a two-electron DQD: interdot tunneling is allowed for the spin-singlet state, but blocked for triplet states. **(b)** Charge stability diagram showing the voltage-space region where PSB occurs. For illustrative purposes, the plungers controlling the logical-spin-pair DQD are labeled P1 and P2, and have voltage detuning ε_{v12}. **(c)** Energy dispersion diagram showing the detuning window in which PSB occurs. All panels assume zero magnetic field ($B = 0$).

---

the singlet configuration—corresponding to a qubit measurement of $|0\rangle$—a $(1,1) \rightarrow (0,2)$ transition occurs, which is detected by a change in current through the SET charge sensor. If, on the other hand, the pair is projected into a triplet configuration—corresponding to a measurement of $|1\rangle$—no transition occurs, and no change in SET current is observed.

PSB readout is one of the standard techniques used for converting qubit spin states into measurable charge states, as described in Section 2.4, and is readily adapted for other spin qubit encodings. A notable advantage of this readout scheme compared to others is that it avoids the need for tunneling between dots and reservoirs. This feature allows PSB readout to be implemented on the interior dots of the Tunnel Falls device, which lack reservoir access, and also makes it ideal for scaling to larger arrays of densely packed spin qubits.

For experiments in this chapter, the PSB readout procedure is also employed for initializing the qubit in the $|0\rangle$ state. In this process, the qubit is first measured before any quantum manipulations are applied, collapsing its state to either $|0\rangle$ or $|1\rangle$. Subsequent operations and a final state readout are performed, but only trials where the initial PSB measurement found the qubit in $|0\rangle$ are recorded—the others are discarded. While this post-selection technique ensures a high-fidelity initialization, it comes at the cost of efficiency, requiring additional repetitions to compensate for discarded trials. The approach works adequately for small-scale experiments, but as processor size increases, it becomes prohibitively inefficient. For future scalability, active initialization methods will be necessary to deterministically prepare all qubits in the desired state before operations.

3.2.3 Quantum Control via the Exchange Interaction

The exchange-only qubit gets its name from the fact that its control is based exclusively on manipulating the exchange couplings between electron spins. These couplings are modulated using baseband voltage pulses applied to the device gates. Unlike other spin qubits, exchange-only qubit operations do not rely on magnetic fields, field gradients, or high-frequency microwaves. This all-electrical, baseband control is a significant advantage for processor scalability, eliminating the need for micromagnets or high-frequency drive circuitry, while also mitigating the potential impact of microwave-induced heating and crosstalk [103, 115, 120–122].

The pairwise exchange interactions in the qubit's three-spin system are described by the Heisenberg Hamiltonian,

$$\hat{H} = \sum_{\langle i,j \rangle} J_{ij}\, \hat{\mathbf{S}}_i \cdot \hat{\mathbf{S}}_j, \tag{3.4}$$

where J_{ij} is the exchange coupling between spins i and j [115]. For the linear spin chain considered here, we take $J_{13} = 0$. The Hamiltonian in Eq. (3.4) can be reduced to an effective Hamiltonian for qubit control in the computational basis $\{|0\rangle, |1\rangle\}$:

$$\hat{H}(t)_{\mathrm{EO}} = -\frac{1}{2}\left[J_z(t)\hat{\sigma}_z + J_n(t)\left(\hat{\sigma}_z \cos\phi - \hat{\sigma}_x \sin\phi\right)\right], \tag{3.5}$$

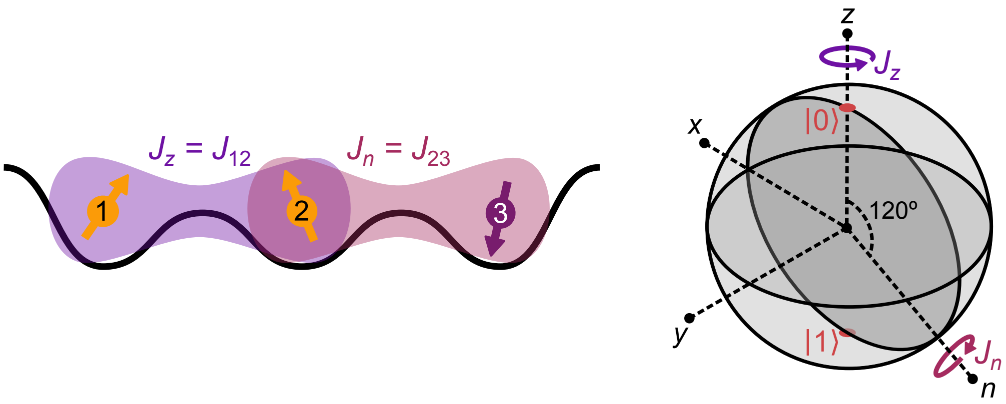

Figure 3.5: Exchange-only qubit rotations on the Bloch sphere. Pulsing device gates to activate the J_z or J_n exchange coupling drives rotations around the z-axis or n-axis of the Bloch sphere. Figure adapted with permission from Ref. [24]. © 2023 by the American Physical Society.

---

where $\phi = 2\pi/3 = 120°$, and the exchange couplings are relabeled as $J_z = J_{12}$ and $J_n = J_{23}$ [103, 123].

When $J_z = J_n = 0$, the qubit is in an idle configuration, with its $|0\rangle$ and $|1\rangle$ states degenerate. Pulsing the confinement gates for electrons 1 and 2 to activate the J_z coupling lowers the energy of $|0\rangle$ with respect to $|1\rangle$, causing the qubit's wavefunction to accumulate a relative phase. This phase evolution can be visualized as a rotation about the z-axis on the Bloch sphere. Similarly, pulsing the confinement gates for electrons 2 and 3 to activate J_n lowers the energy of $|1\rangle$ and drives a Bloch-sphere rotation about an axis defined by the unit vector $\hat{\mathbf{n}} = \cos\phi\,\hat{\mathbf{z}} - \sin\phi\,\hat{\mathbf{x}}$ [124]. The pair of exchange couplings and their corresponding rotation axes in the Bloch sphere are illustrated in Fig. 3.5. Having two independent rotation axes provides the ability to access any point on the Bloch sphere by pulsing exchange on and off, granting us full control over the qubit's quantum state. Importantly, exchange interactions only affect the S_{12} quantum number while preserving the system's total spin, ensuring that qubit operations do not cause leakage out of the computational subsystem [103, 115].

Exchange Pulse Calibration

Before implementing quantum logic gates, it is necessary to calibrate gate voltage pulses to accurately control rotations on the Bloch sphere. With two rotation axes corresponding to the two exchange couplings, we can break the triple dot down into two DQDs and calibrate each interaction independently.

Recall that the exchange coupling magnitude is closely related to the amount of spatial overlap between electron wavefunctions. Experimentally, there are two distinct ways to modify this coupling for each spin pair [102,125,126]. The first approach, sometimes referred to as **tilt control**, is to vary the DQD's detuning parameter ε using the plunger voltages, as mentioned in Section 2.3.4. Increasing $|\varepsilon|$ will cause more of the higher-energy electron's wavefunction to leak into the lower-energy dot, leading to greater wavefunction overlap and strengthening J. The second method, known as **symmetric control**, is to adjust the tunnel coupling parameter t_c via the barrier voltage. Increasing t_c allows both electrons' wavefunctions to spread across the DQD, enhancing their overlap. This mode of operation maintains the symmetry of the dots' chemical potentials, ensuring the DQD remains at its **symmetric operating point (SOP)** with $\varepsilon = 0$. We can conceptualize the tilt and symmetric control methods as defining two orthogonal axes for manipulating exchange, as Fig. 3.6(a) depicts. When we pulse the couplings in our qubit, we are free to use either approach separately, or both in tandem.

To calibrate our pulses, we first tune the qubit's triple dot to the (1,1,1) charge configuration and establish PSB readout for the logical spin pair. To account for capacitive crosstalk in the device, we implement virtual gates, as described in Section 2.2.3. The DQD virtual voltage detunings ε_{v12} and ε_{v23} are primarily controlled by the plunger gates P1, P2, and P3, while the tunnel couplings are primarily controlled by the barrier gates B1 and B2 with virtual voltages u_{B1} and u_{B2}, as indicated in Fig. 3.6(b). Next, we characterize each exchange interaction by performing what is commonly called a **fingerprint measurement** [102]. This involves initializing the qubit in the $|0\rangle$ state, pulsing one DQD's detuning and barrier

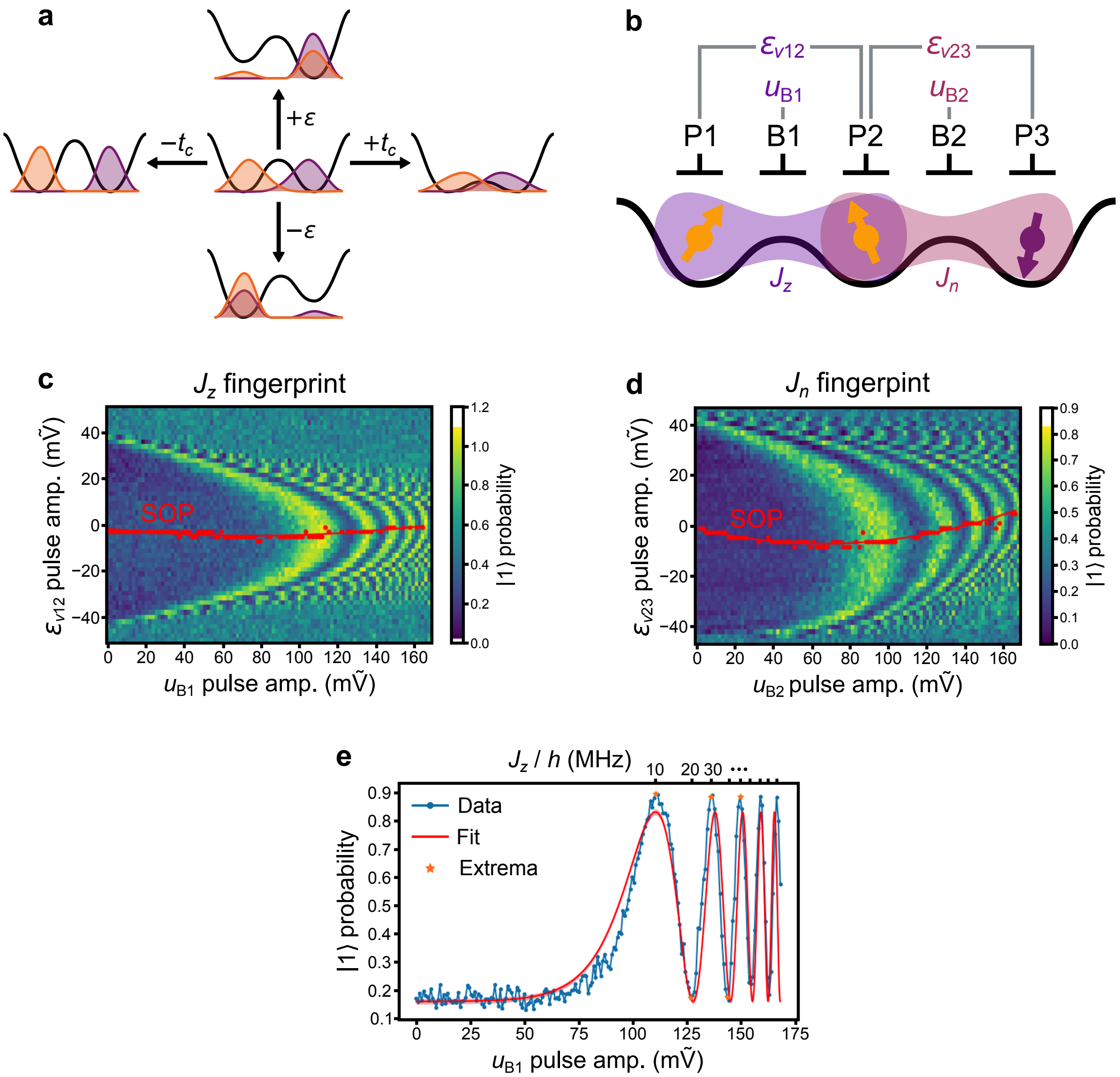

Figure 3.6: Exchange pulse calibration for qubit control. **(a)** Tilt (ε) and symmetric (t_c) control axes for manipulating exchange coupling in a DQD. **(b)** Triple-dot potential showing virtual voltage parameters for driving exchange pulses. **(c,d)** Fingerprint measurements characterizing the qubit's J_z and J_n exchange couplings. Points corresponding to SOP manipulation are marked in red. **(e)** J_z exchange oscillations measured as a function of barrier pulse amplitude at the SOP. The data are fit to extract a voltage-to-rotation mapping for qubit control pulses. Virtual voltage units are abbreviated by '$\tilde{\text{V}}$.'

---

voltages simultaneously to activate a specific exchange coupling, and then reading out the qubit's final state.[6] Figs. 3.6(c) and 3.6(d) show fingerprint measurements for the J_z and J_n exchange couplings as a function of detuning and barrier pulse amplitude. The plot axes mirror those defined in Fig. 3.6(a), mapping out a full control phase space for the qubit. As the exchange pulses drive rotations around the Bloch sphere, the qubit's $|1\rangle$-state probability oscillates cyclically, producing a series of fringes. Along each fringe, the magnitude of the exchange coupling is constant. The name 'fingerprint' is well-chosen—not only because it describes the measurement's characteristic fringe pattern, but also because no two exchange fingerprints are the same. The unique asymmetries in the measurement plots arise from local disorder in the materials and electric fields that confine each spin pair [102].

In each fingerprint, we can identify an axis of maximal symmetry. This locus of points, plotted in red in Figs. 3.6(c) and 3.6(d), corresponds to the DQD being manipulated at its SOP. Due to local disorder, the ε_v pulse amplitude needed to maintain symmetric operation is nonzero and varies as a function of the applied barrier pulse, introducing curvature to the symmetry axis. The extracted loci are used to implement symmetric control over the qubit's exchange couplings. During quantum gate sequences, all manipulation is performed in the (1,1,1) charge configuration with both DQDs biased to their SOP. This mode of operation improves fidelity by reducing the qubit's sensitivity to charge noise [102, 123, 125].

To create a final voltage-to-rotation mapping for exchange pulses, we measure J_z and J_n oscillations at the DQD SOPs. Figure 3.6(e) displays this calibration measurement for the J_z coupling, which is essentially a high-resolution line cut along the red symmetry axis in Fig. 3.6(c). The z-axis rotation angle induced by a J_z pulse of duration t_{pulse} is given by

$$\theta_z(u_{\text{B1}}, t_{\text{pulse}}) = \frac{1}{\hbar}\int_0^{t_{\text{pulse}}} J_z(u_{\text{B1}}, t)\, dt \longrightarrow \frac{t_{\text{pulse}}}{\hbar}\, J_z(u_{\text{B1}}), \tag{3.6}$$

---

[6] The measurement sequence for acquiring J_z fingerprints also includes n-axis rotations performed before and after each J_z pulse to bring the qubit state into and out of the $x - y$ plane of the Bloch sphere. These pre- and post-manipulations are necessary for observing rotations about the z-axis. In the lingo of quantum computing experiments, we might describe a J_n fingerprint measurement to be 'Rabi-like,' and a J_z fingerprint to be 'Ramsey-like.'

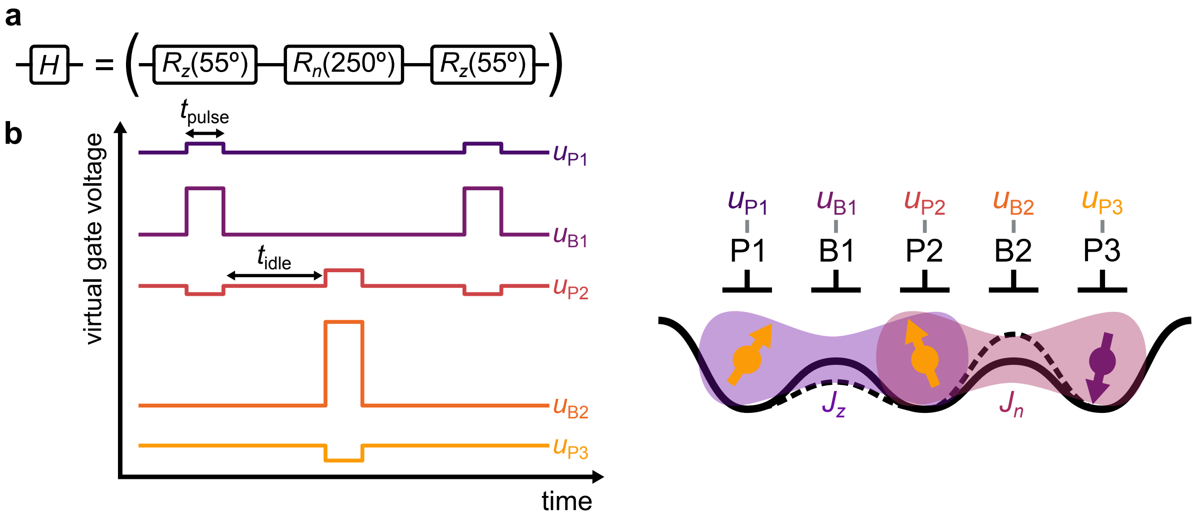

Figure 3.7: Exchange-pulse decomposition for a single-qubit Hadamard gate. **(a)** Quantum circuit for an exchange-only Hadamard gate, implemented by three alternating rotations around the Bloch sphere's z- and n-axes. **(b)** Example virtual voltage pulse sequence for driving the rotations in (a). Virtual voltages primarily correspond to the physical device gates indicated in the triple-dot diagram.

where the simplification after the arrow assumes that J_z is driven by a rectangular u_{B1} pulse, as is typical in most experiments. The oscillation extrema marked by stars in Fig. 3.6(e) correspond to z-axis rotations of π, 2π, 3π, etc. For the pulse time of $t_{\text{pulse}} = 50$ ns used in this measurement, they indicate the pulse amplitudes where $J_z(u_{\text{B1}})/h = 10$, 20, 30 MHz, and so on, following from Eq. (3.6). The oscillation fringes get closer together at higher pulse amplitudes due to the approximately exponential scaling of exchange coupling with barrier voltage [72,102]. The data in Fig. 3.6(e) are fit to a model that extracts $\theta_z(u_{\text{B1}}, t_{\text{pulse}})$, and a similar approach is used to extract $\theta_n(u_{\text{B2}}, t_{\text{pulse}})$ [103]. These relations enable us to determine the precise barrier pulse needed to drive a desired rotation on the Bloch sphere.[7]

Single-Qubit & Two-Qubit Gates

In typical qubit operation, only one exchange coupling is pulsed at a time. Arbitrary single-qubit gates are implemented by interleaving calibrated z-axis and n-axis rotations [103]. For

---

[7] Following this procedure, the voltage-to-rotation mapping can be further refined by performing additional calibration measurements with more intricate pulse sequences. For more information, refer to Ref. [103].

example, a Hadamard gate can be realized with a sequence consisting of a 55° rotation about the z-axis, a 250° rotation about the n-axis, and a second 55° rotation about the z-axis, as indicated in Fig. 3.7(a). The complete set of single-qubit Clifford gates can be decomposed into sequences of one to four rotations in the form

$$C_i = R_n(\theta_4)\, R_z(\theta_3)\, R_n(\theta_2)\, R_z(\theta_1), \tag{3.7}$$

where i indexes the gate in the Clifford group, and $R_z(\theta) = \exp\left(i\theta\hat{\sigma}_z/2\right)$ and $R_n(\theta) = \exp\left[-i\theta\left(\hat{\sigma}_z + \sqrt{3}\hat{\sigma}_x\right)/4\right]$ are the operators for z-axis and n-axis rotations, respectively [103]. Figure 3.7(b) illustrates a time trace for a series of rectangular voltage pulses that might be used to implement the Hadamard gate in panel (a). The pulses have a fixed duration of t_{pulse}, with idle periods of t_{idle} in between. Pulses applied to the virtual barriers modulate the exchange couplings, while smaller detuning pulses applied via the virtual plungers maintain symmetric operation. Two-qubit gates, while not demonstrated in this chapter, can be achieved using control sequences that include exchange pulses between spins in neighboring qubits [58, 115, 127–130].[8]

Unlike most other qubits, the exchange-only qubit's rotation axes are non-orthogonal in the Bloch sphere. As a consequence, the control sequences for exchange-only gates are less efficient than for other encodings, requiring more rotations to implement the same operations. For instance, executing the 24 single-qubit gates in the Clifford group require an average of 2.7 rotations in the exchange-only framework, compared to 1.9 rotations for other qubit types [103]. Two-qubit gates are significantly more costly, with an average of 41.1 exchange pulses needed for the 11,520 two-qubit Clifford gates [58]. The added complexity in pulse design is a notable drawback of the exchange-only encoding, resulting in longer gate times and the risk of lower fidelity. Recent research has aimed at reducing the control overhead for exchange-only qubits by identifying shorter two-qubit gate sequences [130], employing

---

[8] Entangling gates can act differently depending on the projections of the qubits' gauge spins, and care must therefore be taken to design operations that preserve the gauge invariance of the encoding [24, 115, 127].

simultaneous pulsing of J_z and J_n [112], and utilizing triangular triple-dot geometries to add a third exchange coupling between spins 1 and 3 [131].

3.2.4 Qubit Fidelity & Error Sources

Error rates for exchange-only qubits are commonly measured using a technique known as **blind randomized benchmarking (BRB)** [103]. The procedure for BRB is diagrammed as a quantum circuit in Fig. 3.8(a). After initializing in the $|0\rangle$ state, a sequence of N randomly drawn gates C_i from the single-qubit Clifford group is applied to the qubit. Next, a recovery gate is applied, randomly selected for each trial to be either $C_{|0\rangle}$, which inverts the manipulation sequence and ideally returns the qubit state to $|0\rangle$, or $C_{|1\rangle}$, which ideally brings the qubit to $|1\rangle$.[9] Lastly, the qubit's final state is read out. In real systems, decoherence and imperfections in the gate operations accumulate throughout the manipulation sequence, preventing perfect recovery to $|0\rangle$ or $|1\rangle$. This accumulation provides a means of extracting the average error for each gate applied during the circuit. Randomized benchmarking methods are insensitive to **state preparation and measurement (SPAM)** errors and scale efficiently, making them ideal for rapid characterization of many qubits [132, 133].

Figure 3.8(b) shows an example BRB dataset measured by Weinstein *et al.* [58]. The qubit's $|0\rangle$ probability is plotted versus the sequence length N, aggregated over many trials of the measurement circuit in panel (a). At small N, the manipulation sequence is too short for significant errors to accumulate, so we should expect the recovery operations to be nearly perfect. The data in Fig. 3.8(b) reflect this: the blue data points—representing trials where $C_{|0\rangle}$ was applied—show a $|0\rangle$ probability near 1; the red data points—representing trials where $C_{|1\rangle}$ was applied—show a probability close to zero. As N increases, more errors accumulate during the circuit, reducing the likelihood of successful recovery. We can gain

---

[9] The random selection of the recovery gate differentiates BRB from the conventional randomized benchmarking protocol, which always applies $C_{|0\rangle}$ [132]. As explained in Ref. [103], using two alternative recovery gates allows for the determination of the exchange-only qubit's leakage error rate as a subset of the total error rate.

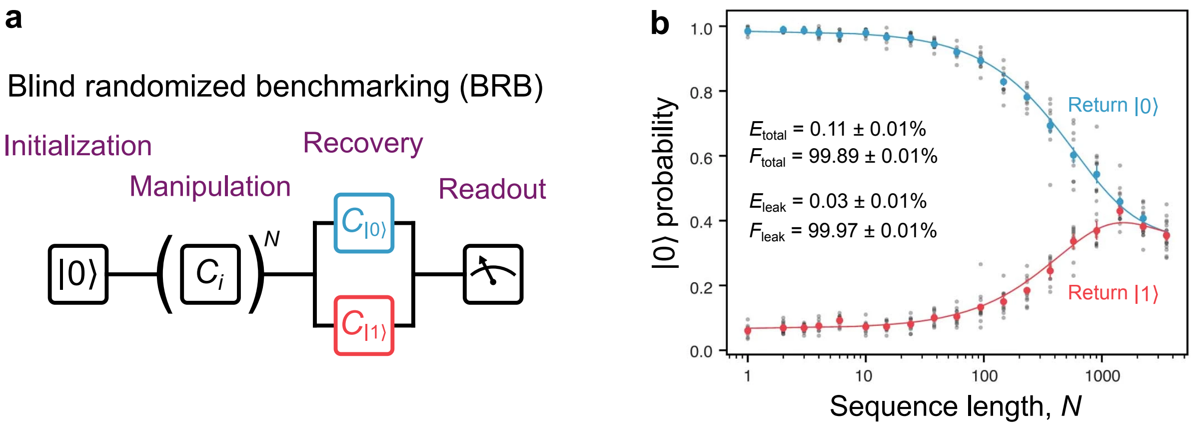

Figure 3.8: Exchange-only qubit fidelity measurement using BRB. **(a)** Quantum circuit for BRB, constructed from N randomly chosen Clifford gates C_i and a randomly selected recovery gate $C_{|0\rangle}$ or $C_{|1\rangle}$. **(b)** Qubit $|0\rangle$ measurement probability versus sequence length N, aggregated from many repetitions of the circuit in (a). Average rates for total and leakage error are estimated by fitting to the $C_{|0\rangle}$ (blue) and $C_{|1\rangle}$ (red) datasets. (b) adapted from Ref. [58].

---

insight into the nature of these errors by observing the decay behavior at large N. Recall from Section 3.2.1 that the three-spin Hilbert space has eight basis states, with two mapping to $|0\rangle$, and two mapping to $|1\rangle$. If the errors during manipulation scatter the qubit's state into an incoherent mixture of $|0\rangle$ and $|1\rangle$, the BRB recovery probability should approach 0.5 $(= 2/4)$ at large N for both $C_{|0\rangle}$ and $C_{|1\rangle}$ sequences. If, on the other hand, the errors result in *leakage* out of the computational subsystem, leading to a uniform mixture of all eight basis states, the measurement probability of $|0\rangle$ should drop to 0.25 $(= 2/8)$. The data in Fig. 3.8(b) appear to asymptotically approach 0.25 at $N \gg 1{,}000$, indicating that leakage plays a prominent role in the exchange-only qubit's error pathways [103].

The blue and red data points in Fig. 3.8(b) can be fit to extract the average error per single-qubit Clifford gate E_{total}. Additionally, these fits provide the average *leakage* error per Clifford E_{leak}, as a subset of the total error rate. Leakage errors are more serious than non-leakage errors because they are bypassed in most quantum error correction codes and can propagate between qubits during entangling gates [58]. For the dataset shown here, leakage errors account for roughly 25% of the total error rate. When discussing qubit performance, the term **gate fidelity** is often used to describe how closely a quantum operation matches its idealized implementation. The BRB error rates are easily translated into average single-qubit Clifford gate fidelities: $F_{\text{total}} = 1 - E_{\text{total}}$ represents the total fidelity, while $F_{\text{leak}} = 1 - E_{\text{leak}}$ defines the non-leakage fidelity. The experiment by Weinstein *et al.* measured an average single-qubit fidelity of approximately 99.9%, and the same article demonstrated an average two-qubit fidelity of 97.1% [58]. For context, it is thought that fault-tolerant quantum computing with known error correction codes may become practical once both single-qubit and two-qubit gate fidelities reach 99.99% [134].

Detailed diagnoses of various error channels in Refs. [58] and [103] have identified hyperfine interactions with nuclear spins as the dominant error mechanism in exchange-only qubit operations—even when devices use isotopically enhanced silicon with a ^{29}Si abundance of 800 ppm. Aside from further isotopic purification, the most straightforward way to mitigate this error source is to speed up gate times, minimizing the qubits' exposure to integrated magnetic field noise during operation sequences. Caution is needed, though, when shortening t_{pulse} and t_{idle} toward this end. Every control circuit has limited bandwidth, and pulsing too quickly has been shown to introduce rotation errors due to distorted voltage signals [103]. Achieving high-fidelity operation is thus a balancing act between fast pulsing and avoiding control errors.

3.3 Assessing the Impact of Crosstalk During Parallel Exchange-Only Qubit Operations

As quantum computing experiments evolve in complexity from small-scale demonstrations to sophisticated orchestrations involving many qubits, managing crosstalk between qubits becomes a critical engineering challenge. Strong and nonlinear crosstalk effects have been observed in microwave-driven spin qubits [122]. In comparison, exchange-only qubits are often regarded as being more robust against crosstalk, thanks to the strong localization of the exchange interaction and the lower propensity for leakage of baseband signals relative to microwave signals in electrical circuits [58,103].[10] However, there is limited experimental data on multi-qubit systems using exchange-only qubits, leaving the impact of crosstalk largely unexamined. In particular, the effects of crosstalk when baseband control signals are applied simultaneously to multiple exchange-only qubits in an array remain unexplored. As we move toward next-generation processors with many qubits, it is important to study crosstalk in these systems, understand its influence on quantum control, and develop strategies to mitigate its effects. The remainder of this chapter focuses on understanding the impact of crosstalk in exchange-only qubit arrays when multiple exchange couplings are pulsed in parallel.

3.3.1 Sequential & Parallel Single-Qubit Operations

In previous experiments with two-qubit processors formed in six-dot linear arrays, single-qubit operations were performed *sequentially* during quantum circuits, as depicted in Fig. 3.9(a) [55, 58]. In this type of control scheme, only one qubit—either Q1 or Q2—is manipulated at a time using interleaved R_z and R_n rotations, while the other remains idle. The qubits' exchange couplings are tuned to be negligible during idling ($J/h \lesssim 10$ kHz), and their sensitivity to effective voltage shifts from cross-capacitance is also low in this regime [$(dJ/dV)/h \lesssim 1$ kHz/mV] [58]. Sequential operation naturally protects against control-signal crosstalk by ensuring that multiple exchange couplings in the array are never simultaneously activated. As illustrated in Fig. 3.9(b), an exchange pulse applied to Q2 may slightly alter the electric potential in Q1 due to mutual capacitances. Nevertheless, Q1's reduced sensitivity during idling ensures that the crosstalk has minimal effect on its exchange couplings, thus preserving its quantum encoding.

---

[10] To understand why baseband signals are less susceptible to leakage, note that the impedance between capacitively coupled circuit components is given by $Z_C = 1/i\omega C$, where ω represents angular frequency. Baseband pulses are composed of lower-frequency components than microwave signals, and therefore encounter larger impedances as they propagate through circuits, resulting in less leakage and better isolation between circuit elements.

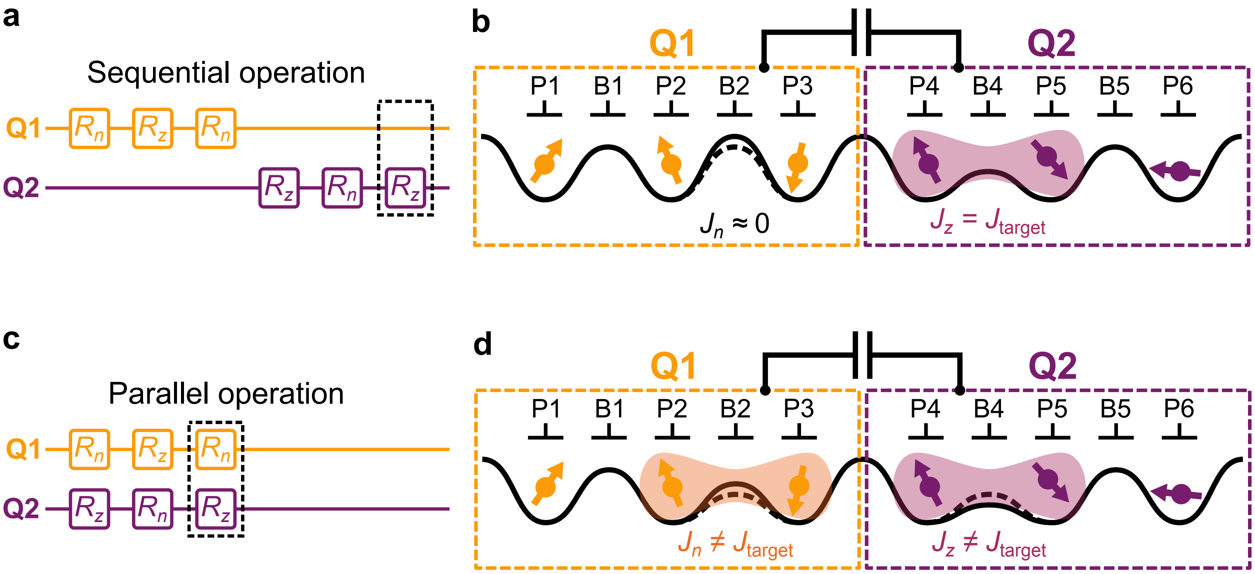

Figure 3.9: Sequential vs. parallel operations in a two-qubit array. **(a)** Sequential operation scheme where only one qubit (Q1 or Q2) is manipulated at a time during quantum circuits. **(b)** Electric potential in the two-qubit linear array during a Q2 R_z rotation [dashed boxed gate in (a)]. Capacitive crosstalk has minimal impact on Q1 while it idles, as its exchange coupling remains inactive ($J_n \approx 0$). **(c)** Parallel operation scheme where exchange couplings in both qubits are pulsed simultaneously during quantum circuits. **(d)** The impact of control-signal crosstalk is felt more strongly during simultaneous R_n and R_z operations [dashed boxed gates in (c)]: both qubits' exchange values deviate from their targeted values ($J_i \neq J_\text{target}$).

Now consider an alternative control scheme, shown in Fig. 3.9(c), where single-qubit gates are executed *in parallel*. In this setup, exchange pulses overlap in time, significantly reducing the overall gate sequence duration. However, this comes with the increased risk of control-signal crosstalk becoming problematic. When exchange couplings pulsed to be active ($J/h \gtrsim 10$ MHz), they are much more sensitive to small effective voltage changes due to crosstalk [$(dJ/dV)/h \gtrsim 1$ MHz/mV] [58]. As Fig. 3.9(d) suggests, even minor shifts in the local electric potential due to crosstalk can prevent pulsed couplings in Q1 and Q2 from reaching their target values. If this crosstalk is not properly accounted for in the control pulse calibration, it will result in qubit errors.

While sequential qubit operation is effective for achieving high-fidelity gates in few-qubit experiments, scaling up processors will require some degree of parallel operation to keep circuit times within acceptable limits (though not necessarily involving nearest-neighbor

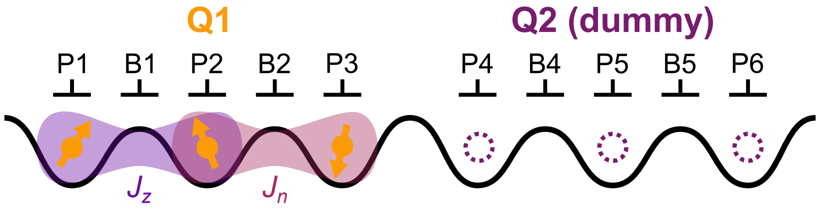

Figure 3.10: Two-qubit test bed for measuring nearest-neighbor crosstalk. The left qubit Q1 is fully calibrated as an exchange-only qubit, while Q2 on the right acts as a 'dummy qubit'. Experiments measure the impact of crosstalk on Q1 while it is operated in parallel with Q2.

---

qubits, as Fig. 3.9 depicts). Since qubits remain vulnerable hyperfine noise while idling (as discussed in Section 3.2.4), there are likely to be coherence tradeoffs between minimizing crosstalk and keeping runtimes short. Exploring these tradeoffs and optimizing exchange-only circuit compilation for coherent control will be essential as devices grow in complexity.

3.3.2 Measuring Crosstalk in Exchange-Only Fingerprints

The twelve-dot linear array in the Tunnel Falls device shown in Fig. 3.1 provides an ideal platform for characterizing the effects of crosstalk in a one-dimensional processor geometry. To investigate parallel operation of nearest-neighbor qubits—representing a worst-case scenario for crosstalk—our experiments primarily focus on a two-qubit test bed formed in the six leftmost dots of the device. Figure 3.10 displays this portion of the array, in which Q1 is a fully-calibrated exchange-only qubit beneath the plungers P1, P2, and P3. The neighboring dots below P4, P5, and P6 comprise a 'dummy qubit' Q2, tuned to the single-electron regime but not calibrated for qubit operations. During experiments, we perform single-qubit operations with Q1 while simultaneously sending baseband pulses to the gates of Q2, allowing us to observe any adverse effects on Q1 caused by crosstalk. Our study does not investigate the impact of crosstalk that might arise from simultaneous exchange pulsing during two-qubit gates.

To measure the impact of 'raw' crosstalk between the qubits, our initial measurements are performed without applying any virtual gate compensation between Q1 and Q2. Specifically, we implement virtual gate voltages defined by the system

$$\left(\begin{array}{c} u_{\mathrm{P1}} \\ u_{\mathrm{B1}} \\ u_{\mathrm{P2}} \\ u_{\mathrm{B2}} \\ u_{\mathrm{P3}} \\ \hdashline u_{\mathrm{P4}} \\ u_{\mathrm{B4}} \\ u_{\mathrm{P5}} \\ u_{\mathrm{B5}} \\ u_{\mathrm{P6}} \end{array}\right) = \left(\begin{array}{ccccc:ccccc} 1 & \beta^1_{\mathrm{B1}} & \beta^1_{\mathrm{P2}} & \beta^1_{\mathrm{B2}} & \beta^1_{\mathrm{P3}} & 0 & 0 & 0 & 0 & 0 \\ 0 & 1 & 0 & 0 & 0 & 0 & 0 & 0 & 0 & 0 \\ \beta^2_{\mathrm{P1}} & \beta^2_{\mathrm{B1}} & 1 & \beta^2_{\mathrm{B2}} & \beta^2_{\mathrm{P3}} & 0 & 0 & 0 & 0 & 0 \\ 0 & 0 & 0 & 1 & 0 & 0 & 0 & 0 & 0 & 0 \\ \beta^3_{\mathrm{P1}} & \beta^3_{\mathrm{B1}} & \beta^3_{\mathrm{P2}} & \beta^3_{\mathrm{B2}} & 1 & 0 & 0 & 0 & 0 & 0 \\ \hdashline 0 & 0 & 0 & 0 & 0 & 1 & \beta^4_{\mathrm{B4}} & \beta^4_{\mathrm{P5}} & \beta^4_{\mathrm{B5}} & \beta^4_{\mathrm{P6}} \\ 0 & 0 & 0 & 0 & 0 & 0 & 1 & 0 & 0 & 0 \\ 0 & 0 & 0 & 0 & 0 & \beta^5_{\mathrm{P4}} & \beta^5_{\mathrm{B4}} & 1 & \beta^5_{\mathrm{B5}} & \beta^5_{\mathrm{P6}} \\ 0 & 0 & 0 & 0 & 0 & 0 & 0 & 0 & 1 & 0 \\ 0 & 0 & 0 & 0 & 0 & \beta^6_{\mathrm{P4}} & \beta^6_{\mathrm{B4}} & \beta^6_{\mathrm{P5}} & \beta^6_{\mathrm{B5}} & 1 \end{array}\right) \left(\begin{array}{c} V_{\mathrm{P1}} \\ V_{\mathrm{B1}} \\ V_{\mathrm{P2}} \\ V_{\mathrm{B2}} \\ V_{\mathrm{P3}} \\ \hdashline V_{\mathrm{P4}} \\ V_{\mathrm{B4}} \\ V_{\mathrm{P5}} \\ V_{\mathrm{B5}} \\ V_{\mathrm{P6}} \end{array}\right). \tag{3.8}$$

In this setup, the crosstalk matrix has a block-diagonal structure, with the upper left block representing Q1's virtual gates and the lower right block corresponding to Q2's virtual gates. The Q1 plungers are virtualized *in the subspace of Q1 gates*, while the Q2 plungers are virtualized *in the subspace of Q2 gates*. Importantly, the matrix elements compensating for crosstalk between Q1 and Q2 are *explicitly set to zero*. This virtual gate implementation should ensure that any crosstalk between the qubits is not masked by plunger voltage compensation. The outer barrier gates B0 and B6 are not indicated in Fig. 3.10 or Eq. (3.8), nor is the barrier B3 separating Q1 and Q2. The voltages applied to these gates remain stationary throughout all experiments.

We begin our investigation by examining the effects of crosstalk on the fingerprints used for exchange pulse characterization and calibration. Figure 3.11(a) describes a portion of a Q1 J_n fingerprint measurement circuit modified for this purpose. As in standard fingerprint measurements, exchange pulses with varying barrier and detuning amplitudes are applied to Q1 to drive n-axis rotations, represented by $R_n(\varepsilon_{v23}, u_{\mathrm{B2}})$ gates in the circuit diagram. Simultaneously with each Q1 exchange pulse, we apply a voltage pulse with a specified amplitude to B4 in Q2; these crosstalk pulses are denoted by $XT_{\mathrm{B4}}(u_{\mathrm{B4}})$ gates. Q1 readout and initialization sequences between exchange pulses are also indicated. A similar experiment can be performed using Q1 J_z fingerprint measurements.

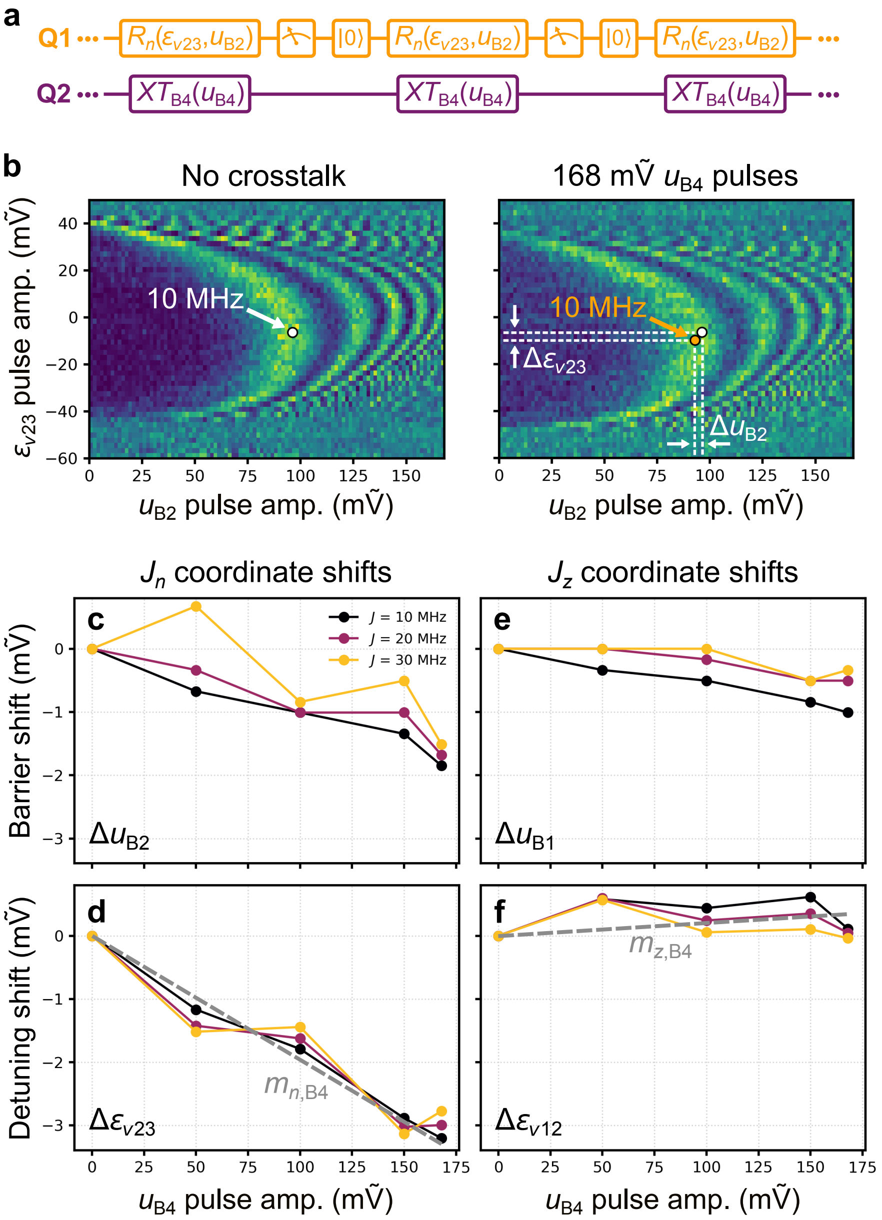

Figure 3.11: Nearest-neighbor crosstalk measured in qubit fingerprints. **(a)** Quantum circuit used for measuring the impact of crosstalk on Q1 J_n fingerprints. Crosstalk pulses are applied to B4 in Q2 during every J_n pulse. **(b)** Comparison of Q1 J_n fingerprints measured with no crosstalk (left) and with crosstalk pulses applied to B4 (right). White and orange dots mark the coordinates for symmetric $J_n/h = 10$ MHz pulses in each case. **(c,d)** Barrier and detuning coordinate shifts extracted from J_n fingerprints for different u_{B4} crosstalk pulse amplitudes. **(e,f)** Coordinate shifts extracted from similar J_z fingerprint measurements.

Figure 3.11(b) compares Q1 J_n fingerprints acquired with and without Q2 crosstalk. The plot on the left shows a control measurement where no crosstalk pulses are applied to

B4 [i.e., $XT_{\mathrm{B4}}(0\ \mathrm{m\tilde{V}})$].[11] The white dot on the first oscillation fringe marks the u_{B2} and ε_{v23} coordinates corresponding to a symmetric $J_n/h = 10$ MHz exchange pulse. The plot on the right shows a measurement with crosstalk pulses of 168 m$\tilde{\mathrm{V}}$[12] applied to B4 [i.e., $XT_{\mathrm{B4}}(168\ \mathrm{m\tilde{V}})$]. Here, the orange dot corresponds to a $J_n/h = 10$ MHz pulse. As a result of the crosstalk, the coordinates for this exchange pulse are shifted by a few m$\tilde{\mathrm{V}}$ along both the barrier and detuning axes, relative to the control measurement; we denote these coordinate shifts as Δu_{B2} and $\Delta\varepsilon_{v23}$, respectively.

Figures 3.11(c) and 3.11(d) display coordinate shifts measured in J_n fingerprints as a function of the B4 crosstalk pulse amplitude. In these measurements, we track the coordinates for symmetric pulses of $J_n/h = 10$, 20, and 30 MHz (plotted in black, purple, and yellow, respectively). The data indicate that the voltage coordinate shifts get larger as the crosstalk pulse amplitude increases, as we would intuitively expect from a cross-capacitance model. Additionally, the shifts appear to be relatively linear with the u_{B4} amplitude, and they are largely consistent across different J_n magnitudes, except for two outliers in panel (c). Coordinate shifts are also extracted from J_z fingerprint measurements and shown in Figs. 3.11(e) and (f). These shifts are smaller than the ones observed in the J_n fingerprints. Once again, this behavior is consistent with a cross-capacitance model: for our device geometry, the Q1 gates that control J_z are positioned farther from B4 than those controlling J_n, and therefore have smaller cross-capacitance.[13]

To look for signs of beyond-nearest-neighbor crosstalk, we perform similar Q1 fingerprint measurements while simultaneously pulsing more distant gates in the qubit array; Fig. 3.12(a) displays the results. Extracted coordinate shifts for 10 MHz exchange pulses are shown with crosstalk pulses applied to B4, B7, and P12. Figure 3.12(b) depicts the positions of these

---

[11] Recall that virtual voltages are represented using imaginary units, abbreviated by ‘$\tilde{\mathrm{V}}$,’ as discussed in Section 2.2.3.

[12] This value is chosen because it is the maximum u_{B4} pulse amplitude that the AWG is capable of generating.

[13] The capacitive coupling between quantum-dot gates separated by a distance r has been observed to follow a $\sim 1/r^3$ dependence [53, 135].

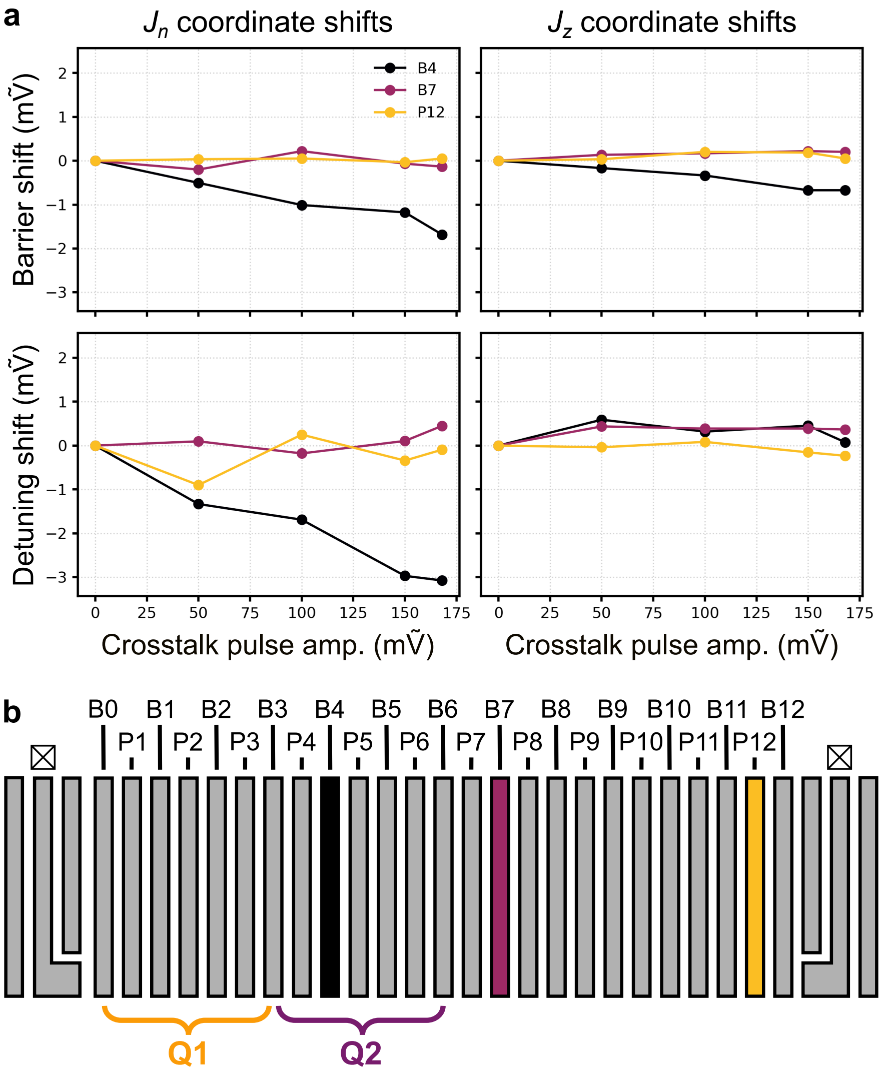

Figure 3.12: Beyond-nearest-neighbor crosstalk measured in qubit fingerprints. **(a)** Exchange pulse coordinate shifts measured while simultaneously pulsing gates B4, B7, and P12. **(b)** Color-coded device map showing the gates pulsed during the measurements in (a).

---

gates in the array. No clear shifts are observed when B7 and P12 are pulsed, indicating that any crosstalk effects are below the sensitivity limits of this measurement. These findings are encouraging for the parallel operation of exchange-only qubits: while simultaneous operation of nearest neighbors in a one-dimensional array may present challenges, crosstalk between more distant qubits appears to be much less problematic.

The measurements presented in Figs. 3.11 and 3.12 use exchange pulse times of $t_{\text{pulse}} =$ 50 ns. We have also measured fingerprint coordinate shifts using 10 and 20 ns pulses, and have conducted comparable experiments where Q2's dc gate voltages are stepped between fingerprint measurements instead of actively pulsed. In all cases, the measured coordinate shifts are consistent, showing no evidence of frequency-domain dependence for qubit crosstalk.

3.3.3 Using Fingerprint Shifts for Virtual Gate Calibration

Now that we have developed an understanding of how baseband crosstalk affects the fingerprints that characterize the exchange interaction, we can start to consider mitigation strategies. The first and most obvious step to take is restoring the Q1-Q2 compensation coefficients in our virtual plunger gates, which were previously set to zero. This measure simply returns us to the standard virtual gates scheme outlined in Section 2.2.3. Given the linear relationship between $\Delta\varepsilon_v$ and the crosstalk pulse amplitude observed in Fig. 3.11 and other measurements, we expect that linear voltage compensation applied to the virtual plungers should effectively offset the fingerprint detuning shifts (countering the barrier shifts would require barrier gate compensation, which is not implemented here).

Interestingly, the data gathered from our fingerprint measurements can be utilized to calibrate the virtual plunger gates for Q1. To show how this works, let us consider the task of adjusting Q1's virtual plunger gates to compensate for B4 crosstalk, which requires determining the coefficients β^1_{B4}, β^2_{B4}, and β^3_{B4}. We estimate these parameters from our fingerprint shift measurements by first performing linear fits to the data in Figs. 3.11(d) and 3.11(f) (shown by dashed gray lines). The slopes from these fits, $m_{z,\mathrm{B4}}$ and $m_{n,\mathrm{B4}}$, are then fed into a simple capacitance model, yielding approximate analytical expressions for the crosstalk coefficients:

$$\begin{aligned}
&\beta^1_{\mathrm{B4}} \approx 0,\\
&\beta^2_{\mathrm{B4}} \approx m_{z,\mathrm{B4}}\sqrt{2},\\
&\beta^3_{\mathrm{B4}} \approx (m_{z,\mathrm{B4}} + m_{n,\mathrm{B4}})\sqrt{2}.
\end{aligned} \tag{3.9}$$

Here, β^1_{B4} is assumed to be negligible given the device geometry, enabling closed-form expressions to be derived for the other two coefficients. The same process can be repeated iteratively to calibrate Q1's plunger compensation for crosstalk from additional gates in the array.

The 'fingerprint calibration method' for virtual gates described here differs significantly from the 'standard calibration method' detailed in Section 3.3.3, as it does not rely on reservoir tunneling measurements. In a qubit array like the Tunnel Falls device, the interior dots only have reservoir access during their initial tune-up, and are later isolated from reservoirs as more dots are added to the system. As a result, virtual gates calibrated at the preliminary stages of experiments are not fine-tuned for the quantum processor's final operating point, often necessitating manual adjustments to the crosstalk matrix elements for better accuracy. The fingerprint calibration method avoids this obstacle, as it is performed *in situ* at the processor's operating point.

Figure 3.13 compares exchange pulse detuning shifts measured using different virtual plunger gate calibrations. In these plots, the black data points represent the baseline case with no Q1-Q2 crosstalk compensation. Measurements using standard virtual gate calibration (without fine-tuning) are displayed in purple, and those using the fingerprint method are shown in yellow. We find that virtual gates implemented using the fingerprint calibration method nearly eliminate the detuning shifts caused by B4 [panel (a)] and P4 [panel (b)] crosstalk (with crosstalk from gates beyond B4 being too weak to induce significant shifts). Furthermore, without any manual fine-tuning, this approach performs as well as or better than the standard calibration procedure, especially when compensating J_n pulses.

It is important to recognize that the fingerprint calibration method, as implemented here, is not scalable for setting up crosstalk compensation in many-qubit systems. It has two major limitations. First, it requires many two-dimensional fingerprint scans to be acquired at high resolution, making it a far more time-consuming approach than the standard calibration method. Second, the relations in Eq. (3.13) are tailored to the specific geometry for this experiment, assuming that the P1 dot experiences negligible crosstalk at the far end of the

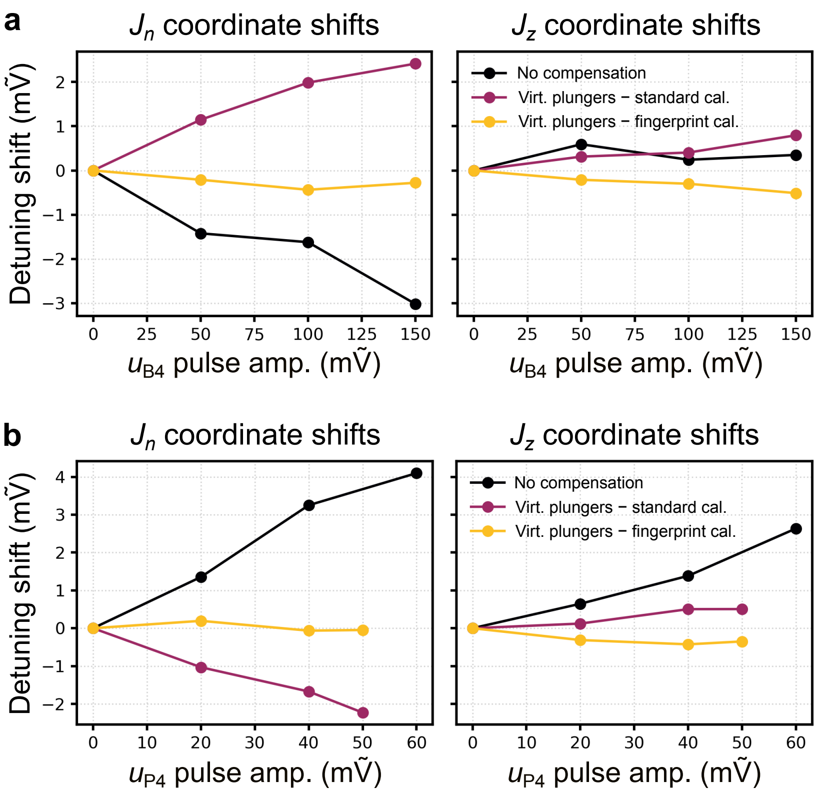

Figure 3.13: Comparison of exchange pulse detuning shifts measured using different virtual plunger gate calibrations. $J_n/h = 10$ MHz detuning coordinate shifts are measured with crosstalk pulses applied to **(a)** B4; and **(b)** P4.

---

one-dimensional array; this assumption will not hold for general device geometries. At the same time, the standard calibration method also faces scalability issues due to its reliance on trial-and-error fine-tuning. As quantum processors grow, it is clear that new methods will be needed for deploying crosstalk compensation at scale. The fingerprint calibration approach presented here is intriguing because it uses feedback from *qubit-based* measurements, highlighting the potential for development of alternative, qubit-based methods for efficiently dialing in crosstalk compensation.

3.3.4 Benchmarking Qubit Error Due to Crosstalk

The ultimate measure of crosstalk's deleterious effect is its impact on quantum gate fidelity. To conclude our investigation of crosstalk during parallel exchange-only qubit operation, we perform a preliminary analysis of crosstalk-induced errors in single-qubit gates.

Thus far, we have observed the effects of crosstalk through shifts of the Q1 fingerprints. The way that these shifts lead to qubit errors is by throwing off the calibration of exchange control pulses. Figure 3.14(a) shows two symmetric exchange pulse calibration curves corresponding to the fingerprint measurements in Fig. 3.11(b). The black curve plots the exponential J_n versus u_{B2} relation in the left fingerprint with no crosstalk, while the orange curve shows the same relation for the right fingerprint, where u_{B4} crosstalk pulses are applied. Due to the barrier coordinate shift between the fingerprints, the calibration curves are offset by an amount $\Delta J_n(u_{\mathrm{B2}})$. If we calibrate Q1 according to the black curve, crosstalk from B4 will cause J_n pulses applied to Q1 to be systematically too large during parallel operations. As illustrated in Fig. 3.14(b), the over-activation of this exchange coupling leads to over-rotations of $\Delta\theta_n = \Delta J_n t_{\mathrm{pulse}}/h$ on the Bloch sphere, and ultimately, to errors in quantum circuits.

To look for signs of crosstalk error, we conduct BRB experiments where 150 m$\tilde{\mathrm{V}}$ crosstalk pulses (XT_j) are simultaneously applied to gate j in Q2 during Q1 Clifford gates, as illustrated in Fig. 3.14(c). Control pulse and idle times of $t_{\mathrm{pulse}} = t_{\mathrm{idle}} = 20$ ns are used. Figure 3.14(d) displays the results, with each data point representing a separate BRB run. The baseline total error rate for Q1 without crosstalk is 1.0 – 1.1%, corresponding to an average gate fidelity of 89.9 – 99.0%. When crosstalk pulses are applied to B4 without Q1-Q2 compensation—representing a worst-case crosstalk scenario—the error rate increases by approximately 0.3 – 0.4% (black data points). Smaller error increases are observed when crosstalk pulses are applied to B5 and B6. Additionally, a single trial with pulses applied to P12 at the far end of the array shows a slight increase in the Q1 error rate, suggesting the possibility that beyond-nearest-neighbor crosstalk may subtly impact qubit fidelity, though further data is needed for confirmation.

Restoring virtual plunger gate compensation between Q1 and Q2 (yellow data points) appears to mitigate a significant portion of crosstalk-induced errors. With this compensation

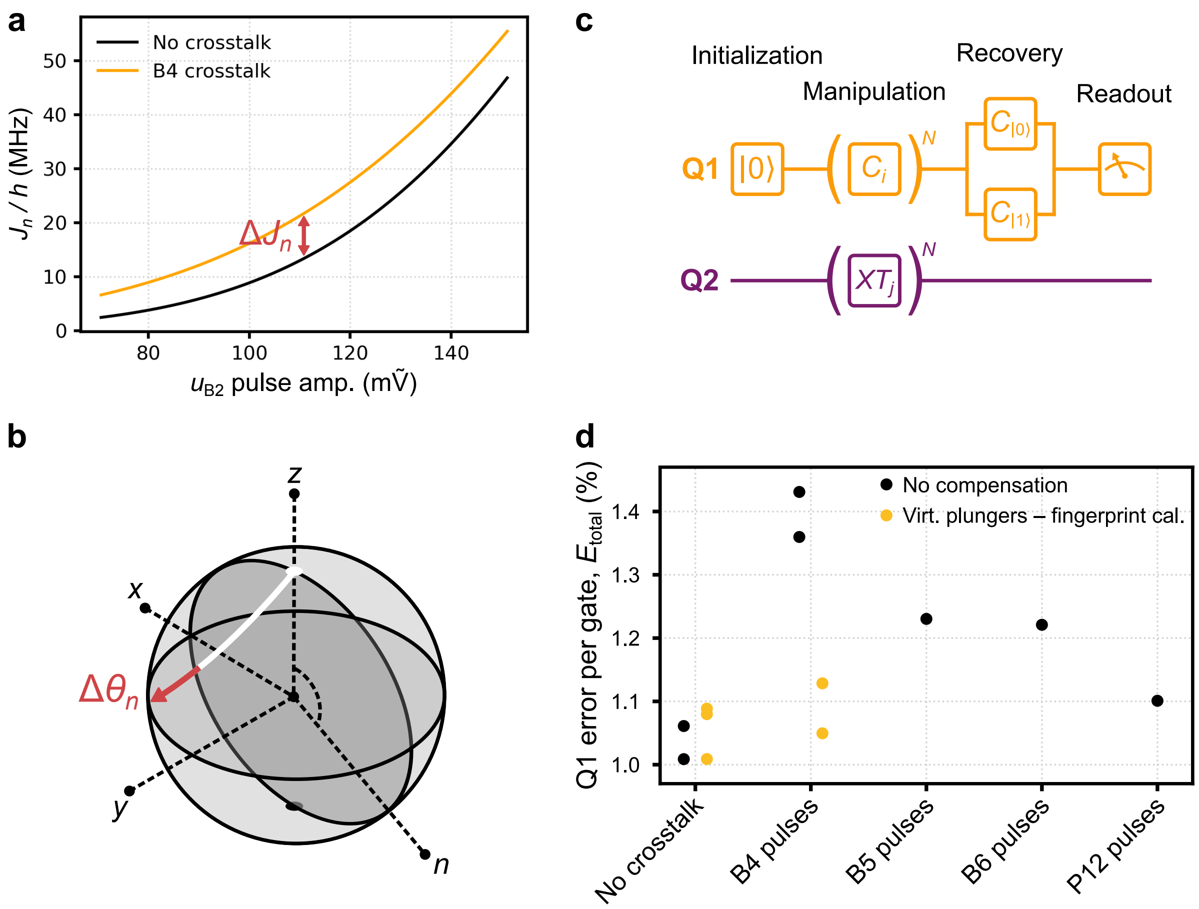

Figure 3.14: BRB measurements of crosstalk-induced qubit errors. **(a)** J_n calibration curves corresponding to the fingerprint measurements in Fig. 3.11(b), with no crosstalk (black) and with crosstalk pulses applied to B4 (orange). **(b)** Bloch sphere n-axis rotation with an overrotation of $\Delta\theta_n$ (red). This qubit control error is caused by a crosstalk-induced deviation ΔJ_n in the exchange pulse calibration. **(c)** Modified BRB circuit used for measuring Q1 errors due to crosstalk. Simultaneous Q2 crosstalk pulses XT_j are applied to gate j during Clifford operations on Q1. **(d)** Q1 error rates measured using the circuit in (c), with crosstalk pulses applied to different gates. Black points correspond to trials with no Q1-Q2 crosstalk compensation; yellow points correspond to trails with compensation applied to the Q1 virtual plunger gates. (b) adapted with permission from Ref. [24]. Ⓒ 2023 by the American Physical Society.

---

applied during B4 crosstalk pulses, the error rate is only slightly above baseline. This improvement is likely due to a combination of reduced rotation errors and stabilization of Q1 at its SOP during manipulation, which minimizes sensitivity to charge noise. We have not explored in these initial experiments whether this implementation of virtual gates reduces crosstalk errors from other Q2 gates. Further investigation will be needed to fully characterize the effectiveness of virtual plunger gate compensation across the array.

3.3.5 Discussion & Outlook

The results presented in this chapter offer crucial insights into how crosstalk affects parallel exchange-only qubit operations, which has significant implications for scaling these systems to larger arrays. Despite exchange-only qubits generally being considered less susceptible to crosstalk compared to other spin qubit encodings, our experiments demonstrate that crosstalk between nearest-neighbor qubits in a one-dimensional array can still cause substantial issues. The primary manifestation of this crosstalk is through shifts in the exchange pulse calibration voltages, which then contribute to gate errors during quantum circuit execution. Our preliminary findings suggest that unmitigated crosstalk-induced errors, at their worst, are comparable in magnitude to other baseline error sources (e.g., charge and hyperfine noise) during parallel single-qubit operations. Even so, the $0.2 - 0.4\%$ increase in error rate caused by nearest-neighbor crosstalk in our experiments would present a significant obstacle to achieving fault-tolerant quantum computing. This underscores the need for further strategies to mitigate crosstalk when operating neighboring qubits simultaneously.

Encouragingly, our studies show that using virtual plunger gates to compensate for crosstalk between qubits helps offset some of its worst effects. This technique, already widely used in quantum-dot qubit architectures, appears effective in reducing crosstalk-induced errors, though there remains room for improvement. To further suppress errors, it will likely be necessary to employ barrier-voltage crosstalk compensation in qubit control schemes. The approximately linear trends observed in the barrier-coordinate shifts in Figs. 3.11(c) and 3.11(e) are interesting, implying that barrier-gate compensation might be achieved using simple linear relations, thus avoiding the complications of nonlinear corrections.

Looking ahead, as we move toward next-generation processors with dozens or hundreds of qubits, additional studies will be necessary to confirm whether these findings extend to more complex architectures, such as two-dimensional qubit arrays. In this geometry, the closer proximity of neighboring qubits could exacerbate capacitive coupling and crosstalk. It will also be important to investigate beyond-nearest-neighbor crosstalk more thoroughly, as subtle long-range interactions, while weaker, could still be detrimental to fault-tolerant operation. Finally, it will be crucial to explore the impact of simultaneous exchange pulses on qubit performance during two-qubit gate sequences to fully understand how crosstalk affects multi-qubit operations.

In conclusion, while the crosstalk effects in simultaneously-operated exchange-only qubits are non-negligible, our results show promising paths forward for mitigating these issues through compensation techniques. As we continue to scale quantum processors to larger arrays, developing scalable solutions for crosstalk compensation and optimizing pulse sequences for coherent control will be essential for ensuring high-fidelity quantum operations.

Part II

Electron-Photon Coupling in Hybrid Quantum-Dot Devices

Chapter 4

Circuit Quantum Electrodynamics with Quantum-Dot Qubits

Having covered the fundamentals of semiconductor qubits, we now begin to explore how superconductors can be integrated to create hybrid systems for quantum computing. This chapter examines how electrons in quantum dots can be coupled to photons in superconducting resonators using techniques borrowed from the superconducting qubit community. We introduce the Jaynes-Cummings model, which provides a framework for qubit-resonator interactions, and show how electron-photon coupling in quantum-dot systems fits into this theoretical structure. Key applications for resonator coupling, such as qubit readout and long-distance two-qubit gates, are then discussed. Finally, we touch on an unconventional ‘longitudinal’ coupling mechanism, setting the stage for a deeper exploration of this coupling in the following chapters.

4.1 Circuit Quantum Electrodynamics

The theoretical groundwork for interfacing solid-state qubits with photons in superconducting resonators, somewhat ironically, traces its origins to the atomic, molecular, and optical (AMO) physics community. The fundamental ideas were initially developed in the context of **cavity quantum electrodynamics (CQED)**, which explores the interaction between atoms and photons within optical cavities. CQED theory is built around a simple model: a quantum harmonic oscillator, representing the cavity, interacting with a two-level quantum system, representing the atom. This foundational model allowed researchers to study and control quantum interactions at a fundamental level [136–138].

In the mid-2000s, amid the early development of superconducting qubits, researchers saw the potential to adapt CQED concepts to solid-state systems. A seminal paper in 2004 by Alexandre Blais and collaborators at Yale formalized a quantum-computing architecture that would become known as **circuit quantum electrodynamics (cQED)**, which reimagined CQED for superconducting circuits [139]. In the cQED framework, a superconducting microwave resonator integrated on-chip serves as an analog to the optical cavity, while the superconducting qubit takes the role of an artificial atom. This setup enables the resonator to read out qubit states and to mediate interactions for two-qubit gates.

The cQED architecture has been remarkably successful, establishing itself as a core technology for developing superconducting quantum processors [140, 141]. However, its utility extends well beyond superconducting qubits. Today, cQED is a standard tool used for addressing a variety of solid-state quantum systems—including quantum-dot qubits [142–145].

4.1.1 A Resonator Boot Camp

Before bringing qubits into the picture, we need to establish a few basic facts about the resonators used in cQED experiments. This section serves as a quick, introductory guide; a more thorough discussion is available in Nathan Holman's thesis [62].

The integrated resonators used in cQED experiments are typically **coplanar waveguide transmission line** segments[1] made from superconducting materials.[2] Due to their historical

---

[1] Although less common, lump-element LC oscillators are also sometimes used as superconducting resonators.

[2] More information on superconductivity is found in Section 7.1.

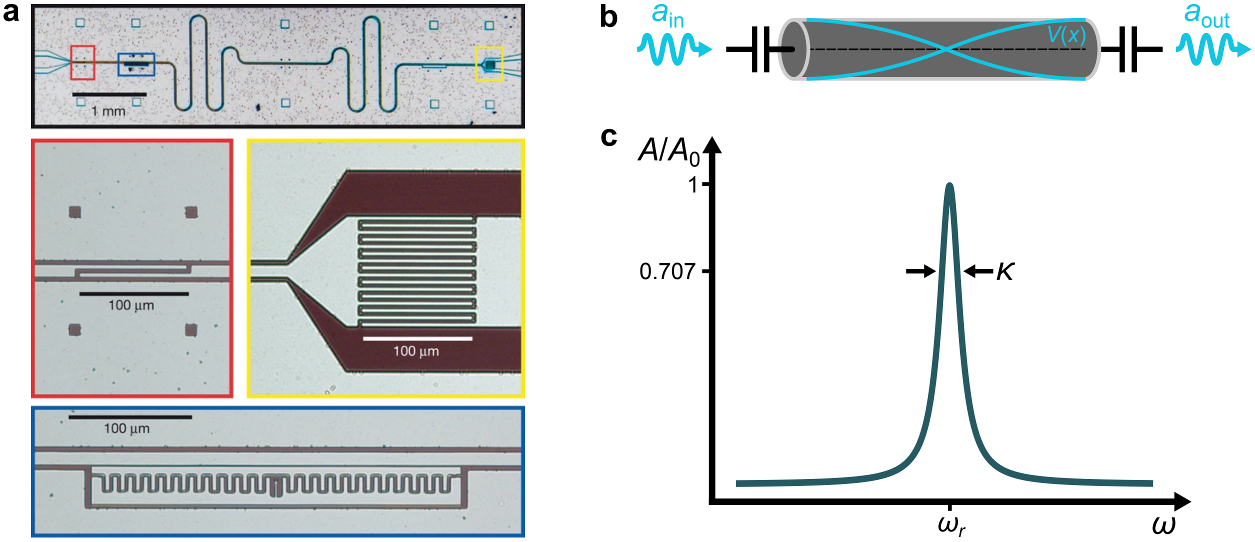

Figure 4.1: Superconducting microwave resonators in cQED experiments. **(a)** cQED chip showing an aluminum transmission-line resonator (upper micrograph) coupled to microwave input/output ports (red and yellow boxes) and a transmon qubit (blue box). **(b)** Typical experimental setup for probing a $\lambda/2$ transmission-line resonator. **(c)** Transmission amplitude response of the resonator, with a peak normalized to $A/A_0 = 1$ at the resonance frequency ω_r. (a) adapted from Ref. [146]. Reproduced with permission from Springer Nature.

connection with optical cavities, these quasi-two-dimensional transmission lines are often still referred to as 'cavities' in the cQED literature; this dissertation uses the terms 'resonator' and 'cavity' interchangeably. Figure 4.1(a) displays a chip used in early cQED experiments by Houck *et al.* [146]. The long, meandering structure in the upper micrograph is an aluminum transmission-line resonator, which is capacitively coupled to microwave input and output ports highlighted in the red and yellow boxes. A transmon qubit, seen in the blue box, is also capacitively coupled to the resonator.

Why are superconducting microwave resonators ideal for interfacing with qubits? Although measuring and manipulating a qubit's quantum state can be experimentally challenging, cQED provides a framework for coupling the qubit to the electric field of a resonator, which is relatively straightforward to control in the laboratory. Through this coupling, the qubit can be addressed indirectly via the resonator field, simplifying certain aspects of operation. Superconducting resonators exhibit exceptionally low energy losses, which helps to reduce decoherence and supports accurate observation of the quantum interactions between the qubit and resonator [62, 147]. Furthermore, the resonators can be fabricated using standard micro- and nanofabrication techniques, and they can transmit signals in the microwave frequency range (typically 1 − 10 GHz). This makes them compatible with readily available telecommunications equipment such as signal generators, amplifiers, attenuators, and power splitters [147].

Measurements on cQED systems are based on probing the transmission properties of the resonator,[3] as illustrated in Fig. 4.1(b). In a typical setup, a microwave tone with a specified frequency, denoted $a_{\text{in}}(\omega)$, is applied to the resonator's input port or a feedline shared by multiple resonators. The signal transmitted through the output port, $a_{\text{out}}(\omega) = A\cos(\omega t+\phi)$, can then be analyzed. The amplitude A and phase ϕ of the transmitted signal can be measured using homodyne or heterodyne detection techniques, as described in Section 5.6.2; in the cQED framework, these components carry information about the qubit as it interacts with the resonator field.

The resonator's **fundamental-mode frequency** ω_r is the frequency at which it naturally oscillates in its lowest energy mode.[4] This frequency depends on the resonator's materials, physical dimensions, and boundary conditions. The resonator in Fig. 4.1(b) is depicted to have a $\lambda/2$ geometry, meaning that a half-wavelength standing voltage wave stretches between its open-circuit boundaries in the fundamental mode [148]. When an input signal is applied at or near ω_r, the resonator's transmission properties exhibit a peak in amplitude, as sketched in Fig. 4.1(c), and a distinct phase response. In this dissertation and elsewhere, it is common to normalize the transmission amplitude peak height by a constant A_0, setting its value to 1 at resonance.

Every resonator has a **photon loss rate** κ, which quantifies the rate at which photons

---

[3] It is also possible to probe cQED systems using the resonator's reflection properties. However, none of the experiments discussed in this dissertation utilize a reflectometry setup.

[4] Transmission-line resonators also support higher-harmonic modes, but in standard cQED operating regimes, only the fundamental mode plays a significant role.

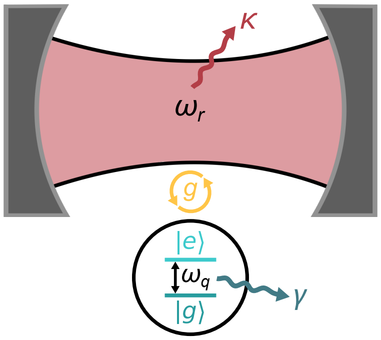

Figure 4.2: Qubit-resonator interaction described by the Jaynes-Cummings model. The resonator is illustrated as an optical cavity, reflecting the Jaynes-Cummings model's origins in AMO physics.

(or energy) are lost from the resonator, due to both internal losses and external coupling to the environment.[5] This loss rate can be determined from the width of the resonance peak at $A/A_0 = 1/\sqrt{2}$, as shown in Fig. 4.1(c). Alternatively, energy loss in the resonator can be described by the **quality factor** Q, which measures how many oscillation cycles the resonator can store energy before it decays. These two loss measures are related by the expression $Q = \omega_r/\kappa$.

4.1.2 The Jaynes-Cummings Model

The term *circuit quantum electrodynamics* might initially sound intimidating to a condensed-matter experimentalist, but in fact, it is a beautifully simple framework. No background in quantum field theory is necessary to develop a powerful and intuitive understanding of the interaction between light and matter in cQED systems. The **Jaynes-Cummings model**, introduced in 1963 by American physicists Edwin Jaynes and Fred Cummings [149], describes this behavior serves as the backbone of cQED.

According to the model, the effective Hamiltonian for a qubit interacting with a quantized

---

[5] The total photon loss rate can be decomposed into internal and external loss rates: $\kappa = \kappa_{\text{int}} + \kappa_{\text{ext}}$. For resonators made from superconductors, κ_{int} is very small. Similarly, the quality factor can be decomposed as $Q^{-1} = Q_{\text{int}}^{-1} + Q_{\text{ext}}^{-1}$. Q is often called the 'loaded quality factor.'

resonator field, as illustrated in Fig. 4.2, is

$$\begin{aligned}\hat{H}_{\mathrm{JC}} &= \hat{H}_q + \hat{H}_r + \hat{H}_{\mathrm{int}} \\ &= \frac{\hbar\omega_q}{2}\hat{\sigma}_z + \hbar\omega_r\left(\hat{a}^\dagger\hat{a} + \frac{1}{2}\right) + \hbar g\left(\hat{a}\hat{\sigma}_+ + \hat{a}^\dagger\hat{\sigma}_-\right).\end{aligned} \tag{4.1}$$

The first term, $\hat{H}_q \sim \hbar\omega_q\hat{\sigma}_z$, represents the diagonalized, two-level Hamiltonian for the qubit, where ω_q is the qubit's transition frequency and $\hat{\sigma}_z$ is the Pauli-z operator in the qubit's energy basis. The second term, $\hat{H}_r \sim \hbar\omega_r\hat{a}^\dagger\hat{a}$, models the single-mode electromagnetic field as a quantum harmonic oscillator. Here, $\hat{a}^\dagger$ and $\hat{a}$ are photon creation and annihilation operators. The photon number operator $\hat{a}^\dagger\hat{a}$ counts the number of photons in the mode, with each photon contributing a quantum of energy $\hbar\omega_r$ to the system. The final term, $\hat{H}_{\mathrm{int}} = \hbar g\left(\hat{a}\hat{\sigma}_+ + \hat{a}^\dagger\hat{\sigma}_+\right)$, describes the interaction between the qubit and resonator. The parameter g is a coupling constant that represents the strength of the interaction. $\hat{\sigma}_+$ and $\hat{\sigma}_-$ are the raising and lowering operators for the qubit, which correspond to transitions between the ground and excited states. We will delve into the specific details of this interaction in quantum-dot systems shortly; for now, we focus on outlining the general behavior predicted by the model.

The qubit-resonator interaction modeled by Eq. (4.1) takes on very different behavior depending on the detuning between the frequencies ω_q and ω_r, and this has important implications for quantum information processing. In the cQED literature, two diverging operating regimes of the Jaynes-Cummings model are typically considered.

The Resonant Regime

The **resonant regime** occurs when the qubit and resonator are tuned to have the same frequency, $\omega_q = \omega_r = \omega_0$, simplifying the system Hamiltonian to

$$\hat{H}_{\mathrm{JC}} \to \hbar\omega_0\left(\frac{1}{2}\hat{\sigma}_z + \hat{a}^\dagger\hat{a} + \frac{1}{2}\right) + \hbar g\left(\hat{a}\hat{\sigma}_+ + \hat{a}^\dagger\hat{\sigma}_-\right). \tag{4.2}$$

The system's low-energy eigenstates can be described using the product states of the qubit and resonator: $|g, n+1\rangle$ and $|e, n\rangle$, where $|g\rangle$ and $|e\rangle$ are the ground and excited states of the qubit, and $|n\rangle$ represents the Fock state with $n = 0, 1, 2...$ photons in the resonator. In the resonant regime, the qubit and resonator become strongly hybridized, leading to the formation of new eigenstates known as **dressed states**,

$$|\pm\rangle = \frac{1}{\sqrt{2}}\left(|g, n+1\rangle \pm |e, n\rangle\right), \tag{4.3}$$

with energy levels separated by $2\hbar g\sqrt{n+1}$.

The aim for most cQED experiments is to apply a very low-power ac drive to the resonator, allowing the qubit to interact with a nominally empty cavity ($n = 0$).[6] In this scenario, the level splitting of $2\hbar g$ is referred to as the **vacuum Rabi splitting**. In the time domain, the system oscillates between $|g, 1\rangle$ and $|e, 0\rangle$ states at a frequency of $2g$, with the qubit and resonator trading a single photon back and forth during each cycle.[7] This coherent exchange of energy is known as **vacuum Rabi oscillation**.

Figure 4.3(a) portrays the experimental signature of a semiconductor DQD qubit interacting with a superconducting resonator in the frequency domain, as reported by Mi *et al.* [150]. The qubit's non-interacting excitation frequency exhibits a parabolic dependence on DQD detuning ε, while the resonator's non-interacting frequency is unaffected by ε (dashed white lines). At $\varepsilon \approx 0$ µeV—where the two systems would come into resonance—both frequencies deviate from their non-interacting trajectories, and an avoided crossing is observed. This is the vacuum Rabi splitting, highlighted by the pair of distinct peaks seen in the blue, $\varepsilon = 0$ line cut in Fig. 4.3(b). Resolving this effect is only possible when the magnitude of the splitting exceeds the widths of the peaks, which are broadened by two loss mechanisms: the

---

[6] In practice, applying an ac drive introduces some additional photons into the resonator. However, by keeping the drive weak, the rate of photon generation remains low, ensuring that the *time-averaged* population stays at $\langle n\rangle < 1$.

[7] This behavior is evident from the structure of the interaction Hamiltonian in Eq. (4.2). The operator product $\hat{a}\hat{\sigma}_+$ describes the qubit absorbing a photon from the resonator, while $\hat{a}^\dagger\hat{\sigma}_-$ represents re-emission of the photon.

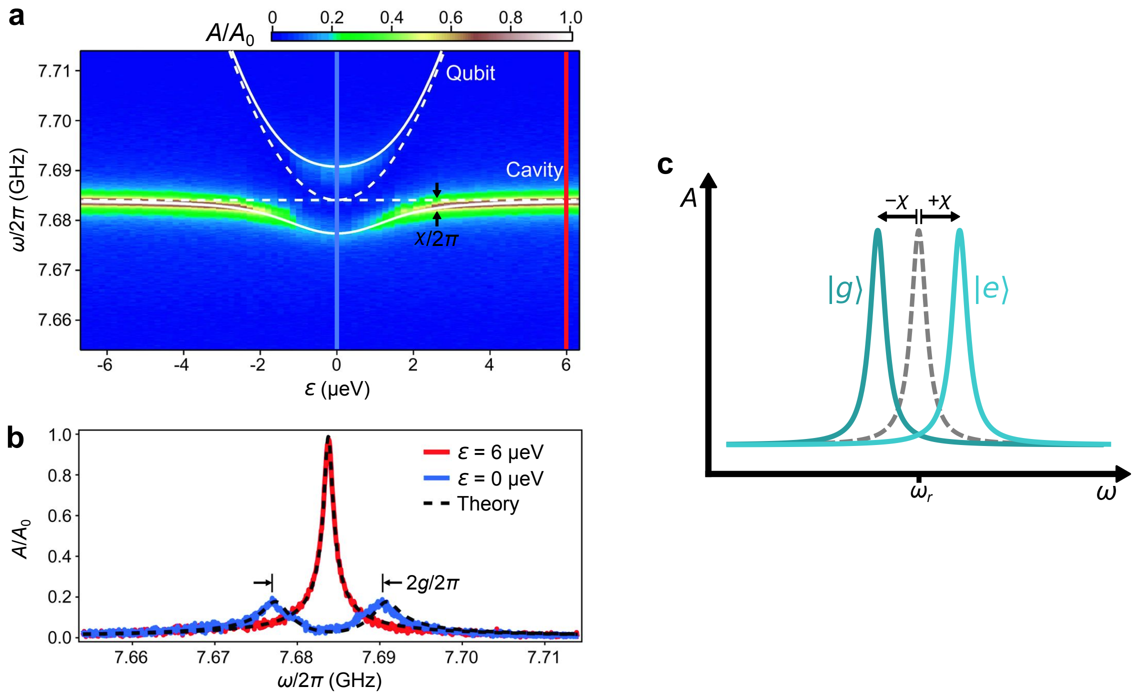

Figure 4.3: Resonant and dispersive regimes of cQED. **(a)** Measurement of a DQD qubit interacting with a superconducting resonator. The normalized resonator transmission amplitude A/A_0 is shown as a function of ω and DQD detuning ε. In the resonant regime ($\varepsilon \approx 0$ μeV), the qubit and resonator are hybridized, inducing a vacuum Rabi splitting. **(b)** Line cuts from (a), highlighting the vacuum Rabi splitting due to strong coupling. **(c)** Illustration of the impact of qubit-resonator coupling in the dispersive regime: the resonator's transmission peak shifts up or down in frequency by an amount χ, depending on the state of the qubit ($|g\rangle$ or $|e\rangle$). (a) and (b) adapted from Ref. [150]. Reprinted with permission from AAAS.

---

resonator's photon loss rate κ and the qubit's decoherence rate γ. The total peak width is determined by $\gamma + \kappa/2$. Thus, the requirement for observing vacuum Rabi splitting is $2g > \gamma + \kappa/2$ [151, 152]. This condition, often expressed as $g > \gamma, \kappa$, is termed **strong coupling** in the cQED literature. The experiment shown in Fig. 4.3 represents the first observance of strong coupling between a gate-defined quantum-dot qubit and a resonator.

A drawback of operating in the resonant regime is that the qubit experiences enhanced spontaneous emission due to its strong coupling with the resonator. This increased decay rate, known as the **Purcell effect**, shortens the qubit's coherence time and causes and limits the number of error-free operations that can be executed during a computation [153–155].

The Dispersive Regime

To mitigate the Purcell effect and ensure longer coherence times, it is generally advantageous to work in the **dispersive regime** of the Jaynes-Cummings model, where the qubit frequency is detuned away from the resonator frequency during quantum operations. Defining the **qubit-cavity detuning** as $\Delta \equiv |\omega_q - \omega_r|$, the Purcell decay rate is given by $\gamma_\kappa = (g/\Delta)^2\kappa$, and the dispersive regime is reached when $\Delta \gg g$. Under this condition, Eq. (4.1) can be expanded to second order in g/Δ,[8] becoming

$$\hat{H}_{\text{JC}} \to \frac{\hbar\omega_q}{2}\hat{\sigma}_z + \hbar\left(\omega_r + \chi\hat{\sigma}_z\right)\left(\hat{a}^\dagger\hat{a} + \frac{1}{2}\right), \tag{4.4}$$

where $\chi = g^2/\Delta$.[9] This Hamiltonian has nearly the same form as the uncoupled qubit-resonator system, except that the resonator picks up a qubit-state-dependent frequency shift of $\pm\chi$, as illustrated in Fig. 4.3(c). A small **dispersive shift** of the cavity frequency is also marked in Fig. 4.3(b), showing that the resonator 'feels' the effect of the qubit even when their frequencies are significantly detuned.

Alternatively, Eq. (4.4) can be written as

$$\hat{H}_{\text{JC}} \to \frac{\hbar}{2}\left(\omega_q + 2\chi\hat{a}^\dagger\hat{a} + \chi\right)\hat{\sigma}_z + \hbar\omega_r\left(\hat{a}^\dagger\hat{a} + \frac{1}{2}\right). \tag{4.5}$$

This form of the Hamiltonian emphasizes the impact of the dispersive interaction on the qubit's frequency, which acquires a photon-number-dependent **ac Stark shift** of $(2n+1)\chi$. When $n = 0$, the qubit is minimally perturbed, and the resulting frequency shift of χ is known as the **Lamb shift**.

In the dispersive regime, the qubit and resonator interact without directly exchanging energy; instead, the coupling is mediated through the exchange of **virtual photons**. This

---

[8] This application of perturbation theory is also called a Schrieffer-Wolff transformation in the context of interacting quantum systems [156].

[9] Note that some authors use a different convention, defining $\chi = 2g^2/\Delta$. Under this convention, $\chi \to \chi/2$ in Eq. (4.4).

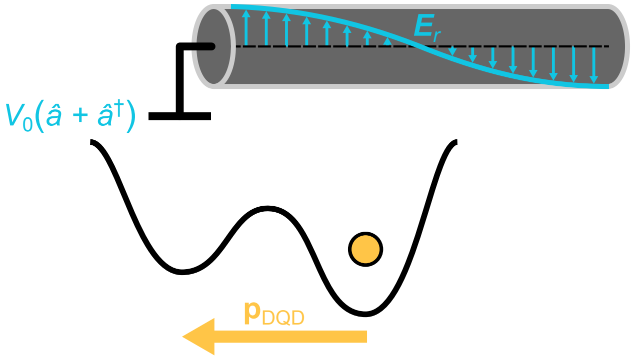

Figure 4.4: Electron-photon coupling in a DQD connected to a superconducting resonator arises from the interaction between the DQD's electric dipole, $\mathbf{p}_{\mathrm{DQD}}$, and the quantized electric field of the resonator, $\mathbf{E}_r$.

lack of direct energy transfer helps shield the qubit from Purcell decay, and protects against leakage of quantum information into the resonator photons [157].

4.1.3 Coupling Quantum Dots to Resonators

Let us now explore precisely how the qubit-resonator interaction works in quantum-dot systems. The simplest model to consider is a single-electron DQD—a charge qubit—with one of its gates tied to the center pin of a transmission-line resonator, as Fig. 4.4 illustrates. We can view the DQD as a tiny electric dipole, $\mathbf{p}_{\mathrm{DQD}} = -e\mathbf{d}$, where the displacement vector $\mathbf{d}$ is defined by the separation between dots ($|\mathbf{d}| \approx 100$ nm). Through its capacitance with the gate electrode, the dipole interacts with the resonator's electric field $\mathbf{E}_r$, such that fluctuations in $\mathbf{E}_r$ perturb the spatial distribution of the electron wavefunction and vice versa. This dipole interaction[10] serves as the physical mechanism underpinning the coupling term in the Jaynes-Cummings Hamiltonian.

---

[10] In triple quantum dots, resonator coupling can also occur through an electric quadrupole interaction [158, 159].

Charge-Photon Coupling

Classically, the DQD-resonator dipole interaction is described by the dot product $-\mathbf{p}_{\mathrm{DQD}} \cdot \mathbf{E}_r$. To derive a quantum mechanical model for the interaction, we recount the work of Childress *et al.* [160], who were the first to apply cQED concepts to semiconductor qubits. The influence of the resonator field can be expressed in terms of quantized voltage fluctuations on coupling gate. In the vacuum state ($n = 0$), the resonator's zero-point voltage fluctuations are represented by the quantum operator $V_0 \left(\hat{a} + \hat{a}^\dagger\right)$, where $V_0 = \omega_r \sqrt{\hbar Z_r / \pi}$ and Z_r is the characteristic impedance of the resonator.[11] The behavior of the DQD's electric dipole is modeled by $(\varepsilon \hat{\sigma}_z + 2t_c \hat{\sigma}_x)/\hbar\omega_q$. We have already encountered this operator in Eq. (2.22) of Section 2.3.1: it is just the Hamiltonian for the charge qubit, rescaled by a factor of $2/\hbar\omega_q$, where $\omega_q = \sqrt{\varepsilon^2 + 4t_c^2}/\hbar$ denotes the charge qubit's excitation frequency.

We now have the necessary ingredients to express the interaction Hamiltonian as

$$\hat{H}_{\mathrm{int}} = \frac{\alpha_g^\varepsilon V_0}{\hbar\omega_q} \left(\varepsilon \hat{\sigma}_z + 2t_c \hat{\sigma}_x\right) \left(\hat{a} + \hat{a}^\dagger\right), \tag{4.6}$$

where the coupling gate's lever arm α_g^ε converts resonator voltage fluctuations into DQD detuning shifts. It is common to consolidate all engineered device parameters into a single variable $g_c = \alpha_g^\varepsilon V_0 / \hbar$, referred to as the **bare charge-photon coupling rate**. We can then rewrite Eq. (4.6) as

$$\hat{H}_{\mathrm{int}} = \hbar g_\parallel \hat{\sigma}_z \left(\hat{a} + \hat{a}^\dagger\right) + \hbar g_\perp \hat{\sigma}_x \left(\hat{a} + \hat{a}^\dagger\right). \tag{4.7}$$

This form emphasizes two distinct interaction mechanisms within the DQD-resonator system: **longitudinal coupling** ($\sim \hat{\sigma}_z$) and **transverse coupling** ($\sim \hat{\sigma}_x$), with effective coupling strengths given by

$$g_\parallel = \frac{g_c \, \varepsilon}{\hbar\omega_q} \qquad \text{and} \qquad g_\perp = \frac{2 g_c t_c}{\hbar\omega_q}. \tag{4.8}$$

The longitudinal term dominates at large $|\varepsilon|$, but vanishes at the interdot transition where

---

[11] For an in-depth discussion on the quantum treatment of resonators, see Nathan Holman's thesis [62].

$\varepsilon = 0$. The behavior is reversed for the transverse term, which has a maximum coupling strength of $g_\perp = g_c$ at $\varepsilon = 0$, but weakens as $\varepsilon \to \pm\infty$. To further understand how these interaction mechanisms differ, it is helpful to explicitly write out their matrix forms in the basis $\{|g,0\rangle, |e,0\rangle, |g,1\rangle, |e,1\rangle, |g,2\rangle, |e,2\rangle ...\}$ [62]:

$$\hbar g_\parallel \hat{\sigma}_z \left(\hat{a} + \hat{a}^\dagger\right) = \hbar g_\parallel \begin{pmatrix} 0 & 0 & -1 & 0 & 0 & 0 & \dots \\ 0 & 0 & 0 & 1 & 0 & 0 & \dots \\ -1 & 0 & 0 & 0 & -\sqrt{2} & 0 & \dots \\ 0 & 1 & 0 & 0 & 0 & \sqrt{2} & \dots \\ 0 & 0 & -\sqrt{2} & 0 & 0 & 0 & \dots \\ 0 & 0 & 0 & \sqrt{2} & 0 & 0 & \dots \\ \vdots & \vdots & \vdots & \vdots & \vdots & \vdots & \ddots \end{pmatrix}; \tag{4.9}$$

and

$$\hbar g_\perp \hat{\sigma}_x \left(\hat{a} + \hat{a}^\dagger\right) = \hbar g_\perp \begin{pmatrix} 0 & 0 & 0 & 1 & 0 & 0 & \dots \\ 0 & 0 & 1 & 0 & 0 & 0 & \dots \\ 0 & 1 & 0 & 0 & 0 & \sqrt{2} & \dots \\ 1 & 0 & 0 & 0 & \sqrt{2} & 0 & \dots \\ 0 & 0 & 0 & \sqrt{2} & 0 & 0 & \dots \\ 0 & 0 & \sqrt{2} & 0 & 0 & 0 & \dots \\ \vdots & \vdots & \vdots & \vdots & \vdots & \vdots & \ddots \end{pmatrix}. \tag{4.10}$$

The longitudinal interaction has no effect on the qubit's state, but generates transitions between successive photon states $[\langle g(e), n+1| \hat{\sigma}_z \left(\hat{a} + \hat{a}^\dagger\right) |g(e), n\rangle \neq 0]$. In contrast, the transverse interaction induces simultaneous transitions in both the qubit and the resonator.

The interaction Hamiltonian may be simplified by neglecting all energy non-conserving terms, indicated as red matrix elements in Eqs. (4.9) and (4.10). This technique, known as the **rotating wave approximation**, is valid for most cQED experiments, where the applied external drives are weak enough not to increase the system's total energy. Interestingly, the approximation completely removes the longitudinal coupling term from the interaction Hamiltonian—a detail that we will return to—and reduces it to

$$\hat{H}_{\text{int}} \to \hbar g_\perp \left(\hat{a}\hat{\sigma}_+ + \hat{a}^\dagger \hat{\sigma}_-\right), \tag{4.11}$$

which matches the form of the Jaynes-Cummings model.

Spin-Photon Coupling

We have shown how a single electron charge can be coupled to a superconducting resonator through an electric-dipole interaction. However, a more challenging question arises: can we achieve a similar coupling for a single electron *spin*? Unlike charge-photon interactions, the magnetic dipole interaction between a single electron spin and a resonator's magnetic field is extremely weak, with coupling rates typically below 1 kHz. As a result, direct spin-photon coupling is generally observed in spin ensembles, where collective coupling to the resonator field can enhance the overall interaction strength [161–163].

To overcome the weakness of direct magnetic-dipole interactions, spins in quantum-dot qubits can be *indirectly* coupled to the resonator's electric field through the same electric-dipole interaction we already considered. This form of coupling is enabled by hybridizing the electron's charge and spin degrees of freedom, allowing spin flips to be induced whenever the electron's spatial wavefunction is perturbed by the resonator fluctuations [144]. In spin-photon coupling experiments involving double or triple quantum dots, charge-spin hybridization is accomplished through various mechanisms, including the exchange interaction [164], spin-orbit coupling [165, 166], or by placing the qubit in a magnetic field gradient generated by micromagnets [167, 168]. In the latter scenario, for a single-spin DQD situated in a transverse magnetic field gradient ΔB, the effective **spin-photon coupling rate** at $\varepsilon = 0$ is approximated by

$$g_s \approx g_c \frac{g' \mu_B \Delta B}{4(2t_c - \hbar\omega_r)}, \tag{4.12}$$

where $g' = 2$ is the electron g-factor [169]. Strong spin-photon coupling rates up to $g_s/2\pi \sim$ 100 MHz have been achieved via the electric-dipole interaction, exceeding direct magnetic-dipole coupling by at least six orders of magnitude [165, 166].[12]

---

[12] The experiment in Ref. [165] utilizes hole spins rather than electron spins.

4.2 Operating Qubits in Quantum Dot-Resonator Hybrid Devices

Turning from theory to experiment, we now examine how electron-photon coupling is implemented in devices and applied to qubit functionality. cQED experiments with quantum-dot qubits are highly sophisticated, pushing the limits of fabrication and engineering in academic-style devices. Nonetheless, the capabilities for qubit readout and non-local entanglement provided by the cQED framework could be pivotal for scaling up quantum processors.

4.2.1 Chip Design & Integration

Figure 4.5(a) shows an example of a typical chip design for electron-photon coupling experiments. This particular sample was fabricated for work at TU Delft as reported by Harvey-Collard *et al.* [169] and Dijkema, Xue *et al.* [157]. The chip design features a $\lambda/2$ superconducting resonator (shown in red) whose transmission properties can be probed via the microwave (MW) input and output ports (shown in brown). At either end of the resonator, two DQD devices are fabricated, as illustrated in Figs. 4.5(b) and 4.5(c). The gate labeled 'Res' in each device is galvanically connected to the center pin of the resonator to enable coupling between the resonator field and the DQD electric dipoles. A dc bias can be applied to this shared gate through the resonator's dc-tap segment (shown in navy), which is a $\lambda/4$ impedance transformer shunted to ground. Cobalt micromagnets are placed over each DQD to generate a magnetic field gradient for spin-photon coupling.

Integrating quantum-dot devices and superconducting resonators on the same chip is no easy task. Preserving the coherence of both systems while achieving strong electron-photon coupling presents significant design challenges, which are only overcome through careful engineering. The first major obstacle is obtaining a large dipole coupling between the qubit and resonator. In superconducting-qubit architectures, this coupling is relatively easy to achieve, as the qubits are formed from large (~ 100 µm) metal islands with substantial

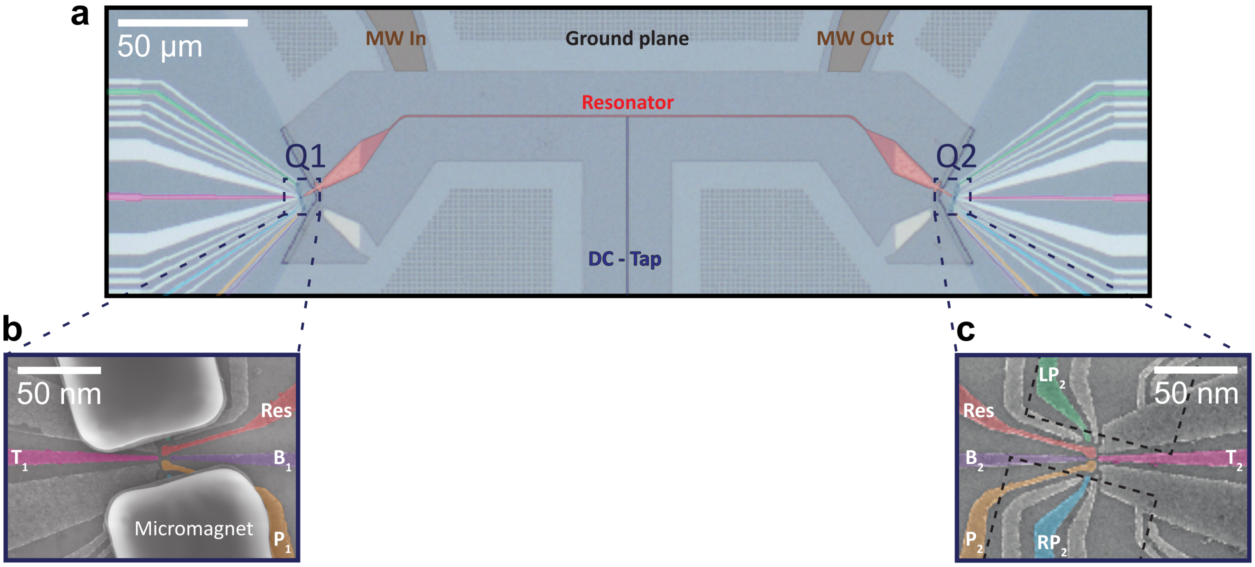

Figure 4.5: On-chip integration of quantum-dot devices and a superconducting resonator. **(a)** Optical micrograph of the chip layout with a $\lambda/2$ superconducting resonator (red) probed via microwave input/output ports (brown). **(b,c)** Scanning electron micrographs of DQD devices at each end of the resonator with cobalt micromagnets. The gates labeled ‘Res’ are connected to the center pin of the resonator, enabling electron-photon coupling. Figure adapted from Ref. [157].

dipole moments. Achieving similar coupling with a single electron in a DQD is much trickier, as its electric dipole moment is significantly smaller [147]. To maximize coupling, quantum-dot devices are positioned at the voltage antinodes of resonators, where the amplitude of voltage fluctuations is greatest. Additionally, given that $g_c \propto \alpha_g^{\varepsilon}\sqrt{Z_r}$, chips are engineered to maximize both the coupling gate's lever arm and the resonator's impedance [62,170,171]. With careful optimization of materials and geometry, charge-photon coupling rates as high as $g_c/2\pi \approx 500$ MHz have been achieved [165].[13]

A second challenge involves designing resonators capable of operating in magnetic fields. There is an inherent conflict between the requirements of spin-qubit encodings, which often require external magnetic fields, and superconductors, which generally do not tolerate large fields. To overcome this, resonators must be fabricated from magnetic field-resistant materials like niobium [150], NbN [165], and NbTiN [166,170], which can withstand fields of a few

---

[13] The charge-photon coupling in Ref. [165] is accomplished for holes rather than electrons.

hundred millitesla during spin-qubit experiments.

A third challenge lies in integrating high-quality-factor resonators with quantum-dot devices. Here, again, opposing requirements between quantum dots and resonators complicate the process. The presence of accumulated 2DEGs and numerous device leads creates a challenging environment for realizing low-loss resonators. The multi-layered fabrication process used for quantum-dot construction can degrade resonator interfaces and introduce impurities that and promote further losses as well. As a result, while cavities with $Q \sim 10^5$ are readily integrated with superconducting qubits, resonators coupled to quantum-dot qubits usually achieve only $Q \sim 10^3$ [152]. Maximizing Q in these devices involves considerable effort on multiple fronts. First, optimizing fabrication processes to create high-quality interfaces and minimize resonator deterioration is crucial. Second, most device designs incorporate passive elements to reduce photon leakage from the resonator. These techniques include etching away the quantum well beneath the resonator to prevent 2DEG accumulation [152, 172] and using quantum dot gate leads with low impedance [172] or integrated microwave filters [152, 173]. Lastly, careful attention is given to the resonator's capacitive coupling to feedlines, the substrate grounding, and the sample packaging to ensure good microwave hygiene [152, 174].

An alternative solution for improving the resonator's quality factor is to fabricate the quantum dots and resonators on separate chips. This is the path taken for the sample featured in Chapters 5 and 6. While integrating multiple chips comes with its own engineering challenges, the approach greatly relaxes fabrication restrictions and has been shown to permit loaded quality factors of $Q > 20{,}000$ [174].

4.2.2 Applications for Electron-Photon Coupling

As we have seen, realizing coherent electron-photon coupling requires an awful lot of work. But what is the payoff? There are three primary applications for resonators coupled to quantum-dot devices in the dispersive cQED framework.

Charge Sensing

The first use case is **dispersive charge sensing**. Because the resonator's transmission properties are sensitive to the electron dynamics within the coupled quantum dots, monitoring transmission as the device gate voltages are varied allows us to identify different charge configurations while tuning into the desired operating regime for qubit experiments [175]. Figure 4.6 shows the charge stability diagram of a DQD mapped out using this method. A continuous probe tone is applied near the cavity's resonant frequency, $\omega_{\text{probe}} \approx \omega_r$, and the normalized transmission amplitude $A(\omega_{\text{probe}})/A_0$ is plotted as a function of the plunger-gate voltages. The normalization constant A_0 is chosen so that $A/A_0 = 1$ when the DQD is in blockade. At $\varepsilon_v \approx 0$, the DQD interacts with the resonator, shifting its frequency by $-\chi$,[14] as illustrated in Fig. 4.6(b). This shift reduces A/A_0 at the probe frequency, producing a visible polarization line in the stability diagram. Charge transition lines are also visible along the equipotentials where electrons tunnel between the DQD and the reservoirs, provided the tunnel rates are comparable to the reservoir frequency [62]. In this context, however, the DQD-resonator interaction is not coherent, as numerous electrons tunnel in and out of the dots during the measurement integration time.[15] Beyond assisting with device tune-up, dispersive charge sensing is useful for other standard quantum-dot measurements, such as lever arm calibration (see Section 5.6.4) and pulsed-gate spectroscopy (see Section 6.5.2).

Qubit Readout

A second function for electron-photon coupling is **dispersive qubit readout**. Recall that in the dispersive regime, the qubit-resonator interaction shifts the resonator's frequency by $\pm\chi$, depending on the qubit's state. This frequency shift alters the resonator's transmission during experiments, allowing the qubit state to be determined from the detected signal [177].

---

[14] Only a negative frequency shift is observed, as the DQD remains in its ground state for this measurement.

[15] Instead of the Jaynes-Cummings model, tunneling between the DQD and reservoirs is described classically using an equivalent circuit approach. In this model, electron tunneling modifies the DQD's complex admittance, which in turn affects the resonator's frequency and quality factor [176].

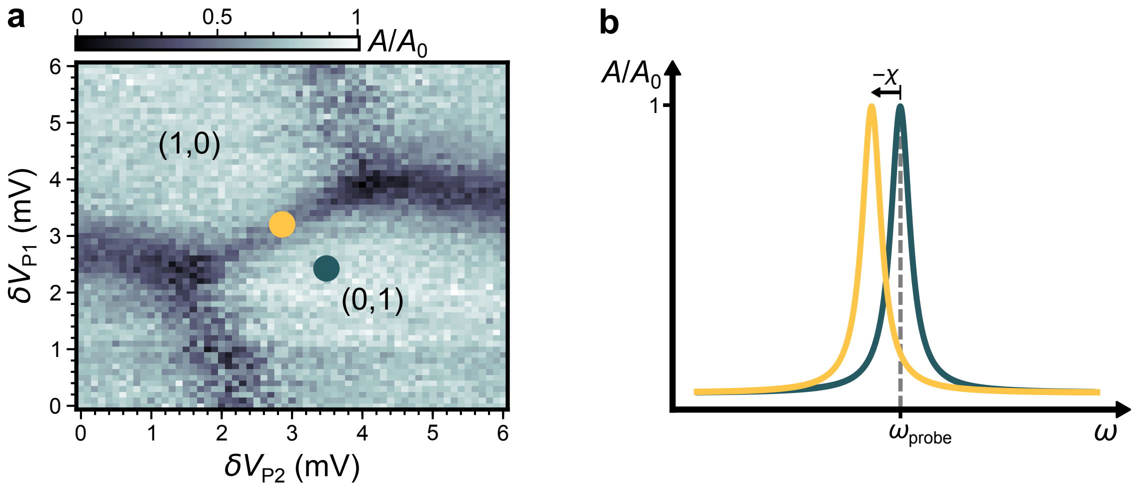

Figure 4.6: Dispersive charge sensing in a DQD. **(a)** Charge stability diagram of a DQD obtained by measuring the normalized resonator transmission amplitude A/A_0 as a function of the plunger gate voltages. **(b)** Illustration of the cavity resonance peaks corresponding to the colored points in (a). At $\varepsilon_v \approx 0$ (yellow), the resonator's frequency is shifted by $-\chi$ due to the dispersive interaction with the DQD.

The qubit oscillations shown in Fig. 4.7 are observed using dispersive readout, where the resonator transmission amplitude is used as a measure of the $|1\rangle$ population. [157].

An important advantage of dispersive readout is its **quantum non-demolition (QND)** nature. When the qubit and resonator are operated at large frequency detuning, the measurement process minimally disturbs the qubit, leaving its state approximately unchanged and preserving any entanglement with other qubits [139].[16] QND readout is a crucial requirement for quantum error correction schemes, which rely on repeated measurements to detect and correct errors without collapsing qubit wavefunctions [2]. Other common approaches for reading out quantum-dot qubits—including Elzerman readout [106] and PSB readout [107]—are not QND, as these methods project the qubit into one of its basis eigenstates. Therefore, dispersive readout using superconducting resonators is an attractive option for making quantum-dot qubits more compatible with proposed error correction codes.

---

[16] The non-destructive nature of dispersive readout is a consequence of the dispersive interaction Hamiltonian in Eq. (4.4) commuting with the qubit Hamiltonian, $[H_{\text{int}}, H_q] = 0$.

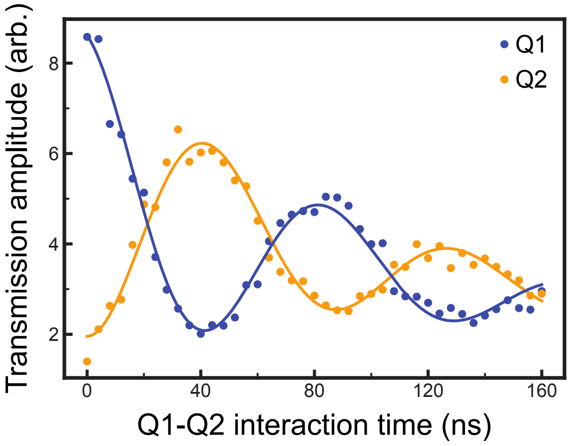

Figure 4.7: Virtual-photon-mediated iSWAP oscillations between two flopping-mode spin qubits (Q1 and Q2) coupled to a shared resonator in the device in Fig. 4.5. The qubits are measured using dispersive readout, where the resonator transmission amplitude is used to infer the $|1\rangle$ population. Figure adapted from Ref. [157].

Remote Two-Qubit Logic

The third and final use case for electron-photon is in generating entanglement across long distances on a quantum processor. In cQED, remote two-qubit gates are performed by mediating interactions between qubits through a shared resonator, allowing qubits that are spatially separated to interact indirectly [139, 178]. This approach, performed in the regime where both qubits are dispersively coupled to the resonator, leverages virtual photons to establish an effective coupling. The Hamiltonian for the qubit-photon-qubit interaction takes the form

$$\hat{H}_{\text{int,2Q}} \approx \hbar J \left(\hat{\sigma}_+^1 \hat{\sigma}_-^2 + \hat{\sigma}_-^1 \hat{\sigma}_+^2 \right), \tag{4.13}$$

where J is the effective coupling strength and $\hat{\sigma}_\pm^i$ are the raising and lowering operators for qubit i [179]. The coupling strength is given by

$$J = \frac{g_1 g_2}{2} \left(\frac{1}{\Delta_1} + \frac{1}{\Delta_2} \right), \tag{4.14}$$

where the qubit-cavity detuning and coupling strength for qubit i satisfy the dispersive condition $\Delta_i \gg g_i$. By carefully tuning these parameters, it is possible to achieve strong, coherent interactions between remote quantum-dot qubits [169, 180].[17]

In the time domain, the Hamiltonian in Eq. (4.13) generates iSWAP oscillations between the qubit states [181]. Figure 4.7 shows an example of these oscillations measured between two flopping-mode spin qubits separated by 250 µm, as demonstrated by Dijkema, Xue *et al.* using the device in Fig. 4.5 [157]. The qubits, labeled Q1 and Q2, are prepared in the state $|10\rangle$ and allowed to interact via the photon-mediated process described above. As the duration of the interaction is swept, the qubit states oscillate periodically with opposite phase. After 21 ns of evolution, the spins in the qubits are maximally entangled, and after 42 ns, their populations are fully swapped.

High-fidelity quantum links that entangle qubits over long distances are essential components in proposed scalable semiconductor qubit architectures [40, 182]. These links expand the connectivity between qubits and provide space for integrated classical electronics on the processor, alleviating the wiring bottleneck for off-chip control lines. While the exchange interaction commonly used in two-qubit gates is limited to distances of around ~ 100 nm, the cavity-mediated, non-local interactions in cQED architectures offer a promising solution for entangling qubits over millimeter length scales.[18]

4.3 A Sneak Peek at Longitudinal Coupling

Everything discussed so far in the chapter has been textbook cQED, with applications based on transverse qubit-resonator coupling in the dispersive regime. However, the experiments presented in Chapters 5 and 6 venture into less explored territory, examining the nature of the longitudinal interaction mechanism that is not captured within the Jaynes-Cummings model. To set the stage for what is coming, we conclude this chapter with some brief remarks

---

[17] Note that Ref. [180] achieves strong spin-photon-spin coupling in the resonant regime rather than the dispersive regime discussed here.

[18] A competing solution for establishing quantum links involves shuttling electrons over long distances using gate voltages, enabling them to interact through direct exchange coupling [70, 182–187].

about the ‘forgotten’ longitudinal coupling and how it differs from conventional transverse coupling.

In Section 4.1.3, we noted that the longitudinal term in the interaction Hamiltonian becomes irrelevant under the assumption of energy conservation within the system, as enforced by the rotating-wave approximation. However, interesting things happen when energy is deliberately added to the system. Specifically, if an ac modulation is applied to the qubit at the resonator frequency, it activates and enlarges the longitudinal interaction, producing a qubit-state-dependent drive of the resonator [188, 189]. This phenomenon has been called **dynamic (or parametric) longitudinal coupling**. In quantum-dot systems, dynamic longitudinal coupling can be achieved by coupling a charge qubit to the resonator and modulating its DQD detuning with a microwave tone so that $\varepsilon(t) = \tilde{\varepsilon}\cos(\omega_r t)$ [190]. This setup takes the system beyond the traditional Jaynes-Cummings framework, as the qubit and resonator now interact through both transverse *and* longitudinal coupling mechanisms.

Due to their distinct Hamiltonian forms [see Eqs. (4.9) and (4.10)], transverse and dynamic longitudinal couplings produce very different effects on the joint qubit-resonator system. In the dispersive regime, transverse coupling results in a qubit-dependent *frequency shift* of the resonator, as previously discussed. In contrast, the qubit-dependent drive from dynamic longitudinal coupling creates a *field shift* within the resonator, which can either suppress or enhance the transmission level at resonance, contingent upon the state of the qubit. The difference between these two interaction mechanisms, as captured by their impact on the cavity resonance peak, is illustrated in Fig. 4.8. A particularly notable feature of the longitudinal coupling is that it can *boost* the transmission amplitude beyond its value in the non-interacting case. This unique effect will serve as a key signature of longitudinal coupling for measurements in Chapters 5 and 6.

Another key distinction between transverse and dynamic longitudinal coupling is that transverse coupling strength is determined by device and qubit properties, whereas dynamic longitudinal coupling is *parametric*, meaning its strength depends on the amplitude of the

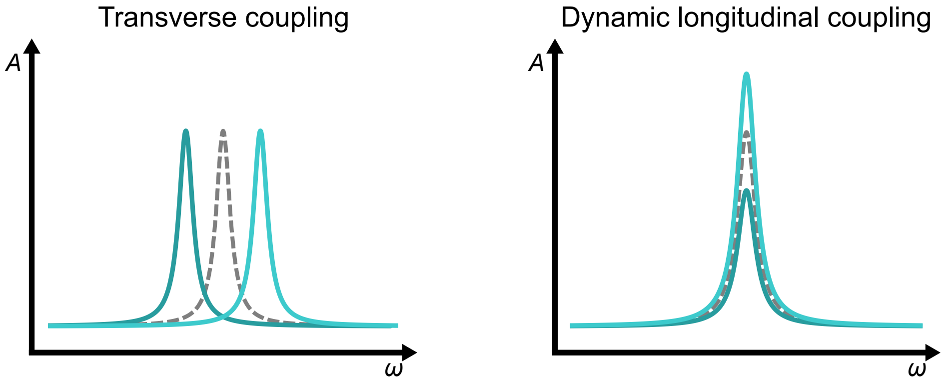

Figure 4.8: Effects of transverse and longitudinal coupling on cavity resonance peaks: transverse coupling causes qubit-dependent frequency shifts; longitudinal coupling causes qubit-dependent field shifts. Non-interacting resonance peaks are shown with dashed gray lines.

applied qubit drive. To explicate this property, let us consider charge-photon coupling in the dispersive regime. For a charge qubit tuned to the charge degeneracy point, the maximum effective coupling strengths are given by

$$\chi = \frac{g_c^2}{\Delta} \qquad \text{and} \qquad \tilde{g}_{\parallel} = \frac{g_c}{\Delta}\frac{\tilde{\varepsilon}}{\hbar} \tag{4.15}$$

for transverse and dynamic longitudinal coupling, respectively.[19] These expressions have three important implications for qubit operation. First, because $\tilde{g}_{\parallel} \propto \tilde{\varepsilon}$, the longitudinal coupling strength can be tuned *in situ* by simply adjusting the microwave drive applied to the qubit. This parametric nature makes longitudinal coupling far easier to control than the transverse coupling χ, which is largely set by the charge-photon coupling rate g_c. Second, $\tilde{g}_{\parallel} > \chi$ when $\tilde{\varepsilon} > \hbar g_c$, meaning that, with a strong enough drive, the longitudinal interaction becomes the dominant coupling mechanism. This allows for flexibility in selecting which interaction plays the primary role in the system's dynamics. Third, dynamic longitudinal coupling enables operation at much larger qubit-cavity detuning values. The transverse coupling χ weakens when Δ is increased; because g_c is fixed by engineered device parameters, this reduction in coupling strength is unavoidable. Due to the relatively modest charge-photon

---

[19] This discussion of coupling strengths is simplified and omits certain numerical factors and assumptions; a more detailed treatment will be provided in Chapter 5.

and spin-photon coupling rates, previous dispersive cQED experiments with quantum-dot qubits have been restricted to detunings of $\Delta/2\pi \lesssim 100$ MHz [157,167,169]. By contrast, the longitudinal coupling $\tilde{g}_{\parallel}$ can be maintained to arbitrarily large Δ by cranking up $\tilde{\varepsilon}$, greatly expanding the frequency range over which cQED experiments can be performed. One caveat to the above discussion is that to prevent the parametric drive from exciting the qubit and introducing errors, it must be kept weak and adiabatic relative to the qubit's energy splitting, such that $\tilde{\varepsilon}$, $\hbar\omega_r \ll \hbar\omega_q$.

A final difference between the two coupling mechanisms is that unlike transverse coupling, which is based on an exchange of photons between the qubit and resonator, longitudinal coupling involves no photon transfer. If the qubit-resonator coupling could be made purely longitudinal, Purcell decay would be eliminated, as the qubit would no longer be able to emit photons into the resonator. Furthermore, resonator photons would be unable to induce spurious qubit transitions—this issue has been observed in superconducting qubits, and is one reason why conventional cQED experiments typically operate with a low average photon number $\langle n \rangle$ [191]. With longitudinal coupling, the resonator can be populated with a larger number of photons without impacting the qubit, thus enabling faster readout [189,190,192] and potentially speeding up two-qubit gates [188, 193, 194]. Clearly, the introduction of longitudinal coupling brings new dynamics to cQED architectures and opens the door to novel applications, which we will begin to explore in the following chapters.

Chapter 5

Longitudinal Coupling Between a Double Quantum Dot & Superconducting Resonator

This chapter has been published as: J. Corrigan*, **Benjamin Harpt***, Nathan Holman, Rusko Ruskov, Piotr Marciniec, D. Rosenberg, D. Yost, R. Das, William D. Oliver, R. McDermott, Charles Tahan, Mark Friesen, and M. A. Eriksson. *Longitudinal coupling between a $Si/Si_{1-x}Ge_x$ double quantum dot and an off-chip TiN resonator.* Physical Review Applied **20**, 064005 (2023). © 2023 by the American Physical Society.

Superconducting cavities have emerged as a key tool for measuring the spin states of quantum dots. So far, however, few experiments have explored longitudinal couplings between dots and cavities, and no solid-state qubit experiments have explicitly probed the 'adiabatic' regime, where the Purcell decay is strongly suppressed. Here, we report measurements of a double-quantum-dot charge qubit coupled to a high-impedance resonator via a 'flip-chip' design geometry. By applying an adiabatic ac drive to the qubit through two different channels, and studying the effects of qubit energy detuning, interdot tunneling, and driving strength, we are able to unequivocally confirm the presence of a longitudinal coupling between the qubit and cavity, while the qubit remains in its ground state. Since this coupling is proportional to

the driving amplitude, and is therefore switchable, it has the potential to become a powerful new tool in qubit experiments.

5.1 Introduction

Quantum couplings between microwave resonators and quantum-dot qubits are expected to form key components in scalable quantum computing architectures [178,195], with potential applications for both readout and couplings between distant qubits. Recent experiments have demonstrated spin-photon interactions [150,164,168,174,196] and photon-mediated spin-spin interactions [180]. Most of these have focused on 'transverse' qubit-cavity couplings, which have some disadvantages, such as the required resonance between the qubit and cavity [144], which can be difficult to engineer and which causes rapid decoherence due to the Purcell effect [153,155,197]. Other types of coupling are therefore also of interest, including dispersive and dynamic longitudinal couplings. The latter are expected to be strong and tunable, enabling fast gates and quantum-nondemolition (QND) measurements [188–190,193,194,198]. Both static [199–202] and dynamic longitudinal couplings [192,203] have been demonstrated experimentally in the superconducting qubit community. Longitudinal coupling schemes have also been proposed for quantum-dot qubits, and although initial experiments appear promising [204], their full potential is not yet known.

In this chapter, we report significant enhancement of transmission through an off-chip microwave cavity, arising from the longitudinal coupling to an ac-driven double quantum dot. The device is tuned to a charge degeneracy point and driven at the cavity resonance frequency through non-standard cavity ports. The crucial signature of the longitudinal coupling mechanism is its change of sign in the resonator response, depending on which of the two dots is driven. The sign change also provides the first direct proof of longitudinal coupling. We further theoretically describe the longitudinal coupling and its effect on cavity transmission, for a range of detuning, tunnel coupling, and ac driving parameters, obtaining

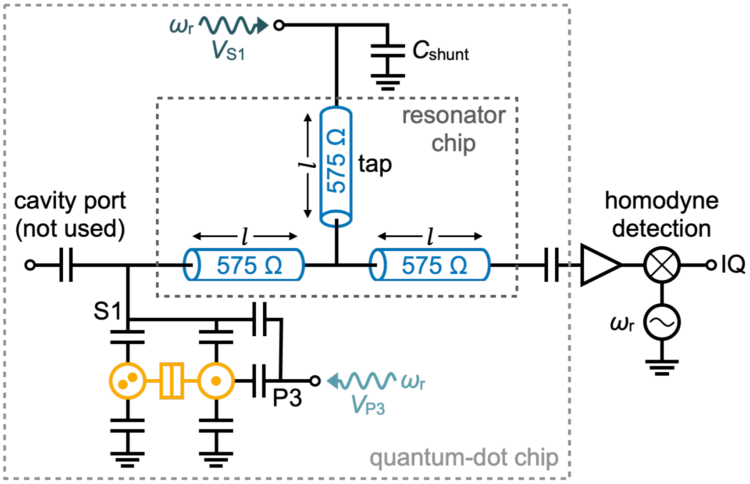

Figure 5.1: Simplified circuit model for the qubit-cavity device. A Si/SiGe double quantum dot (yellow) is capacitively coupled to a high-impedance microwave resonator cavity through gate Sl. (The circuit element between the two dots represents a tunnel coupling in parallel with a capacitor.) The cavity is made from three TiN coplanar waveguide segments (blue) of length $l = 2.02$ mm and characteristic impedance $Z_{0,r} \approx 575\ \Omega$. One of the segments is a voltage-node tap with large shunt capacitance $C_{\text{shunt}} \approx 100$ pF, used for voltage biasing S1. The resonator is vertically integrated on a separate chip from the quantum dots, as indicated (see also Fig. 5.2). During the experiments described below, a microwave tone at cavity frequency $\omega_r/2\pi = 1.304$ GHz is applied through non-standard cavity ports, to either S1 (via the tap segment) or plunger gate P3. Transmission through the cavity is measured using a homodyne detection scheme. For further details of the device, see Fig. 5.5 and Section 5.6.1.

---

good agreement with the experimental results.

5.2 Experimental Demonstration of Longitudinal Coupling

The sample used in this experiment is a 3D-integrated, high-impedance TiN coplanar waveguide resonator on a silicon chip coupled to a Si/SiGe quantum-dot chip, as depicted schematically in Fig. 5.1, pictorially in Fig. 5.2, and explained in further detail in Ref. [174]. The 3D nature of the device relieves both wiring and fabrication constraints. Wiring is simplified by allowing more space on the qubit die for qubit gate lines and fanout; the low-impedance

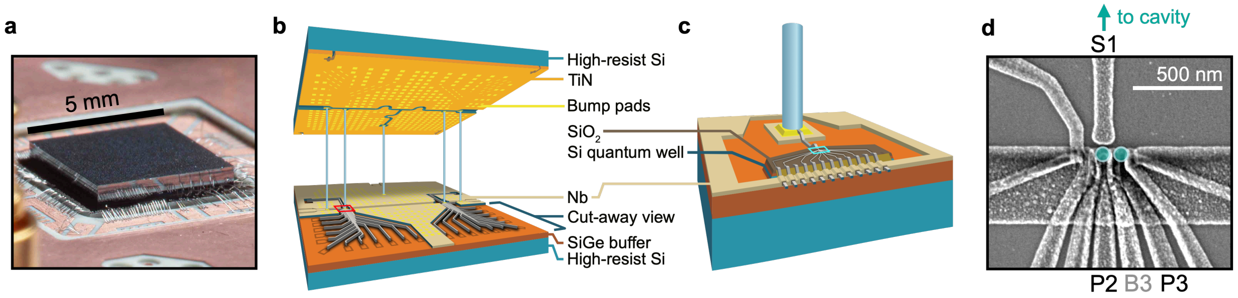

Figure 5.2: Vertical integration of a quantum-dot qubit and an off-chip microwave cavity. **(a)** Image of a connected and wirebonded qubit-cavity flip-chip device. **(b)** Schematic of a 3D-integrated sample, where a high-impedance TiN resonator die is galvanically connected to a Si/SiGe quantum-dot die. **(c)** Blow-up of the bump-bond pad near a double-dot mesa. This region is enclosed by the red rectangle in (b). **(d)** Scanning electron micrograph of a double quantum dot nominally identical to the one used in these experiments. The device is enclosed in the blue rectangle in (c). The cavity is driven by high-frequency lines connected to gates P3 or S1. Plunger gate P2 and barrier gate B3 are also indicated.

gates reduce cavity losses [172]. Fabrication is simplified because the qubit and cavity chips are no longer constrained to follow the same lithographic processes. Figure 5.2(d) shows a scanning electron micrograph of a device nominally identical to the one used in the experiment, in which the quantum dots are capacitively coupled to the resonator through a tap segment on the resonator chip, which is shunted by a large parallel plate capacitor on the quantum-dot chip. Galvanic contacts between the dies are achieved using underbump metal pads [Fig. 5.2(c)] formed at the voltage antinodes near the quantum dots, and at the end of the tap segment. SPICE simulations indicate that the fundamental resonant mode used in this work, with frequency $\omega_r/2\pi = 1.304$ GHz, has weight at both these antinodes and in the tap segment.

Figures 5.3(a) and 5.3(b) show interdot charging transitions of a three-electron double dot, formed under plunger gates P2 and P3, tuned to its (2,1) or (1,2) charge occupations, as labeled. The data are obtained as a function of the dc voltages applied to gates P2 and P3, while simultaneously ac-modulating the voltages on gates S1 [Fig. 5.3(a)] or P3 [Fig. 5.3(b)] at the cavity resonant frequency. As explained in Section 5.6.2, the recorded IQ signal is proportional to the microwave signal transmitted through the cavity, which is

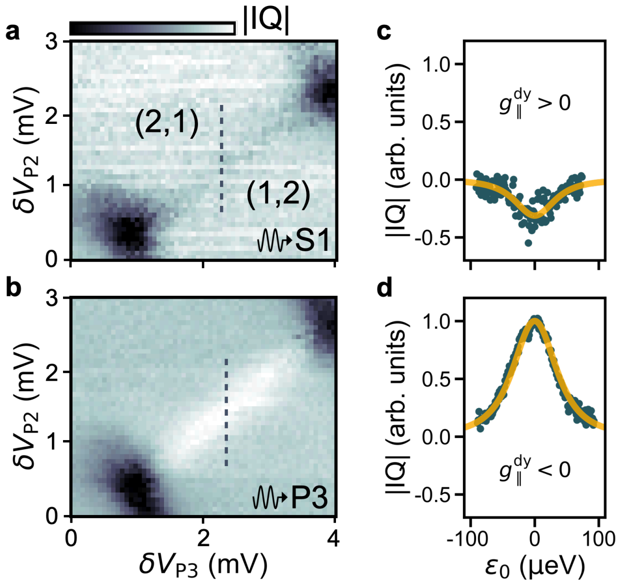

Figure 5.3: Double-dot stability diagrams, as measured via an off-chip microwave cavity. **(a,b)** IQ transmission measurements of a double dot tuned near its (2,1) – (1,2) charge-occupation transition. The double-dot detuning parameter $\varepsilon(t) = \varepsilon_0 + \delta\varepsilon(t)$ is driven by modulating the voltages on gates (a) S1 or (b) P3, with no other changes in device tuning. **(c,d)** Line cuts across the interdot charging transitions, indicated by the dashed lines in (a), (b). Fits are performed using Eq. (5.3) (solid yellow curves), following the procedure described in Section 5.6.3. Arbitrary IQ units have been rescaled, as described in Section 5.6.3, using the same scaling factor in (a) – (d).

measured via a homodyne detection scheme. A dc offset in the homodyne IQ output, which was not calibrated away during experiments, has been subtracted from all data presented in this work.

The resonator response observed in Fig. 5.3(a) is primarily achieved through a longitudinal curvature coupling ($g_{\parallel}^{\text{dy}} > 0$) induced by driving the qubit at the cavity resonant frequency. A line cut through the charging transition, shown in Fig. 5.3(c), provides a clearer view of the suppressed transmission amplitude as a function of the double-dot detuning ε_0, as computed using the measured lever arm $\alpha_{\text{P2},\varepsilon} = 0.11$ eV/V (see Section 5.6.4). A dispersive shift ($\delta\omega$) of the cavity resonance frequency, arising from the energy curvature of the double-dot energy levels, further contributes to suppression of the signal. However, through the analysis below, we find its effect to be much weaker than that of the longitudinal coupling. Note here that by adiabatically sweeping the gate voltages in this stability diagram, we ensure that the qubit remains in its ground state at all times. Thus, here, and throughout this work, it is the magnitude of qubit-cavity coupling, not the qubit state itself, that changes near the charging transition.

The behavior observed in Fig. 5.3(b), and its corresponding line cut in Fig. 5.3(d) is extraordinary for being opposite of the conventional behavior, and clearly inconsistent with a dispersive frequency shift. Instead, it indicates an enhancement of the stationary field in the resonator. Remarkably, the observed qubit-cavity coupling ($g_{\parallel}^{\mathrm{dy}} < 0$) not only has the opposite sign as the response in Fig. 5.3(a), it is also much larger in magnitude and provides a much cleaner signal. This is because P3's detuning lever arm $\alpha_{\mathrm{P3},\varepsilon} = 0.09$ eV/V is more than twice as large as S1's, $\alpha_{\mathrm{S1},\varepsilon} = 0.04$ eV/V. Therefore, modulating the voltage on P3 applies a stronger drive to the qubit, which increases the magnitude of the coupling and the measured resonator response. Aside from our choice of driving gate, there are no other electrostatic changes in the double-dot detuning or tunnel coupling between Figs. 5.3(a) and 5.3(b). Hence, the heightened response in Fig. 5.3(b),[1] which we show below to be proportional to the amplitude of the qubit drive, has immediate and important consequences for qubit readout.

5.3 Theory

To understand these different effects, we construct a Hamiltonian for our qubit system. As argued in Section 5.6.1, since we work in an operating regime very near the charging transition, $\varepsilon_0 = 0$, and since the data in Figs. 5.3(c) and 5.3(d) appear symmetric about $\varepsilon_0 = 0$, it should be a good approximation to ignore other nearby level crossings. We therefore treat the system as a simple charge qubit, in which an excess electron moves

---

[1] The different background noise levels observed in the experimental configurations of Figs. 5.3(a) and 5.3(b) can be partially explained by the different numbers of microwave photons in the resonator (see Section 5.6.5), since the noise level scales as $1/\sqrt{\langle n \rangle}$ [205].

between two sides of a double dot, atop a fixed (1,1) charge configuration. The resulting qubit Hamiltonian is given by $H_q = (\varepsilon/2)\sigma_z + t_c\sigma_x$, where the double-dot detuning parameter $\varepsilon = \varepsilon_0 + \varepsilon_q \cos(\omega t)$ includes both static and driving terms, t_c is the tunnel coupling between the two dots, and σ_x and σ_z are Pauli operators acting on the charge basis of left or right-localized states. Since σ_z is proportional to the charge-dipole operator of the double dot and $(a + a^\dagger)$ corresponds to the quantum field of the resonator ($a^\dagger$ and a are photon creation and annihilation operators), the full Hamiltonian of the coupled qubit-cavity system is given by $H = H_q + \hbar\omega_r a^\dagger a + 2\varepsilon_r \cos(\omega_r t)(a + a^\dagger) + \hbar g_0 \sigma_z (a + a^\dagger)$, where g_0 is the bare coupling between the resonator and double dot, and we have included a resonant cavity-driving term, with amplitude $2\varepsilon_r$. In the absence of coupling ($g_0 = 0$) or qubit driving ($\varepsilon_q = 0$), the bare qubit energy is given by $E_{q0} = \hbar\omega_{q0} = \sqrt{\varepsilon_0^2 + 4t_c^2}$.

In all of the experiments reported here, the device is operated in the adiabatic coupling regime $\omega_r \ll \omega_{q0}$, in which the resonator is unable to excite the qubit. We further consider the weak-driving, dispersive limit, $\varepsilon_q, \hbar g_0 \ll t_c$. As explained in Section 5.6.1, an effective Hamiltonian can be derived under these assumptions. Moving to a frame rotating at the cavity frequency, performing a rotating-wave approximation, and retaining coupling terms up to order $\mathcal{O}[\varepsilon_q g_0, g_0^2]$, the system Hamiltonian reduces to

$$H_\rho \approx \frac{E_{q0}}{2}\tilde{\sigma}_z + \varepsilon_r(\tilde{a} + \tilde{a}^\dagger) + \frac{\hbar g_\parallel^{\mathrm{dy}}}{2}\tilde{\sigma}_z(\tilde{a} + \tilde{a}^\dagger) + \hbar\delta\omega\,\tilde{\sigma}_z\left(\tilde{a}^\dagger\tilde{a} + \frac{1}{2}\right), \tag{5.1}$$

where the tildes on the operators $\tilde{\sigma}_z$, $\tilde{a}$, and $\tilde{a}^\dagger$ indicate that they are defined in the rotating frame of the qubit energy-basis states (see Section 5.6.1). The effective coupling terms are given by

$$g_\parallel^{\mathrm{dy}} = \frac{4t_c^2 g_0 \varepsilon_q}{E_{q0}^3} \qquad \text{and} \qquad \delta\omega = \frac{8\hbar t_c^2 g_0^2}{E_{q0}^3}. \tag{5.2}$$

Such couplings can be observed as effective shifts in the cavity field or cavity energy that depend on the state of the qubit. They are known as energy-curvature or quantum-capacitance couplings [190, 194], and we refer to $g_\parallel^{\mathrm{dy}}$ and $\delta\omega$ here as the dynamic longitudinal and dispersive couplings, respectively. It can be seen that $\delta\omega$ differs from the conventional definition [141] of the dispersive coupling ($\chi = g_\perp^2/\omega_q = \delta\omega/2$) by a factor of 2, due to our experiment being performed in the ultra-dispersive or 'adiabatic' regime, $\omega_r \ll \omega_q$ (see Section 5.6.1).

Although the microwave resonator cannot excite the qubit in the present scheme, the qubit has a measurable effect on the resonator through $\delta\omega$ and $g_\parallel^{\mathrm{dy}}$, with the latter being proportional to the ac drive applied to the qubit detuning parameter, ε_q. It is crucial to note that an ac drive applied through gate S1 in Fig. 5.2(d) primarily affects the left dot, while an ac drive on gate P3 primarily affects the right dot. The two drives therefore act on ε_q with opposite sign. On the other hand, the two driving channels act on the cavity (and therefore ε_r) with the same sign. Here, S1 drives the cavity directly, while P3 drives the cavity indirectly through crosstalk between the two gates. As explained in Section 5.6.1, this difference in signs is crucial for observing opposing behaviors in Figs. 5.3(a) and 5.3(b). Indeed, for future qubit readout experiments, it could be preferable to drive the qubit on the same side as the resonator coupling (i.e., through P2 rather than P3), so that $\delta\omega$ and $g_\parallel^{\mathrm{dy}}$ affect the resonator in tandem, rather than opposition, to achieve a stronger total effect.

Finally, we provide an expression for the output of our homodyne detector (see Section 5.6.2), which converts the signal transmitted through the microwave cavity into a dc voltage:

$$\mathrm{IQ}_- = c\frac{(\varepsilon_r/\hbar) - (g_\parallel^{\mathrm{dy}}/2)}{\sqrt{\delta\omega^2 + \kappa^2/4}}. \tag{5.3}$$

Here, the minus sign in the subscript indicates that the qubit is always in its ground state, c is a proportionality constant, relating the signal transmitted through the microwave cavity to the output voltage from the IQ mixer, and $\kappa/2\pi$ is the photon loss rate from the cavity.

5.4 Analysis of Coupling Parameters

Equations (5.1) – (5.3) are used to quantitatively fit the data in Figs. 5.3(c) and 5.3(d), to determine the different coupling parameters. The fitting procedure is explained in detail in Section 5.6.3, and the results are shown here as yellow curves. After fitting, we subtract the asymptotic background signal in IQ_{-}, which varies around 10% between the two drive configurations. Note that the proportionality constant c in Eq. (5.3) is related to the measurement setup rather than the qubit-cavity coupling, and cannot be measured directly. Since ε_r and $g_{\parallel}^{\mathrm{dy}}$ are both multiplied by c, their values cannot be determined independently. However, the tunnel coupling t_c can be obtained without ambiguity from the fitting procedure, and the bare qubit-cavity coupling $g_0/2\pi = 5.5$ MHz can be determined from measured device parameters (see Section 5.6.4). Combining these results with knowledge of the applied drive power allows us to estimate ε_r and $g_{\parallel}^{\mathrm{dy}}$ in the current experiments, as described below.

We now further explore the physics of $g_{\parallel}^{\mathrm{dy}}$ by varying different device parameters that affect the coupling strength. (For all remaining measurements reported here, the ac drive is applied to gate P3.) Figure 5.4(a) shows ε_0 line cuts, labeled (i) – (iii), for three different ac driving amplitudes ε_q. The IQ units for this plot are normalized to the height of the tallest peak [(iii)], and the plots are shifted vertically for clarity. The reported ε_q units are also relative, since we cannot determine this parameter precisely. We see that the transmission peaks increase significantly in height with ε_q. For comparison, we note that these data were acquired at a similar device tuning as Fig. 5.3, where the relative ε_q value was 3.5.

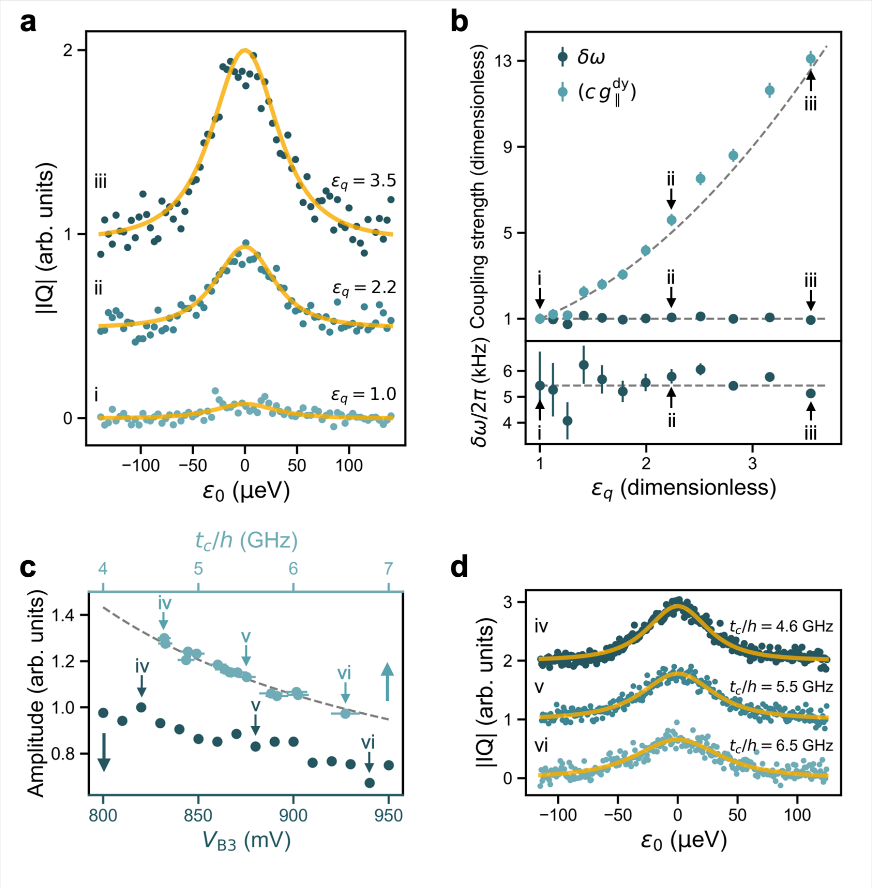

Figure 5.4: Dependence of the cavity transmission and cavity-qubit couplings on ac driving amplitude and tunnel coupling, for P3 driving near the interdot charging transition. **(a)** IQ transmission traces for three different values of the ac driving strength (dimensionless units, see main text): (i) $\varepsilon_q = 1.0$, (ii) 2.2, and (iii) 3.5. Data are normalized to the height of the tallest peak [(iii)], and the traces are offset vertically by 0.5 for clarity, after subtracting off background levels. Yellow curves are fits to Eq. (5.3). **(b)** Upper plot: fitting values for the product $(c\,g_\parallel^{\mathrm{dy}})$ and for $\delta\omega$, evaluated at the peak value $\varepsilon_0 = 0$, as a function of ε_q (also dimensionless). Lower plot: same $\delta\omega$ results, plotted in absolute units. In both panels, the dashed gray curves correspond to expected scaling behavior: no ε_q dependence for $\delta\omega$, and parabolic dependence for $(c\,g_\parallel^{\mathrm{dy}})$. Arrows indicate the traces shown in (a). **(c)** Dark teal data points: transmission peak amplitudes vs. tunnel-barrier gate voltage (bottom axis). Background levels have been subtracted and normalized to the height of the tallest peak. Light teal data points: peak amplitude vs. tunnel coupling t_c (top axis), determined from transmission peak fits. These data points have been offset by 0.3 arbitrary units for clarity. The amplitudes follow a $1/t_c$ trend (gray-dashed curve). (Note that the top and bottom axes are not linearly related, as the dependence of t_c on V_{B3} is generally exponential.) **(d)** IQ transmission traces for the voltage values indicated by arrows in (c): (iv) $V_{\mathrm{B3}} = 820$, (v) 880, or (vi) 940 mV. The data are fit to Eq. (5.3) (yellow curves), yielding t_c values 4.6, 5.5, and 6.5 GHz, respectively. For clarity, each of the traces is offset by 1 in these arbitrary units.

We can extract the quantum couplings $\delta\omega$ and $g_{\parallel}^{\mathrm{dy}}$ at different driving strengths ε_q by fitting the transmission peaks to Eq. (5.3), following the procedure described in Section 5.6.3. Three such fits are shown in yellow in Fig. 5.4(a). Figure 5.4(b) shows the full set of fitting results for $\delta\omega$, and the product parameter $(c\, g_{\parallel}^{\mathrm{dy}})$ (see Sections 5.6.2 and 5.6.3), evaluated at the $\varepsilon_0 = 0$ transmission peak, as a function of ε_q. The points corresponding to the three data sets in Fig. 5.4(a) are indicated by arrows. Because we are unable to estimate parameters c and $g_{\parallel}^{\mathrm{dy}}$ independently in this fitting procedure, we scale $\delta\omega$ and $(c\, g_{\parallel}^{\mathrm{dy}})$ by their values at $\varepsilon_q = 1$ in the top panel. (In the bottom panel, $\delta\omega$ is also reported in dimensionful units.) We note that the $(c\, g_{\parallel}^{\mathrm{dy}})$ results in Fig. 5.4(b) follow a parabolic scaling law with respect to ε_q (dashed gray curve). Since $c \propto \varepsilon_q$ for our homodyne detection scheme, as explained in Section 5.6.2, we infer that $g_{\parallel}^{\mathrm{dy}} \propto \varepsilon_q$, as consistent with Eq. (5.2). This confirms the parametric nature of $g_{\parallel}^{\mathrm{dy}}$, and has important implications for qubit tunability, as we discuss below.

The dispersive-like coupling term $\delta\omega$ is not expected to exhibit ε_q dependence. Unfortunately, the peak-fitting procedure described above does not enable a direct measurement of $\delta\omega$ because of its small size compared to $g_{\parallel}^{\mathrm{dy}}$; however, it does allow us to determine t_c. In Fig. 5.4(b), we therefore plot $\delta\omega$ computed from Eq. (5.2). Alternatively, we can also obtain direct measurements of $\delta\omega$ in a slightly different tuning regime, as described in Section 5.6.7, obtaining results very similar to Fig. 5.4(b). These combined results indicate that $\delta\omega$ does not depend on the driving strength ε_q, as consistent with our theoretical understanding, and they confirm that the dispersive-like coupling is very small in the ultra-dispersive regime, with $\delta\omega/2\pi \approx 2.6 - 6.2$ kHz.

We can also explore the variation of $g_{\parallel}^{\mathrm{dy}}$ with tunnel coupling. In this case, Fig. 5.4(c) indicates that the transmission peak amplitude decreases with t_c. (Here, we only vary V_{B3}, keeping all other device parameters fixed.) Note that this experiment was performed on a different date, resulting in different device tunings than Figs. 5.3, 5.4(a), and 5.4(b), and a different value of $g_0/2\pi = 4.1$ MHz (see Section 5.6.4), due to electrostatic drift.

To analyze the data, we first extract the peak heights. This is done using a Lorentzian fitting form, to avoid assumptions about the physical model; however, results are essentially identical to fits using Eq. (5.3). The Lorentzian peak heights are plotted in Fig. 5.4(c) after normalizing the data to the tallest peak, labeled (iv). We also fit the IQ peaks to Eq. (5.3). The detailed fitting procedure is described in Section 5.6.3. Three example fits are shown in Fig. 5.4(d), corresponding to the three labeled points (iv) – (vi) in Fig. 5.4(c). The peak heights are re-plotted in Fig. 5.4(c) as a function t_c/h, as determined through this procedure. The behavior is consistent with our expectations from Eqs. (5.2) and (5.3), that peak amplitude $\sim g_{\parallel}^{\mathrm{dy}} \propto 1/t_c$.

The global parameter c in Eq. (5.3) precludes being able to specifically determine ε_r or ε_q in our fitting procedure. However, by taking into account the full microwave power budget, including input power and all significant attenuation sources, we estimate P3 driving amplitudes as large as $\varepsilon_q/h \approx 152$ MHz in these experiments (see Section 5.6.5). Indeed, we expect P3 to provide the largest longitudinal interaction, due to its strong capacitive coupling to the dot. Using this estimate and fitting results for t_c, we use Eq. (5.2) to estimate $|g_{\parallel}^{\mathrm{dy}}/2\pi| \approx 12 - 68$ kHz in the current experiments, including Figs. 5.3 and 5.4. Since $g_{\parallel}^{\mathrm{dy}}$ is proportional to ε_q, we emphasize that it should be possible to further enhance the coupling through stronger driving, while still remaining in the weak-driving regime. Although we did not explore this possibility here, it remains an important direction for future work. To estimate coupling values that could potentially be achieved in the present device, we take $\varepsilon_q/t_c = 0.1$ as an upper bound on weak driving, yielding a maximum value of $|g_{\parallel}^{\mathrm{dy}}/2\pi| = 0.28$ MHz, which is much larger than our estimates for $\delta\omega$, described above.

It is crucial to note that the current experiments are performed in the far-detuned regime, $\omega_{q0}/\omega_r \gtrsim 7$, which we refer to as 'adiabatic' here, because the resonator cannot excite the qubit. To our knowledge, previous longitudinal coupling experiments have never accessed this extreme-detuning regime, either in superconducting [192, 203] or quantum-dot qubit implementations [204]. The adiabatic regime has several appealing features: (1) Purcell decoherence is strongly suppressed, since we are far from resonance; (2) there are no engineering constraints related to satisfying a resonance condition; (3) the coupling can be turned on and off via the driving term ε_q. Focusing on this final point, we note that when $\varepsilon_q = 0$, the total coupling is reduced to the small, residual dispersive coupling $\delta\omega$. When larger couplings are desired, they can be achieved by increasing ε_q up to the upper bound on weak driving. A useful figure of merit is therefore given by the tunability ratio, $|g_\parallel^{\mathrm{dy}}/\delta\omega| = \varepsilon_q/2\hbar g_0$, which can be large when the driving amplitude ε_q is much larger than the zero-point fluctuations of the cavity, as felt by the dot. Estimates for the current device indicate a tunability factor of 18.4. However, we expect that tunability factors as large as 79 could be achieved for the tunnel couplings measured here, if the drive was increased to the weak-driving limit. These estimates differ considerably from recent experiments in GaAs [204], where much larger values of the dispersive coupling $\delta\omega/2\pi \sim 0.1 - 0.25$ MHz were obtained,[2] due to the large bare resonator coupling g_0. A larger longitudinal coupling $g_\parallel^{\mathrm{dy}}/2\pi \sim 1$ MHz was also observed in Ref. [204], yielding figures of merit in the range of $1 - 5$, much smaller than those reported here. These differences emphasize the inherent competition between the strength ($\propto g_0$) and the tunability ($\propto g_0^{-1}$) of the longitudinal coupling, where g_0 is an engineered variable.

5.5 Conclusions

In conclusion, we have explored the energy curvature couplings $\delta\omega$ and $g_\parallel^{\mathrm{dy}}$ between a Si/SiGe double-dot charge qubit and an off-chip, high-impedance microwave resonator. By varying the tunnel coupling and applying the drive through different channels and at different strengths, we are able to prove the existence of the dynamic longitudinal coupling. We estimate its potential strength here as $|g_\parallel^{\mathrm{dy}}/2\pi| \approx 68$ kHz, which can be increased to 0.28 MHz upon stronger driving, even in the far-detuned regime. We compare $g_\parallel^{\mathrm{dy}}$ to the dispersive coupling $\delta\omega$, finding $|g_\parallel^{\mathrm{dy}}/\delta\omega| > 18$ here, and potentially up to 79 under optimal conditions.

---

[2] Here, we compare to the dispersive coupling definition χ_B used in Ref. [204], which is unconventional [141], and differs from our definition of $\delta\omega$ by a factor of 2.

Moreover, such strong coupling ($|g_{\parallel}^{\mathrm{dy}}/\delta\omega| \gg 1$) is achieved here in the ultra-dispersive ('adiabatic') regime, which has not been previously explored. Crucially, such strong, dispersive couplings reduce engineering constraints and suppress Purcell decoherence. We conclude that such longitudinal driving forms an important tool for future quantum-dot qubit experiments.

Acknowledgments

The authors thank HRL for support and L. F. Edge for providing the Si/SiGe heterostructure used in this work. Research was sponsored in part by the Army Research Office (ARO) under Award Numbers W911NF-17-1-0274 and W911NF-23-1-0110, and by the Department of Defense. J. C. acknowledges support from the National Science Foundation Graduate Research Fellowship Program under Grant No. DGE-1747503 and the Graduate School and the Office of the Vice Chancellor for Research and Graduate Education at the University of Wisconsin-Madison with funding from the Wisconsin Alumni Research Foundation. We acknowledge the use of facilities supported by NSF through the UW-Madison MRSEC (DMR-2309000) and the MRI program (DMR–1625348). Work done at MIT Lincoln Laboratory was funded in part by the Assistant Secretary of Defense for Research & Engineering under Air Force Contract No. FA8721-05-C-0002. The views, conclusions, and recommendations contained in this document are those of the authors and are not necessarily endorsed nor should they be interpreted as representing the official policies, either expressed or implied, of the Army Research Office (ARO) or the U. S. Government. The U. S. Government is authorized to reproduce and distribute reprints for Government purposes notwithstanding any copyright notation herein.

5.6 Supplementary Information

These supplemental materials provide additional data and details about the methods used in this work.

5.6.1 Derivation of the Curvature Coupling Terms

In this work, we have studied the interactions between an off-chip microwave resonator and a charge qubit. Although we do not explicitly perform qubit operations, the work is motivated by qubit operations, including readout. In some cases, the qubit of interest could be a charge qubit, for which the information is stored in the charge degree of freedom. In other cases, the information is stored as a spin, then converted to charge information to facilitate readout. In both cases, the simplest system we could consider comprises a single electron in a double dot. However, the motivation for the current work lies with experiments performed on the quantum dot hybrid qubit, which can be viewed as a cross between a spin and a charge qubit [206, 207]. The device incorporates an odd number of three or more electrons in a double dot, and the corresponding gate operations are performed in the vicinity of a charging transition ($\varepsilon \approx 0$), where one of the electrons tunnels between the dots. Below, we first explain why the following theoretical analysis can be framed in terms of the simpler problem, comprising a double dot with one electron.

The relevant basis states for the quantum dot hybrid qubit are fourfold, including two charge configurations and a pair of spin-orbit states, with a characteristic energy splitting approximately equal to the singlet-triplet splitting E_{ST} of the dot containing an even number of electrons. When E_{ST} is somewhat larger than both the detuning parameter ε and the interdot tunnel coupling t_c, we may ignore one or both of the high-energy excited states. For example, in many cases, it is sufficient to consider a three-level description [208]. In the present work, we do not exploit the full hybrid-qubit functionality, and we further make use of the fact that the data in Figs. 5.3 and 5.4 of the main text appear symmetric with respect to $\varepsilon_0 = 0$ (as consistent with $\varepsilon_q, t_c < E_{\mathrm{ST}}$) and do not hint at nearby energy-level anticrossings, thus reinforcing such an approximate two-level description. We may therefore restrict our analysis to just the two lowest-energy states. The resulting qubit Hamiltonian is then given by $H_q = (\varepsilon/2)\sigma_z + t_c\sigma_x$.

To construct the full Hamiltonian, we consider the circuit illustrated in Fig. 5.5, which

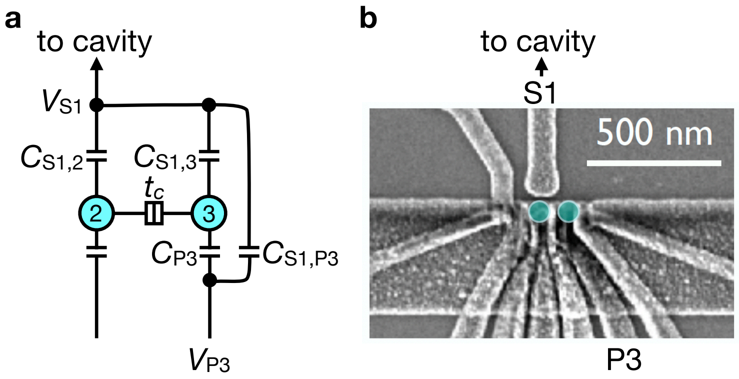

Figure 5.5: **(a)** Simplified circuit diagram of a double dot coupled to an external microwave cavity. Direct capacitances $C_{\mathrm{S1,2}}$ and C_{P3} between the dots and gates S1 and P3 are indicated. Cross capacitances $C_{\mathrm{S1,3}}$ and $C_{\mathrm{S1,P3}}$ are also indicated, as is the double-dot tunnel coupling t_c. (Note that other capacitances are present in our system, such as couplings to ground, which do not play a direct role in the current discussion and are not shown here.) The voltage V_{S1} on gate S1 also couples to the cavity. Voltages V_{S1} and V_{P3} may both include an ac drive, although only one gate is driven at a time. **(b)** A triple-dot device, operated in double-dot mode, reproduced from Fig. 5.2(d) of the main text. In (a), the two activated dots are labeled 2 and 3.

---

indicates the relevant voltages and capacitances in our device, formed of a double dot coupled to a microwave cavity. As described in the main text, microwave driving tones are applied in two ways to this circuit.

In the first driving mode, an ac voltage is applied to gate S1, which has two effects on the Hamiltonian. First, the drive causes a modulation of the double-dot detuning parameter (primarily via dot 2), as described by the Hamiltonian term $(\varepsilon_2/2)\cos(\omega t)\sigma_z$, where ε_2 is the driving amplitude of the detuning parameter via dot 2. There is also a secondary effect of driving gate S1, due to the cross-capacitances labelled $C_{\mathrm{S1,3}}$ and $C_{\mathrm{S1,P3}}$ in Fig. 5.5(a), which slightly reduces the total detuning drive. Such cross-capacitances modify the primary capacitive couplings; however, their effect is not leading order, and therefore modest, and will be neglected here. A much more important contribution to the Hamiltonian, associated with S1-driving, is the cavity coupling, which takes the form $2\varepsilon_r\cos(\omega t)(a + a^\dagger)$. We note that the driving amplitudes ε_2 and ε_r arise from the same voltage oscillations on gate S1, and are therefore proportional. Although it is possible to specify this proportionality constant in terms of lever arms, it is convenient to simply define $\varepsilon_r = \beta_2\varepsilon_2$. In the fitting procedure described below, β_2 and ε_2 are chosen as fitting parameters, while ε_r becomes a dependent parameter.

The P3 driving mode also modulates the detuning parameter (primarily via dot 3), as described by the Hamiltonian term $(\varepsilon_3/2)\cos(\omega t)\sigma_z$, where ε_3 is the driving amplitude of the detuning parameter via dot 3. Note that although we have neglected cross-capacitances in the S1-driving Hamiltonian, it is very important to include them for the case of P3 driving. This is because the cross-capacitances are solely responsible for driving the cavity in this scenario. To account for this, we introduce the proportionality relation $\varepsilon_r = \beta_3\varepsilon_3$. The cross-capacitance also has a secondary effect on the total detuning through dot 2, of the form $\varepsilon_2 = (\beta_3/\beta_2)\varepsilon_3$. The total driving amplitude for the detuning parameter is therefore slightly reduced to $(1 - \beta_3/\beta_2)\varepsilon_3$ due to crosstalk.

For the experiments described here, it is crucial to note that the S1 and P3 driving terms contribute to the total detuning with opposite sign, because they are applied on opposite sides of the double dot. Taking into account both driving terms, the total detuning thus becomes

$$\varepsilon = \varepsilon_0 + \varepsilon_q \cos(\omega t), \qquad \text{where} \qquad \varepsilon_q = \varepsilon_2 - \left(1 - \frac{\beta_3}{\beta_2}\right)\varepsilon_3. \tag{5.4}$$

On the other hand, the two driving terms contribute to the cavity drive with the same sign:

$$\varepsilon_r = \beta_2\varepsilon_2 + \beta_3\varepsilon_3. \tag{5.5}$$

In both of these equations, we emphasize that only one of the drives, ε_2 or ε_3, is active at a time. The full Hamiltonian is finally given by

$$H = \frac{\varepsilon_0 + \varepsilon_q \cos(\omega_r t)}{2}\sigma_z + t_c\sigma_x + 2\varepsilon_r \cos(\omega_r t)(a + a^\dagger) + \hbar\omega_r a^\dagger a + \hbar g_0 \sigma_z (a + a^\dagger), \tag{5.6}$$

where in addition to the terms already discussed, the fourth term describes a microwave cavity with resonant frequency ω_r, and the fifth term describes a coupling of strength g_0 between the cavity and the qubit. As a note of clarification, the parameter β_2 is used here to describe the relation between the oscillating chemical potential of dot 2 and the cavity drive, while g_0 describes the capacitive coupling between the qubit electron and the cavity. Also note that we have set all driving frequencies equal to the cavity resonance frequency, as consistent with the experiments. We have also ignored any phase difference between the drives applied to S1 and P3, which could arise due to different capacitances on different arms of the quantum dot circuit. This seems justified, to a first approximation, because the drive responses appear 180° out of phase; however, we would generally expect such a phase difference to suppress the overall magnitude of the P3 response.

The key to deriving an effective curvature Hamiltonian is the following adiabatic approximation: when $\hbar\omega_r \ll 2t_c$, the qubit responds adiabatically to the Hamiltonian driving terms (including the cavity coupling g_0). In other words, the driving terms are unable to excite the qubit. In this adiabatic regime (which is valid for our experiments), the slowly varying terms may be absorbed into the qubit Hamiltonian, giving

$$H = \frac{\tilde{\varepsilon}}{2}\sigma_z + t_c\sigma_x + 2\varepsilon_r\cos(\omega_r t)(a + a^\dagger) + \hbar\omega_r a^\dagger a, \tag{5.7}$$

where

$$\tilde{\varepsilon} = \varepsilon_0 + \varepsilon_q\cos(\omega_r t) + 2\hbar g_0(a + a^\dagger). \tag{5.8}$$

With regard to qubit dynamics, $\tilde{\varepsilon}$ may simply be viewed as a resonator-dependent 'constant.' Diagonalizing within the qubit subspace then gives

$$H' = \frac{E_q}{2}\tilde{\sigma}_z + 2\varepsilon_r\cos(\omega_r t)(a + a^\dagger) + \hbar\omega_r a^\dagger a, \tag{5.9}$$

where

$$E_q = \sqrt{4t_c^2 + [\varepsilon_0 + \varepsilon_q\cos(\omega_r t) + 2\hbar g_0(a + a^\dagger)]^2}, \tag{5.10}$$

and $\tilde{\sigma}_z$ is a Pauli matrix in the qubit frame.

We now further assume that the experiments operate in the weak-driving regime, such that $\varepsilon_q, \hbar g_0 \ll t_c$. Taylor expanding Hamiltonian (5.9) up to order $\mathcal{O}[g_0^2, g_0\varepsilon_q]$ then gives

$$H' \approx \frac{E_{q0}}{2}\tilde{\sigma}_z + \hbar\left[g_\parallel^{\rm st} + g_\parallel^{\rm dy}\cos(\omega_r t)\right]\tilde{\sigma}_z\left(a + a^\dagger\right) + \frac{\hbar\delta\omega}{2}\tilde{\sigma}_z\left(a + a^\dagger\right)^2 + 2\varepsilon_r\cos(\omega_r t)\left(a + a^\dagger\right) + \hbar\omega_r a^\dagger a \quad (5.11)$$

where

$$E_{q0} = \sqrt{\varepsilon_0^2 + 4t_c^2} \qquad \text{(static qubit energy)}, \quad (5.12)$$

$$g_\parallel^{\rm st} = \frac{\varepsilon_0 g_0}{E_{q0}} \qquad \text{(static longitudinal coupling)}, \quad (5.13)$$

$$g_\parallel^{\rm dy} = \frac{4t_c^2 g_0 \varepsilon_q}{E_{q0}^3} \qquad \text{(dynamic longitudinal coupling)}, \quad (5.14)$$

$$\delta\omega = \frac{8t_c^2\hbar g_0^2}{E_{q0}^3} \qquad \text{(dispersive coupling)}. \quad (5.15)$$

We have dropped two inconsequential terms in Eq. (5.11). The first is a term $\propto \varepsilon_q\cos(\omega_r t)\tilde{\sigma}_z$, which adiabatically modifies the qubit energy, but averages to zero in time-averaged experiments like the ones described here. The second term is the $\mathcal{O}[\varepsilon_q^2]$ term in the Taylor expansion, which causes weak oscillations $\propto \varepsilon_q^2\cos^2(\omega_r t)\tilde{\sigma}_z$ in the laboratory frame, and a small, constant shift of the qubit energy splitting in the rotating frame, but does not affect the results described below.

We can simplify Eq. (5.11) by noting that 'counter-rotating' terms proportional to a^2 or $a^{\dagger 2}$ do not conserve energy and may therefore be eliminated through a rotating wave approximate, giving

$$H' \approx \frac{E_{q0}}{2}\tilde{\sigma}_z + \hbar\left[g_\parallel^{\rm st} + g_\parallel^{\rm dy}\cos(\omega_r t)\right]\tilde{\sigma}_z\left(a + a^\dagger\right) + \hbar\delta\omega\,\tilde{\sigma}_z\left(a^\dagger a + \frac{1}{2}\right) + 2\varepsilon_r\cos(\omega_r t)\left(a + a^\dagger\right) + \hbar\omega_r a^\dagger a. \quad (5.16)$$

Finally, moving to the rotating frame defined by $U = \exp(-i\omega_r t\, a^\dagger a)$ and applying a rotating wave approximation, we find that

$$H_\rho = U^\dagger H' U - i\hbar U^\dagger \frac{d}{dt} U \approx \frac{E_{q0}}{2}\tilde{\sigma}_z + \frac{\hbar g_\parallel^{\mathrm{dy}}}{2}\tilde{\sigma}_z\left(\tilde{a} + \tilde{a}^\dagger\right) + \hbar\delta\omega\,\tilde{\sigma}_z\left(\tilde{a}^\dagger\tilde{a} + \frac{1}{2}\right) + \varepsilon_r\left(\tilde{a} + \tilde{a}^\dagger\right), \quad (5.17)$$

where $\tilde{a}^\dagger$ and $\tilde{a}$ are photon creation and annihilation operators in the rotating frame. Equation (5.17) contains all the curvature couplings.

As noted in the main text, the definition of the dispersive coupling $\delta\omega$ used in the preceding equations differs from the conventional definition of the dispersive coupling χ by a factor of two. To understand this, we note that Eq. (5.17) can also be solved using a standard Schrieffer-Wolff perturbation method, yielding

$$\delta\omega \approx g_\perp^2\left(\frac{1}{\omega_q - \omega_r} + \frac{1}{\omega_q + \omega_r}\right). \quad (5.18)$$

In the conventional dispersive regime, where $|\omega_q - \omega_r| \ll \omega_r$, the second term in Eq. (5.18) is counterrotating (small), and is therefore dropped in many calculations, yielding the conventional dispersive result, $\delta\omega \approx g_\perp^2/\Delta = \chi$, where $\Delta = |\omega_q - \omega_r|$. However in the ultra-dispersive regime, $\omega_r \ll \omega_q$, both terms have the same magnitude, and we obtain $\delta\omega \approx 2g_\perp^2/\omega_q \approx 2\chi$.

5.6.2 IQ Equations

Equation (5.17) is now used to calculate the dynamics of the density matrix. Expressing the photonic terms of the density matrix in the coherent-state basis $\{|\tilde{\alpha}\rangle\}$, where $a|\tilde{\alpha}\rangle = \tilde{\alpha}|\tilde{\alpha}\rangle$, yields the following dynamical equations:

$$\frac{d\tilde{\alpha}_\pm}{dt} = -i\left(\pm\delta\omega - i\frac{\kappa}{2}\right)\tilde{\alpha}_\pm - i\left(\frac{\varepsilon_r}{\hbar} \pm \frac{g_\parallel^{\mathrm{dy}}}{2}\right), \quad (5.19)$$

where the tilde notation ($\tilde{\alpha}_\pm$) indicates that we are working in the rotating frame [190]. Here, the ± sign corresponds to the eigenvalues of $\tilde{\sigma}_z$ in Eq. (5.17); the cavity evolution therefore depends on the state of the qubit. Note that the first brackets in Eq. (5.19) correspond to diagonal terms in Eq. (5.17), with respect to the photon operators, while the second brackets correspond to off-diagonal terms. Also note that we have introduced an energy-nonconserving term with strength κ to account for photon loss from the cavity, at a rate $\kappa/2\pi$. In the transmission experiments described in the main text, we probe the stationary states of the cavity ($\tilde{\alpha}_\pm^{\mathrm{st}}$), which can be obtained from Eq. (5.19) by setting $d\tilde{\alpha}_\pm/dt = 0$, giving

$$\tilde{\alpha}_\pm^{\mathrm{st}} = -\frac{(\varepsilon_r/\hbar) \pm (g_\parallel^{\mathrm{dy}}/2)}{\pm\delta\omega - i\kappa/2}. \tag{5.20}$$

The coherent state amplitudes $\tilde{\alpha}_\pm$ are proportional to the output (transmitted) amplitude of the resonator $\tilde{A}$, which can be measured using a homodyne circuit. The technique converts the rapidly oscillating microwave transmission field to a dc signal. In brief, a copy of the ac input drive (applied to gates S1 or P3) is multiplied by the output signal from the cavity, using an IQ mixer. A second copy of the input signal, which is phase-shifted by $\pi/2$, is also multiplied by the output signal. Time averaging these separate products provides measurement of the I and Q quadratures of the cavity transmission. The cavity input fields in this calculation are defined as

$$a_{\mathrm{in}}^I = A\cos(\omega_r t) \qquad \text{and} \qquad a_{\mathrm{in}}^Q = -A\sin(\omega_r t), \tag{5.21}$$

and the cavity output field is defined as

$$a_{\mathrm{out}} = \tilde{A}\cos(\omega_r t + \phi_{\mathrm{out}}), \tag{5.22}$$

where ϕ_{out} represents the phase shift of the transmitted signal. We note that the input field strength A differs for drives applied to gates S1 versus P3 at a given microwave generator power, due to their distinct circuit paths and microwave attenuations. The product signals are given by

$$I = \overline{a_{\rm in}^{I} a_{\rm out}} = \frac{A\tilde{A}}{2}\cos(\phi_{\rm out}) \qquad \text{and} \qquad Q = \overline{a_{\rm in}^{Q} a_{\rm out}} = \frac{A\tilde{A}}{2}\sin(\phi_{\rm out}), \tag{5.23}$$

where the bar notation denotes time averaging. The combined IQ output is then given by

$$\mathrm{IQ}_{\pm} \equiv \sqrt{I^2+Q^2} = c|\alpha_{\pm}| = c\frac{(\varepsilon_r/\hbar) \pm (g_{\parallel}^{\rm dy}/2)}{\sqrt{\delta\omega^2+\kappa^2/4}}, \tag{5.24}$$

where the prefactor c accounts for the details of the measurement and room-temperature circuitry, including attenuation, signal amplification, and other effects. This factor prevents us from obtaining an absolute estimate of the various coupling terms directly from $\mathrm{IQ}_{\pm}$. For interpreting the measurements in Figs. 5.4(a) and 5.4(b) of the main text, we point out that $c \propto A \propto \varepsilon_q$, which can be seen by combining Eq. (5.24) with the fact that $|\alpha_{\pm}| \propto \tilde{A}$. Finally, we note that the qubit remains in its ground state in all of the experiments described here, so we only need to consider the minus sign in Eq. (5.24).

5.6.3 Fitting Procedure

In this section, we explain the fitting procedure related to Eq. (5.24). We note that a dc offset in the homodyne IQ output, which was not calibrated away during experiments, has been subtracted from all data presented in this work.

Figure 5.3 Fits

The data in Fig. 5.3 of the main text are fit to Eq. (5.24). For the case of S1 driving, we set $\varepsilon_3 = 0$, obtaining

$$\mathrm{IQ}_{-} = c\,\varepsilon_2 \frac{(\beta_2/\hbar) - (2t_c^2 g_0/E_{q0}^3)}{\sqrt{\delta\omega^2+\kappa^2/4}} \qquad \text{(S1 drive)}, \tag{5.25}$$

	$(c\,\varepsilon_2)\,/\,10^{-5}$ (V GHz)	$(c\,\varepsilon_3)\,/\,10^{-5}$ (V GHz)	$\beta_2\,/\,10^{-2}$	$\beta_3\,/\,10^{-3}$	t_c (GHz)
Fig. 5.3(c,d)	2.52 ± 0.21	12.93 ± 0.60	1.27 ± 0.11	2.89 ± 0.14	6.14 ± 0.21
Fig. 5.4(a)(i)	–	0.92 ± 0.02	–	3.09 ± 0.04	5.57 ± 1.34
Fig. 5.4(a)(ii)	–	4.84 ± 0.06	–	3.09 ± 0.04	5.24 ± 0.26
Fig. 5.4(a)(iii)	–	12.81 ± 0.17	–	3.09 ± 0.04	5.90 ± 0.14
Fig. 5.4(d)(iv)	–	12.77 ± 0.00	–	2.93 ± 0.02	4.65 ± 0.08
Fig. 5.4(d)(v)	–	12.66 ± 0.00	–	2.93 ± 0.02	5.51 ± 0.09
Fig. 5.4(d)(vi)	–	12.57 ± 0.00	–	2.93 ± 0.02	6.55 ± 0.15

Table 5.1: Best-fit parameters and uncertainties obtained using the fitting procedures described in Section 5.6.3.

---

while for P3 driving, we set $\varepsilon_2 = 0$, obtaining

$$\mathrm{IQ}_- = c\,\varepsilon_3 \frac{(\beta_3/\hbar) + (1-\beta_3/\beta_2)(2t_c^2 g_0/E_{q0}^3)}{\sqrt{\delta\omega^2 + \kappa^2/4}} \qquad \text{(P3 drive).} \tag{5.26}$$

In these equations, we note that $E_{q0} = E_{q0}(\varepsilon_0, t_c)$ and $\delta\omega = \delta\omega(\varepsilon_0, t_c, g_0)$. Since the parameters $g_0/2\pi = 5.5$ MHz and $\kappa/2\pi = 125$ kHz are determined independently using methods described in Section 5.6.4 below, and the data are obtained as a function of ε_0, the resulting fitting parameters are given by $(c\,\varepsilon_2)$, $(c\,\varepsilon_3)$, β_2, β_3, and t_c.

The data in Figs. 5.3(c) and 5.3(d) are fit simultaneously (i.e., both datasets are fit with a single call to the fitting function) to Eqs. (5.25) and (5.26), respectively. This ensures that the common fitting parameters in both equations, β_2 and t_c, are optimized between the two datasets. The best-fit parameters and uncertainties from this fitting procedure are reported in Table 5.1, and are latter used in calculating the Hamiltonian terms below, in Table 5.4.

After fitting, we compute and subtract the asymptotic value $\mathrm{IQ}_-(\varepsilon_0 \to \infty) = 2c\varepsilon_r/\hbar\kappa$ from both line cuts in Fig. 5.3. This value varies slightly (∼10%) between the two drive configurations, most likely due to a small difference in attenuation on the drive lines. Since the parameter c cannot be independently determined, the line cuts in Fig. 5.3(d) are rescaled to have the peak value 1, while the line cuts in Fig. 5.3(c) are scaled by the same factor. The parameters $(c\,\varepsilon_2)$ and $(c\,\varepsilon_3)$ have effectively arbitrary units, although we report them here in units of volts × gigahertz, corresponding to the dc output voltages from the homodyne measurements.

Figure 5.4 Fits

The IQ transmission peaks shown in Fig. 5.4(a) of the main text [and the larger set of peaks leading to Fig. 5.4(b)] are fit to Eq. (5.26) at each value of the ac driving amplitude ε_q. Our fitting procedure is as follows. The fitting parameter β_3 is held fixed across all peaks, since we do not expect its value to change as a function of ε_q. We also set β_2 to the value of 1.27×10^{-2} extracted from the Fig. 5.3 fits, because we are unable to obtain a precise estimate of this quantity without an S1-driven dataset to fit simultaneously. The parameters $g_0/2\pi = 5.5$ MHz and $\kappa/2\pi = 125$ kHz are determined independently using methods described in Section 5.6.4, below. This leaves the product $(c\,\varepsilon_3)$ and t_c as the remaining fitting parameters for each peak. After fitting, we compute and subtract the asymptotic background level $\mathrm{IQ}_-(\varepsilon_0 \to \infty) \propto c\varepsilon_q$ from the traces in Fig. 5.4(a).

The peaks shown in Fig. 5.4(c) of the main text [and the larger set of peaks leading to Fig. 5.4(d)] are fit to Eq. (5.26) at each value of barrier voltage V_{B3} using a similar procedure. Once again, we hold β_3 fixed across all fits and set $\beta_2 = 1.27 \times 10^{-2}$; $(c\,\varepsilon_3)$ and t_c are again the remaining fitting parameters for each peak. However, in this case we have $g_0/2\pi = 4.1$ MHz, due to a different device tuning for these measurements.

After fitting, we again determine and subtract the asymptotic background level $\mathrm{IQ}_-(\varepsilon_0 \to \infty)$ from the traces in Fig. 5.4(d). The small (∼1%) variation observed in the background is due to time variation in the electrostatic environment and/or change in the lever arm $\alpha_{\mathrm{P3},\varepsilon}$ as a function of V_{B3}.

The best-fit parameters and uncertainties for Figs. 5.4(a) and 5.4(d) are reported in Table 5.1, and corresponding Hamiltonian terms are reported in Table 5.4.

Peak amplitudes plotted in Fig. 5.4(c) are extracted by applying Lorentzian fits to the data; these amplitudes are also shown as dark teal circles in Fig. 5.8(a) below. The arbitrary units in Figs. 5.4(c) and 5.4(d) are scaled so that the tallest peak (labeled iv) has amplitude 1.

5.6.4 Device Parameter Measurements

Gate Lever Arms

We extract gate-to-dot lever arms by measuring thermal broadening of electron transitions [209]. At finite temperature, thermal fluctuations of the chemical potential lead to charge transitions of finite energy width, which we measure by sweeping the dc plunger voltage V_{P3} through a dot 3 charging transition, which occurs at the voltage V_0. In the limit $k_B T_e \gg \hbar\omega_r$, the transition linewidth is thermally limited, and the resonator's response to electron tunneling should follow the derivative of the Fermi-Dirac distribution,

$$|\mathrm{IQ}| = -|A|\,\mathrm{sech}^2\left[\frac{\alpha_{\mathrm{P3},3}(V_{\mathrm{P3}} - V_0)}{2k_B T_e}\right] + B, \tag{5.27}$$

where k_B is the Boltzmann constant, T_e is the electron temperature, A is the resonator suppression amplitude, B is the blockade transmission signal, and $\alpha_{\mathrm{P3},3}$ is the P3-to-dot 3 lever arm [22]. As the cryostat temperature is varied, the electron temperature has been observed to follow the trend

$$T_e = \sqrt{T_{\mathrm{mc}}^2 + T_{e0}^2}, \tag{5.28}$$

where T_{mc} is the cryostat mixing chamber temperature and T_{e0} is the base electron temperature when T_{mc} is extrapolated to zero [76].

Working at a device tuning comparable to the one used in measurements for Figs. 5.3 and 5.4(d)(vi), we measure reservoir transition widths at several cryostat temperatures. We then extract a base electron temperature $T_{e0} = 212$ mK and a P3-to-dot 3 lever arm $\alpha_{\mathrm{P3},3} = 0.149$ eV/V by fitting to Eqs. (5.27) and (5.28). The electron temperature extracted from the fitting is well described by Eq. (5.28), as demonstrated in Fig. 5.6.

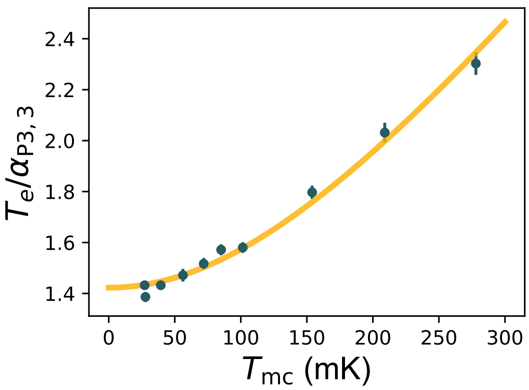

Figure 5.6: Data obtained from thermal broadening measurements for $\alpha_{\mathrm{P3,3}}$. Data points extracted from charge-transition line fits are plotted against the mixing chamber temperature. Fitting these data to Eq. (5.28) yields $\alpha_{\mathrm{P3,3}} = 0.149$ eV/V and the base electron temperature $T_{e0} = 212$ mK.

The other plunger lever arms are calculated from the slopes of transition lines in stability diagrams where both plungers are swept:

$$\alpha_{\mathrm{P3},\varepsilon} = \alpha_{\mathrm{P3,3}} - \alpha_{\mathrm{P3,2}} = \alpha_{\mathrm{P3,3}} \frac{m_{\mathrm{pol}}}{m_3} \left(\frac{m_3 - m_2}{m_2 + m_{\mathrm{pol}}} \right), \tag{5.29}$$

$$\alpha_{\mathrm{P2},\varepsilon} = \alpha_{\mathrm{P2,2}} - \alpha_{\mathrm{P2,3}} = \frac{\alpha_{\mathrm{P3},\varepsilon}}{m_{\mathrm{pol}}}, \tag{5.30}$$

$$\alpha_{\mathrm{P2,2}} = \frac{m_3 \alpha_{\mathrm{P2},\varepsilon} + \alpha_{\mathrm{P3},\varepsilon}}{m_3 - m_2}, \tag{5.31}$$

where $m_i = (\Delta V_{\mathrm{P2}}/\Delta V_{\mathrm{P3}})_i$ are the slopes of dot 2 transition lines, dot 3 transition lines, or polarization lines in $V_{\mathrm{P2}} - V_{\mathrm{P3}}$ space. Similarly, the detuning lever arm for gate S1 is estimated using

$$\alpha_{\mathrm{S1},\varepsilon} = \alpha_{\mathrm{S1,2}} - \alpha_{\mathrm{S1,3}} = \alpha_{\mathrm{P2,2}} \left(\frac{\Delta V_{\mathrm{P2}}}{\Delta V_{\mathrm{S1}}} \right)_2 - \alpha_{\mathrm{P3,3}} \left(\frac{\Delta V_{\mathrm{P3}}}{\Delta V_{\mathrm{S1}}} \right)_3, \tag{5.32}$$

where S1 lever arms are calculated from the slopes of transition lines in two-dimensional scans in which both gates are swept.

Lever arms used for each fit are reported in Table 5.2. We have measured $\alpha_{\mathrm{P2,2}}$ and

	$\alpha_{\mathrm{P2},\varepsilon}$ (eV/V)	$\alpha_{\mathrm{P3},\varepsilon}$ (eV/V)	$\alpha_{\mathrm{S1},\varepsilon}$ (eV/V)	$Z_{0,r}$ (Ω)	$\omega_r/2\pi$ (GHz)	$\kappa/2\pi$ (kHz)	$g_0/2\pi$ (MHz)
Fig. 5.3(c,d)	0.11	0.09	0.04	575	1.3038	124.5	5.5
Fig. 5.4(a,b)	0.11	0.09	0.04	575	1.3038	124.5	5.5
Fig. 5.4(c,d)	0.10	0.10	0.03	575	1.3038	124.5	4.1

Table 5.2: Device parameters obtained using the methods described in Section 5.6.4.

$\alpha_{\mathrm{P3},3}$ at several additional device tunings using both thermal broadening and electron transport bias spectroscopy techniques in order to further verify that the above method provides reasonable estimates.

Qubit-Cavity Bare Coupling

The bare qubit-cavity coupling g_0 is calculated from device parameters according to the equation [160]

$$g_0 = \frac{\alpha_{\mathrm{S1},\varepsilon}\,\omega_r}{2e}\sqrt{\frac{2Z_{0,r}}{h/e^2}}. \tag{5.33}$$

Here, the characteristic impedance of the resonator, $Z_{0,r} = 575\ \Omega$, is estimated from a quasi-static impedance analysis performed using COMSOL Multiphysics [174]. The values of $Z_{0,r}$ and g_0 used in each fit are reported in Table 5.2.

Microwave Resonator Parameters

The cavity resonant frequency ω_r and loaded quality factor Q_L are extracted from resonance transmission curves measured with a vector network analyzer. Complex-plane fits to the curves yield $Q_L = 10,470 \pm 32$ for S1-drive and $Q_L = 10,476 \pm 46$ for P3-drive; the two values are very similar, and we use their average in our analysis. The cavity decay rate $\kappa = \omega_r/Q_L$ can then be calculated. Both ω_r and κ are reported in Table 5.2.

5.6.5 Microwave Drive Energy & Cavity Photon Number

Drive Energy Upper Bound

While the analysis method used in the main text does not provide a precise measure of the qubit detuning drive amplitude ε_q, we can obtain a rough estimate by considering the microwave power applied in experiments. For the measurements reported in Fig. 5.3 of the main text, a microwave generator is used to apply a driving power of 6 dBm to the measurement circuit, which is configured with approximately 33 dB of attenuation at room temperature. The measurements in Figs. 5.4(a) and 4(b), use −5 to 6 dBm generator power and 33 dB room-temperature attenuation; those in Figs. 5.4(c) and 4(d) use 15 dBm of generator power and have 42 dB of room-temperature attenuation. For all measurements, an additional 40 dB of attenuation is incurred inside the cryostat. Furthermore, the quantum dot device is engineered with buried coplanar waveguide bias leads whose characteristic impedance is $Z_{0,\mathrm{g}} \approx 1\ \Omega$ [174]. Microwave attenuation at the bias leads has not been fully characterized; however, based on SPICE simulations of our device, we expect a minimum attenuation of 10 dB due to impedance mismatch between the leads and the 50 Ω coaxial cabling inside the cryostat. Summing the above contributions gives an estimated input power of $P_{\mathrm{in}} \lesssim -77$ dBm $= 20$ pW for all measurements.

When ac modulation is applied to plunger gate P3, the detuning drive amplitude is related to the input power by

$$\varepsilon_q \approx \varepsilon_3 = -\alpha_{\mathrm{P3},\varepsilon}\sqrt{2Z_{0,\mathrm{g}}P_{\mathrm{in}}}, \tag{5.34}$$

where $\alpha_{\mathrm{P3},\varepsilon}$ is the detuning lever arm, and the factor of $\sqrt{2}$ converts between rms and peak voltage amplitudes. Note that for this estimate, we ignore the small crosstalk correction proportional to (β_3/β_2) seen in Eq. (5.4). Equation (5.34) is not applicable for the measurements reported in Figs. 5.3(a) and 5.3(c). In those experiments, the gate S1 is driven through the $\lambda/4$ resonator segment, resulting in additional voltage attenuation. We estimate the re-

	Driving gate	P_{in} (pW)	ε_q/h (MHz)	ε_r/h (kHz)	$\langle n\rangle$
Fig. 5.3(a,c)	S1	20	27	340	30
Fig. 5.3(b,d)	P3	20	−137	397	41
Fig. 5.4(a,b)	P3	2 to 20	−39 to −137	119 to 424	4 to 46
Fig. 5.4(c,d)	P3	20	−152	447	51

Table 5.3: Upper-bound estimates for the ac detuning drive amplitude and cavity photon number computed in Section 5.6.5.

sulting ε_q values by multiplying the output of Eq. (5.34) by the ratio of best-fit parameters $(c\,\varepsilon_2)/(c\,\varepsilon_3)$ reported in Table 5.1. Thus for all experiments performed here, we estimate drive amplitudes of $|\varepsilon_q/h| \lesssim 152$ MHz, obtaining the full set of results listed in Table 5.3. These drive strengths are comparable to those used in similar qubit experiments [96].

We emphasize again that these values should be treated as approximate upper bounds due to the uncertainty in attenuation at the quantum dot bias leads.

Photon Number

The average number of photons populating the resonator $\langle n\rangle$ is given by the stationary value of the cavity coherent state $\tilde{\alpha}^{\text{st}}_{\pm}$. Squaring Eq. (5.20) gives

$$\langle n\rangle = |\tilde{\alpha}^{\text{st}}_{\pm}|^2 \approx \frac{4\varepsilon_r^2}{\hbar^2\kappa^2}. \tag{5.35}$$

Note that this quantity is dominated by the direct resonator drive, and we neglect small contributions from the couplings $g_{\parallel}^{\text{dy}}$ and $\delta\omega$. Using Eq. (5.5) and values from Tables 5.1 and 5.3 to compute ε_r, we estimate photon populations of $\langle n\rangle \lesssim 50$ for all measurements reported here. The full set of results are listed in Table 5.3.

The number of thermal photons in the resonator due to finite system temperature and blackbody radiation from resistive loads is of order $\langle n\rangle \sim 1$ [210]. This residual population should be negligible for most measurements, compared to photons produced by direct resonator drive.

	t_c/h (GHz)	$\delta\omega/2\pi$ (kHz)	$g_{\parallel}^{\mathrm{dy}}/2\pi$ (kHz, approx.)	$\lvert g_{\parallel}^{\mathrm{dy}}/\delta\omega\rvert$
Fig. 5.3(c)	6.1	4.9	12.1	2.5
Fig. 5.3(d)	6.1	4.9	−61.4	12.4
Fig. 5.4(a)(i)	5.6	5.4	−19.3	3.5
Fig. 5.4(a)(ii)	5.2	5.8	−45.7	7.9
Fig. 5.4(a)(iii)	5.9	5.1	−63.9	12.4
Fig. 5.4(d)(iv)	4.6	3.7	−67.6	18.4
Fig. 5.4(d)(v)	5.5	3.1	−57.0	18.4
Fig. 5.4(d)(vi)	6.5	2.6	−47.9	18.4

Table 5.4: Estimated energy coupling parameters for experiments reported in the main text. The tunnel coupling t_c is obtained from fitting; dot-cavity couplings $\delta\omega$ and $g_{\parallel}^{\mathrm{dy}}$ are computed according to Eqs. (5.14) and (5.15) using t_c and parameters from Tables 5.2 and 5.3. Note that the values for $g_{\parallel}^{\mathrm{dy}}$ are upper-bound approximations, based on the ε_q values reported in Table 5.3. The reported values all correspond to the peaks, centered at $\varepsilon_0 = 0$.

We have considered the impact of higher-order corrections to the curvature couplings that may become significant at large photon number [190]. For our system, we expect such corrections to be unimportant when $\langle n \rangle \lesssim 10^3 - 10^4$, due to the quantum-nondemolition nature of the curvature interactions and the fact that we work in the adiabatic coupling regime.

5.6.6 Calculated Energy Couplings

Using methods described here and in the main text, we obtain estimates for t_c, g_0, etc. In Table 5.4, we report these t_c values and the corresponding energy couplings, computed using Eqs. (5.14) and (5.15).

5.6.7 Additional Data: Direct Measurement of Dispersive-like Coupling

For all the figures shown in the main text, the dispersive coupling $\delta\omega$ was estimated from Eq. (5.15), where t_c values were obtained from the fitting analysis described in the main

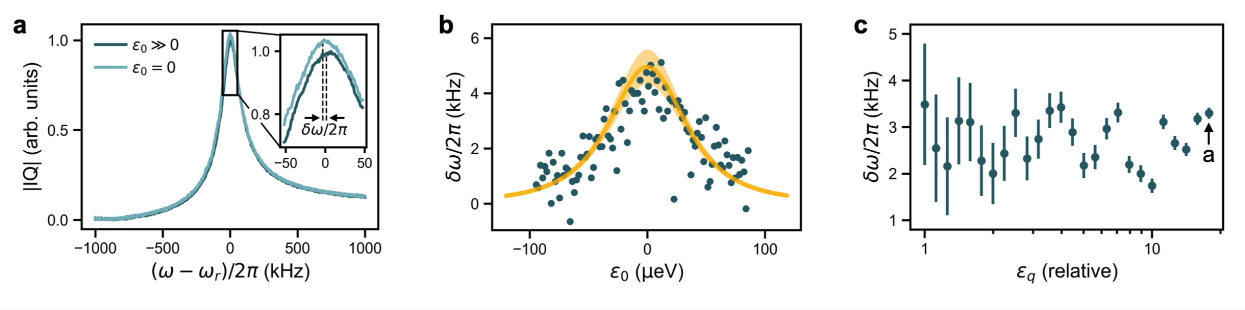

Figure 5.7: Direct measurements of the dispersive-like coupling from cavity resonance shifts, for an ac drive applied to gate P3. **(a)** Cavity transmission as a function of driving frequency $\omega/2\pi$, measured at the interdot charging transition ($\varepsilon_0 = 0$, lighter blue), and deep within the Coulomb blockade regime ($\varepsilon_0 \gg 0$, dark blue). Inset: zoomed-in view showing the small shift of the resonant peak due to the dispersive-like coupling $\delta\omega$. **(b)** Resonant peak shifts are obtained as a function of ε_0. The dark yellow curve and light yellow 1σ confidence interval show the prediction for $\delta\omega$, obtained from Eq. (5.15), using fitting results for t_c obtained in Fig. 5.3(d) of the main text. **(c)** Directly measured resonant frequency shifts plotted as a function of ac driving amplitude ε_q, in relative units. The data point corresponding to (a) is indicated with an arrow.

---

text, and g_0 was estimated using the geometrical parameters of the device. However, $\delta\omega$ can also be measured directly from the shift of the cavity resonance frequency, when the cavity is coupled to the double dot. Figure 5.7(a) shows a typical analysis, where the ac drive is applied to gate P3. Here, the dark blue cavity resonance peaks are obtained deep in the Coulomb blockade regime ($\varepsilon_0 \gg 0$), where the qubit-cavity coupling is tiny. The lighter-blue curve is obtained at the interdot charging transition ($\varepsilon_0 = 0$), where the coupling is strongest. Equation (5.15) gives a prediction for the state-dependent frequency shift, which is analogous to the effect of χ in the conventional dispersive regime. The blown-up peaks (inset) show the frequency shift caused by the dispersive-like coupling, with $\delta\omega/2\pi \approx 3.3$ kHz. In the ultra-dispersive limit, such shifts are found to be much smaller than the resonant linewidth. We note that the double dot remains in its ground state for all experiments in this work, so the direction of the resonance shift caused by the coupling is always toward lower frequencies.

This peak-shift analysis is repeated for different detuning values about the interdot charging transition, as shown in Fig. 5.7(b). Here, the experimental tuning is the same tuning used for Figs. 5.3(b) and 5.3(d) of the main text. (Note that, although the measured frequency shifts are actually negative, we plot their absolute value here, since $\delta\omega$ is defined as a positive quantity in Section 5.6.1.) We note that the yellow curve shown in the figure is not a fit; rather, it shows the *predicted* frequency shift obtained from Eq. (5.15), using the t_c values obtained from the fit shown in Fig. 5.3(d) of the main text. Here, the lighter yellow shading corresponds to the 1σ confidence interval, estimated from parameter uncertainties of the fitting algorithm. The good agreement between the direct measurement and the theoretical prediction supports our theoretical interpretation of the results and validates our fitting methods.

Finally, in Fig. 5.7(c), we show the experimentally measured frequency shifts as a function of the ac driving strength ε_q. Here, the specific data point corresponding to Fig. 5.7(a) is indicated by the arrow. While some spread is observed in the data, we observe no systematic variation of $\delta\omega$, which agrees with the conclusions of Fig. 5.4(b) of the main text. We note however that the two data sets were acquired at different device tunings, and therefore are not directly related.

5.6.8 Additional Data: Low-Barrier-Voltage Behavior

The fitting results reported in Table 5.4 confirm that smaller t_c values yield larger absolute values of $g_{\parallel}^{\mathrm{dy}}$, as desired for strong qubit-resonator couplings. In this section, we explore the possibility of extending the data in Fig. 5.4(c) of the main text to lower t_c values.

Figure 5.8(a) shows results of such an analysis, which includes all the data shown in Fig. 5.4(c), but also includes data obtained at lower values of V_{B3}, where we expect to observe lower t_c values. Using the same IQ peak-fitting procedure as in Fig. 5.4(d), we also determine the corresponding t_c values for this data, as reported in Fig. 5.8(b). The data reveal surprising behavior that is inconsistent with a continuous downward trend of t_c, in the low-V_{B3} regime. Indeed, for V_{B3} values below those reported in Fig. 5.4(c), the t_c results remain roughly constant, but exhibit distinct nonmonotonic features.

To explain this behavior, we note that lower V_{B3} values should yield larger tunnel barriers

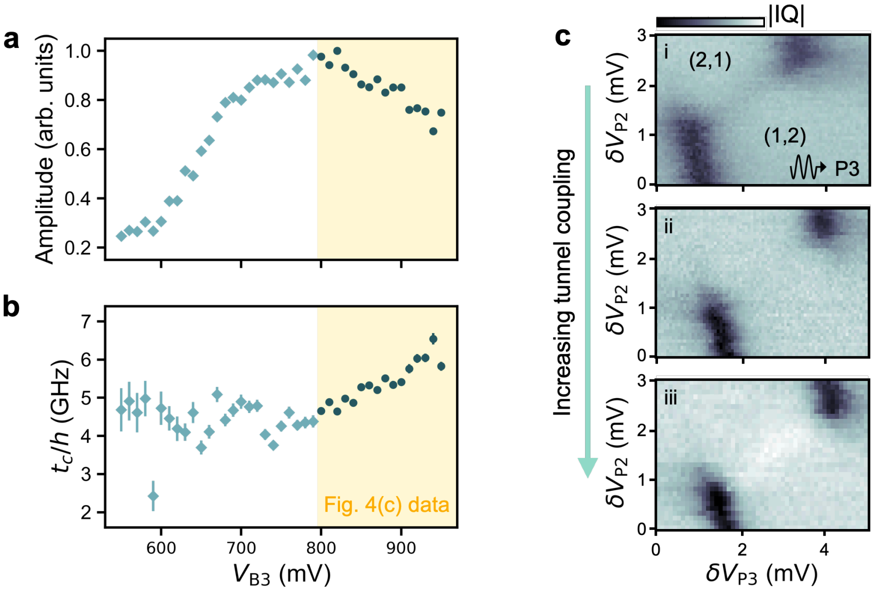

Figure 5.8: Cavity transmission responses measured for P3 driving near the interdot charging transition, extending the data set in Fig. 5.4(c) of the main text to lower V_{B3} values. **(a)** Cavity transmission peak amplitudes, extracted by fitting transmission peaks to Lorentzian forms as a function of dc barrier voltage V_{B3}. The data have been normalized so that the largest measured amplitude corresponds to 1 arbitrary unit. Error bars are smaller than the markers. **(b)** Tunnel coupling t_c as a function of V_{B3} estimated from transmission peak fits to Eq. (5.26). The low-t_c outlier at $V_{B3} = 590$ mV is believed to be the result of electrostatic instability during the measurement of that trace. In both (a) and (b), the dark teal circle markers at $V_{B3} \geq 800$ mV correspond to data shown in Fig. 5.4(c) of the main text; light teal diamond markers at $V_{B3} < 800$ mV show an extended data set discussed in Section 5.6.8. **(c)** Three other device tunings, measured in sequence, and measured separately from the data in (a) and (b). Moving from (i) to (iii), the response changes from a dip in (i) to a peak in (iii), passing through a region of no response, (ii).

---

between dots 2 and 3. Such behavior is not observed in Fig. 5.8(b). Instead, the data are consistent with raising the tunnel barrier so far that the dots are squeezed out the top side of the gated region, in the device shown in Fig. 5.2(d) of the main text. This can occur here because no screening gate is present in the top portion of the device, and the dots are therefore more weakly confined in this region. The distinct features observed in Fig. 5.8(b) are likely caused by first one, then the other of the dots being squeezed out of its intended location. The sudden drop of amplitude in Fig. 5.8(a), at $V_{B3} \approx 700$ mV, correlates with the onset of the rightmost bump feature in Fig. 5.8(b). We speculate that this occurs when dot

3 leaves its intended confinement location, resulting in a sudden reduction of the lever arm between dot 3 and gate P3; in turn, this causes a sudden drop in the driving amplitude, ε_3.

To summarize, reducing V_{B3} below 800 mV in this device does not appear to cause the intended effect of lowering t_c. The IQ peak-fitting results in this regime are therefore meaningless, because the fitting equations do not include the relevant physics. We emphasize, however, that such behavior occurs here, only because of the device geometry, and would not be expected to occur in a device with an additional, top screening gate. It is therefore important to explore the possibility of lowering t_c values in future experiments. We also note that intentionally shifting the lateral positions of the quantum dots may provide additional means for tuning $g_{\parallel}^{\mathrm{dy}}$ and $\delta\omega$ independently.

5.6.9 Additional Data: Cavity Drive via a Second On-Chip Device

Charge sensing in the main text is performed by applying an ac drive to device gates S1 or P3. We are also able to charge sense by driving the plunger gate of a second, unaccumulated quantum dot device on the qubit die. The second device is nominally identical to the qubit device used in main-text experiments with an upper screening gate connected to the same microwave resonator, as shown in Fig. 5.9(a). The ac drive excites the cavity and modulates the S1 gate voltage. Charge stability diagrams acquired with this technique, therefore, look very similar to those acquired when driving S1, with a dip in the IQ signal at the polarization line. Figure 5.9(b) shows a stability diagram acquired at the same tuning as the Fig. 5.3 measurements. The line cut in Fig. 5.9(c) shows the cavity response near the charge degeneracy point.

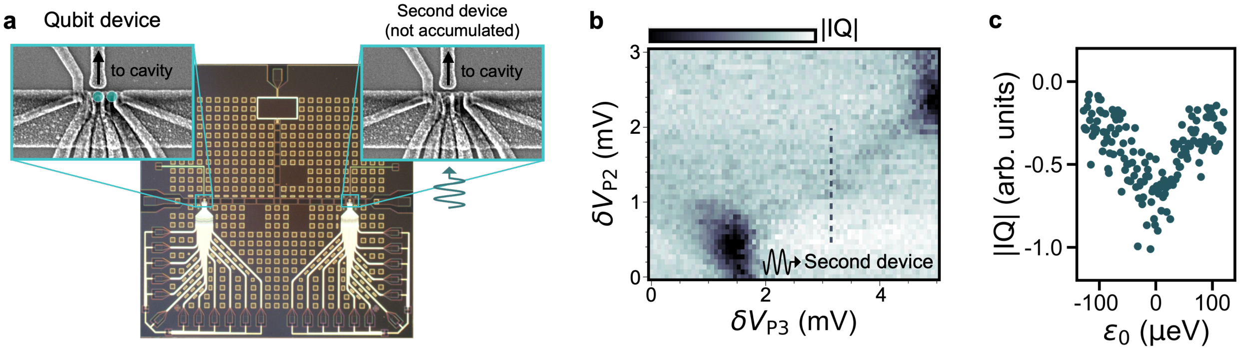

Figure 5.9: Cavity drive via a second on-chip device. **(a)** Dark-field optical micrograph of the qubit die with two quantum dot devices located in the blue boxed regions. Scanning electron micrographs of the nominally identical devices are also shown. A 1.3 GHz microwave drive applied to the center plunger gate of the right-side device excites the resonator and can be used for charge sensing. **(b)**IQ transmission measurement of the double dot tuned to its (2,1) – (1,2) charge occupation transition while driving the cavity via the second device plunger. **(c)** Line cut across the interdot charge transition indicated in (b). Resonator transmission is suppressed at the charge degeneracy point. The scaling used for the arbitrary units here is the same used in Fig. 5.3.

5.6.10 Additional Data: Transmission Enhancement at Other Electron Occupations

Main-text experiments are performed at the (2,1) – (1,2) charge configuration. However, we have observed resonator transmission enhancement at several additional interdot transitions when longitudinal coupling is activated via the P3 drive. The large charge stability diagram in Fig. 5.10(a) shows enhanced transmission for at least four transitions: (2,1) – (1,2); (3,1) – (2,2); (2,2) – (1,3); and (3,2) – (2,3). Higher-resolution scans at the latter three transitions are shown in Fig. 5.10(b). We note that some transitions in Fig. 5.10(a) appear to show suppressed transmission [e.g., (4,0) – (3,1)], while others have no visible polarization line [e.g., (1,1) – (0,2)]. We believe this variation in resonator response is strongly dependent on tunnel coupling for each configuration, as discussed in the main text. It may further depend on multi-electron states for some charge occupations; this topic lies beyond the scope of our analysis.

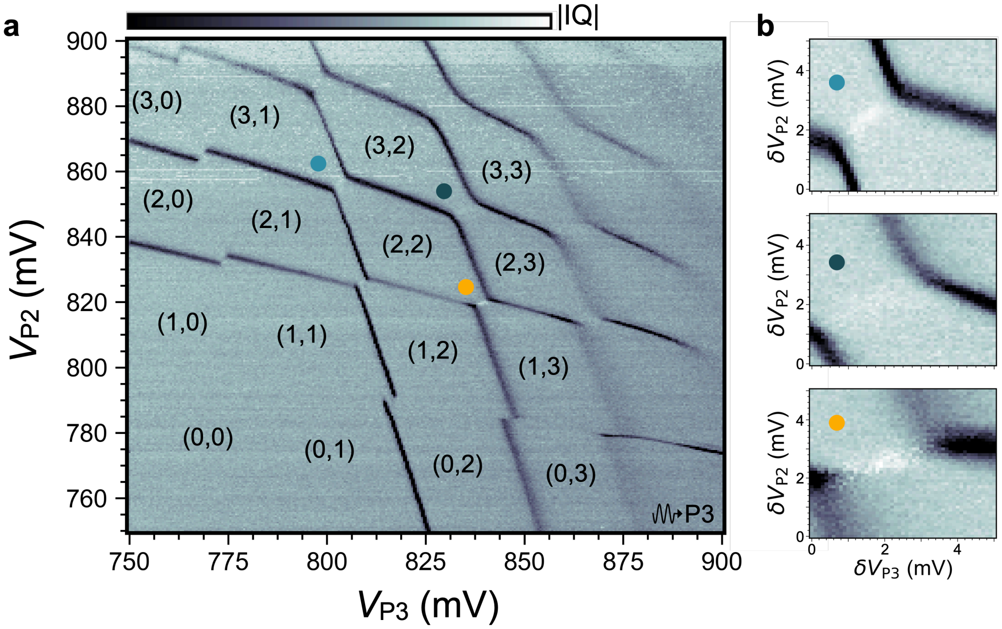

Figure 5.10: Enhanced transmission at several charge occupations. (a) Large-scale charge stability diagram for the double quantum dot. Experiments in the main text are performed at the (2,1)-(1,2) charge occupation. Enhanced resonator transmission is also visible at several polarization lines for the same tuning. (b) Zoomed-in stability diagrams showing enhanced resonator transmission at the polarization lines. Colored circles correspond to matching circles in (a), which indicate the voltage-space location for each scan. All plots are acquired at the same barrier and screening-gate voltage tunings. Color scale is the same as in (a).

5.7 Device Fabrication & Experimental Setup

Detailed information regarding fabrication of the flip-chip device and the measurement circuit used for experiments performed in this work can be found in Ref. [174].

Chapter 6

Ultra-Dispersive Qubit Readout Using Longitudinal Coupling

This chapter is under review for publication, and is available as a preprint manuscript: **Benjamin Harpt***, J. Corrigan*, Nathan Holman, Piotr Marciniec, D. Rosenberg, D. Yost, R. Das, Rusko Ruskov, Charles Tahan, William D. Oliver, R. McDermott, Mark Friesen, and M. A. Eriksson. *Ultra-dispersive resonator readout of a quantum-dot qubit using longitudinal coupling.* arXiv:2407.08869 (2024).

We perform readout of a quantum-dot hybrid qubit coupled to a superconducting resonator through a parametric, longitudinal interaction mechanism. Our experiments are performed with the qubit and resonator frequencies detuned by ~ 10 GHz, demonstrating that longitudinal coupling can facilitate semiconductor qubit operation in the 'ultra-dispersive' regime of circuit quantum electrodynamics.

6.1 Introduction

Coupling semiconductor qubits to superconducting resonators using circuit quantum electrodynamics (cQED) techniques is an important element in proposed quantum computing architectures [40,160]. Transverse coupling schemes based on qubit-resonator photon exchange are conventionally studied for this purpose. However, the transverse interaction becomes weak when the qubit and resonator frequencies are far from resonance, which could constrain operation protocols for large-scale processors. Longitudinal interactions offer an intriguing alternative for quantum coupling, as they do not require frequency resonance [188]. These couplings have attracted growing attention, and although they have recently been observed in semiconductor-qubit systems [204, 211, 212], they have not yet been utilized to extend device functionality. Here, as an initial use case for longitudinal coupling in quantum-dot qubits, we demonstrate excited-state resonator readout and spectroscopy at qubit frequencies far beyond the typical cQED operating range.

6.2 Ultra-Dispersive Qubit-Resonator Coupling

Experiments are performed using a Si/SiGe quantum-dot qubit device coupled to an off-chip, TiN microwave resonator. The qubit and resonator are fabricated on separate dies and vertically integrated in a flip-chip architecture, shown in Fig. 6.1(a) [174,211]. Figure 6.1(b) shows a scanning electron micrograph of a nominally-identical device with a simplified schematic of the measurement circuit. A double quantum dot (DQD) formed under plunger gates P2 and P3 is coupled to the resonator field through capacitance with gate C; the estimated charge-photon coupling rate is $g_c/2\pi \approx 3.2$ MHz.

During experiments, a continuous ac drive is applied to P3 at the resonator fundamental-mode frequency of $\omega_r/2\pi \approx 1.304$ GHz. This drive modulates the DQD energy detuning adiabatically with amplitude $\tilde{\varepsilon}$, activating a dynamic longitudinal coupling with the resonator photons [188, 190, 204, 211, 212]. The effective interaction Hamiltonian is

$$\tilde{H}_{\parallel} = \hbar\, \tilde{g}_{\parallel}^{0} \cos\left(\omega_r t\right) \hat{\sigma}_z \left(\hat{a} + \hat{a}^{\dagger}\right), \tag{6.1}$$

where $\tilde{g}_{\parallel}^{0}$ denotes the coupling strength, $\hat{\sigma}_z$ is the Pauli-z operator in the qubit energy basis, and $\hat{a}$ and $\hat{a}^{\dagger}$ are photon annihilation and creation operators. The coupling $\tilde{g}_{\parallel}^{0}$ gives

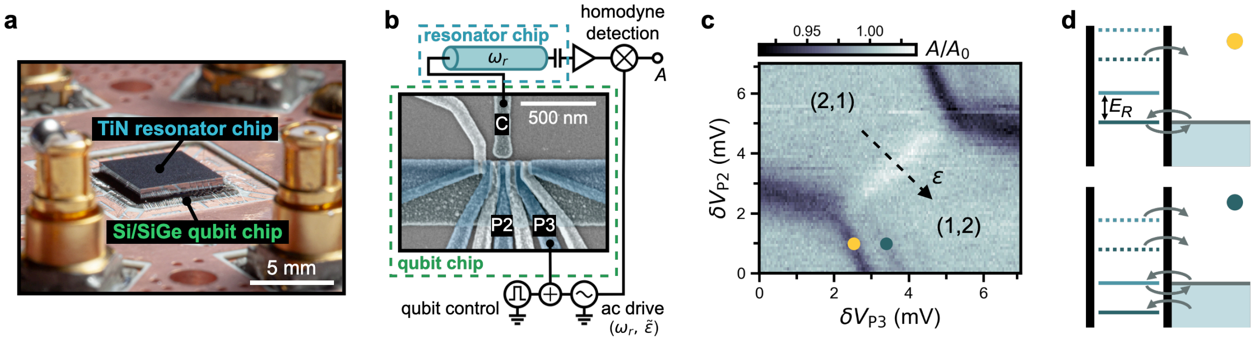

Figure 6.1: Pulsed-gate spectroscopy of a 3D DQD-resonator device. **(a)** Photo of the packaged sample, comprising a Si/SiGe quantum-dot qubit device and TiN microwave resonator integrated in a flip-chip architecture. **(b)** Simplified circuit schematic for experiments. A false-color, scanning electron micrograph of a quantum-dot device nominally identical to the one used in experiments is shown. A DQD is formed under gates P2 and P3 and capacitively coupled to the off-chip resonator via gate C. Qubit control pulses and an ac drive at frequency ω_r are applied to P3 (dc voltage sources are not shown). The resonator transmission amplitude A is measured using homodyne detection. **(c)** Normalized transmission amplitude A/A_0 measured as a function of dc plunger voltages V_{P2} and V_{P3} near the (2,1) – (1,2) charge transition. A pulsed gate voltage is applied for spectroscopy of the right dot. Reservoir tunneling resonances with the lowest two energy states are marked with yellow and teal circles. **(d)** Energy level configurations corresponding to the equipotentials marked in (c). The dot's energy levels are cycled between lower (solid) and upper (dashed) positions by the alternating-voltage waveform. Arrows indicate electron tunneling pathways between the dot and reservoir.

---

rise to a qubit-state-dependent resonator drive, which can be measured through changes in its stationary field amplitude. Figure 6.1(c) shows the normalized resonator transmission amplitude A/A_0 measured near the (2,1) – (1,2) interdot charge transition. The axis for DQD detuning ε is indicated, where the total detuning, $\varepsilon(t) = \varepsilon_0 + \tilde{\varepsilon}\cos(\omega_r t)$, includes a dc component ε_0. The normalization constant A_0 is defined by the transmission level at $\varepsilon_0 \gg 0$. A boost in A/A_0 measured around $\varepsilon_0 = 0$ is a telltale indicator of $\tilde{g}_{\parallel}^{0}$ coupling the DQD to the resonator for this measurement configuration, as shown in Chapter 5.

In the following experiments, we operate our device as a quantum-dot hybrid qubit (QDHQ) [206, 207, 213–216]. The qubit excitation frequency at $\varepsilon_0 = 0$ in Fig. 6.1(c) is $\omega_q/2\pi \approx 2\Delta_1/h = 14.6 \pm 1.2$ GHz, where the interdot tunnel coupling Δ_1 is extracted through fits to the resonator transmission peak (see Section 6.5.2 for further details). At large $|\varepsilon_0|$, ω_q is set by the left- or right-dot singlet-triplet splitting, E_L or E_R. We measure E_R using time-averaged pulsed-gate spectroscopy [217], with an alternating-voltage waveform applied to P3. Reservoir tunneling resonances for the ground and first-excited states are marked in Fig. 6.1(c) with yellow and teal circles, respectively. These resonances occur along equipotentials where a dot energy level aligns with the reservoir Fermi energy, as depicted in Fig. 6.1(d). From the voltage splitting between resonances, we estimate $E_R/h = 34.8 \pm 1.2$ GHz $\approx \omega_q/2\pi$ for $\varepsilon_0 \gg 0$ (see Section 6.5.2). We note that the magnitude of $\tilde{\varepsilon}$ is kept much smaller than $\hbar\omega_q$ and all tunnel couplings for our measurements, so the ac drive cannot excite the qubit.

The above measurements demonstrate operation in the 'ultra-dispersive' coupling regime, which we define by the condition $g_c \ll \omega_r \ll \omega_q$. Dynamic longitudinal coupling is an important mechanism for working in this regime; through parametric driving, its coupling strength, $\tilde{g}_{\parallel}^0 \propto (\partial^2 E_q/\partial\varepsilon^2)\,\tilde{\varepsilon}$, where $(\partial^2 E_q/\partial\varepsilon^2)$ is the qubit's energy curvature, can be made significantly larger than the effective transverse coupling, which is considerably weakened at $\omega_q \gg \omega_r$ [190, 211, 212, 218]. For this work, we estimate longitudinal coupling to be the dominant interaction by an order of magnitude (see Section 6.5.3), and in the experiments below, we show how this coupling can be used for QDHQ state readout in the ultra-dispersive regime.

6.3 Qubit Readout & Spectroscopy

Figure 6.2(a) illustrates the QDHQ energy levels and a two-step qubit control sequence with fast voltage pulses applied to P3. The logical states $|0\rangle$ and $|1\rangle$ and leakage state $|2\rangle$ are defined as energy eigenstates for the lowest three levels. In the first control step [panel (i)], ε_0 is pulsed from ε_m to ε_p for an interval of $t_{\text{pulse}} = 2$ ns. The detuning amplitude of the pulse is given by $\varepsilon_{\text{pulse}} = \varepsilon_p - \varepsilon_m$. As the pulse shuttles the qubit through the $|0\rangle - |1\rangle$ energy anticrossing at $\varepsilon_0 = 0$, fractional excited-state occupation is generated through

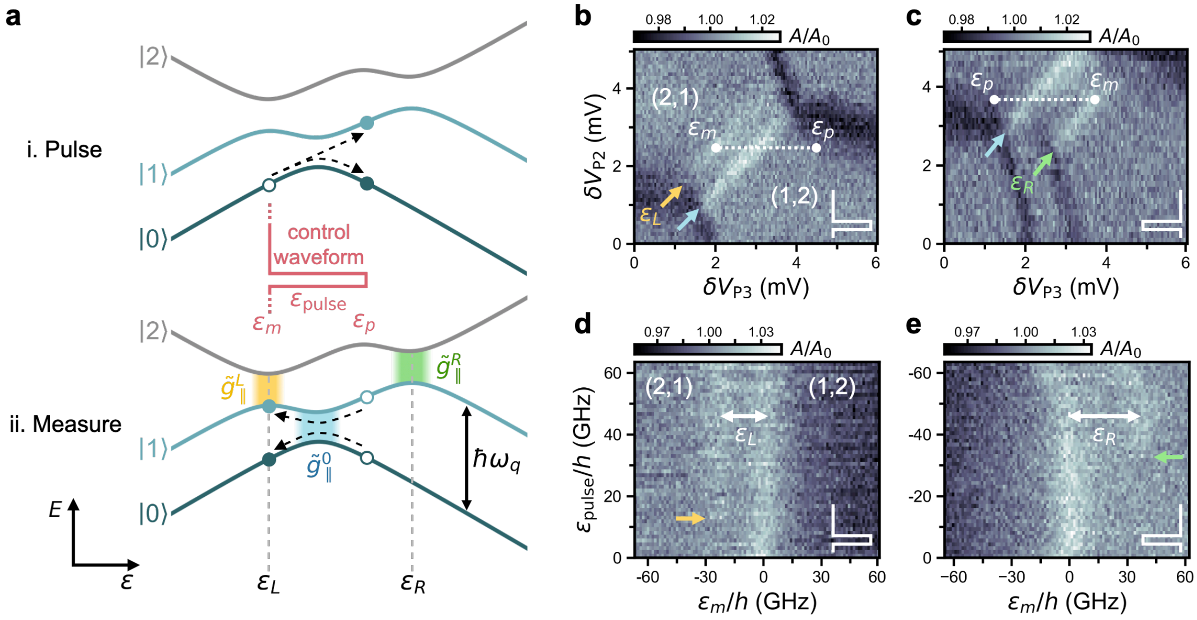

Figure 6.2: QDHQ readout and spectroscopy using longitudinal coupling. **(a)** QDHQ energy level diagram and qubit control scheme. The pulsed voltage waveform is applied to P3. Dashed lines illustrate qubit dynamics and state transitions. **(b,c)** A/A_0 measured as a function of dc voltages $V_{\rm P2}$ and $V_{\rm P3}$ with positive-amplitude [panel (b)] and negative-amplitude [panel (c)] control pulses applied simultaneously. Dashed white lines indicate the scale of detuning pulses. Signal boosts marked with arrows are from longitudinal coupling at the corresponding-color (blue, yellow, and green) anticrossings in (a). **(d,e)** A/A_0 as a function of measurement detuning ε_m and pulse amplitude $\varepsilon_{\rm pulse}$. Arrows highlight $|1\rangle$-state occupation thresholds. The $|1\rangle - |2\rangle$ energy anticrossing detunings ε_L and ε_R can be estimated from the distance between transmission peaks.

Landau-Zener transitions [99,219]. In the second control step [panel (ii)], ε_0 is pulsed back to ε_m and maintained there for a measurement time of $t_{\rm meas} = 48$ ns. Qubit-resonator coupling during this interval generates the transmission signal used for readout. We note that no coherent oscillations are observed in our measurements, likely because the manipulation scheme frequently involves idling in the detuning range $\Delta_1 < |\varepsilon_0| < E_{L(R)}$, where the qubit is highly susceptible to charge noise [207, 214]. The control protocol can be easily modified to avoid these detuning zones in future experiments.

The above pulse sequence is cycled while simultaneously sweeping the dc voltages $V_{\rm P2}$ and $V_{\rm P3}$ near the (2,1) – (1,2) transition. Figures 6.2(b) and 6.2(c) show time-averaged A/A_0 measurements with opposite-amplitude pulses applied, $\varepsilon_{\rm pulse}/h \approx 63$ GHz and -63 GHz, respectively; these amplitudes are indicated by dashed white lines. In both plots, a peak in A/A_0 is visible at $\varepsilon_m = 0$ (blue arrows), where the adiabatic qubit modulation near the heightened energy curvature of the $|0\rangle - |1\rangle$ anticrossing enlarges $\tilde{g}_{\parallel}^{0}$ [190, 211]. Additional boosts in A/A_0 at $|\varepsilon_m| \neq 0$ (yellow and green arrows) are the result of resonator coupling through occupation of the first excited state. These features are caused by qubit modulation near a $|1\rangle - |2\rangle$ anticrossing at $\varepsilon_m = \varepsilon_L$ [Fig. 6.2(b)] or $\varepsilon_m = \varepsilon_R$ [Fig. 6.2(c)], activating an excited-state coupling channel, which we label $\tilde{g}_{\parallel}^{L}$ and $\tilde{g}_{\parallel}^{R}$, respectively. DQD-resonator coupling involving excited silicon valley states has been observed previously, but was mediated through the transverse interaction [220]; the A/A_0 peak in our measurements is the key signature of longitudinal coupling.

A crucial feature of the couplings $\tilde{g}_{\parallel}^{L}$ and $\tilde{g}_{\parallel}^{R}$ is that they are only active when the logical state $|1\rangle$ is populated. As a consequence, the resonator transmission signal observed at ε_L or ε_R reflects the qubit's time-averaged $|1\rangle$ occupation. Figures 6.2(d) and 6.2(e) show experiments demonstrating that this signal can be used to detect the qubit state. The A/A_0 peaks are measured as a function of ε_m and $\varepsilon_{\text{pulse}}$. For small pulse amplitudes ($|\varepsilon_{\text{pulse}}| \ll |\varepsilon_{L(R)}|$), the qubit's prepared state is $|0\rangle$, and no signal boost occurs at $\varepsilon_{L(R)}$. When the control pulse becomes large enough to generate excitation into $|1\rangle$, the prepared state is no longer $|0\rangle$, and the signal at $\varepsilon_{L(R)}$ increases via the excited-state resonator coupling $\tilde{g}_{\parallel}^{L(R)}$. In our measurements, the ε_L peak in Fig. 6.2(d) becomes visible at a threshold amplitude of $\varepsilon_{\text{pulse}}/h \approx 13$ GHz (yellow arrow), and the ε_R peak in Fig. 6.2(e) appears at $\varepsilon_{\text{pulse}}/h \approx -33$ GHz (green arrow). The dependence of the signal at ε_L or ε_R on the qubit's prepared state implies that QDHQ readout can be performed at these working points using longitudinal coupling.

The data in Fig. 6.2 contain spectroscopic information about the qubit's energy parameters. Using these measurements and additional numerical analysis methods outlined in Section 6.5.2, we are able to reconstruct the full QDHQ Hamiltonian and compute the qubit frequency. We estimate $\omega_q/2\pi = 20.6 \pm 0.6$ GHz and 32.4 ± 2.9 GHz at the ε_L and ε_R

readout operating points. This affirms the ultra-dispersive nature of our experiments, since qubit-resonator detuning in this regime, $\Delta = |\omega_q - \omega_r| \sim 2\pi \times 10$ GHz, is one to three orders of magnitude larger than typically used for dispersive-cQED experiments [157, 167, 177, 178].

6.4 Discussion

The experiments above outline a method for ultra-dispersive QDHQ readout based on longitudinal coupling. This approach differs from charge-based QDHQ readout [207, 213–216], as well as from dispersive readout using transverse coupling, which has been demonstrated with other spin qubit encodings [157, 167, 221]. In comparison, our method offers several potential benefits for qubit operation, which can be explored in future experiments. First, it implements, in principle, a quantum-nondemolition measurement, as $\tilde{H}_{\parallel}$ [Eq. (6.1)] commutes with the qubit Hamiltonian [190, 222]. Second, it requires no qubit-resonator photon exchange, minimizing pathways for Purcell decay [154] and measurement-induced dephasing [191] intrinsic to transverse interactions [188]. As a result, it is possible to operate at higher photon populations without perturbing the qubit, facilitating fast and high-fidelity readout [189, 192]. We also expect the probability of state transitions due to the ac qubit drive to be low, provided that it is weak and adiabatic. Third, our readout is performed at DQD detuning points where qubit relaxation involves a slow spin-flip mechanism, which may provide a T_1 advantage compared to reading out at the $\varepsilon_0 = 0$ measurement point, where no spin flip is required. We emphasize that slow qubit relaxation could be helpful for improving measurement fidelity and achieving single-shot readout in near-term experiments, where relatively weak coupling may necessitate longer integration times. Finally, our technique works in the ultra-dispersive regime, where transverse coupling is suppressed. Our work demonstrates that qubits can be measured through longitudinal interactions while far-detuned from the readout resonator, allowing space for a wide range of qubit frequencies. Longitudinal coupling, therefore, is a promising tool for mitigating engineering bottlenecks and scaling quantum processors.

Acknowledgements

The authors thank HRL Laboratories for support and L. F. Edge for providing the Si/ $Si_{1-x}Ge_x$ heterostructure used in this work. This research was sponsored in part by the Army Research Office under Awards No. W911NF-17-1-0274 and No. W911NF-23-1-0110. J. C. acknowledges support from the U. S. National Science Foundation Graduate Research Fellowship Program under Grant No. DGE-1747503 and the Graduate School and the Office of the Vice Chancellor for Research and Graduate Education at the University of Wisconsin-Madison with funding from the Wisconsin Alumni Research Foundation. The authors acknowledge the use of facilities supported by the National Science Foundation through the University of Wisconsin-Madison Materials Research Science and Engineering Center (Grant No. DMR-2309000) and the Major Research Instrumentation (MRI) program (Grant No. DMR-1625348). This material is based in part upon work supported by the Under Secretary of Defense for Research and Engineering under Air Force Contract No. FA8702-15-D-0001. Any opinions, findings, conclusions, or recommendations expressed in this material are those of the author(s) and do not necessarily reflect the views of the Under Secretary of Defense for Research and Engineering and are not necessarily endorsed by nor should they be interpreted as representing the official policies, either expressed or implied, of the Army Research Office or the U. S. Government. The U. S. Government is authorized to reproduce and distribute reprints for U. S. Government purposes notwithstanding any copyright notation herein.

6.5 Supplementary Information

These supplemental materials provide additional data and details about the methods used in this work.

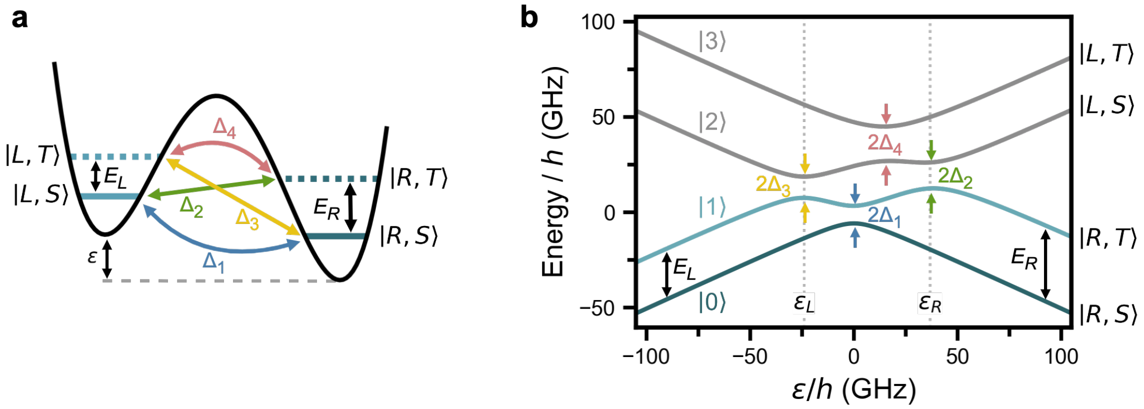

Figure 6.3: QDHQ states and energy levels. **(a)** Electrostatic potential for a three-electron DQD. Quantum-dot energy levels are labeled corresponding to the basis states of Eq. (6.2); the third electron's level occupation determines the state of the system in this basis. E_L and E_R denote the singlet-triplet splitting for each dot, and Δ_1 through Δ_4 are interdot tunnel couplings. **(b)** Energy levels of the system in (a) as a function of ε. Qubit logical-state levels are colored teal. The energy eigenstates $|0\rangle$ through $|3\rangle$ are asymptotically equal to the basis states in Eq. (6.2) at large $|\varepsilon|$. Detuning values of the $|1\rangle$ – $|2\rangle$ anticrossings are labeled ε_L and ε_R.

6.5.1 Qubit Hamiltonian & Logical States

The QDHQ combines the charge and spin degrees of freedom of a three-electron DQD depicted in Fig. 6.3(a). The DQD is operated with two electrons in one dot and a single electron in the other dot. In the absence of tunnel coupling, the eigenstates of the four-level system pictured can be defined in the charge-spin basis:

$$\begin{aligned} |L,S\rangle &\equiv |S\rangle\,|{\downarrow}\rangle\,; \qquad & |L,T\rangle &\equiv \sqrt{\frac{1}{3}}\,|T_0\rangle\,|{\downarrow}\rangle - \sqrt{\frac{2}{3}}\,|T_-\rangle\,|{\uparrow}\rangle\,; \\ |R,S\rangle &\equiv |{\downarrow}\rangle\,|S\rangle\,; \qquad & |R,T\rangle &\equiv \sqrt{\frac{1}{3}}\,|{\downarrow}\rangle\,|T_0\rangle - \sqrt{\frac{2}{3}}\,|{\uparrow}\rangle\,|T_-\rangle\,. \end{aligned} \tag{6.2}$$

In these definitions, $|S\rangle \equiv (|{\uparrow\downarrow}\rangle - |{\downarrow\uparrow}\rangle)/\sqrt{2}$ is the spin-singlet state, while $|T_0\rangle \equiv (|{\uparrow\downarrow}\rangle + |{\downarrow\uparrow}\rangle)/\sqrt{2}$ and $|T_-\rangle \equiv |{\downarrow\downarrow}\rangle$ are spin-triplet states of the doubly-occupied dot; $|{\uparrow}\rangle$ and $|{\downarrow}\rangle$ denote spin-up and spin-down electrons in the singly-occupied dot.

The bare (i.e., undressed) DQD Hamiltonian in the charge-spin basis ordered $\{|L,S\rangle\,,$

$|L,T\rangle, |R,S\rangle, |R,T\rangle\}$ is

$$H_q = \begin{pmatrix} \varepsilon/2 & 0 & \Delta_1 & -\Delta_2 \\ 0 & \varepsilon/2 + E_L & -\Delta_3 & \Delta_4 \\ \Delta_1 & -\Delta_3 & -\varepsilon/2 & 0 \\ -\Delta_2 & \Delta_4 & 0 & -\varepsilon/2 + E_R \end{pmatrix}, \tag{6.3}$$

where E_L and E_R are the singlet-triplet energy level splittings in the left and right dot, respectively. There are four interdot tunnel coupling parameters, denoted Δ_1 through Δ_4, which lead to hybridization of the eigenstates in Eq. (6.2). Figure 6.3(b) plots the energy levels of H_q as a function of ε for our device, with parameter values derived in the following sections. For this work, we define the qubit logical states $|0\rangle$ and $|1\rangle$ as the two lowest-energy eigenstates of H_q [teal-colored energy levels in Fig. 6.3(b)]. At large DQD detuning, these logical states are asymptotically equal to the basis states in Eq. (6.2).

6.5.2 Qubit Spectroscopy Analysis Methods

The following sections describe analysis procedures used for estimating the QDHQ energy parameters. Before plotting or analysis, all data are normalized by the constant A_0, which denotes the transmission amplitude measured with the DQD in Coulomb blockade. A_0 is determined independently for each dataset. The estimated values and uncertainties of all parameters are summarized in Table 6.1 below.

Quantum-dot gate lever arms

The device gate lever arms convert changes in gate voltage to calibrated movement of the quantum-dot chemical potentials, and are used throughout the analyses below. We measure gate-to-dot lever arms from the thermal broadening of reservoir tunneling transition lines, as detailed in Section 5.6.4, obtaining $\alpha^L_{\mathrm{P2}} \equiv |\partial\mu_L/\partial V_{\mathrm{P2}}| = 0.140 \pm 0.005$ eV/V and $\alpha^R_{\mathrm{P3}} \equiv |\partial\mu_R/\partial V_{\mathrm{P3}}| = 0.149 \pm 0.003$ eV/V, where μ_L and μ_R are the chemical potentials of the left and right dot. The DQD detuning lever arms for gates P3 and C are calculated using the slopes of reservoir transitions in two-dimensional voltage sweeps:

$$\alpha^{\varepsilon}_{\mathrm{P3}} \equiv \frac{\partial \varepsilon_0}{\partial V_{\mathrm{P3}}} = \alpha^{R}_{\mathrm{P3}} - \alpha^{L}_{\mathrm{P2}} \left|\frac{\delta V_{\mathrm{P2}}}{\delta V_{\mathrm{P3}}}\right|_{L} = 0.105 \pm 0.005\ \mathrm{eV/V}; \tag{6.4}$$

$$\alpha^{\varepsilon}_{\mathrm{C}} \equiv \left|\frac{\partial \varepsilon_0}{\partial V_{\mathrm{C}}}\right| = \alpha^{L}_{\mathrm{P2}} \left|\frac{\delta V_{\mathrm{P2}}}{\delta V_{\mathrm{C}}}\right|_{L} - \alpha^{R}_{\mathrm{P3}} \left|\frac{\delta V_{\mathrm{P3}}}{\delta V_{\mathrm{C}}}\right|_{R} = 0.023 \pm 0.004\ \mathrm{eV/V}. \tag{6.5}$$

In these equations, the quantity $|\delta V_i/\delta V_j|_{L(R)}$ represents the slope of a left-dot (right-dot) reservoir transition in (V_j, V_i) parameter space. The values of all lever arms are found to remain roughly constant between the main-text device tunings of Fig. 6.1(c) and Fig. 6.2.

Interdot tunnel couplings & $|1\rangle - |2\rangle$ anticrossing detunings: $\boldsymbol{\Delta_1}$, $\boldsymbol{\Delta_2}$, $\boldsymbol{\Delta_3}$, $\boldsymbol{\varepsilon_L}$, $\boldsymbol{\varepsilon_R}$

The interdot tunnel coupling parameters can be extracted by fitting the resonator transmission peaks generated by longitudinal coupling at the QDHQ energy anticrossings. Figure 6.4(a) shows an A/A_0 peak acquired near the $|0\rangle - |1\rangle$ anticrossing at the same device tuning used for Fig. 6.1(c) of the main text. We do not apply any control pulses during this measurement; consequently, the DQD remains in its ground state, and can be modeled as a single-electron charge qubit with tunnel coupling Δ_1. Following the derivation in Section 5.6.2, the transmission response for a resonator interacting with the ac-driven charge qubit is given by

$$\frac{A}{A_0} = \frac{1 - \hbar\, \tilde{g}^{0}_{\parallel}/2\, \beta\, \tilde{\varepsilon}}{\sqrt{1 + (2\, \delta\omega_0/\kappa)^2}}, \tag{6.6}$$

where $\tilde{g}^{0}_{\parallel} = -4 g_c \Delta_1^2 \tilde{\varepsilon}/E^3_{\mathrm{cq},0}$ and $\delta\omega_0 = 8\hbar g_c^2 \Delta_1^2/E^3_{\mathrm{cq},0}$ are dynamic longitudinal and dispersive transverse coupling strengths, and $E_{\mathrm{cq},0} = \sqrt{\varepsilon_0^2 + 4\Delta_1^2}$ is the bare charge qubit excitation energy. The constant β parameterizes direct excitation of the resonator through gate capacitance, and κ is the photon loss rate.

To analyze the data in Fig. 6.4(a), they are fit using Eq. (6.6), with Δ_1 and β as the fitting parameters. The value of $\kappa/2\pi = 125$ kHz is known from resonance linewidth measurements,

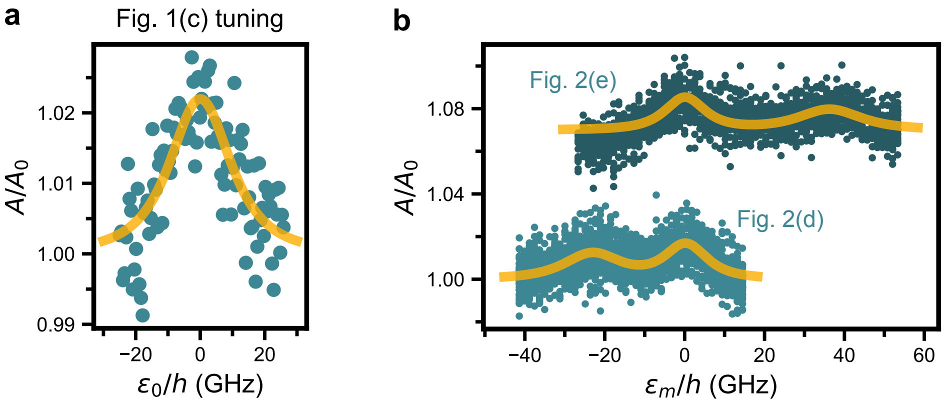

Figure 6.4: Curve-fitting analysis of resonator transmission peaks. **(a)** A/A_0 near the $|0\rangle - |1\rangle$ anticrossing, measured at the same device tuning as Fig. 6.1(c). The data are fit using Eq. (6.6) (yellow curve). **(b)** Combined traces from Figs. 6.2(d) (light teal points) and 6.2(e) (dark teal points; offset for clarity). The data are fit using Eq. (6.8) (yellow curves).

---

and the charge-photon coupling rate,

$$\frac{g_c}{2\pi} = \frac{1}{2\pi}\frac{\omega_r\,\alpha_{\mathrm{C}}^{\varepsilon}}{2e}\sqrt{\frac{2Z_r}{h/e^2}} = 3.2\ \mathrm{MHz}, \tag{6.7}$$

is calculated using Eq. (6.5) and the resonator characteristic impedance, $Z_r \approx 575\ \Omega$ [160, 174]. The result is shown by the yellow curve in Fig. 6.4(a), yielding an estimated tunnel coupling of $\Delta_1/h = 7.3 \pm 0.6$ GHz for Fig. 6.1(c).

The data points in Fig. 6.4(b) show 41 overlaid traces from Fig. 6.2(d) (light teal) and 25 traces from Fig. 6.2(e) (dark teal) where $|\varepsilon_{\mathrm{pulse}}|$ is large enough to generate occupation in $|1\rangle$. These two datasets have been vertically offset for clarity, and we have shifted traces from the top portion of Fig. 6.2(e) horizontally to correct for electrostatic device drift during the measurement. As explained in the main text, two peaks are observed in each dataset, with the additional A/A_0 peaks at ε_L and ε_R arising from the excited-state resonator couplings $\tilde{g}_{\parallel}^{L}$ and $\tilde{g}_{\parallel}^{R}$. While these peaks can be fit individually, we find that a straightforward expansion of Eq. (6.6) to include additional coupling terms enables the pair of peaks in each dataset to be fit together. In this case,

$$\frac{A}{A_0} = \frac{1 - \hbar(\tilde{g}_\parallel^0 + c_L\,\tilde{g}_\parallel^L + c_R\,\tilde{g}_\parallel^R)/2\,\beta\,\tilde{\varepsilon}}{\sqrt{1 + (2\,\delta\omega_0/\kappa)^2 + (2\,c_L\,\delta\omega_L/\kappa)^2 + (2\,c_R\,\delta\omega_R/\kappa)^2}}, \tag{6.8}$$

where $\tilde{g}_\parallel^{L(R)} = -4g_c\Delta_{3(2)}^2\tilde{\varepsilon}/E_{\mathrm{cq},L(R)}^3$ and $\delta\omega_{L(R)} = 8\hbar g_c^2\Delta_{3(2)}^2/E_{\mathrm{cq},L(R)}^3$. The quantity $E_{\mathrm{cq},L(R)} = \sqrt{(\varepsilon_0 - \varepsilon_{L(R)})^2 + 4\Delta_{3(2)}^2}$ approximates the charge-qubit-like energy splitting of the $|1\rangle - |2\rangle$ anticrossing near $\varepsilon_{L(R)}$. Finally, the parameters $c_L, c_R \in [0,1]$ represent the qubit's time-averaged $|1\rangle$ occupation, which influences the height of the A/A_0 peaks measured at ε_L and ε_R. Although we have not explicitly characterized these parameters, we find that the simple assumption that $c_L = c_R = 1$ provides a good match to experimental data, corresponding to the qubit's T_1 time being long relative to the pulse cycle duration. It is important to recognize that the strength of each resonator coupling is sharply peaked at a specific anticrossing and suppressed elsewhere. As a result, in our device—where the QDHQ anticrossings are well separated in ε—a maximum of one coupling channel is active at any given time.

To estimate the QDHQ energy parameters, we fit the data in Fig. 6.4(b) using Eq. (6.8) with $\varepsilon_0 \to \varepsilon_m$ and $c_L = c_R = 1$, producing the yellow curves. In fitting the dataset from Fig. 6.2(d), we fix $\tilde{g}_\parallel^R = \delta\omega_R = 0$ (since these couplings are inactive), yielding parameter estimates of $\Delta_1/h = 4.0 \pm 0.2$ GHz, $\Delta_3/h = 5.4 \pm 0.2$ GHz, and $\varepsilon_L/h = -23.4 \pm 0.4$ GHz. For the Fig. 6.2(e) dataset, with $\tilde{g}_\parallel^L = \delta\omega_L = 0$, we obtain $\Delta_1/h = 3.7 \pm 0.2$ GHz, $\Delta_2/h = 6.0 \pm 0.4$ GHz, and $\varepsilon_R = 36.2 \pm 0.6$ GHz. The two estimates for Δ_1 are in approximate agreement, and we use their average value going forward.

Right-dot singlet-triplet splitting: E_R (pulsed-gate spectroscopy)

Pulsed-gate spectroscopy is performed by applying an alternating-voltage pulse train to the plunger P3. Figure 6.5(a) depicts an idealized voltage waveform with peak-to-peak amplitude V_{pulse} and a duty cycle defined by $D \equiv t_+/(t_+ + t_-)$, where t_+ and t_- are the periods of the high-voltage (V_+) and low-voltage (V_-) pulse stages. The voltage pulses cycle the right-

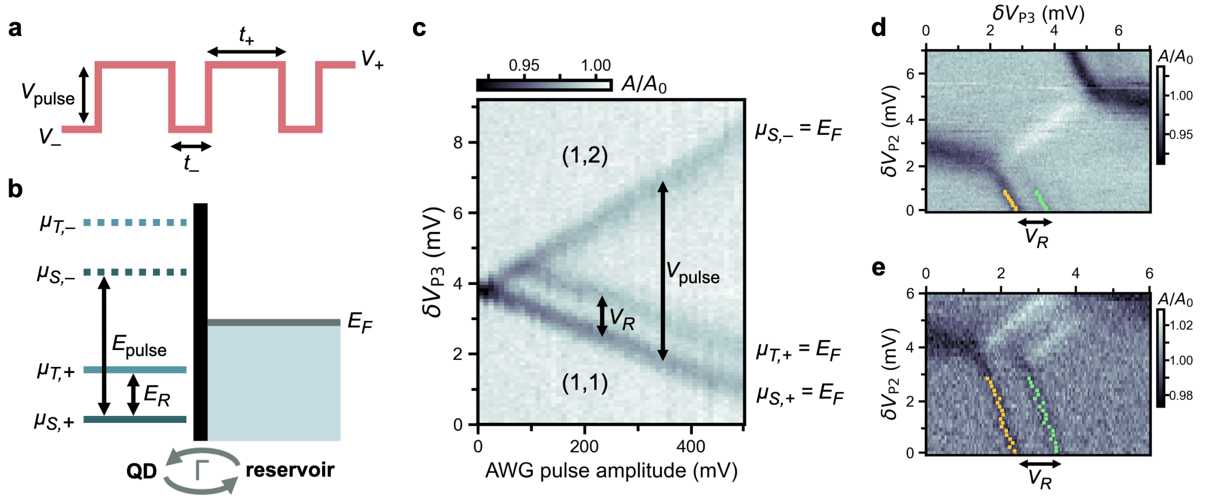

Figure 6.5: Pulsed-gate spectroscopy measurement and analysis. **(a)** Idealized pulsed-voltage waveform applied to gate P3 during measurements. **(b)** Diagram showing cyclic pulsing of the two lowest right-dot energy levels, split by energy E_R. We label the chemical potential for the spin-singlet ground state $\mu_{S,+}$ during the high-voltage pulse stage and $\mu_{S,-}$ during the low-voltage stage; the spin-triplet, excited-state chemical potential during each stage is $\mu_{T,+}$ and $\mu_{T,-}$. Electrons tunnel cyclically between the dot and neighboring reservoir during pulsing with an overall rate Γ. **(c)** Typical pulsed-gate spectroscopy measurement: A/A_0 as a function of V_{P3} and AWG pulse amplitude (measured in instrument units). Dips in A/A_0 are caused by resonant electron tunneling. **(d)** Data from Fig. 6.1(c) with extracted coordinates for the $\mu_{S,+}$ and $\mu_{T,+}$ tunneling resonances marked with yellow and green points, respectively. The voltage splitting V_R between resonances is used to estimate E_R. **(e)** Data from Fig. 6.2(c) with an extended measurement range for the V_{P2} axis. Tunneling resonance coordinates are marked as in (d) and used to estimate E_R.

---

dot energy levels between upper and lower positions separated by $E_{\text{pulse}} = \alpha^R_{\text{P3}} V_{\text{pulse}}$, as diagrammed in Fig. 6.5(b).

Figure 6.5(c) shows an illustrative measurement of A/A_0 at the (1,1) – (1,2) reservoir transition as a function of V_{P3} and arbitrary waveform generator (AWG) pulse amplitude. We note that this measurement is acquired at a different device tuning than the main-text experiments, and the microwave resonator drive is delivered through an alternative on-chip port rather than through P3. The duty cycle of the applied pulse train is $D = 0.6$, with $t_+ = 3$ ns and $t_- = 2$ ns. The reservoir energy barrier and pulse-train frequency are calibrated so that the total electron tunneling rate Γ sharply increases at tunings where a dot energy level aligns with the reservoir Fermi energy E_F. The onset of resonant tunneling at these points changes the dot's complex admittance, thereby suppressing A/A_0. The features in Fig. 6.5(c) closely resemble those of time-averaged pulsed-gate spectroscopy measurements using conventional integrated charge sensors and lock-in techniques (e.g., Ref [217]). For AWG pulse amplitudes below ~ 100 mV, two tunneling resonances are visible, corresponding to P3 voltages where $\mu_{S,+} = E_F$ and $\mu_{S,-} = E_F$. The splitting between these features provides a direct measurement of the on-chip amplitude V_{pulse}. At larger amplitudes, the pulse window straddles the first excited energy level, and a third resonance, corresponding to $\mu_{T,+} = E_F$, is observed. The singlet-triplet splitting,

$$E_R = \mu_{T,+} - \mu_{S,+} = \alpha^R_{\text{P3}} V_R, \tag{6.9}$$

may be estimated from this measurement using the voltage splitting V_R between the $\mu_{S,+}$ and $\mu_{T,+}$ tunneling resonances.

The pulse train applied in Fig. 6.1(c) of the main text is configured with $V_{\text{pulse}} \approx 1.7$ mV, $t_+ = 15$ ns, and $t_- = 2$ ns. (As an aside, we speculate that no A/A_0 boost from the $\tilde{g}^R_{\parallel}$ resonator coupling is observed in this experiment because the duty cycle $D = 0.88$ is too small to provide sufficient signal integration time at ε_R.) To estimate E_R, voltage coordinates of the tunneling resonances are extracted using phenomenological double-Lorentzian fits. These coordinates are overlaid on the measurement data in Fig. 6.5(d), with yellow pixels corresponding to the $\mu_{S,+}$ resonance and green pixels corresponding to the $\mu_{T,+}$ resonance. The $\mu_{S,-}$ resonance is faintly visible as well. We estimate $V_R = 0.97 \pm 0.03$ mV from the average voltage splitting between resonance coordinates, which equates to $E_R = 34.8 \pm 1.2$ GHz using Eq. (6.9).

Reservoir tunneling resonances are also observed in the lower part of Fig. 6.2(c). The control pulse waveform used for this readout experiment has a very large duty cycle of $D = 0.96$, with $t_+ = t_{\text{meas}} = 48$ ns and $t_- = t_{\text{pulse}} = 2$ ns. Only the resonances associated with $\mu_{S,+}$ and $\mu_{T,+}$ tunneling are visible due to the extreme duty cycle. Figure 6.5(e) shows the same measurement as Fig. 6.2(c), but with an extended V_{P2} sweep range. We extract $V_R = 1.15 \pm 0.08$ mV and $E_R = 41.3 \pm 2.9$ GHz from the tunneling resonances using the analysis method described above. This E_R value is larger than the value measured in Fig. 6.5(d). The discrepancy is likely due to variation in electrostatic device tuning between the measurements; singlet-triplet splitting has been shown to change substantially as a function of quantum-dot confinement and lateral position due to local interface disorder [77].

Finally, we note that we are only able to implement pulsed-gate spectroscopy for the right quantum dot in this device, as the left-dot plunger P2 is not connected to coaxial wiring for high-frequency pulsing. The left dot's singlet-triplet splitting E_L is therefore estimated based on other measurement data and numerical calculations described in the next section.

Other Hamiltonian parameters: E_L, Δ_4

The main-text experiments do not provide direct measurements of the left-dot singlet-triplet splitting E_L or the tunnel coupling Δ_4. However, we are able to estimate these parameters through numerical analysis. We first diagonalize the qubit Hamiltonian in Eq. (6.3) as a function of E_L and Δ_4 with the other matrix entries fixed to the values derived above. Then, we compute the $|1\rangle - |2\rangle$ energy anticrossing detunings ε_L and ε_R for each diagonalized matrix and compare them to the experimentally measured values. Figure 6.6(a) summarizes the results of this analysis, with color-filled contours bounding the regions of (E_L, Δ_4) parameter space in which the calculated ε_L and ε_R values match experimental results to within 1σ or 2σ experimental uncertainty. The closest match to our measurements occurs at the coordinate pair marked with an '×' in the plot; from these coordinates, we estimate the qubit parameters in the Fig. 6.2 measurements to be $E_L/h = 27.0 \pm 0.4$ GHz and $\Delta_4/h = 10.4 \pm 0.7$ GHz (the uncertainties are given by the 1σ contour dimensions about this point).

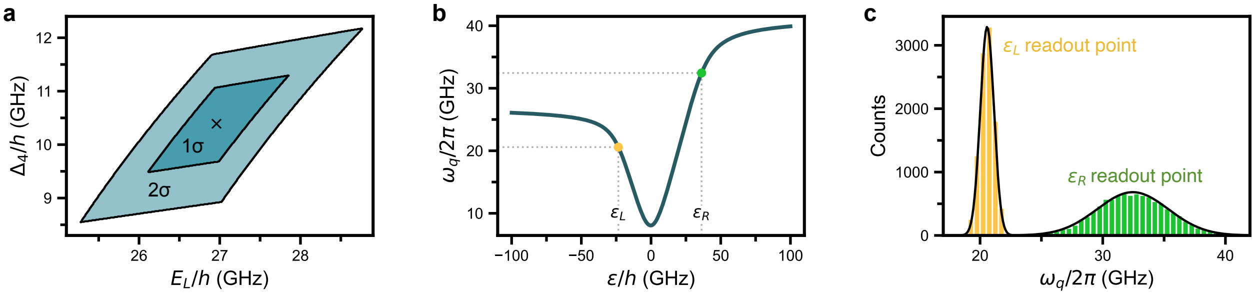

Figure 6.6: Qubit spectroscopy numerical analysis. **(a)** Contours showing regions of (E_L, Δ_4) parameter space in which calculated ε_L and ε_R values match Fig. 6.2 measurements to within 1σ or 2σ experimental uncertainty. The closest-match parameter coordinates marked with an '×' are used as E_L and Δ_4 estimates for main-text experiments. **(b)** Qubit frequency ω_q as a function of ε. Yellow and green circles mark frequencies at the ε_L and ε_R readout operating points. **(c)** Results of a Monte Carlo simulation calculating qubit frequency at the ε_L (yellow histogram) and ε_R (green histogram) readout operating points. Black curves show Gaussian fits to the histograms.

Qubit frequency at the readout operating points

With all QDHQ parameters estimated, the qubit frequency ω_q can be calculated by diagonalizing the Hamiltonian in Eq. (6.3). Figure 6.6(b) plots ω_q as a function of ε. For our work, we are particularly interested in the qubit frequency at the readout operating points marked by green and yellow circles in the plot. Using the Hamiltonian parameters for the Fig. 6.2 measurements found above, we compute $\omega_q/2\pi = 20.6 \pm 0.6$ GHz at the ε_L readout point and $\omega_q/2\pi = 32.4 \pm 2.9$ GHz at the ε_R readout point.

The qubit frequency uncertainties are obtained through a Monte Carlo simulation. In each simulation iteration, Hamiltonian parameter entries are drawn from Gaussian distributions whose means and standard deviations correspond to the values and uncertainties computed in previous sections. Figure 6.6(c) charts histograms of the readout-point qubit frequencies after 10,000 iterations. The frequency uncertainties are extracted through Gaussian fits to the histograms.

6.5.3 Qubit-Resonator Coupling Strengths & Measurement Rate

To provide a representative estimate of the longitudinal and transverse interaction strengths in this work, we adopt an approach similar to that in Section 5.6.5, using parameter values obtained by fitting the data in Fig. 6.4(a).

The transverse coupling $\delta\omega_0$ is heavily suppressed in the ultra-dispersive regime. At $\varepsilon_0 = 0$, where the transverse interaction is maximized, we calculate a coupling strength of only

$$\frac{\delta\omega_0}{2\pi} = \frac{1}{2\pi}\frac{\hbar g_c^2}{\Delta_1} = 1.4\ \text{kHz}. \tag{6.10}$$

The longitudinal coupling $\tilde{g}_{\parallel}^{0}$ depends on the ac drive applied to the qubit. Figure 6.4(a) is measured using a microwave source output power of 9 dBm. The 50 Ω coaxial cabling on the drive line is configured with 39 dB of attenuation at room temperature and 40 dB within the cryostat. Based on SPICE simulations, we estimate an additional 10 dB of attenuation due to impedance mismatch at the device gate leads, which are buried coplanar waveguides engineered to have a low characteristic impedance of $Z_g \approx 1\ \Omega$ [174, 211]. Factoring in this attenuation, the on-chip drive power is estimated to be $P = -80$ dBm $= 10$ pW, which generates an ac detuning amplitude of $\tilde{\varepsilon}/h = \alpha^{\varepsilon}_{\mathrm{P3}}\sqrt{2Z_gP}/h = 113.3$ MHz. Using this value, we compute

$$\frac{|\tilde{g}_{\parallel}^{0}|}{2\pi} = \frac{1}{2\pi}\frac{g_c\tilde{\varepsilon}}{2\Delta_1} = 24.6\ \text{kHz} \tag{6.11}$$

at $\varepsilon_0 = 0$, where the coupling is at its strongest.

Based on these values, we expect that longitudinal coupling dominates the quantum measurement rate Γ_{meas} in our experiments, such that $\Gamma_{\text{meas}}/2\pi \approx \tilde{g}_{\parallel}^{2}/2\pi\kappa \sim 5$ kHz [190, 222]. We note that Γ_{meas} can be substantially increased by enhancing g_c and $\tilde{\varepsilon}$, while simultaneously optimizing κ and the relevant tunnel couplings. For example, the charge-photon coupling g_c can be engineered to be more than 10 times larger (as demonstrated experimentally in, e.g., Refs. [157, 167]), while maintaining $\tilde{\varepsilon}/\hbar g_c \gg 1$.

We emphasize that the coupling values above should be treated as rough estimates, given that they are not directly measured, and the microwave environment of the device is not fully characterized. The key takeaway is that the longitudinal coupling is found to be an order of magnitude larger than the residual transverse coupling. Based on the A/A_0 peaks observed in our measurements and the parameter values reported in Table 6.1, we expect that longitudinal coupling serves as the primary qubit-resonator interaction mechanism for all experiments.

6.5.4 Parameter Table

Resonator properties	**Determination**	**Value**	**Units**
Fundamental-mode frequency, $\omega_r/2\pi$	measured	1.30380	GHz
Photon decay rate, $\kappa/2\pi$	measured	124.5 ± 0.5	kHz
Loaded quality factor, Q_L	measured	$10,476 \pm 46$	
Characteristic impedance, Z_r	calculated	575	Ω
Charge-photon coupling rate, $g_c/2\pi$	calculated	3.16 ± 0.55	MHz
DQD properties			
P2-left dot lever arm, α^L_{P2}/h	measured	33.9 ± 1.2	GHz/mV
P3-right dot lever arm, α^R_{P3}/h	measured	36.0 ± 0.7	GHz/mV
P3 detuning lever arm, $\alpha^\varepsilon_{\mathrm{P3}}/h$	measured	25.4 ± 1.2	GHz/mV
Coupling-gate detuning lever arm, $\alpha^\varepsilon_{\mathrm{C}}/h$	measured	5.6 ± 1.0	GHz/mV
Electron temperature, T_e	measured	213 ± 6	mK
Fig. 6.1(c)			
Microwave source output power	controlled	9	dBm
Pulse peak-to-peak voltage amplitude, V_{pulse}	controlled	1.7	mV
Pulse-sequence high-voltage period, t_+	controlled	15	ns
Pulse-sequence low-voltage period, t_-	controlled	2	ns
Pulse-sequence duty cycle, D	controlled	0.88	
Pulse-sequence repetitions per data point	controlled	8.8×10^6	
Interdot tunnel coupling, Δ_1/h	measured	7.3 ± 0.6	GHz
Right-dot tunneling resonance voltage splitting, V_R	measured	0.97 ± 0.03	mV
Right-dot singlet-triplet splitting, E_R/h	measured	34.8 ± 1.2	GHz
Minimum qubit frequency, $\omega_q(\varepsilon_0 = 0)/2\pi$	calculated	14.6 ± 1.2	GHz
Maximum qubit frequency, $\omega_q(\varepsilon_0 \gg 0)/2\pi$	calculated	34.8 ± 1.2	GHz
Transverse coupling strength, $\delta\omega_0(\varepsilon_0 = 0)/2\pi$	calculated	1.4	kHz
Longitudinal coupling strength, $\lvert\tilde{g}^0_\parallel(\varepsilon_0 = 0)\rvert/2\pi$	calculated	24.6	kHz

Figs. 6.2(b,c,d,e)	**Determination**	**Value**	**Units**
Microwave source output power (b,c)	controlled	5	dBm
Microwave source output power (d,e)	controlled	7	dBm
Pulse detuning amplitude (b,c), $\lvert\varepsilon_{\text{pulse}}\rvert/h$	controlled	63.5	GHz
Pulse detuning amplitude (d,e), $\lvert\varepsilon_{\text{pulse}}\rvert/h$	controlled	0 to 63.5	GHz
Pulse phase period, t_{pulse} $(= t_-)$	controlled	2	ns
Measurement phase period, t_{meas} $(= t_+)$	controlled	48	ns
Pulse-sequence duty cycle, D	controlled	0.96	
Pulse-sequence repetitions per data point (b,c)	controlled	4×10^6	
Pulse-sequence repetitions per data point (d,e)	controlled	2×10^6	
Interdot tunnel coupling, Δ_1/h	measured	3.9 ± 0.1	GHz
Interdot tunnel coupling, Δ_2/h	measured	6.0 ± 0.4	GHz
Interdot tunnel coupling, Δ_3/h	measured	5.4 ± 0.2	GHz
Interdot tunnel coupling, Δ_4/h	calculated	10.4 ± 0.7	GHz
Left-dot singlet-triplet splitting, E_L/h	calculated	27.0 ± 0.4	GHz
Right-dot tunneling resonance voltage splitting, V_R	measured	1.15 ± 0.08	mV
Right-dot singlet-triplet splitting, E_R/h	measured	41.3 ± 2.9	GHz
$\lvert 1\rangle - \lvert 2\rangle$ anticrossing detuning, ε_L/h	measured	-23.4 ± 0.4	GHz
$\lvert 1\rangle - \lvert 2\rangle$ anticrossing detuning, ε_R/h	measured	36.2 ± 0.6	GHz
Minimum qubit frequency, $\omega_q(\varepsilon_0 = 0)/2\pi$	calculated	7.8 ± 0.2	GHz
Maximum qubit frequency, $\omega_q(\varepsilon_0 \gg 0)/2\pi$	calculated	41.3 ± 2.9	GHz
Readout-point qubit frequency, $\omega_q(\varepsilon_0 = \varepsilon_L)/2\pi$	calculated	20.6 ± 0.6	GHz
Readout-point qubit frequency, $\omega_q(\varepsilon_0 = \varepsilon_R)/2\pi$	calculated	32.4 ± 2.9	GHz

Table 6.1: Summary of device and measurement parameters used throughout this work. Parameters are classified into one of three categories: ‘controlled’ variables with values chosen as part of the experiment protocol; ‘measured’ values determined primarily through direct measurement; and ‘calculated’ values determined primarily through a numerical calculation or simulation described in previous sections.

6.5.5 Experimental Setup

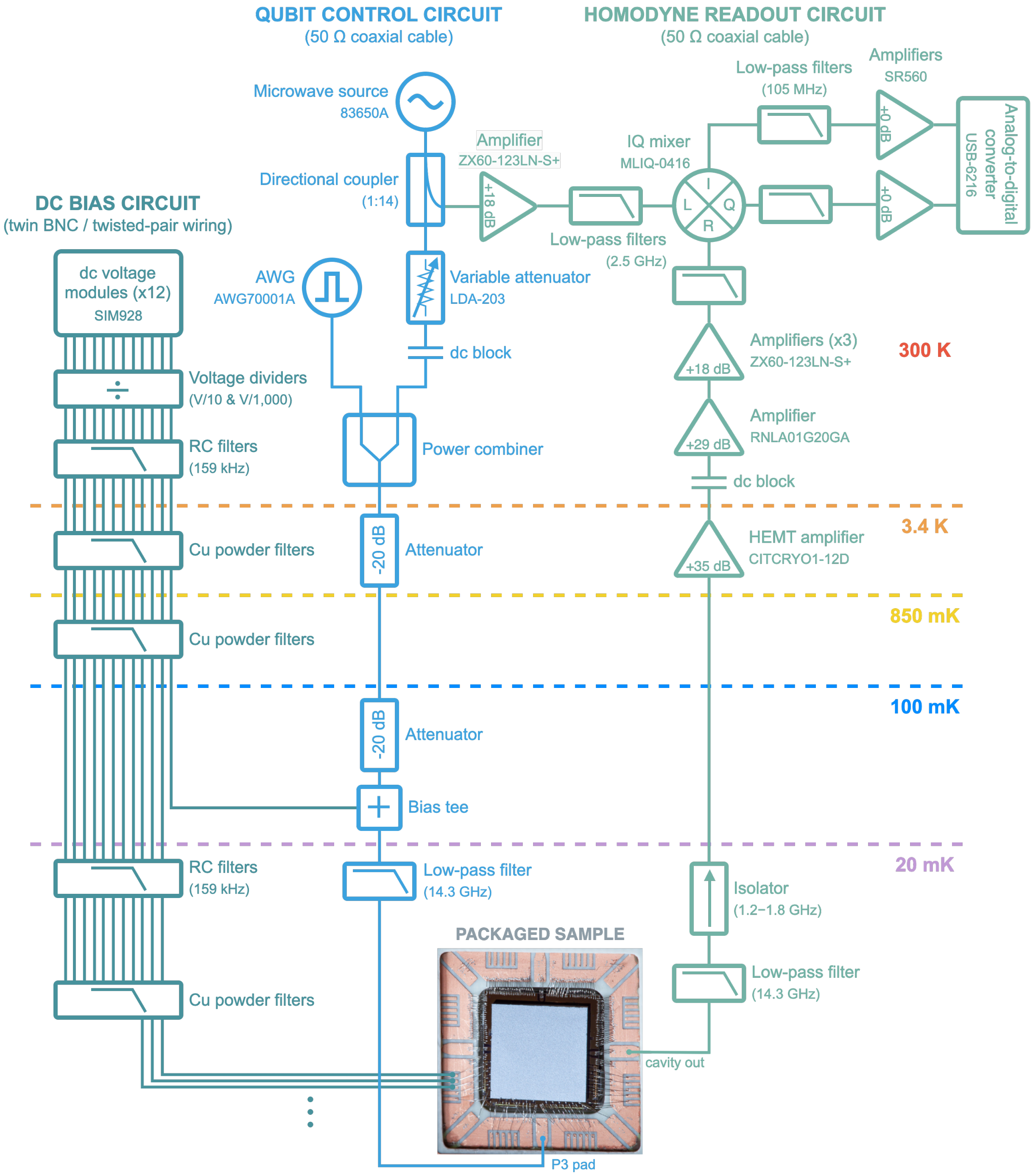

Figure 6.7: Wiring diagram for the measurement instrumentation. Experiments are performed in a Leiden Cryogenics CF-450 dilution refrigerator with a mixing-chamber base temperature around 20 mK.

Part III

Making Qubits with Hybrid Junctions

Chapter 7

The Physics of Superconductor-Semiconductor Hybrid Junctions

We will now turn our attention away from quantum-dot qubits to explore other types of qubits based on superconductor-semiconductor hybrid physics. These qubits take the integration of superconductors and semiconductors a step beyond the quantum dot-resonator systems we covered earlier, employing hybrid junctions to form the qubits themselves. This chapter introduces the foundational concepts of superconductor-semiconductor hybrid junctions, beginning with an overview of bulk superconductivity and building up to more complex junction configurations. We examine key physical phenomena, such as Andreev reflection, the proximity effect, and Andreev bound states, which are central to understanding mesoscopic hybrid systems. The discussion then focuses on various qubit platforms that utilize hybrid junctions, highlighting how each platform harnesses the unique physics of these systems for quantum control.

7.1 Bulk Superconductivity

Superconductivity was discovered in 1911 by the Dutch physicist Heike Kamerlingh Onnes. Three years before, Onnes had developed a technique to liquefy helium, allowing him to study materials at extremely low temperatures from his laboratory in Leiden. In the course of his experiments, Onnes observed something incredible: the electrical resistance of mercury dropped suddenly to zero when it was cooled to a temperature of 4.2 K [223]. A second experimental signature of superconductivity was uncovered in 1933, when Walther Meissner and Robert Ochsenfeld showed that superconductors expel magnetic fields (a behavior later dubbed the **Meissner effect**) [224].

The theoretical understanding for these phenomena emerged in pieces over the following decades. The **London equations** of 1935, which described the electromagnetic properties of superconductors, offered early insight to explain experimental findings [225]. In 1950, Vitaly Ginzburg and Lev Landau developed the **Ginzburg-Landau theory**, a macroscopic, phenomenological model that introduced the concept of a complex order parameter varying smoothly over space [226]. These developments culminated in the **BCS theory** of 1957, formulated by John Bardeen, Leon Cooper, and Robert Schrieffer, which offered a comprehensive microscopic explanation for superconductivity [227]. Theoretical efforts to understand the origins of high-temperature superconductivity—and to predict candidate materials for room-temperature superconductivity—continue today, over a century after Onnes' discovery.

With a vast canon of literature, a full accounting of the theory of superconductivity lies well beyond the scope of this chapter. Instead, I will summarize essential takeaways from the Ginzburg-Landau and BCS theories, building up a minimal framework to understand the physics of mesoscopic superconducting devices. An in-depth description of both theories can be found in Michael Tinkham's *Introduction to Superconductivity* [228], the conventional textbook on the subject. Chapter 6 of Max Hays' thesis [147] also provides an excellent introduction to BCS theory, with a narrower scope but better figures and explanations than Tinkham's treatment.

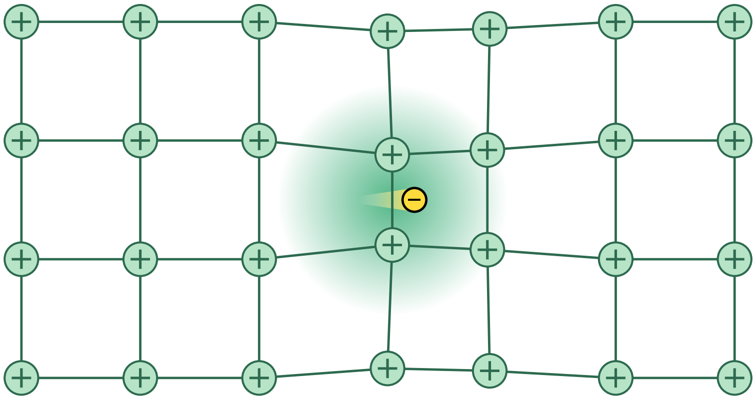

Figure 7.1: Exaggerated lattice distortion as an electron moves through a crystal. In superconductors, the movement of ions creates a region of positive charge and gives rise to the phonon-mediated electron pairing interaction.

7.1.1 Cooper Pairs

At the heart of superconductivity is the formation of **Cooper pairs**, which arise from an attractive interaction between electrons with opposite spin and momentum [229]. The existence of such an interaction is counterintuitive, given that electrons in free space repel each other through the Coulomb force. In a crystal lattice, however, an attractive potential can be mediated by phonons. An electron moving through the lattice slightly distorts the spacing of the surrounding ions, creating a region of positive charge which can attract another electron, as illustrated in Fig. 7.1. In superconductors at sufficiently low temperatures, the phonon-mediated attraction mechanism is strong enough to overcome Coulomb repulsion and bind pairs of electrons together. The length scale over which electrons are paired is characterized by the **superconducting coherence length**, which is usually ~ 100 nm to 1 µm, depending on the material—much longer than the Fermi wavelength.[1]

The Cooper pairs in a superconductor behave not as fermions but as composite bosons. As such, they obey Bose-Einstein statistics and are able to occupy a single energy state. As a superconducting material is cooled below its **critical temperature**, the condensation of

---

[1] Cooper pairs are often depicted in drawings—including some in this dissertation—with their constituent electrons closely bound together, like atoms in a molecule. This is not a physically accurate depiction; the phonon-mediated pairing in superconductors is a *long-range* interaction.

Cooper pairs into a collective ground state marks a quantum phase transition and the onset of superconductivity. The Cooper pair condensate acts as a single, macroscopic quantum state—its wavefunction extends throughout the entire material—which can flow in a highly coherent manner, carrying **supercurrent** without energy dissipation.

In many mesoscopic applications, the Cooper pair condensate is conveniently represented using the **Ginzburg-Landau order parameter** $\psi_{\mathrm{GL}}(\mathbf{x})$, which can be written as

$$\psi_{\mathrm{GL}}(\mathbf{x}) = |\psi_{\mathrm{GL}}(\mathbf{x})| e^{i\varphi(\mathbf{x})}. \tag{7.1}$$

The order parameter is a complex scalar field, defined such that its magnitude squared gives the local density of Cooper pairs: $|\psi_{\mathrm{GL}}(\mathbf{x})|^2 \equiv n_S(\mathbf{x})$.[2] Its behavior is governed by a pair of differential equations called the Ginzburg-Landau equations. A **superconducting phase parameter** $\varphi(\mathbf{x})$ is also associated with the condensate. The existence of a well-defined quantum phase across the entire superconducting material underpins many of the unique properties of superconductors—we will soon see that it plays a crucial role in the behavior of superconducting junctions. Gradients in $\varphi(\mathbf{x})$ drive the flow of supercurrent through a material.

7.1.2 Density of States

The formation of Cooper pairs dramatically alters the distribution of energy states inside a superconductor. The density of states $\nu(E) = dN/dE$ describes the number of fermionic states available at each energy for particles to occupy. In a normal metal, the density of states near the Fermi level is relatively constant, $\nu(E) \approx \nu_N$. However, after undergoing a

---

[2] This definition and the conventional use of the Greek letter 'ψ' make it tempting to think of the Ginzburg-Landau order parameter as a quantum-mechanical wavefunction. While there is an undeniable qualitative resemblance—this is likely why Ginzburg and Landau chose 'ψ' as a variable name—the order parameter is *not* a wavefunction. One obvious difference is that $|\psi_{\mathrm{GL}}|^2$ corresponds to physical density of particles rather than a probability density. Another is that ψ_{GL} evolves according to the Ginzburg-Landau equations rather than the Schrödinger equation.

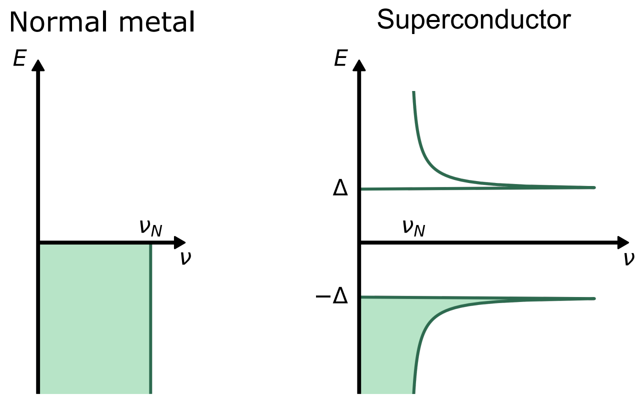

Figure 7.2: Comparison of the density of states $\nu(E)$ between a normal metal and a superconductor at $T = 0$. Shading indicates filled fermionic states. An energy gap of 2Δ forms in the superconductor density of states.

superconducting phase transition, it is modified to

$$\nu(E) = \begin{cases} \nu_N \dfrac{E}{\sqrt{E^2 - \Delta^2}} & |E| \geq \Delta\,, \\ 0 & |E| < \Delta\,, \end{cases} \tag{7.2}$$

where the energy E is measured with respect to the Fermi level. Figure 7.2 plots the density of states, showing a region with no states available in the energy window $|E| < \Delta$. This **superconducting gap** in the density of states emerges as a consequence of the electron pairing mechanism, which lifts an electron-hole degeneracy in the material's band structure and opens an avoided crossing of strength 2Δ in the energy spectrum. Inside the gap, Cooper pairs reside at the superconductor's Fermi energy, but no fermionic states exist.[3] The divergences at the edges of the gap, $E = \pm\Delta$, are known as **coherence peaks**; these are formed as the pairing interaction 'pushes' states away from the Fermi energy, creating a 'pile-up' in density at the gap boundaries.

The presence of the superconducting gap is central to many of the remarkable behaviors of superconductors. For instance, it is the gap which enables the flow of supercurrent without

---

[3] Remember that the Cooper pairs are *bosons*, so their (infinite) density of states is not represented in Eq. (7.2).

energy dissipation. Low-energy scattering events, which give rise to electrical resistance in normal metals, are vastly suppressed in superconductors because of the absence of available scattering states within the gap. Cooper pairs are therefore able to move coherently through the lattice without disruption, unaffected by impurities, defects, or phonons.

7.1.3 Quasiparticle Excitations

Now that we have discussed Cooper pairs in superconductors, we turn our attention to the *unpaired* particles with energies outside the gap. In a normal metal, we would identify the positive-energy particles as electrons and the negative-energy particles as holes. This is not the case for superconductors, whose single-particle states are not pure electrons or pure holes but a *mixture of both.* These particles arise as a consequence of the electron pairing mechanism, which mixes electron and hole operators in the many-body Hamiltonian of BCS theory. To diagonalize the Hamiltonian and obtain its energy spectrum, it is necessary to transform to a basis in which the effective **quasiparticles** are coherent superpositions of electrons and holes, called **Bogoliubons**.[4]

By diagonalizing the BCS Hamiltonian, the energy eigenvalues of Bogoliubons are found to be

$$E_k = \pm\sqrt{\epsilon_k^2 + \Delta^2}, \tag{7.3}$$

where

$$\epsilon_k = \frac{\hbar^2 k^2}{2m} - \mu \tag{7.4}$$

is the quasiparticle kinetic energy. We see from Eq. (7.3) that Bogoliubons must have $|E_k| \geq \Delta$, reflecting the gap in the density of states. The corresponding Bogoliubon eigenstates $\mathbf{\Psi}_+$ and $\mathbf{\Psi}_-$ define two types of quasiparticles with positive and negative energies, respectively.

---

[4] The mathematical trick of transforming to a basis in which the effective particles are composite 'quasiparticles' is a frequently used tool in condensed matter theory called a Bogoliubov transformation. Both the technique and the resulting Bogoliubon quasiparticles are named after Nikolay Bogoliubov, who used the method to diagonalize the BCS Hamiltonian [230].

These wavefunctions are superpositions of electrons and holes, and it is illuminating to represent them using a spinor notation to highlight their mixed nature:

$$\boldsymbol{\Psi}_+ = \begin{pmatrix} u_k \\ v_k \end{pmatrix} \qquad \text{and} \qquad \boldsymbol{\Psi}_- = \begin{pmatrix} -v_k^* \\ u_k^* \end{pmatrix}, \tag{7.5}$$

where the upper spinor component is the electron amplitude in the superposition, and the lower component is the hole amplitude. The complex parameters u_k and v_k are known as the **coherence factors** and satisfy the normalization condition $|u_k|^2 + |v_k|^2 = 1$. These are energy-dependent quantities with magnitudes given by

$$|u_k|^2 = \frac{1}{2}\left(1 + \frac{\epsilon_k}{E_k}\right) \qquad \text{and} \qquad |v_k|^2 = \frac{1}{2}\left(1 - \frac{\epsilon_k}{E_k}\right), \tag{7.6}$$

indicating that the electron-like or hole-like nature of a Bogoliubon depends on its energy. At the gap edge ($\epsilon_k = 0$), the quasiparticle states are equal electron-hole superpositions with $|u_k| = |v_k| = 1/\sqrt{2}$.

In the superconducting ground state, all negative-energy ($\boldsymbol{\Psi}_-$) quasiparticle states are occupied, and all positive-energy states ($\boldsymbol{\Psi}_+$) are vacant. External perturbations can excite the superconductor out of this ground state. One way that this occurs, illustrated in Fig. 7.3(a), is by kicking Bogoliubons up from negative to positive energy. Equation (7.3) indicates that the minimum energy required to do so is 2Δ. Alternatively, excitations can occur through the breaking of Cooper pairs into individual quasiparticles, as shown in Fig. 7.3(b).[5] Since the energy cost to promote each Bogoliubon from the Fermi-level condensate to the gap edge is Δ, the minimum energy needed to break a Cooper pair—the Cooper pair binding energy—is also 2Δ for this type of excitation.

---

[5] Note that the BCS Hamiltonian requires fermionic parity to be conserved. So in an isolated superconductor, Bogoliubons are always created or destroyed in pairs for any process.

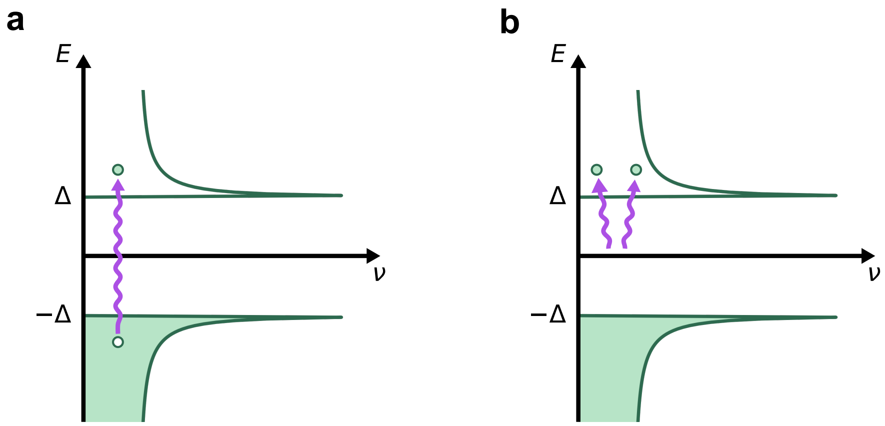

Figure 7.3: Two quasiparticle excitation pathways in a superconductor. **(a)** A Bogoliubon is promoted from negative to positive energy. **(b)** Two new Bogoliubons are created from the breaking of a Cooper pair in the condensate. In both cases, the minimum excitation energy is 2Δ.

7.1.4 Critical Parameters

Superconductivity can only be maintained when the energy of external perturbations is kept well below the Cooper pair binding energy—which is typically ~ 1 meV for the materials used in hybrid devices. Dumping too much energy into the condensate disrupts the electron pairing, causing the material to revert to its normal, resistive state. Three critical parameters define the energetic conditions under which superconducting pairing can occur and place operational limits on applications for these materials.

We have already alluded to the **critical temperature** (T_c) as the quantum phase transition temperature for superconductivity. Above this temperature, thermal energy is sufficient to break Cooper pairs. Similarly, the **critical magnetic field** (B_c) is the maximum field that a superconductor can withstand. Beyond this field, the energy of the magnetic flux lines penetrating the superconductor causes the breakdown of Cooper pairs and a transition to the normal state.[6] Finally, the **critical current density** (J_c) is the maximum current per unit area that a superconductor can carry before the self-induced magnetic field exceeds

---

[6] In type II superconductors, this transition occurs in two stages: first, the magnetic field partially penetrates the superconductor in quantized vortices (creating a mixed state), and beyond a higher critical field, superconductivity is completely destroyed. The hybrid devices that we will consider usually employ type I superconductors, which transition abruptly to the normal state.

B_c and quells superconductivity.

The BCS theory provides a well-known formula for the energy gap at zero temperature in terms of the critical temperature. The relationship is given by

$$\Delta(0) = 1.76 k_B T_c. \tag{7.7}$$

For temperatures close to T_c, the temperature dependence of the energy gap can be approximated by

$$\Delta(T) \approx 3.06\, k_B\, T_c \sqrt{1 - \frac{T}{T_c}}. \tag{7.8}$$

This formula shows that the gap closes smoothly as $T \to T_c$.

7.2 The N-S Junction

Having studied bulk superconductivity, we now explore the physics of superconducting junctions. We begin with the **normal metal-superconductor (N-S) junction**, formed when a normal metal (N) is brought into contact with a superconductor (S). As we will see, the interplay between normal and superconducting states at the interface gives rise to unique transport processes and creates a hybrid region with properties of both materials.

7.2.1 Andreev Reflection

Consider an electron moving through an N-S junction, crossing from the normal metal into the superconductor. If the electron's energy is greater than Δ, it can simply enter the superconductor, where it is converted into a quasiparticle with the same energy [Fig. 7.4(a)]. On the other hand, if the electron's energy is less than Δ, there are no available fermionic states within the superconducting gap for it to occupy. At first glance, it might seem that transport through the junction would be blocked for low-energy electrons. However, an alternative transport process provides a way for electrons to cross the N-S interface. The

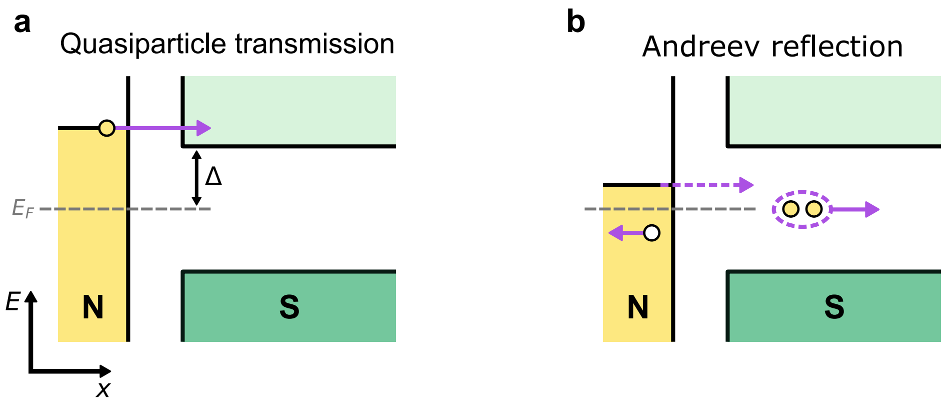

Figure 7.4: Transport through an N-S junction. **(a)** An incident electron with energy $E > \Delta$ is transmitted into the superconductor as a quasiparticle excitation. **(b)** An electron with energy $E < \Delta$ crosses the interface through Andreev reflection, leaving behind a reflected hole in the normal metal. Energy is measured relative to the superconductor's Fermi level.

---

incoming electron can grab a partner from the Fermi sea, creating a Cooper pair, and the bound electrons can then enter the superconductor together. As a result, a hole is left behind in the normal metal, traveling in the opposite direction [Fig. 7.4(b)]. This transport process, in which an incident electron is, in a sense, reflected back as a hole, is termed **Andreev reflection** after the Russian physicist Alexander F. Andreev [231]. While this simple transport mechanism may seem somewhat mundane compared to other topics in this dissertation, it is the central phenomenon underlying all the richness of superconductor-semiconductor hybrid physics.

A quantitative theory for transport through an N-S junction was worked out by Blonder, Tinkham, and Klapwijk in 1982, [232]. These authors used a scattering approach, which we review here, to extend Andreev's original derivation [231]. The transport processes are governed by the Bogoliubov-de Gennes (BdG) equations, a generalization of the Schröinger equation for quasiparticles in a superconductor. In one dimension, the coupled differential equations can be written as

$$\begin{pmatrix} \hat{H}_0 & \Delta(x) \\ \Delta^*(x) & -\hat{H}_0^* \end{pmatrix} \mathbf{\Psi}(x) = E\,\mathbf{\Psi}(x), \tag{7.9}$$

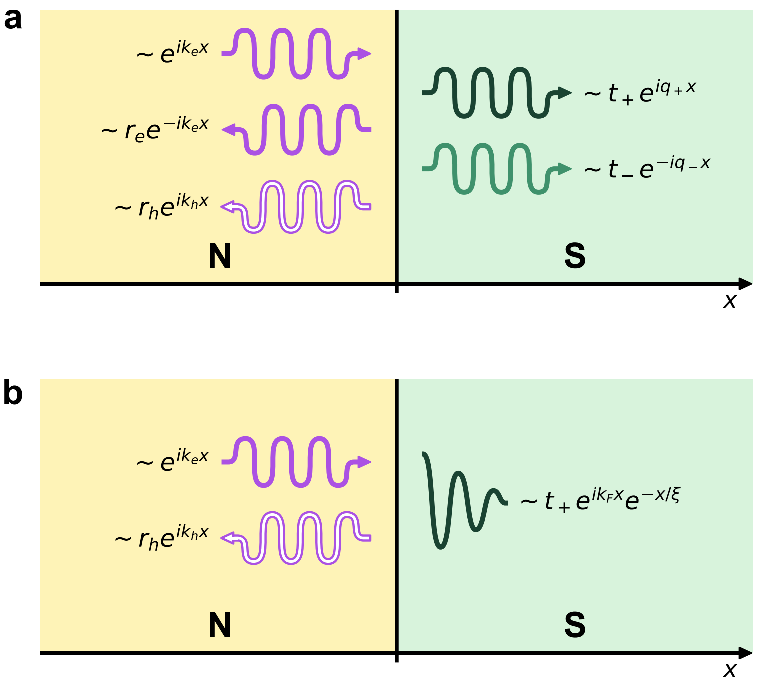

Figure 7.5: Solutions to the BdG equations in an N-S junction. **(a)** General solution with waveforms representing an incident electron, reflected electron, reflected hole, and two types of transmitted quasiparticles. **(b)** Solution with $E < \Delta_0$ and no scattering. The quasiparticle waveform decays exponentially inside the superconductor.

---

where $\hat{H}_0$ is the single-particle Hamiltonian,

$$\hat{H}_0 = -\frac{\hbar^2}{2m}\frac{d^2}{dx^2} - \mu. \tag{7.10}$$

The spinnor wavefunction

$$\mathbf{\Psi}(x) = \begin{pmatrix} u(x) \\ v(x) \end{pmatrix} \tag{7.11}$$

uses the same notation as the Bogoliubon definitions in Eq. (7.5), with components representing electron and hole amplitudes.

We will consider a junction with a normal metal at $x < 0$ and a superconductor at $x > 0$. For simplicity, we can treat the complex **superconducting pair potential** $\Delta(x)$ as a step function:

$$\Delta(x) = \begin{cases} 0 & x < 0\,, \\ \\ \Delta_0\, e^{i\varphi} & x \geq 0\,, \end{cases} \tag{7.12}$$

where Δ_0 and φ are real constants without any positional variation. In the normal metal ($x < 0$), there is no pairing and the BdG equations decouple into

$$\begin{aligned} \hat{H}_0\, u(x) &= E\, u(x), \\ -\hat{H}_0^*\, v(x) &= E\, v(x). \end{aligned} \tag{7.13}$$

The solutions for an electron with energy $E > 0$ incident from the normal metal take the form

$$\mathbf{\Psi}_N(x < 0) = \begin{pmatrix} 1 \\ 0 \end{pmatrix} e^{ik_e x} + r_e \begin{pmatrix} 1 \\ 0 \end{pmatrix} e^{-ik_e x} + r_h \begin{pmatrix} 0 \\ 1 \end{pmatrix} e^{ik_h x}, \tag{7.14}$$

where $k_e = \sqrt{2m(\mu + E)/\hbar^2}$ and $k_h = \sqrt{2m(\mu - E)/\hbar^2}$. We can interpret $\mathbf{\Psi}_N$ a superposition of individual particles propagating in the normal metal: the first term is for the incident electron; the second term is for an electron reflected at the interface; and the final term is for a reflected hole (with the wavevector $+k_h$ corresponding to travel in the *negative* direction). The reflection amplitudes for electron and hole elastic scattering are r_e and r_h, respectively. These terms are depicted in Fig. 7.5(a). In the superconductor ($x > 0$), the BdG equations are

$$\begin{pmatrix} \hat{H}_0 & \Delta_0 e^{i\varphi} \\ \Delta_0 e^{-i\varphi} & -\hat{H}_0^* \end{pmatrix} \begin{pmatrix} u(x) \\ v(x) \end{pmatrix} = E \begin{pmatrix} u(x) \\ v(x) \end{pmatrix}, \tag{7.15}$$

whose solutions can be written as

$$\mathbf{\Psi}_S(x > 0) = t_+ \begin{pmatrix} \tilde{u} \\ \tilde{v} \end{pmatrix} e^{iq_+ x} + t_- \begin{pmatrix} \tilde{v} \\ \tilde{u} \end{pmatrix} e^{-iq_- x}. \tag{7.16}$$

The terms in $\mathbf{\Psi}_S$, depicted in Fig. 7.5(a), correspond to transmitted quasiparticles with wavevectors

$$q_\pm = \sqrt{\frac{2m}{\hbar^2}\left(\mu \pm \sqrt{E^2 - \Delta_0^2}\right)}\,, \tag{7.17}$$

and transmission amplitudes t_+ and t_-. The electron-hole amplitudes $\tilde{u}$ and $\tilde{v}$ must satisfy the constraint[7]

$$|\tilde{u}|^2 = 1 - |\tilde{v}|^2 = \frac{1}{2}\left(1 + \frac{\sqrt{E^2 - \Delta_0^2}}{E}\right). \tag{7.18}$$

The plane-wave form of $\mathbf{\Psi}_S$ implies that for $E > \Delta_0$, transmission from the normal metal into the superconductor with freely propagating quasiparticles is allowed, as we have already noted. The more interesting scenario, for our purposes, is when $E < \Delta_0$. We will consider this 'sub-gap' case in more detail and see that the BdG solutions give rise to Andreev reflection. To simplify our treatment, we focus on an ideal, ballistic junction with no scattering at the interface, such that $r_e = t_- = 0$. In this setup, the normal-metal solution becomes

$$\mathbf{\Psi}_N(x < 0) = \begin{pmatrix} 1 \\ 0 \end{pmatrix} e^{ik_e x} + r_h \begin{pmatrix} 0 \\ 1 \end{pmatrix} e^{ik_h x}. \tag{7.19}$$

Inside the superconductor, the expressions for q_+ and q_- in Eq. (7.17) become complex since $\sqrt{E^2 - \Delta_0^2}$ is imaginary. As a result, there are no propagating-wave solutions in the bulk superconductor. However, an *evanescent* quasiparticle solution is allowed near the interface:

$$\mathbf{\Psi}_S(x > 0) = t_+ \begin{pmatrix} u_0 \\ v_0 \end{pmatrix} e^{ik_F x}\, e^{-x/\xi}, \tag{7.20}$$

---

[7] Note that in order to find general solutions to the BdG equations, we allow the complex amplitudes $\tilde{u}$ and $\tilde{v}$ to be defined for all energies. This is different from the BCS coherence factors u_k and v_k in Eq. (7.6), which are only defined for $|E_k| > \Delta$.

where the electron-hole amplitudes are now explicitly defined as

$$\begin{aligned} u_0 &= e^{i\varphi/2}\sqrt{\frac{1}{2}\left(1 + i\frac{\sqrt{\Delta_0^2 - E^2}}{E}\right)}, \\ v_0 = u_0^* &= e^{-i\varphi/2}\sqrt{\frac{1}{2}\left(1 - i\frac{\sqrt{\Delta_0^2 - E^2}}{E}\right)}. \end{aligned} \tag{7.21}$$

The form of Eq. (7.20) describes a wave with an envelope that decays exponentially over the length scale $\xi = \hbar v_F/\sqrt{\Delta_0^2 - E^2}$, where $v_F = \hbar k_F/m$ is the Fermi velocity.[8] The constituent waveforms for both regions are sketched in Fig. 7.5(b).

Matching the solutions at the material interface, $\mathbf{\Psi}_N(0) = \mathbf{\Psi}_S(0)$, we can eliminate t_+ and solve for the hole reflection amplitude, obtaining

$$r_h = \frac{v_0}{u_0} = e^{i\phi_A}\,e^{-i\varphi} = r_A\,e^{-i\varphi}, \qquad \phi_A = -\arccos\left(\frac{E}{\Delta_0}\right). \tag{7.22}$$

The reflected hole acquires two distinct phase factors: it inherits the phase of the superconductor, φ; it also gains an energy-dependent phase ϕ_A linked to the Andreev reflection process. For convenience, we have introduced the **Andreev reflection coefficient** r_A to quantify the φ-independent part of the amplitude. In the scenario considered here, with $E < \Delta_0$ and no scattering, $r_A = e^{i\phi_A}$ and $|r_A|^2 = 1$, meaning the electron is fully Andreev reflected. In situations where $E > \Delta_0$ or a scattering potential is present at the interface, the coefficient's amplitude decreases below unity, resulting in only partial Andreev reflection (see Ref. [232] for general solutions to the scattering problem).

The Andreev reflection mechanism is fundamental to how current flows through N-S junctions. In the process we have considered, an electron with charge $-e$ is removed from the normal metal, and a hole with charge $+e$ is added. Given that no charge is added to

---

[8] In order to arrive at the form of Eq. (7.20), it is necessary to linearize the quasiparticle wavevector as $q_+ \approx k_F + i/\xi$, where $k_F = \sqrt{2m\mu/\hbar^2}$ is the Fermi wavevector. This approximation is justified under the assumption that $\mu \gg \sqrt{\Delta_0^2 - E^2}$.

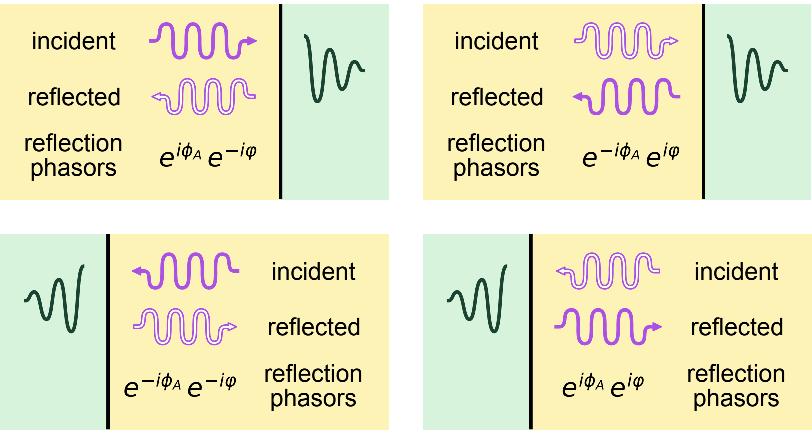

Figure 7.6: Summary of phase shifts acquired by the reflected particle during different Andreev reflection processes.

---

the Bogoliubon states in the superconductor, the question arises: *where did the net* $-2e$ *charge go?* The answer, as stated earlier, is that the charge is injected as a Cooper pair into the superconducting condensate. The impact of this double charge transfer can be measured directly in ballistic N-S junctions, which exhibit a doubling in conductance when they transition from the normal state to the superconducting state [232, 233].

We conclude this section with two further observations. Firstly, there is a small mismatch between the momenta of the incoming electron and outgoing hole. Overall momentum conservation requires that

$$k_e - k_h = q_+ \approx \frac{\sqrt{E^2 - \Delta_0^2}}{\hbar v_F} \ll k_F. \tag{7.23}$$

Thus, the Andreev-reflected hole carries slightly less momentum than the incident electron. Secondly, the scenario we have focused on, with an incident electron and reflected hole, is only one possible way for Andreev reflection to play out. The reverse process can also occur: an incident hole is Andreev-reflected as an electron, removing a Cooper pair from the condensate. In this case, the Andreev reflection phase acquired is $-\phi_A$. Moreover, if we swap the spatial orientation of the normal metal and superconductor (creating an S-N junction), the reflection phases flip signs. Figure 7.6 summarizes the phase shifts acquired by the reflected particles in each possible Andreev process.

7.2.2 The Proximity Effect

In our derivation of Andreev reflection, we treated the transition from normal metal to superconductor as an abrupt one, modeling the pair potential $\Delta(x)$ as a step function at the junction interface. For real materials systems, this transition is rarely so sharp. Atomistic disorder blurs the boundary between materials and often induces diffusive scattering, hindering the passage of particles through the junction. It also takes a finite amount of time for Cooper pairs to form and dissociate as they cross the interface. As a result, the transition from normal metal to superconductor is gradual, spanning an extended boundary between the materials. This boundary region, which exists in a sort of intermediate phase, is precisely the *hybrid* zone that matters for superconductor-semiconductor hybrid physics, as we will see.

Modeling transport through a fully realistic junction is a tall order beyond the scope of this dissertation, but even our idealized step-potential system reveals hints of a smooth variation between phases, as T. M. Klapwijk highlights in Ref. [234]. To gain insight into this extended transition, we first examine what happens to electrons after they enter the superconductor. We have already noted that the amplitudes $u(x)$ and $v(x)$ decay exponentially. These evanescent waves carry a quasiparticle current with density

$$J_Q(x) = \frac{e\hbar}{m}\,\mathrm{Im}\left(u^*\frac{\partial u}{\partial x} + v^*\frac{\partial v}{\partial x}\right) = 2ev_F e^{-2x/\xi}, \tag{7.24}$$

penetrating a distance $\sim \xi/2$ into the superconductor before the carriers are converted into Cooper pairs. The supercurrent density increases at the same rate the quasiparticle current dies away: $J_S(x) = 2ev_F(1 - e^{2x/\xi})$. The physical explanation behind this gradual conversion from quasiparticle current to supercurrent is that it takes a finite amount of time for the electron pairs to interact and develop phase coherence as they cross the interface into the

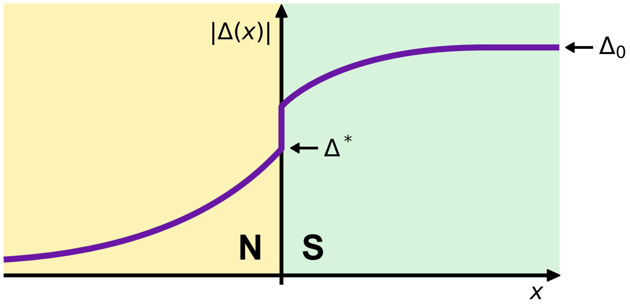

Figure 7.7: Superconducting pair potential magnitude $|\Delta(x)|$ near the interface of an N-S junction. Andreev transport across the interface modifies the density of states in both materials and creates an induced superconducting gap in part of the normal metal—this is known as the proximity effect. The functional form for $\Delta(x)$ is derived in Ref. [235].

superconductor.

On the other side of the interface, pairs of quasiparticles exiting the superconductor maintain their correlations for some time after crossing into the normal metal. This can be seen by inserting the BdG solutions from Eq. (7.19) into the Cooper pair spatial correlation function, yielding

$$\langle \psi_\uparrow(x)\, \psi_\downarrow(x) \rangle = \sum_{E>0} v^*(x)\, u(x) [1 - 2\nu(E)], \tag{7.25}$$

where $\nu(E)$ is the density of states. The product $v^*(x)\, u(x) \propto e^{i(k_e - k_h)x}$ in the summand is not a constant; since $k_e \neq k_h$ [Eq. (7.23)], it is a nontrivial function of E, giving each energy level a different weight in the sum. The end result is that superconducting correlations are nonzero in the part of the normal metal adjacent to the interface. This effect is commonly described as Cooper pairs 'leaking' into the normal metal.[9]

Remarkably, the Cooper pairs that venture into the normal metal endow it with a superconducting gap. The pair potential,

$$\Delta(x) = V_N(x)\, \langle \psi_\uparrow(x)\, \psi_\downarrow(x) \rangle = V_N(x) \sum_{E>0} v^*(x)\, u(x) [1 - 2\nu(E)], \tag{7.26}$$

---

[9] The sum in Eq. (7.25) does not have an closed-form solution except in the $T \approx T_c$ limit [235], so it is not possible to write out an explicit penetration depth for Cooper pairs leaking into the normal metal.

is finite in the normal region even when interactions between electrons are *repulsive* [$V_N(x) < 0$].[10] This observation sheds light on a phenomenon known as the **proximity effect**: when a normal metal is brought into contact with a superconductor, the superconducting correlations can extend into the normal region, altering its density of states and introducing an **induced superconducting gap (or mini-gap)**. The induced gap is always smaller than the gap of the parent superconductor and decays away in the normal metal bulk, as illustrated in Fig. 7.7. Conversely, the proximity effect also modifies the superconductor. The suppression of $|\Delta(x)|$ in the superconductor near the interface is known as the **inverse proximity effect**. This occurs due to the penetration of normal metal states into the superconducting region.

The behavior of the induced gap itself can vary based on the presence of sub-gap states. In systems with a **hard gap**, the density of states within the induced gap is zero, reflecting the complete absence of sub-gap quasiparticle states. In contrast, a **soft gap** indicates a nonzero density of states within the induced gap, typically due to disorder or inelastic scattering, leading to residual sub-gap quasiparticles. The distinction between hard and soft gaps is crucial for understanding the quality of the proximity effect and the dynamics of induced superconductivity in hybrid systems.

The magnitude of the induced gap, Δ^*,[11] and the length scale over which it diminishes depend strongly on the junction materials and on interface disorder. For some N-S pairs (e.g., bismuth and YBCO), the proximity effect is completely negligible; for others (e.g., copper and niobium) the proximitized region extends over mesoscopic length scales. A comprehensive theoretical description of the proximity effect in real systems is tricky, and can involve treatment of atomistic disorder, many conduction modes, and multiple types of scattering processes (see, for example, Refs. [236,237]). Nevertheless, our toy-model analysis provides some useful insight, illustrating that Andreev reflections at the interfaces of N-S

---

[10] While our Andreev reflection derivation assumed a step-function form for the pair potential, the correct method to determine $\Delta(x)$ from first principles is to solve Eq. (7.26) self-consistently with the BdG equations [235].

[11] Specifically, we define Δ^* as the value of $|\Delta(x=0)|$ on the normal-metal side of the interface. We will continue to use the notation Δ_0 and Δ^* to refer to the parent gap and induced gap magnitudes.

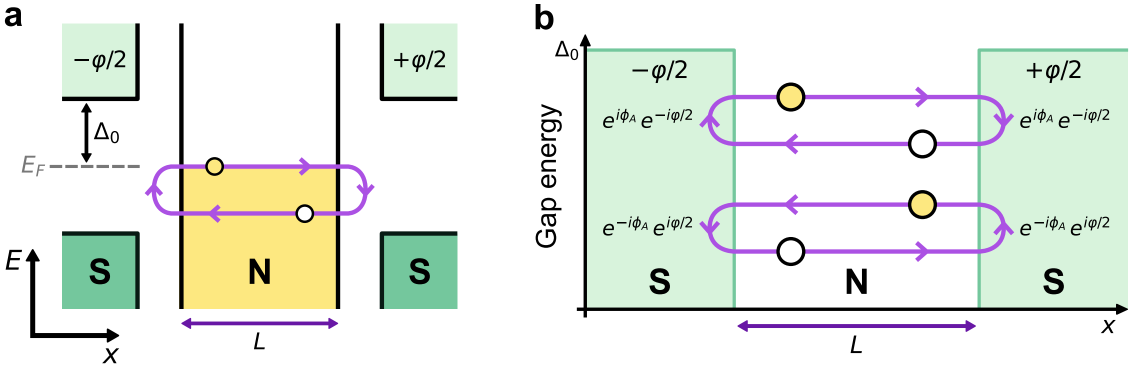

Figure 7.8: Transport through an S-N-S junction. **(a)** A carrier with energy $E < \Delta_0$ is Andreev-reflected at both interfaces, creating a cyclic transport loop. **(b)** The superconducting gap at the interfaces creates a square-well potential of depth Δ_0. Clockwise and counterclockwise transport loops are shown with phase shifts acquired from Andreev reflection at each interface.

---

junctions are the microscopic foundation giving rise to the proximity effect.

7.3 The S-N-S Junction

Now that we have studied in detail what happens at the interfaces between normal metals and superconductors, we can build up the junction complexity. Attaching a superconductor to the other side of the normal metal creates a **superconductor-normal metal-superconductor (S-N-S) junction**. The addition of a second interface introduces a new type of quantum state and unexpected phenomena, making these junctions essential components in many technological applications.

7.3.1 Andreev Bound States

Consider the one-dimensional S-N-S junction illustrated in Fig. 7.8(a) with a normal metal of length L sandwiched between two superconductors. For simplicity, we will ignore the proximity effect in the normal region and take the superconductors to be made from the same material with a gap of Δ_0. However, since the superconductors are separated from each other, they are allowed to take different *phases*. Let the phase difference across the junction be φ. Without loss of generality, we can distribute this difference evenly between the two pieces of superconductor, taking the left side's phase to be $-\varphi/2$ and the right side's phase be $+\varphi/2$. In experiments, this type of phase difference can be generated by embedding the junction in a superconducting loop threaded with magnetic flux from an out-of-plane field.

Imagine an electron with energy $E < \Delta_0$ moving rightward through the normal-metal region of the junction. From our previous discussion, we know that the electron undergoes Andreev reflection when it reaches the interface with the right-side superconductor. The resulting hole, moving leftward, propagates through the normal metal until it, too, is Andreev-reflected at the left-side interface, returning the system to its initial state with a rightward-moving electron. The cycle of reflections can continue indefinitely, creating a transport loop depicted in Fig. 7.8(a). As a result, a carrier always remains 'trapped' inside the normal region, giving rise to spatially localized states with discrete energy levels. The scenario is analogous to the classic quantum mechanics problem of determining the bound states in a finite square well. For the S-N-S junction we consider, a potential well is formed by the superconducting gap energy Δ_0 at each interface, as Fig. 7.8(b) depicts. The bound-state solutions within this well are known as **Andreev bound states (ABS)**, derived by Beenaker and Van Houten [238] and Furusaki and Tsukada [239] in 1991.

ABS are born out of constructive interference between the Andreev reflection phases at each interface. For the 'clockwise' transport loop we have described, shown by the upper path in Fig. 7.8(b), Andreev reflection shifts the carrier's phase by $\phi_A - \varphi/2$ at each interface (see Fig. 7.6 to review the phase shifts for each reflection). Mathematically, the condition for constructive interference is that the total phase shift for the cycle is a multiple of 2π:

$$2\phi_A - \varphi = 2\pi n, \tag{7.27}$$

where n is an integer [147].[12] The reverse transport cycle, shown by the lower, counterclockwise path in Fig. 7.8(b), results in an identical interference condition. Inserting the definition of ϕ_A from Eq. (7.22), the interference condition leads to a pair of bound-state energy levels

$$E_A(\varphi) = \pm\Delta_0 \cos\left(\frac{\varphi}{2}\right), \tag{7.28}$$

with the negative branch corresponding to the clockwise transport loop and the positive branch corresponding to the counterclockwise loop for $0 < \varphi < \pi$ (the loop directions associated with each branch are reversed for $-\pi < \varphi < 0$). This equation describes an ideal case without considering disorder in the junction. However, in real systems, carriers may scatter at the interfaces or as they pass through the normal metal, altering the ABS energy spectrum. We can account for this scattering by introducing a parameter τ into our model which quantifies the normal-region transmission probability; in the literature, this parameter is often labeled **junction transparency**. Using a scattering matrix formalism to model transport through the junction, the modified Andreev spectrum can be worked out to be

$$E_A(\varphi) = \pm\Delta_0\sqrt{1 - \tau \sin^2\left(\frac{\varphi}{2}\right)}, \tag{7.29}$$

which simplifies to Eq. (7.28) when $\tau = 1$ (perfect transmission) [238]. Figure 7.9(a) plots the ABS energy levels, both with and without scattering. For both cases, the levels vary in energy with the junction phase difference, reaching their minimum energy magnitude at $\varphi = \pi$. The presence of scattering in the normal region mixes the transport loops and opens an avoided level crossing of $2\Delta_0\sqrt{1-\tau}$ at this minimum. An example of experimentally measured ABS, visible in the density of states of a carbon-nanotube S-N-S device, is shown in Fig. 7.9(b), adapted from Ref. [240] by Pillet *et al.*[13]

---

[12] In Eq. (7.27), we are neglecting an additional dynamical phase acquired by the carriers as they propagate through the normal metal. This is safe to do as long as the junction length is short compared to the zero-energy coherence length, $L \ll \xi_0$, where $\xi_0 = \hbar v_F/\Delta_0$.

[13] The pair of ABS in this measurement have their minimum energy magnitude at $\varphi = 0$ rather than $\varphi = \pi$, due to the convention the authors chose for defining φ in their junction phase-biasing scheme.

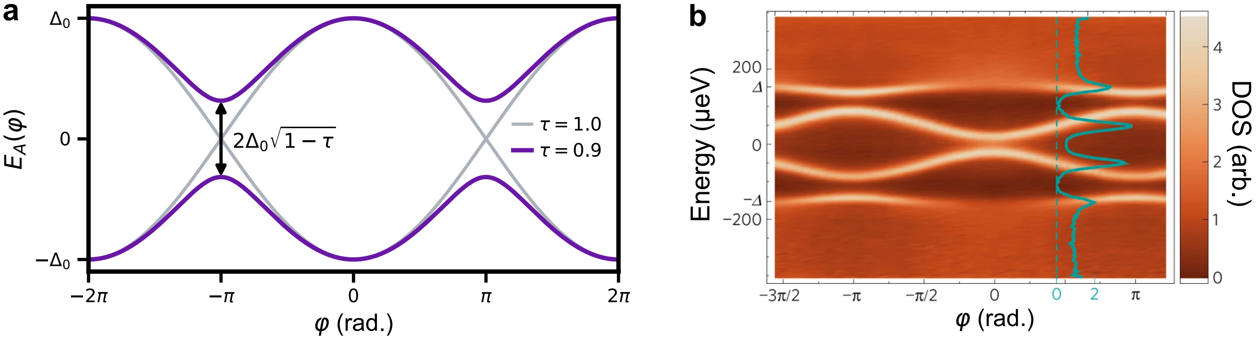

Figure 7.9: ABS energy levels. **(a)** Energy levels plotted for an S-N-S junction with no scattering ($\tau = 1$; gray) and with scattering in the normal metal ($\tau < 1$; purple). **(b)** ABS measured in the density of states (DOS) of a carbon-nanotube S-N-S device. A DOS line cut is overlaid in teal. Figure adapted from Ref. [240]. Reproduced with permission from Springer Nature.

The emergence of bound states in S-N-S junctions provides a new perspective for understanding these systems. Rather than tracking the transport of individual electrons and holes, ABS allow us to conceptualize the junctions' behavior in terms of discrete quantum states and their occupation. Much like bound states in a square well, Andreev levels are fermionic modes capable of hosting particles. In the ABS abstraction, these particles are best understood as quasiparticles, formed from the superposition of electrons and holes in the underlying transport cycles. Importantly for applications in quantum information processing, the ABS quasiparticles inherit spin and charge from the electrons and holes of which they are built. Consequently, Andreev levels exhibit a twofold spin degeneracy unless disrupted by an external magnetic field or spin-orbit coupling. Figure 7.10(a) illustrates an S-N-S junction using the ABS framework. The quasiparticles occupying the Andreev levels are drawn with half-filled circles to emphasize their dual electron-hole composition, with the spin degeneracy of each level clearly shown.

7.3.2 The Josephson Effect

The ABS abstraction not only simplifies our understanding of the quantum states within S-N-S junctions but also offers insight into how these states contribute to current transport.

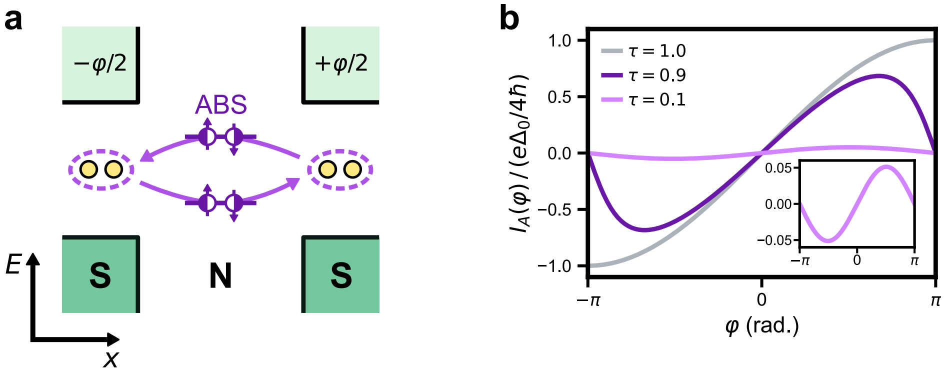

Figure 7.10: Current flow through ABS. **(a)** ABS in an S-N-S junction occupied by spin-1/2 quasiparticles. Arrows illustrate pathways for Cooper pairs to move between superconductors via occupation of the ABS, valid for $0 < \varphi < \pi$. **(b)** Josephson supercurrent carried by ABS quasiparticles in junctions of different transparencies. Inset: zoomed-in view of the curve for a low-transparency ($\tau = 0.1$) junction.

At low energies, ABS serve as microscopic channels through which current flows across the junction. A Cooper pair approaching the junction can break into two quasiparticles, each occupying an ABS. The quasiparticles can then traverse the normal-metal region while maintaining their phase coherence, and upon reaching the opposite side, recombine into a Cooper pair, effectively transporting a pair of charges across the junction. This transport process, illustrated in Fig. 7.10(a), is dual to our earlier description of individual electrons and holes crossing the junction and undergoing Andreev reflection at the interfaces, while being somewhat simpler to conceptualize. The current carried through each Andreev level varies with the junction phase:

$$I_A(\varphi) = \frac{2e}{\hbar}\frac{\partial E_A}{\partial \varphi}. \tag{7.30}$$

By convention, the sign of $I_A(\varphi)$ indicates to the direction of Cooper pair movement across the junction. In our junction, when $0 < \varphi < \pi$, current is carried from left to right through the negative-energy ABS, and from right to left through the positive-energy ABS (the current-flow directions are flipped when $-\pi < \varphi < 0$).

Remarkably, Eq. (7.30) implies a flow of a *persistent supercurrent* through S-N-S junctions when $\varphi \neq 0$. Consider the junction in its ground state, free from any external perturbation.

All states with $E < 0$ are occupied, and the negative-energy Andreev level hosts a spin-degenrate pair of quasiparticles, which, from Eq. (7.30), transport a current [63]

$$I_A(\varphi) = \frac{e\Delta_0}{2\hbar} \frac{\tau \sin\varphi}{\sqrt{1 - \tau \sin^2(\varphi/2)}}. \tag{7.31}$$

Since no voltage bias is required to generate this current, it is identified as supercurrent which flows between the superconducting leads, unimpeded by the normal-metal barrier. This phenomenon is known as the **dc Josephson effect** after the theorist Brian Josephson who predicted it in 1962 [241], and the S-N-S junction is commonly referred to as a **Josephson junction**.[14] The Josephson supercurrent, plotted in Fig. 7.10(b), is a periodic, sine-like function with a strong forward skew for highly transparent junctions. In the low-transparency regime where $\tau \ll 1$, Eq. (7.31) takes a simplified, sinusoidal form more commonly associated with the Josephson effect:

$$I_A(\varphi) \approx I_c \sin\varphi, \tag{7.32}$$

where $I_c = e\Delta_0\tau/2\hbar$ is the junction's critical current value. There is also an **ac Josephson effect**, in which the junction's phase evolves cyclically in time when a voltage V is applied. The rate of phase winding, which we do not derive here, is $\dot{\varphi} = 2eV/\hbar$ [241].

Josephson junctions exhibit a variety of interesting and useful behavior. They are a workhorse circuit element in many superconducting qubits thanks to their nonlinear inductance. Two Josephson junctions wired in parallel in a superconducting loop can produce a macroscopic quantum interference pattern which is extremely sensitive to magnetic field variation. These **superconducting quantum interference devices (SQUIDs)** are frequently used for magnetometry in various applications.

Before moving on, we note that the energy and current relations derived in this section

---

[14] The Josephson effect is actually a general phenomenon that occurs whenever two superconductors are placed in close proximity with some 'weak link' separating them. In our case, the weak link is a normal metal, but it can also be an insulator (S-I-S junction) or a physical constriction in a continuous piece of superconducting metal (S-c-S junction). All of these are examples of Josephson junctions.

are for one-dimensional S-N-S junctions with a single conduction channel, describing an ideal quantum point contact. In practice, systems typically contain multiple channels, each with a distinct transparency. As a result, these junctions host a more extensive set of ABS with energies

$$E_{A,i}(\varphi) = \pm\Delta_0\sqrt{1 - \tau_i \sin^2\left(\frac{\varphi}{2}\right)}, \tag{7.33}$$

where τ_i denotes the transparency of the mode i. The Josephson supercurrent flowing through a multi-channel junction is summed over all the modes:

$$I_A(\varphi) = \frac{2e}{\hbar}\sum_i \frac{\partial E_{A,i}}{\partial \varphi} = \frac{e\Delta_0}{2\hbar}\sum_i \frac{\tau_i \sin\varphi}{\sqrt{1 - \tau_i \sin^2(\varphi/2)}}. \tag{7.34}$$

In the low-transparency limit, this relation simplifies to Eq. (7.32) with $I_c = (\pi\Delta_0/2e)G_N$, where the normal-state conductance is given by the Landauer formula, $G_N = (2e^2/h)\sum_i \tau_i$ [242].

7.4 The Josephson Field-Effect Transistor

At last, we are ready to bring semiconductors into the picture and explore superconductor-semiconductor hybrid junctions. Our discussion will focus on a special class of S-N-S junctions where the normal 'metal' is replaced by a semiconductor (Sm), forming a **superconductor-semiconductor-superconductor (S-Sm-S) junction**. This system exhibits all the physical phenomena we have covered so far, including Andreev reflection, the proximity effect, ABS, and Josephson physics. What distinguishes S-Sm-S junctions is that the proximitized region between the superconductors maintains its semiconductor properties—most notably, the carrier density in this region is tunable via the field effect, allowing the superconducting behavior of the junction to be controlled by gates. For this reason, S-Sm-S junctions are frequently implemented as a gated quantum device known as a **Josephson field-effect transistor (JoFET)** [243]. Figure 7.11(a) provides a schematic

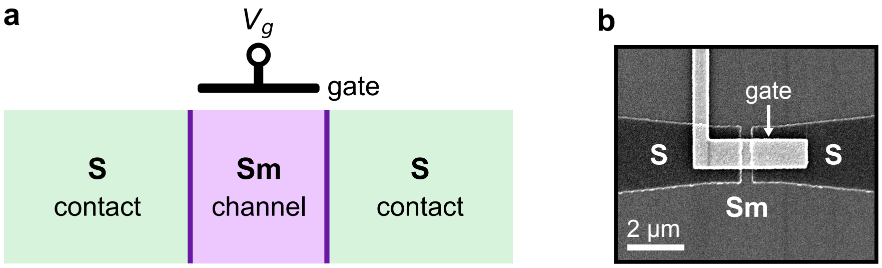

Figure 7.11: The Josephson field-effect transistor (JoFET). **(a)** Scehmatic representation of an S-Sm-S junction realized as a JoFET. A voltage V_g is applied to the channel gate. **(b)** Scanning electron micrograph of a JoFET fabricated on a semiconductor heterostructure.

---

representation of a JoFET. The device derives its name from its three-terminal geometry—with two superconductring **contacts** and a gated semiconductor **channel**—which mirrors that of a conventional field-effect transistor. A variety of semiconductor nanostructures can be used to create JoFETs, including quantum wells [244], nanowires [245], nanotubes [246], and 2D materials [247]. An example of a real, planar-geometry JoFET fabricated on a semiconductor heterostructure is shown in Fig. 7.11(b).

Electrostatic tuning in a JoFET impacts the junction's transport behavior in multiple ways. Within the semiconductor channel, adjusting the gate voltage modifies both the density and spatial distribution of carriers through the field effect, which in turn influences the frequency of scattering events. At the S-Sm interfaces, the applied electric field can screen defects and modulate the Schottky barrier between materials, affecting the amplitudes for scattering and Andreev reflection [248, 249]. As a result of these combined effects, the passage of Cooper pairs into the semiconductor is highly sensitive to electrostatic gating. Consequently, many of the junction properties we have discussed—including the magnitude and hardness of the induced superconducting gap, the junction transparency, and the critical current—become functions of the gate voltage V_g. Theoretically, it has been shown that for short junctions, the critical current scales as

$$I_c(V_g) \propto \Delta^*(V_g)\ \tau(V_g) \propto n^{2/3}, \tag{7.35}$$

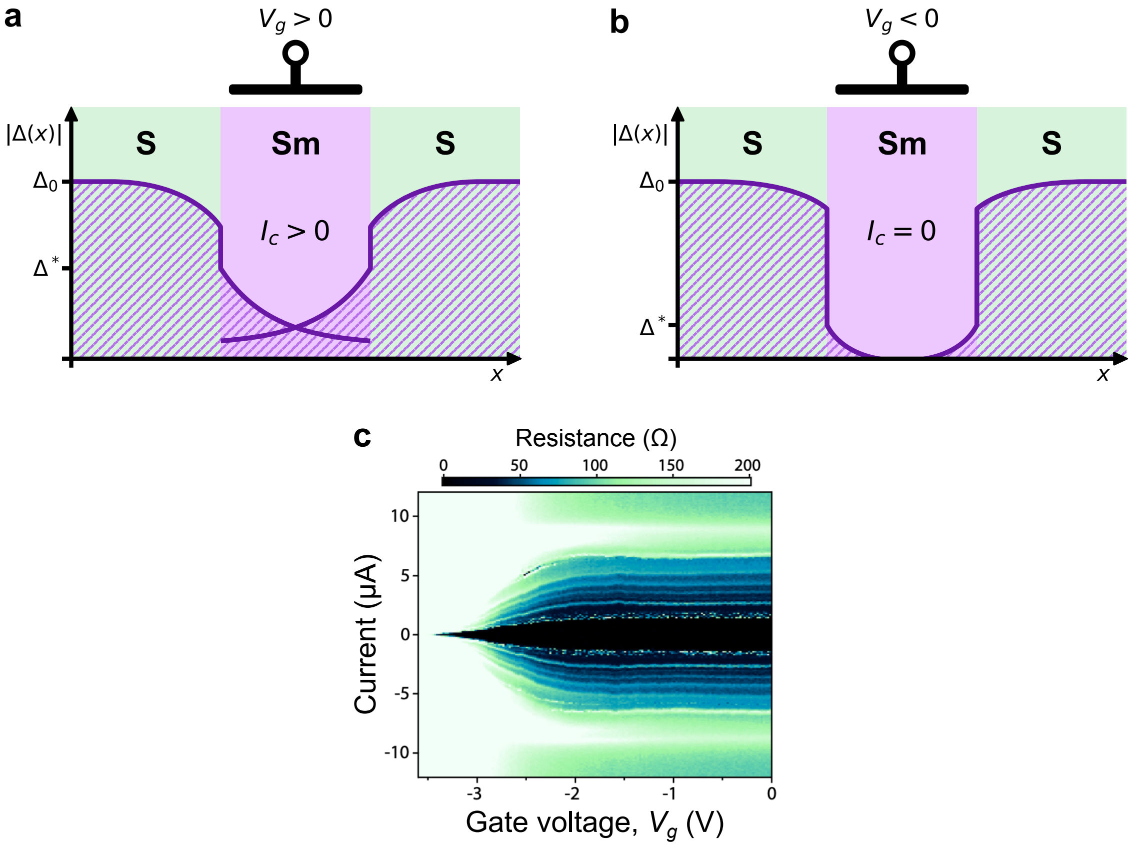

Figure 7.12: Gate-tunable superconductivity in a JoFET. **(a)** Effective gap plotted across the junction when $V_g > 0$. In this regime, the entire channel is proximitized, and the junction is in the superconducting state with $I_c > 0$. **(b)** Same as (a), but when $V_g < 0$. In this regime, the induced gap vanishes inside the channel, and the junction conducts in the normal state with $I_c = 0$. **(c)** Experimentally measured tunability of the critical current an InAs-based JoFET. Figure adapted with permission from Ref. [251]. © 2016 by the American Physical Society.

---

where n is the carrier density in the semiconductor channel; for longer junctions, the dependence on carrier density can be stronger than $\sim n^{2/3}$ [248–250]. In practice, however, the complex interplay of materials properties and the multifaceted impact of electrostatic gating makes it challenging to develop a theoretical model for realistic systems. Therefore, the precise form of $I_c(V_g)$ is typically determined experimentally for each specific device [249].

Figure 7.12 provides an illustrative example of JoFET behavior, shedding light on how the field effect can be used to tune the junction between different conduction regimes. The pair potential $|\Delta(x)|$ is plotted across the junction, with a gap induced from the contacts on both sides of the semiconductor. Assuming an n-type channel, applying a positive gate voltage ($V_g > 0$) pulls more carriers into the channel and enhances the proximity effect, inducing a gap of magnitude Δ^* that spans the entire channel length, as shown in panel (a). In this regime, a persistent Josephson supercurrent flows through the channel, with a critical current $I_c > 0$. Conversely, applying a negative gate voltage ($V_g < 0$) diminishes the proximity effect, reducing both Δ^* and I_c. When V_g is sufficiently negative, the induced gap can be fully suppressed in the center of the channel, and the junction transitions into the normal state, with $I_c = 0$, as shown in panel (b). An experimental demonstration of this behavior is seen in Fig. 7.12(c), which has been adapted from Ref. [251] by Shabani *et al.* In this measurement of an InAs-based JoFET, the junction transitions from normal to superconducting around $V_g \approx -3.5$ V. As the gate voltage is further increased, the critical current grows and eventually stabilizes to $I_c \approx 1.5$ µA. The horizontal 'stripes' visible outside the superconducting region are created by multiple-Andreev-reflection transport processes.

Although the examples in Fig. 7.12 refer to n-type JoFETs with electron carriers in the channel, we should remember that Andreev reflection, which underlies the proximity effect, involves both electron and hole processes symmetrically. Therefore, it is equally possible to construct a p-type JoFET with hole carriers in the channel. All of the same junction physics applies, with the only difference being that the dependence of the field-effect accumulation on V_g is inverted.

In addition to the field effect, the proximitized channel of a JoFET inherits other properties from the semiconductor, including those relevant to spin physics, such as the g-factor and spin-orbit interaction. These properties are vitally important: as we are about to see, the unique combination of spin physics and superconductivity in hybrid junctions opens the door to many applications in quantum information processing.

7.5 Constructing Qubits from Hybrid Junctions

Superconductor-semiconductor hybrid junctions form a versatile building block for making qubits. Their ability to leverage both gate-tunable superconductivity and spin physics provides a route to controlling quantum states with high precision. We will briefly discuss three classes of qubits realized using hybrid junctions: gatemon qubits, Andreev qubits, and topological qubits. Each of these qubits uses different aspects of the junctions' physics, from tunable Josephson energy to Andreev states and Majorana modes.

7.5.1 Gatemon Qubits

Gatemon qubits utilize the gate-tunable Josephson effect in S-Sm-S junctions. These qubits are based on the widely used transmon qubit design, with logical states defined by the anharmonic energy levels of a superconducting circuit [11,12]. However, instead of using a traditional Josephson junction as a circuit element, the gatemon employs a JoFET, as diagrammed in Fig. 7.13(a). In this circuit, the energy separation between states is directly influenced by the Josephson energy,

$$E_J(V_g) = \frac{\hbar}{2e} I_c(V_g), \tag{7.36}$$

which is a function of the gate voltage, thanks to the JoFET's semiconductor channel. By tuning E_J via the field effect, it is possible to control the qubit frequency and perform qubit operations. Gatemon qubits implemented using nanowire [252,253] and quantum-well [254] JoFETs have demonstrated relatively high coherence times, while offering the advantage of electric-field tunability, making them attractive for scalable quantum processors.

7.5.2 Andreev Qubits

Andreev qubits encode quantum information in the ABS formed within S-N-S junctions. These qubits can be made by embedding a JoFET in a flux-bias loop, as shown in Fig. 7.13(b).

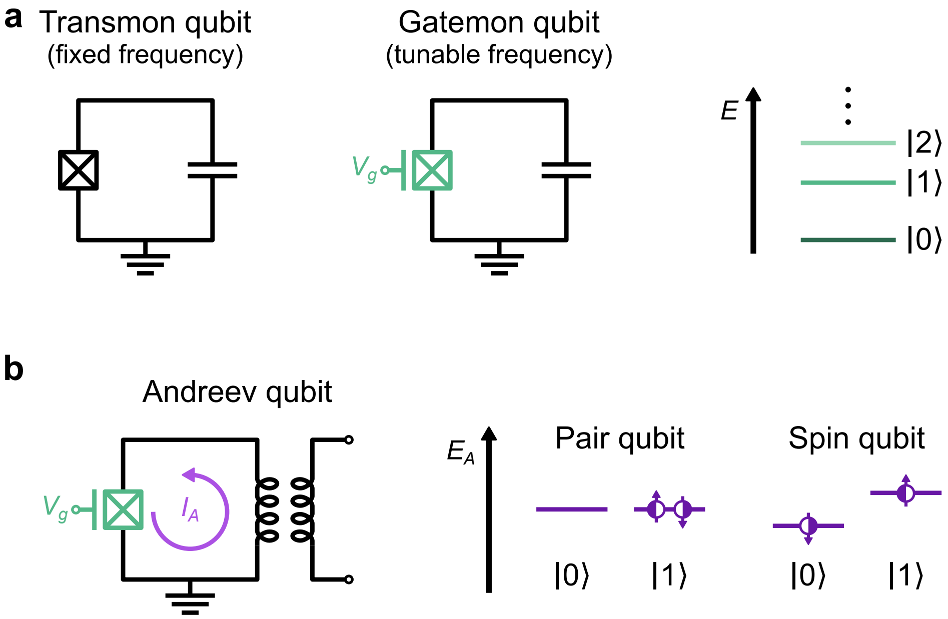

Figure 7.13: Qubits built from hybrid junctions. Superconducting circuit schematics and energy-level encodings for defining **(a)** gatemon qubits and **(b)** Andreev qubits. The '⊠' symbol is used to represent a Josephson junction element in the circuit schematics.

The ABS-mediated supercurrent I_A running through the loop can be inductively coupled to a superconducting circuit, enabling manipulation and measurement of the ABS with cQED techniques, thus providing a versatile platform for quantum control.

The first Andreev qubits, known as **Andreev pair qubits**, were realized by encoding quantum information in the occupation of a spin-degenerate pair of Andreev levels given by Eq. (7.29) [143, 255]. In this scheme, the qubit's $|0\rangle$ state is defined by the absence of quasiparticles occupying these levels, while the $|1\rangle$ state corresponds to both levels being occupied by a pair of quasiparticles, as Fig. 7.13(b) illustrates. Qubit operations are achieved by applying microwaves at a frequency $f = 2E_A(\varphi)/h$. A tone of this frequency provides the precise energy required to break a Cooper pair in the condensate and populate the Andreev levels with the resulting quasiparticles, effectively driving transitions between $|0\rangle$ and $|1\rangle$. The qubit frequency can be tuned by varying φ and by dynamically adjusting the junction transparency using the JoFET's gate voltage. Despite this versatility, the Andreev pair qubit's design suffers from challenges, primarily due to its susceptibility to **quasiparticle**

poisoning—a process in which unwanted quasiparticles, generated by thermal excitations or external noise, infiltrate the system and occupy the Andreev levels, causing decoherence.

To overcome these limitations, the **Andreev spin qubit** was developed, utilizing the spins of the quasiparticles occupying the ABS [256,257]. This approach leverages spin-orbit coupling and Zeeman splitting in the JoFET's semiconductor channel to separate the ABS into distinct spin states, which can be manipulated using microwave pulses.[15] Encoding quantum information into spin states makes the qubit less vulnerable to quasiparticle poisoning.

In many ways, Andreev spin qubits bear a resemblance to another system we examined in earlier chapters: quantum-dot spin qubits coupled to resonators. Both platforms encode quantum information in long-lived fermionic spin states, exploiting the relative stability of spin over charge to reduce susceptibility to noise. A key distinction between these systems lies in how the qubits couple to their respective electromagnetic environments. In quantum-dot spin qubits, the coupling to a resonator relies on the tiny dipole of an electron in a DQD, resulting in a relatively weak interaction. In contrast, Andreev spin qubits achieve much stronger resonator coupling, as the interaction is mediated by the macroscopic supercurrent flowing through a Josephson junction. This supercurrent effectively amplifies the coupling strength, enabling more efficient qubit-resonator interactions, which in turn facilitates faster qubit control and readout [147].

7.5.3 Topological Qubits

The most exotic, ambitious, and potentially groundbreaking application of hybrid junctions would be in realizing a **topological qubit** which is protected against decoherence and errors at the hardware level. The history of this qubit is as captivating as the physics behind it; its conceptual roots trace back to the enigmatic Italian physicist Ettore Majorana. In

---

[15] Note that we are sweeping a lot of details under the rug here—driving spin flips to transition between $|0\rangle$ and $|1\rangle$ in this system involves the use of higher-energy states and Raman processes [257].

1937, Majorana theorized the existence of a special type of fermion that acts as its own antiparticle—the so-called **Majorana fermion** [258]. While extensive searches have failed to uncover Majorana fermions as elementary particles in nature, theorists later recognized that something analogous could exist as a quasiparticle in condensed matter systems. In these systems, **Majorana zero modes (MZMs)** emerge as zero-energy edge states within topological phases of matter. MZMs are always created and destroyed in pairs, and, like Majorana's elusive particle, they act as their own antiparticle—if two MZMs are brought into contact, they annihilate one another.

Another intriguing aspect of MZMs is their exotic exchange statistics. In three dimensions, particles are classified as either bosons or fermions, depending on how the wavefunction of a multi-particle system transforms under the exchange of identical particles. Swapping the spatial positions of two particles leads to the transformation

$$\psi(x_2, x_1) = \begin{cases} \psi(x_1, x_2) & \text{for bosons,} \\ -\psi(x_1, x_2) & \text{for fermions.} \end{cases} \tag{7.37}$$

Another class of particles with more intricate exchange statistics, known as **anyons**, can exist in fewer than three dimensions. **Abelian anyons**—such as the quasiparticles found in the $\nu = 3/2$ fractional quantum Hall state—accumulate a general phase factor upon exchange:

$$\psi(x_2, x_1) = e^{i\theta_{12}}\, \psi(x_1, x_2), \tag{7.38}$$

where θ_{12} is a system-dependent constant. **Non-Abelian anyons**—including MZMs—obey more complex exchange relations. When two non-Abelian anyons are swapped, the system's wavefunction does not accumulate a global phase but instead undergoes a nontrivial evolution:

$$\psi(x_2, x_1) = \mathbf{R}_{12}\, \psi(x_1, x_2), \tag{7.39}$$

where $\mathbf{R}_{12}$ is a unitary operator. In systems with multiple non-Abelian anyons, pairs of particles can be exchanged in non-commutative sequences. The operation of physically moving the particles around to execute these sequences is commonly referred to as **braiding**—as illustrated in Fig. 7.14(a), the worldlines of the interchanged particles resemble braided cords [259].

Together, the self-antiparticle nature and exotic exchange statistics of MZMs establish a new framework for **topological quantum computing**, first envisioned by the Russian physicist Alexei Kitaev [260]. Quantum information can be encoded non-locally in the combined parity state of a pair of MZMs. Since these quasiparticles can be spatially separated from each other, they offer inherent protection against local sources of noise or decoherence. Any perturbation that does not simultaneously affect both MZMs leaves the encoded information intact. By braiding groups of MZMs in particular sequences, quantum gate operations can be performed, relying on the system's topology[16] to ensure robustness against errors. After implementing gates in this manner, the parity of each MZM pair can be measured by bringing the quasiparticles together, allowing them to self-annihilate in a process known as **fusion readout**. In summary, MZMs in one- or two-dimensional solid-state systems possess all the essential properties to act as error-resistant topological qubits, positioning them as strong candidates to revolutionize fault-tolerant quantum computing.

Realizing Majoranas in Hybrid Junctions

Realizing MZMs experimentally has been, and remains, a significant challenge. In 2001, Alexei Kitaev proposed a theoretical model, now known as the **Kitaev chain**, consisting of a chain of spin-polarized fermions with superconducting pairing, in which MZMs naturally emerge at the ends of the chain [262]. Kitaev's toy-model system provides motivation to search for MZMs in **topological superconductors**, which exhibit spin-polarized, or 'p-

---

[16] The mathematical topology underlying these systems is beyond the scope of this dissertation. For further reading, I recommend the excellent review article by Lahtinen and Pachos [259] or Benjamin Woods' thesis [261].

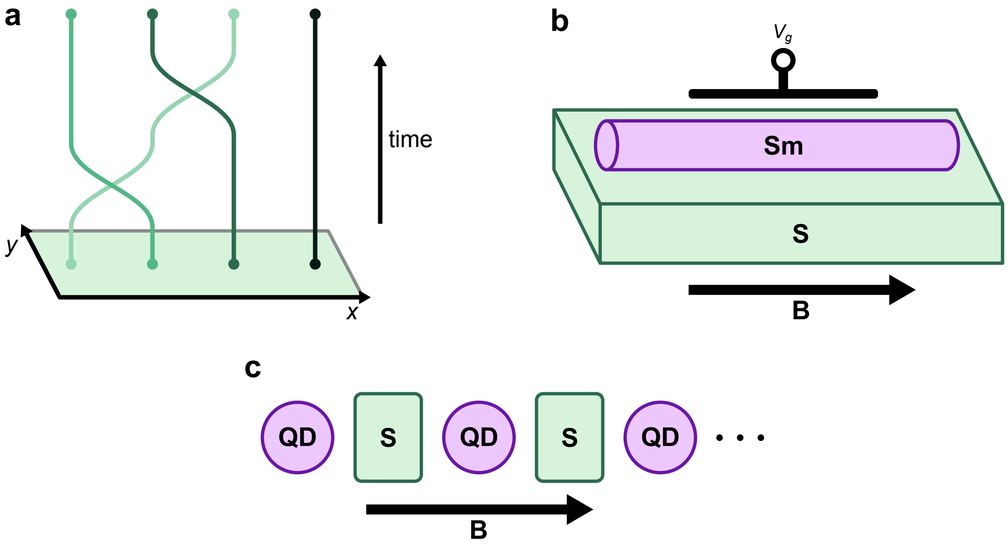

Figure 7.14: MZMs in topological hybrid junctions. **(a)** Particle worldlines illustrating non-Abelian braiding in a two-dimensional system with four MZMs. **(b)** Depiction of a Majorana nanowire. An external magnetic field is applied to proximitized semiconductor nanowire with spin-orbit coupling. The system can be tuned into an engineered topological phase by adjusting the gate voltage V_g and field $\mathbf{B}$, resulting in MZMs localized at the nanowire tips. **(c)** Diagram of an artificial Kitaev chain constructed from an alternating array of quantum dots and superconductors. When the tunnel rates and external field $\mathbf{B}$ are properly tuned, MZMs are localized in the outer dots. In a chain of sufficient length, the MZMs are topologically protected.

wave,' electron pairing—distinct from the conventional superconducting pairing between electrons of opposite spin. In these systems, spatially localized MZMs are predicted to appear at the boundary between the topological superconductor and surrounding regions of trivial topology.

While naturally occurring topological superconductors have yet to be observed, several platforms have been proposed to synthetically engineer topological superconductivity in hybrid junctions. The first of these proposals were introduced by Lutchyn *et al.* [263] and Oreg *et al.* [264] in 2010. Their approach, depicted in Fig. 7.14(b), involves placing a semiconductor nanowire with strong spin-orbit coupling in close proximity to a conventional superconductor, creating an S-Sm junction. When a magnetic field is applied along the wire, the combination of proximity-induced superconductivity, spin-orbit coupling, and Zeeman splitting mimics the the p-wave pairing mechanism of a topological superconductor. The proximitized nanowire can be tuned into a phase of topological superconductivity by adjusting the magnetic field strength and chemical potential. The onset of this phase is marked by the appearance of MZMs at the junction boundaries, as well as by the emergence of a **topological gap** in the density of states, which separates the zero-energy MZMs from higher-energy excitations. This gap ensures that small perturbations do not disrupt the MZMs' quantum state (similar to how the conventional superconducting gap prevents Cooper pairs from scattering). In the years following the original Majorana nanowire proposal, two-dimensional hybrid-junction platforms have also been suggested for realizing MZMs, including phase-tuned JoFETs and gate-defined nanowires in planar heterostructures [251, 265–268].

Over the past fifteen years, each of these hybrid-junction systems has been extensively studied in experiments, with several works reporting the observation of signatures consistent with MZMs or topological superconductivity [269–278]. However, a key challenge in all of these platforms is the presence of disorder. Impurities and defects in the proximitized semiconductor or surrounding materials can lead to the appearance of trivial zero-energy states that are not topologically protected, yet indistinguishable from MZMs in many types of experiments [261]. This issue has led to several high-profile claims of MZM discovery being retracted or reconsidered upon realizing that the observed signals were likely due to disorder-induced trivial states [279]. To combat the problem, Microsoft's topological quantum computing group has introduced a rigorous protocol for experimentally identifying MZMs, designed to be robust against false-positive signatures caused by disorder [280]. In 2023, the same team was able to measure zero-energy states meeting their stringent criteria in gate-defined nanowires—though whether these states are true MZMs remains a subject of ongoing debate in the research community [281]. With 'smoking gun' evidence for MZMs still lacking, the challenge of overcoming disorder and unambiguously distinguishing between topological and trivial states in hybrid junctions remains one of the biggest obstacles in the field.

Recently—some two decades after Kitaev's original proposal—the Kitaev chain concept has resurfaced and garnered renewed interest as a platform for realizing MZMs. Artificial Kitaev chains can be constructed using a different type of hybrid-junction system depicted in Fig. 7.14(c): a linear array of spins trapped in proximitized quantum dots with an applied magnetic field [282]. Minimal versions of these chains, made from two spin-polarized quantum dots coupled to a shared superconducting lead, have been experimentally implemented in both one-dimensional [283] and two-dimensional platforms [284]. These experiments have successfully measured zero-energy **poor man's Majorana** states, which approximate some of the characteristics of MZMs, but lack topological protection [285, 286]. However, by extending the length of the chain and fine-tuning the couplings, it is believed that fully topologically protected MZMs can be realized. Importantly, the quantum dot-based approach is also considered more robust against disorder than nanowire or JoFET-based systems, making it a compelling direction for ongoing experimental efforts [282].

7.5.4 Important Junction Properties

As we conclude our discussion of hybrid-junction qubits, we summarize the junction properties that are most essential for achieving qubits with high performance and fidelity. Many of these properties are directly linked to the quality of the S-Sm interfaces in the junction. Achieving pristine interfaces is crucial for hybrid-junction qubits and poses a significant challenge in materials engineering. One is reminded of Wolfgang Pauli's quote: *"God made the bulk; surfaces were invented by the Devil"* [287].

A **hard induced superconducting gap** is one of the most fundamental requirements for hybrid junctions used in qubit applications [267, 268]. Any sub-gap quasiparticle states can introduce decoherence through quasiparticle poisoning. For robust qubit coherence, the induced gap must be devoid of low-energy excitations, ensuring a clear energy separation that isolates the qubit from environmental noise and disturbances.

In addition to a hard gap, a **large induced superconducting gap** is critical for both topological and Andreev qubits. For topological qubits, the maximum achievable topological gap—the energy scale that protects MZMs from thermal excitations and noise—is approximately half of the induced superconducting gap at zero magnetic field [279]. A larger topological gap directly translates into better protection for the MZMs, which enhances the fault tolerance of the qubit. For Andreev qubits, the size of the induced gap sets an upper bound on the energy scale of the system. A larger induced gap creates more room for spin-splitting, making it easier to resolve and manipulate the spin states of the ABS. It also reduces the probability of leakage into unwanted states.

Strong spin-orbit coupling and a **large *g*-factor** are essential for generating Zeeman splitting and manipulating spin states in both topological and Andreev spin qubit encodings. Herein lies a potential pitfall of forming highly transparent junction interfaces: if the hybridization between materials becomes too pronounced, the semiconductor can inherit the properties of the parent superconductor, leading to a weakening of the g-factor and spin-orbit interaction [279]. It is therefore important to carefully engineer interfaces to achieve the right degree of S-Sm coupling.

A significant challenge in realizing topological superconductivity is the need for **resilience to magnetic fields**. Conventional approaches to engineering topological superconductivity typically require a field of around 1 T to reach the topological phase [267, 268]. For hybrid junctions to be effective in such systems, they must maintain a substantial induced gap even in the presence of large fields. In experiments, magnetic fields are typically applied parallel with the device substrate, as superconducting thin films can endure higher in-plane fields than out-of-plane fields. To ensure the induced gap remains stable over a range of fields, the parent superconductor should possess an in-plane critical field of $B_{c,\parallel} \gtrsim 1$ T.

Finally, **minimal disorder** in hybrid junctions is paramount for achieving good qubits. Disorder can degrade junction performance in several ways. At S-Sm interfaces, disorder can soften the superconducting gap and reduce the strength of the proximity effect, making it difficult to induce a robust superconducting state in the semiconductor. For topological qubits, disorder can hinder the spatial separation of MZMs, which is essential for their

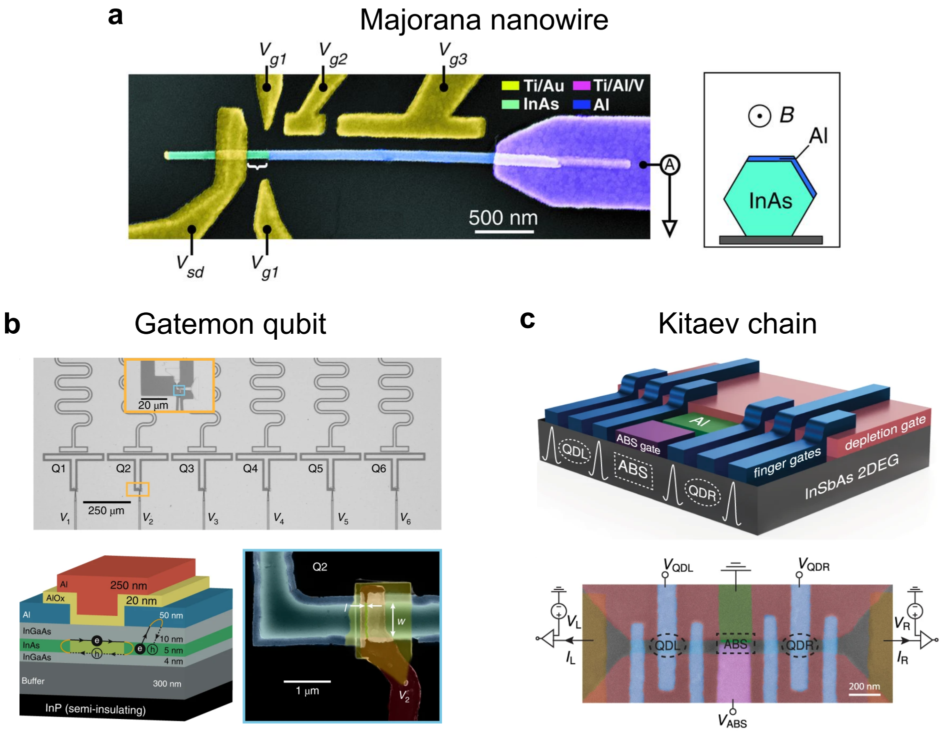

Figure 7.15: Examples of devices made from III-V hybrid junctions: **(a)** an InAs-Al Majorana nanowire; **(b)** a gatemon qubit utilizing a planar InAs-Al JoFET element; and **(c)** an artificial Kitaev chain formed in an InSbAs 2DEG proximitized by aluminum. (a) adapted from Ref. [271]. Reprinted with permission from AAAS. (b) adapted from Ref. [254]. Reproduced with permission from Springer Nature. (c) adapted from Ref. [288].

---

topological protection, and can also lead to false MZM signatures in experiments [261, 267, 268]. Achieving high-quality junctions with minimal disorder is challenging, as it requires precise control over the material growth and fabrication processes.

To date, the best candidate systems for meeting the criteria outlined above have been hybrid junctions made from III-V semiconductors (such as InAs or InSb) proximitized by superconductors like aluminum or NbTiN. Examples of devices made using III-V hybrid junctions are shown in Fig. 7.15. These systems have shown promise in numerous experiments and are widely used in gatemon, Andreev, and topological qubit research [147, 251, 267, 268, 279, 289]. However, they are not without drawbacks. First, these materials—especially III-V nanowires—are not particularly clean, and still contain too much disorder to realize a topological qubit. Second, the arsenide, gallium, indium, and antimony atoms which make up common III-V semiconductors have a high abundance of nuclear spins. Andreev spin qubits built from these materials suffer from rapid decoherence due to hyperfine interactions with the nuclei [257, 290]. And third, III-V semiconductor materials are not readily compatible with CMOS processes used in advanced semiconductor manufacturing. Given these limitations, there is ongoing interest in exploring alternative hybrid systems that can provide cleaner environments, reduced decoherence, and improved integration. Finding new material combinations that meet these stringent criteria remains a key challenge in advancing hybrid-junction qubit architectures.

Chapter 8

Superconducting Alloys for Proximitizing Germanium

This chapter focuses on the development and characterization of superconducting alloys for proximitizing germanium in hybrid superconductor-semiconductor devices. We begin by discussing the unique advantages and drawbacks of Ge/SiGe planar heterostructures, highlighting their promise as a platform for hosting hybrid-junction qubits. Following this, we explore the proximity effect in germanium and review various approaches for inducing superconductivity in germanium-based hybrid junctions. A detailed analysis of superconducting germanosilicide alloys that can be used to proximitize germanium provides insights into optimizing the induced superconducting gap. We conclude with an investigation of two candidate superconducting alloys, their fabrication, and their transport properties, emphasizing the challenges and opportunities for creating high-quality proximitized germanium systems suitable for qubit applications.

8.1 Ge/SiGe Planar Heterostructures

Achieving vertical confinement in germanium is, in many ways, a mirror image of the approach used in silicon, as discussed in Section 2.1.1. Figure 8.1(a) displays a Ge/SiGe

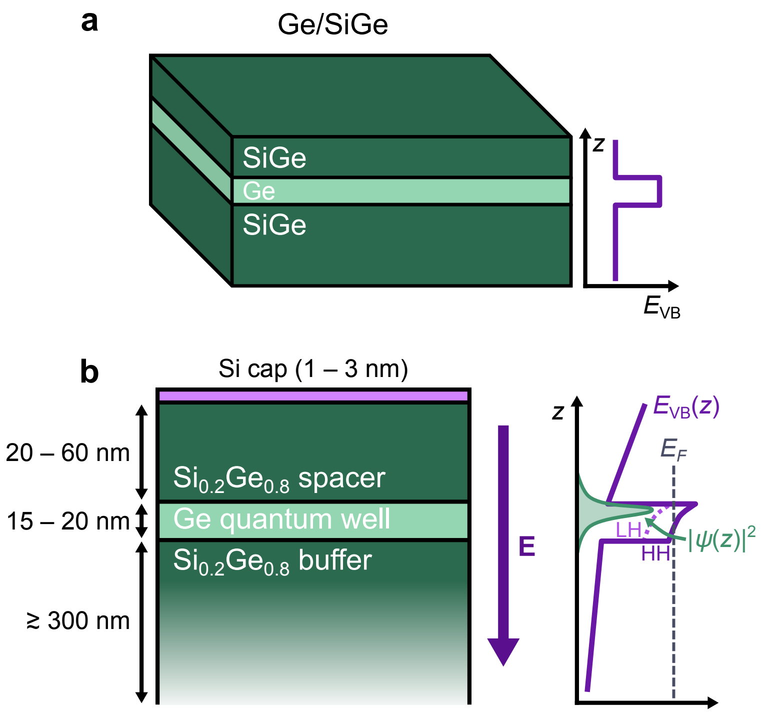

Figure 8.1: Germanium heterostructures for vertical hole confinement. **(a)** Ge/SiGe heterostructure with its valence-band energy maximum E_{VB} displayed as a function of depth. **(b)** Typical semiconductor stack for Ge/SiGe heterostructures. Application of a vertical electric field $\mathbf{E}$ promotes 2DHG accumulation within the quantum well and pulls hole wavefunctions $\psi(z)$ against the upper Ge-SiGe interface. Heavy-hole states are favored due to the energy splitting between the heavy hole (HH) and light hole (LH) band edges.

---

planar heterostructure, made from a germanium quantum well sandwiched between layers of SiGe. Unlike the Si/SiGe system, which confines electrons by forming a conduction-band minimum, the Ge/SiGe heterostructure creates a valence-band maximum to trap *hole*-type carriers along the vertical (z) dimension. A detailed view of the semiconductor stack, with typical layer thicknesses, is shown in Fig. 8.1(b). Applying a vertical electric field using positive device gate voltages accumulates a **two-dimensional hole gas (2DHG)** within the quantum well. The heavy-hole (HH) band edge is approximately 40 meV higher in energy than the light-hole (LH) band edge, making heavy-hole states dominant in the 2DHG [291]. Notably, because the valence-band maximum lies at the center of the Brillouin zone, germanium exhibits no valley physics.

8.1.1 Platform Advantages & Drawbacks

The planar Ge/SiGe platform offers several benefits that make it an appealing candidate for hosting hybrid-junction qubits. First, it has exceptionally low materials disorder, as evidenced by high hole mobilities, with peak values exceeding 10^6 $\mathrm{cm}^2/\mathrm{V}\cdot\mathrm{s}$ in some 2DHGs [291–293]. Second, germanium 2DHGs display a strong and tunable spin-orbit interaction, shaped by the interplay between heavy-hole and light-hole bands, and further modulated by the local strain and electrostatic environment [294]. Third, germanium has a low abundance (roughly 7%) of nonzero nuclear spins, which can be further reduced through isotopic purification, minimizing nuclear spin-induced decoherence [295, 296]. Moreover, the hyperfine interaction between nuclear spins and hole spins in germanium is naturally weak because the hole p-orbitals vanish at the nucleus [297]. Finally, the planar geometry of Ge/SiGe heterostructures, combined with their CMOS-compatibility, offers exceptional flexibility for designing scalable quantum computing architectures. This platform has already demonstrated the ability to host superconducting circuits [298–300] and highly coherent spin qubits [301–303], showcasing its versatility for a wide range of quantum technologies. The potential for monolithic integration of both quantum and classical components, while leveraging advanced semiconductor manufacturing techniques, positions the Ge/SiGe quantum computing ecosystem as a strong candidate for the development of large-scale processors [294].

One drawback of planar Ge/SiGe for hybrid-junction applications is g-factor anisotropy due to the nature of the heavy-hole states in the valence band. Although the platform features a large out-of-plane g-factor, its in-plane g-factor is quite small, with values well below 1 [294, 304]. This g-factor weakness is particularly troublesome for MZM proposals where an in-plane magnetic field is required to generate Zeeman splitting. While some simulations suggest that it may still be possible to induce a topological phase in gate Ge/SiGe defined nanowires using a conventional high-field approach [305–307], the weak in-plane g-factor may necessitate the use of alternative Majorana schemes that operate at lower fields [265,308,309].

In comparison to the leading hybrid-junction systems based on III-V semiconductors, planar Ge/SiGe offers an order-of-magnitude or better improvement in carrier mobility, strongly suppressed nuclear-spin noise, and superior integration with foundry manufacturing practices, while having a comparable spin-orbit length [292].[1] Although the small in-plane g-factor for germanium 2DHGs poses a challenge for certain MZM architectures, Ge/SiGe heterostructures present a new and compelling alternative to the III-V platform for constructing hybrid-junction qubits.

8.2 The Proximity Effect in Germanium

In addition to the benefits discussed above, the energy band structure of holes confined within Ge/SiGe heterostructures creates a favorable landscape for proximity-induced superconductivity. A wide range of metals, including superconductors, exhibit Fermi level pinning close to the valence band of edge in germanium [291]. This pinning effect facilitates the formation of contacts with very low Schottky barriers to germanium hole gasses, allowing the easy passage of Cooper pairs into the semiconductor to induce superconductivity [294].

A strong proximity effect has been observed in germanium-based junctions, with the first measurement occurring in Ge/Si core/shell nanowires in 2006 [310]. It took another 12 years for the proximity effect to be measured in planar germanium 2DHGs. The first hybrid-junction device in this geometry was a Ge/SiGe JoFET proximitized by aluminum leads [311]. Since then, research using planar germanium hybrid junctions has rapidly expanded, driven by the potential of these systems for qubit applications. JoFETs have been fabricated in Ge/SiGe heterostructures using several parent superconductors, demonstrating both the dc and ac Josephson effects [292, 299, 312–315]. Experiments in these devices have showcased the merits of the platform's low disorder and high carrier mobility. The proximity-induced superconductivity penetrates deep into the semiconductor, allowing

---

[1] We should be careful about making direct comparisons of spin-orbit coupling between III-V electron gasses and germanium 2DHGs, as the interaction mechanisms are different for electrons and holes. In the former system, the spin-orbit energy term scales linearly with momentum, but the latter has a cubic scaling [294, 305].

Josephson supercurrent to be measured in JoFETs with channel lengths as long as 6 µm [313]. Furthermore, these junctions have displayed ballistic superconducting transport [313] and near-unity transparency [292, 315]. Beyond standalone JoFETs, planar germanium hybrid junctions have been integrated into a variety of quantum devices, including gate-tunable SQUIDs [292, 299, 312, 314, 316, 317], a Josephson-junction array with 510 superconducting islands [292], a gatemon qubit [318], a proximitized quantum dot [319], and a flip-chip readout circuit [299]. In the flip-chip experiment, a superconducting resonator was employed to perform ABS spectroscopy and measure the junction parity. Notably, the observed parity lifetime of several seconds in this work indicates an exceptionally low rate of quasiparticle poisoning in the proximitized germanium system.

8.2.1 Approaches for Proximitizing Germanium

One obstacle to inducing superconductivity in Ge/SiGe is that the quantum well is buried within the heterostructure beneath the silicon cap and SiGe spacer layers. Three distinct strategies have been employed to navigate this challenge and proximitize germanium 2DHGs.

The Etched Mesa Method

A brute-force way to contact the germanium quantum well with a superconductor is to etch the heterostructure into a mesa, allowing superconducting metal to be deposited over the exposed germanium in the side walls, as shown in Fig. 8.2(a). This approach has been utilized to fabricate germanium JoFETs with superconducting contacts made from aluminum [312] and Al/Nb bilayers [314]. The drawback of this method is that the etching process is inherently damaging to the pristine semiconductor crystal, resulting in a disordered S-Sm interface. Consequently, the induced superconducting gaps in these devices have been soft, and this issue is likely to persist unless significantly gentler etching and passivation techniques are developed to create a cleaner interface.

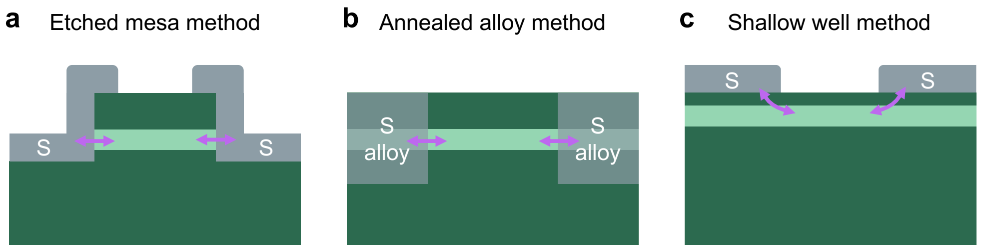

d

Contact material	Al	Al/Nb bilayer	Al	PtSiGe	Al
Parent gap, Δ_0 (μeV)	200 – 300*	486	200 – 300*	76†	200 – 300*
Induced gap, Δ^* (μeV)	100		200	48 – 70	150
Induced gap quality	soft	soft	soft	hard	hard
Critical field, $B_{c,\parallel}$ (T)	> 1.5*		> 1.5*	0.4	> 1.5*
Transparency, τ	low	0.88 – 0.90	0.60 – 0.70	0.94 – 0.96	
Junction disorder	Etch process creates disordered S-Sm interface		Clean S-Sm interface formed through alloy in-diffusion		Shallow well reduces 2DHG mobility ($\mu_h \approx$ 10,000 cm²/V·s)

Figure 8.2: Three approaches for proximitizing germanium: **(a)** the etched mesa method; **(b)** the annealed alloy method; and **(c)** the shallow well method. The strategies are illustrated using S-Sm-S junctions; for simplicity, accumulation gates are not shown. **(d)** Table comparing proximity effect metrics for each method. *Aluminum parent superconductor values estimated based on similar thin films in III-V hybrid junctions [267]. †PtSiGe parent gap estimated from the BCS prediction in Eq. (7.7) with $T_c = 500$ mK. All other data obtained from Refs. [292, 299, 311–315].

The Annealed Alloy Method

An alternative method for contacting the germanium well without any material removal is to form a superconducting alloy directly *within* the semiconductor stack, as depicted in Fig. 8.2(b). This can be accomplished by depositing a metallic thin film followed by rapid thermal annealing, which causes the metal to diffuse into the substrate, where it alloys with the silicon and germanium atoms. By forming the S-Sm interface within the semiconductor crystal and avoiding exposure to air, this method produces a significantly cleaner interface compared to the etched mesa method.

Early devices fabricated using in-diffused aluminum contacts resulted in proximitized 2DHGs with soft induced gaps [311, 313]. A breakthrough came later, when Tosato *et al.* were able to induced a hard superconducting gap using an annealed alloy of PtSiGe [292].

The high quality of the Ge-PtSiGe interface was demonstrated in JoFETs with near perfect junction transparency.[2] However, the magnitude of the superconducting gap induced by PtSiGe is only $\Delta^* \approx 50 - 70$ µeV, considerably smaller than the proximity gaps from other parent superconductors [292, 315].

The Shallow Well Method

A third approach involves growing the Ge/SiGe heterostructure with an extremely shallow quantum well, following a technique originally developed for proximitizing InAs 2DEGs [251]. As Fig. 8.2(c) illustrates, Cooper pairs can tunnel into the germanium well from a superconductor deposited on the heterostructure surface, provided that the SiGe spacer is sufficiently thin. Using this method, a hard proximity gap of $\Delta^* = 150$ µeV has been realized in 5 nm-deep germanium wells with cold-deposited aluminum leads [299].

However, reducing the depth of the quantum well comes at a cost. Without a thick spacer layer to shield the 2DHG, holes in the quantum well are more susceptible to scattering by impurities in the material stack above the heterostructure. This issue was evident in the shallow-well sample of Ref. [299], which exhibited a peak hole mobility of only 10,000 $\mathrm{cm}^2/\mathrm{V} \cdot \mathrm{s}$. Compromising in this manner on the low-disorder environment typically offered by Ge/SiGe heterostructures undermines one of the platform's key advantages.

8.2.2 A Better Hybrid System?

Over the past few years, the development of proximitized germanium 2DHGs has seen notable progress, demonstrating their potential as a platform for hybrid-junction qubits. However, key advancements such as the implementation of Andreev qubits, Majorana nanowires, or Kitaev chains in germanium-based devices have yet to be achieved. The preferred platforms

---

[2] Recall from Section 7.5.4 that contacts with excessively high transparency can actually be a bad thing for qubit applications, since strong coupling to the superconductor can weaken the semiconductor's g-factor and spin-orbit interaction. Possible evidence of g-factor renormalization in Ge-PtSiGe junctions has been observed in recent experiments [319]. The issue could be addressed by using electrostatic gating to fine-tune the S-Sm coupling so that it remains in the optimal range.

for these high-impact experiments remain III-V nanowires and 2DEGs proximitized by aluminum, largely due to their superior proximity effect, honed through more than a decade of sustained improvements in materials growth and fabrication techniques. These systems exhibit hard induced gaps of at least 200 µeV; they can withstand in-plane magnetic fields above 1 T; and they typically feature aluminum layers deposited *in-situ* during semiconductor growth, forming an epitaxial or near-epitaxial interface with minimal disorder. In contrast, as Fig. 8.2(d) summarizes, none of the existing methods for proximitizing germanium have yet achieved a combination of all of these critical attributes. Evidently, further improvements in proximitizing germanium are still needed to position it as a leading material choice for constructing hybrid-junction qubits.

8.3 Superconducting Germanosilicide Development

Of the three methods we have discussed for proximitizing germanium, the annealed alloy approach is arguably the most promising. Its primary advantage lies in its ability to preserve the low-disorder environment that makes planar Ge/SiGe such an attractive platform for hybrid-junction qubits. Moreover, the annealed alloy method does not require any specialized equipment or conditions during deposition of the superconductor to achieve a high-quality S-Sm interface, adding a desirable simplicity to the contact fabrication process. However, it relies on stochastic thermal diffusion and solid-phase reactions to drive the alloying, which can introduce a degree of process variability. The resulting alloys can be highly sensitive to the specific annealing conditions and materials used, necessitating meticulous optimization of fabrication recipes. The extensive and largely unexplored phase space of potential metals and annealing conditions holds promise for identifying alloys that could more effectively proximitize germanium. In the remainder of this chapter, we will explore a small corner of this phase space in detail.

Compound	T_c **(K)**	**Reference**
PtSi	0.88	[322]
PdSi	0.93	[322]
VSi	17.0	[321]
PdGe	unknown	[322]
PtGe	0.40	[322]
MoGe	1.2 – 1.4	[321]
RhGe	1.0 – 2.1	[322]
IrGe	0.9 – 4.7	[322]
VGe	6.0	[321]
NbGe	22.3	[323]
PtSiGe	0.50	[292]

Table 8.1: Known silicide, germanide, and germanosilicide superconductors, listed with their critical temperatures, T_c. For simplicity, the stoichiometric ratios for the crystal phases are suppressed.

8.3.1 Candidate Alloys

There is a substantial body of research focused on the alloying of silicon, germanium, and SiGe with various metals to form **silicides**, **germanides**, and **germanosilicides**. This effort is largely motivated by the microelectronics industry's use of these materials in creating low-resistance electrical contacts [320]. There is also a long history of discovering superconductivity in these compounds, with findings dating back to at least the 1950s [321–324]. Table 8.1 lists a collection of known superconducting alloys. Although no superconducting germanosilicides other than PtSiGe have been reported to my knowledge, we can use the properties of the binary silicides and germanides as a basis to predict the behavior of ternary alloys—for example, the critical temperature of PtSiGe falls in between those of PtGe and PtSi.

Unfortunately, most of the candidate compounds for proximitizing germanium suggested by Table 8.1 are ruled out due to a thermal processing constraint for Ge/SiGe heterostructures. The germanium quantum well is grown at a temperature of 500°C, and the heterostructure must be kept below this temperature during subsequent processing steps to preserve the integrity of the sharp Ge-SiGe interfaces [291,292]. However, thin films of molybdenum, rhodium, iridium, vanadium, and niobium only begin to react with germanium at temperatures that approach or surpass the 500°C thermal budget, preventing their integration into the semiconductor stack through rapid thermal annealing [325]. The thermal processing restriction leaves us only two alloys to consider for superconducting contacts: PtSiGe and PdSiGe.

PtSiGe

We have already discussed PtSiGe as a known superconductor which forms high-quality contacts with germanium. The biggest drawback of this alloy is its small gap of only $\Delta_0 \approx 76$ µeV, based on its 500 mK critical temperature and the BCS prediction of Eq. (7.7) [292]. The gap induced when it couples to germanium is even smaller, which may limit potential applications for topological superconductivity. Another concern is thermal stability during the formation of PtSiGe alloys. X-ray diffraction studies on annealed PtGe alloys have identified diffraction peaks corresponding to several different metallic phases with varying elemental compositions and crystal structures, emerging simultaneously throughout the process temperature range of 330 – 400°C [325]. This variability presents both a challenge and an opportunity. On the one hand, there is risk of sample-to-sample variation, which could impact reproducibility. On the other hand, fine-tuning the processing conditions might lead to the discovery of an optimized recipe that results in a larger superconducting gap.

PdSiGe

The status of PdSiGe as a superconductor remains unknown, to my knowledge. PdSi superconducts with a critical temperature close to 1 K (better than PtSi or PtGe), offering a glimmer of hope that PdSiGe might induce a larger gap than PtSiGe. In contrast, only a “trace superconducting phase” has been observed in PdGe [322]. Should PdSiGe be confirmed as a superconductor, it would be an appealing material from a fabrication perspective.

Palladium is a user-friendly metal to work with, non-oxidizing and easy to deposit and lift off using electron-beam evaporation. Furthermore, palladium annealed into germanium forms a stable, single-phase alloy over a wide temperature range of 330 – 740°C [325]. These potential upsides of PdSiGe make it an intriguing material for proximitizing germanium, warranting further investigation.

8.3.2 Sample Preparation

To investigate the superconducting properties of PtSiGe and PdSiGe films, we prepare samples of both alloys. The Si/SiGe heterostructure used in these experiments, which features a 16 nm-thick germanium well and 22 nm-thick SiGe spacer, was grown by the Scappucci Lab at TU Delft. For our PtSiGe samples, our objective is to replicate previously reported findings while also exploring whether the alloy can be optimized for a larger superconducting gap or improved thermal stability during annealing. For PdSiGe, our focus is on determining whether the alloy is superconducting and, if so, measuring its properties to compare against the established PtSiGe benchmark.

The basic recipe for creating germanosilicide contacts using the annealed alloy method is illustrated in Fig. 8.3(a), following a procedure outlined in Refs. [291, 292, 311] and others. The process begins with the patterning of contact leads using photo- or electron-beam lithography. Next, a metallic film is deposited. To promote good in-diffusion of the metal, it is essential to strip the SiO_x native oxide layer from the silicon cap prior to metal deposition. This is typically accomplished by briefly dipping the sample (usually for 15 – 30 seconds) in a buffered oxide etchant (BOE) solution immediately before loading it into the deposition chamber and pumping to vacuum. Following the metal liftoff, the sample is annealed in an inert gas environment. This step drives the metal into the heterostructure and activates solid-phase reactions between the metal and semiconductor atoms, leading to the formation of the alloy.

Tosato *et al.* have conducted a limited investigation into some of the process parameters

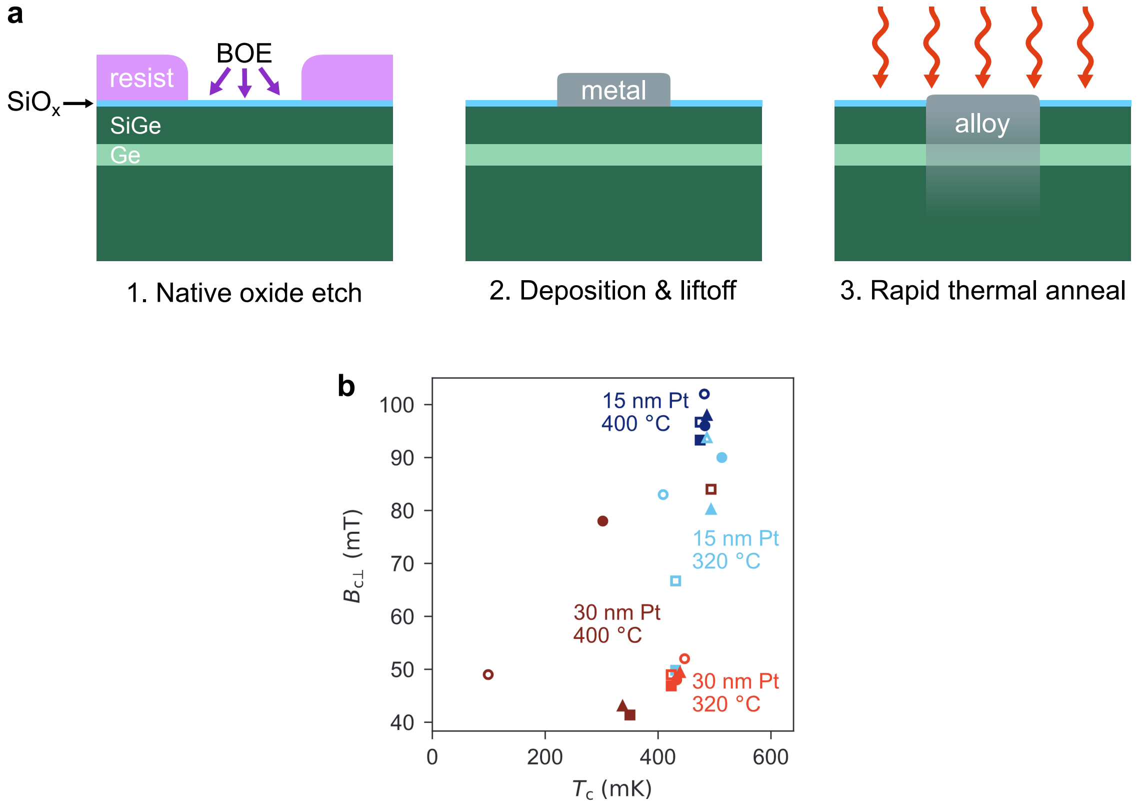

Figure 8.3: Germanosilicide sample preparation. **(a)** Processing recipe for germanosilicide samples. **(b)** Critical temperature T_c and critical out-of-plane magnetic field $B_{c\perp}$ for PtSiGe films fabricated with different processing conditions. Filled (unfilled) markers indicate an anneal time of 15 (30) minutes. Marker shapes signify different ALD processes. Figure adapted from Ref. [292].

---

for fabricating PtSiGe contacts [292]. Their study characterized alloys formed with 15 and 30 nm deposited platinum films, using anneal times of 15 and 30 minutes and temperatures of 320°C and 400°C. Some of the tested films also included an Al_2O_3 layer, grown using various atomic layer deposition (ALD) recipes. Figure 8.3(b), adapted from Ref. [292], summarizes the results of the study. The findings indicate that thinner platinum films create alloys with significantly higher B_c values for superconductivity. However, changes to the anneal time or the ALD processing conditions do not appear to have any significant impact on these properties.

For our PtSiGe samples, we opt to follow the same platinum deposition parameters utilized by Tosato *et al.* for JoFET fabrication, with 15 nm films deposited at a rate of

Sample ID	**Lithography**	**BOE**	**Metal film**	**Anneal (°C)**
QT568-DA	photo	6:1	Pt, 15 nm	400
QT568-FA	e-beam	20:1	Pt, 15 nm	375
QT568-FB	e-beam	20:1	Pt, 15 nm	400
QT568-FC	e-beam	20:1	Pt, 15 nm	425
QT568-HB	e-beam	6:1	Pt, 15 nm	400
QT568-IB	e-beam	20:1	Pt, 15 nm	400
QT568-IC	e-beam	20:1	Pt, 15 nm	400
QT568-ID	e-beam	20:1	Pt, 15 nm	450
QT568-EA	photo	6:1	Pd, 15 nm	400
QT568-EB	photo	6:1	Pd, 15 nm	350

Table 8.2: Processing information for germanosilicide samples.

0.5 Å/s via electron-beam evaporation. However, considering the temperature sensitivity of the platinum-germanium alloying process, we test a broader set of annealing temperatures ranging from 375 – 450°C, in 25°C intervals. Additionally, we explore the impact of etching the native oxide using two different concentrations of BOE—20:1 and 6:1 NH_4F:HF by volume—as the effects of this variable have have not been documented in the literature. The higher acid concentration in 6:1 BOE is expected to attack the oxide more aggressively. For our PdSiGe films, we follow a similar procedure, depositing 15 nm of palladium at 1.0 Å/s and annealing the samples at 350°C and 400°C. In this case, only 6:1 BOE is used for oxide removal. All samples are annealed in a nitrogen environment for 15 minutes.

On each sample, we pattern the film into wires of varying lengths for transport characterization, as well as test structures with narrow strips of alloy for electron-microscope imaging. The films are patterned for liftoff using a combination of electron-beam and photolithography, with 495 PMMA A4 as the e-beam resist and APOL-LO 3202 as the photoresist. In principle, the lithography process should not affect the formation of the alloy. Table 8.2 provides an overview of all 10 germanosilicide samples along with their relevant processing information.

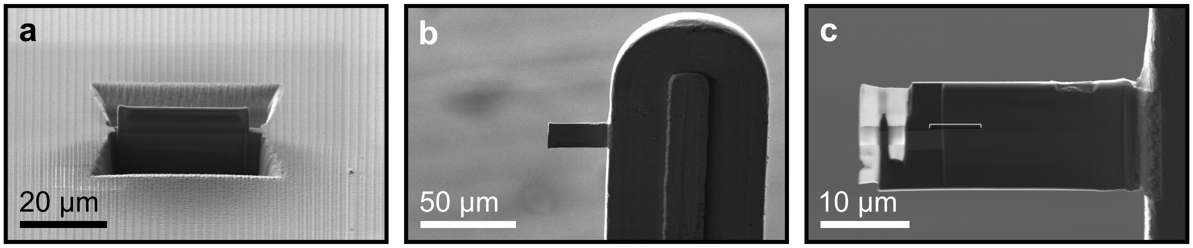

Figure 8.4: Scanning electron micrographs illustrating different stages of preparing a lamella for TEM imaging using a FIB. The lamella is shown: **(a)** just before lift-out from the sample substrate; **(b)** attached to a TEM post; and **(c)** after being thinned to the point of electron transparency.

8.3.3 Optical & TEM Characterization

After fabrication, all samples are visually inspected under a microscope to assess the evenness of alloying over micron length scales. Typically, the films darken and lose their metallic luster after annealing as the metal diffuses into the semiconductor stack. In a subset of samples, lamellae are carefully cut from the substrate and thinned to less than 100 nm in thickness using a focused ion beam (FIB), as illustrated in Fig. 8.4. We then image the lamellae using transmission electron microscopy (TEM), a technique which provides a cross-sectional view of the films, enabling us to analyze the diffusion depth and microscopic structure of the alloys. Although we have not performed elemental analysis using techniques like EDS, EELS, or HAADF-STEM, the alloy crystals containing heavy platinum and palladium atoms transmit far fewer electrons than the surrounding materials, making them easy to pick out in TEM images. We can also discern other features of the heterostructure, such as the quantum well, based on structural contrast and differential FIB milling of the material layers during lamella preparation.

PtSiGe

Optical surveying of the PtSiGe films reveals uneven alloy formation in many of the samples. Figure 8.5 compares micrographs of two PtSiGe wires fabricated with 20:1 and 6:1 BOE dips. The lateral uniformity is notably worse for the sample etched in the lower-concentration 20:1

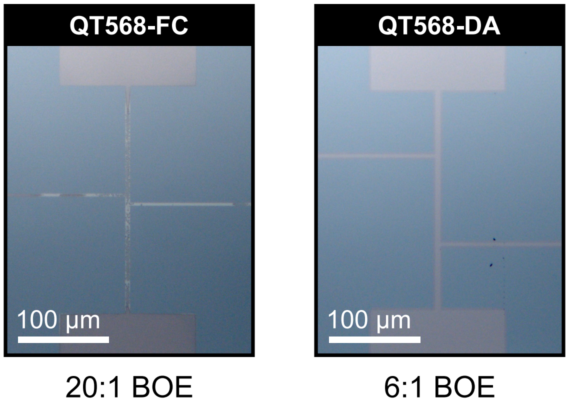

Figure 8.5: Optical micrographs comparing PtSiGe films processed with BOE concentrations of 20:1 (left) and 6:1 (right). The film treated with the lower-concentration 20:1 solution contains visible patches of non-diffused platinum.

---

solution, with bright patches of non-diffused platinum visible along the wire leads. A similar trend is observed in many of the 20:1 BOE samples, suggesting that incomplete removal of the SiO_x layer likely obstructed the platinum from diffusing in uniformly across the substrate.

Figure 8.6 presents TEM micrographs of alloys annealed at different temperatures. Compared to the non-annealed control sample shown in panel (a), the annealed films in (b) and (c) clearly exhibit platinum diffusion and annealing below the substrate surface. Although a polycrystalline PtSiGe alloy is found in samples annealed at both 400°C and 450°C, the shapes and sizes of the crystals differs markedly between films.

The sample annealed at 400°C in Figs. 8.6(b), (d), and (f) shows nearly complete in-diffusion of the platinum, with very little of the deposited metal remaining on the heterostructure surface. The alloy's crystals range in size from roughly $50 - 150$ nm along their largest dimension, with many being large enough to extend into the quantum well. In contrast, the film annealed at 450°C in Figs. 8.6(c) and (e) exhibits a bimodal distribution of crystal sizes. In some regions of the film, large crystals penetrate more than 100 nm deep into the heterostructure [Fig 8.6(e)], while in other areas, tiny (< 20 nm) crystals are scattered within the SiGe spacer above the well [Fig 8.6(c)]. This sample also has a significant amount of metal remaining on the substrate surface. Overall, the alloy's nanostructure is

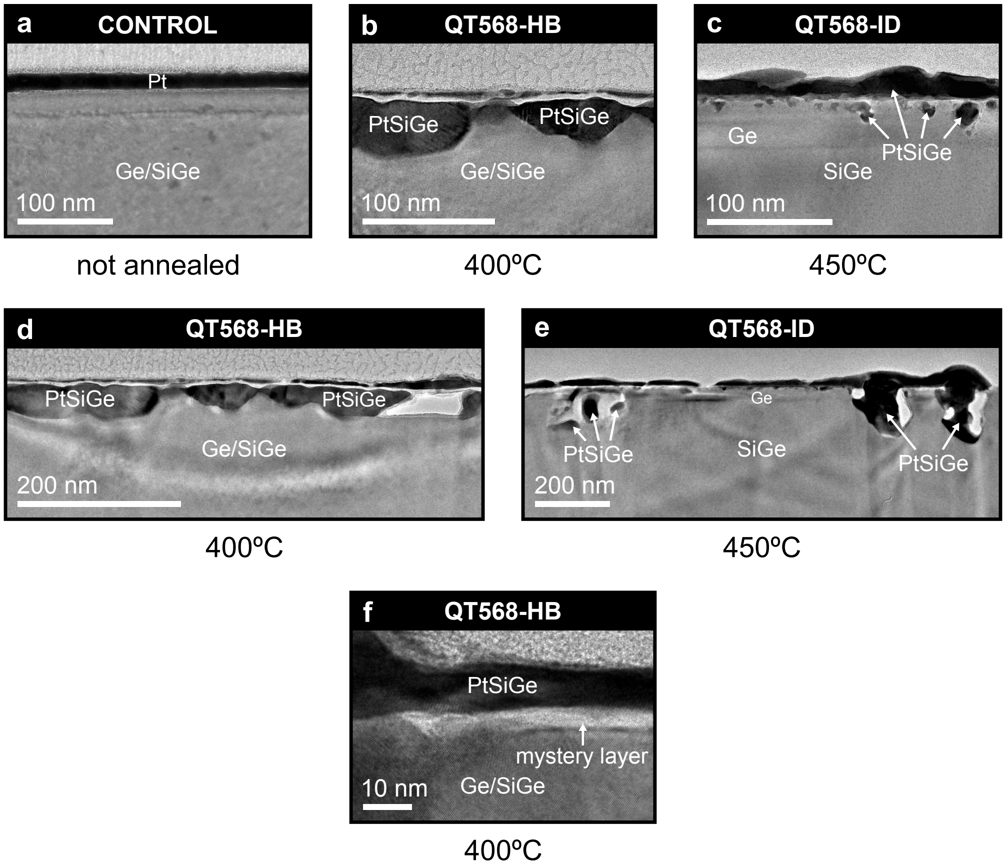

Figure 8.6: TEM micrographs of PtSiGe alloys annealed at different temperatures.

---

somewhat unusual, and it is unclear whether the bimodal distribution of crystals is due to the intrinsic diffusion behavior of the platinum, or if unremoved SiO_x obstructed diffusion in certain areas, contributing to the observed features—only one lamella was prepared from this sample, making it difficult to draw definitive conclusions.

All annealed PtSiGe samples contain a thin amorphous layer, with thickness varying from 1 – 5 nm, located near the heterostructure surface. The layer appears lightly colored in TEM images and is shown in more detail in Fig. 8.6(f). Without chemical analysis, the origin of this layer remains uncertain. The bright coloration might suggest the presence of lower-Z materials. We speculate that this layer could be silicon-rich, originating from the cap. It may also be an oxide that was either not removed by the pre-deposition etch (although we note that similar layers are observed in samples dipped in both concentrations of BOE) or

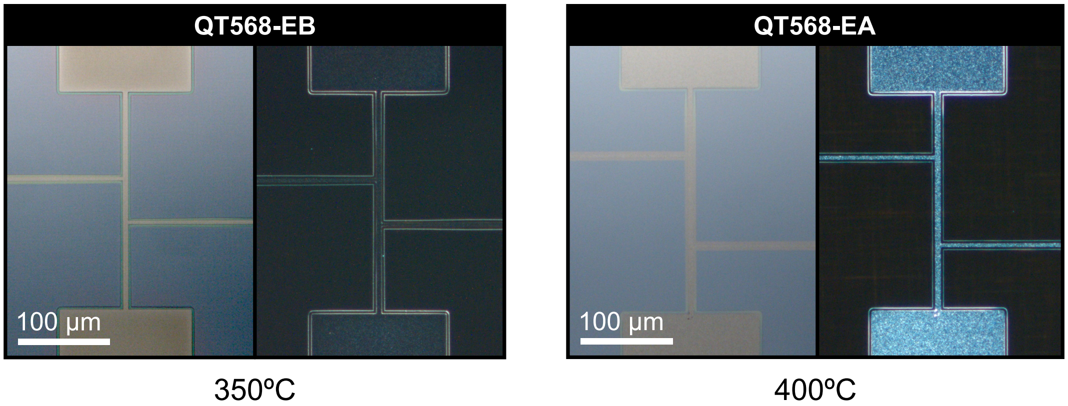

Figure 8.7: Optical micrographs comparing PdSiGe samples annealed at 350°C (left) and 400°C (right). The films have very different surface textures, as is especially apparent in the dark-field photos.

---

precipitated at a elevated temperatures during thermal processing.

PdSiGe

Visually comparing the PdSiGe films, as in Fig. 8.7, reveals a noticeable difference in surface texture between samples. The film annealed at 350°C appears dull and smooth, while the film annealed at 400°C has a rough, grainy surface texture, suggestive of uneven alloying. Both samples were treated with a 6:1 BOE etch, implying that the difference in surface texture is unrelated to native oxide removal.

TEM analysis shows that the film alloyed at 350°C in Figs. 8.8(a) and (b) is laterally continuous, with relatively uniform crystals extending to the upper interface of the germanium well. This film is the most spatially uniform among the PtSiGe and PdSiGe alloys studied. In contrast, the sample alloyed at 400°C in Figs. 8.8(c) and (d) is less laterally uniform, with gaps between crystals, and does not reach as deeply into the heterostructure.

8.3.4 Transport Characterization

We investigate the superconducting properties of the germanosilicide alloys through transport measurements at millikelvin temperatures. Our experiments utilize a dc four-probe

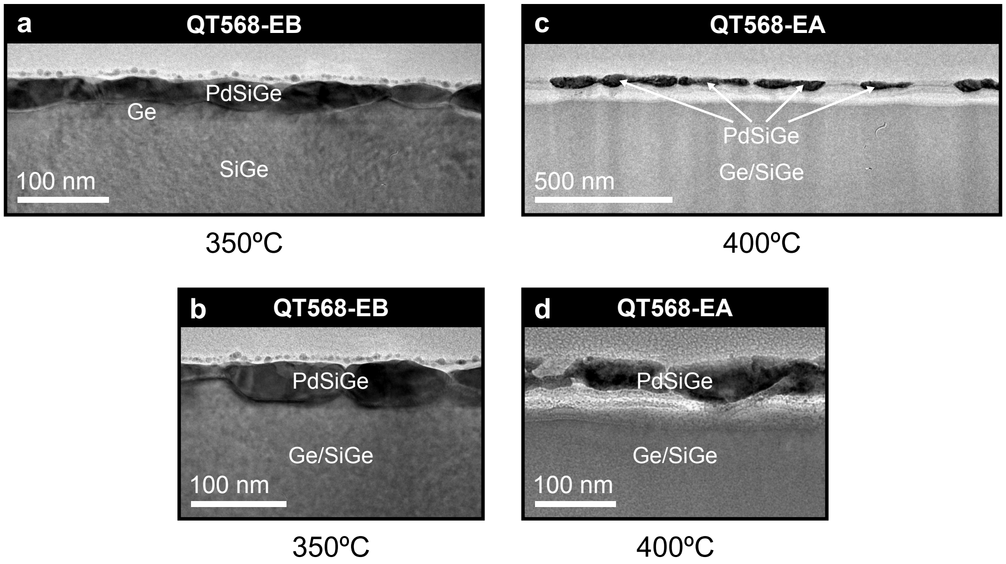

Figure 8.8: TEM micrographs of PdSiGe alloys annealed at different temperatures.

configuration on patterned germanosilicide wires, with measurements conducted in an Oxford Triton 400 dilution refrigerator. Since pure palladium and platinum do not superconduct at any temperature achievable in a fridge, the onset of superconductivity is a strong indicator of successful germanosilicide alloying. Figure 8.9 shows a representative example of current vs. voltage ($I-V$) measurements acquired at different cryostat temperatures. As the PtSiGe wire in this experiment is heated, the critical current gradually decreases, and the zero-resistance plateau shrinks until disappearing completely, indicating a transition to the normal state at the critical temperature.

For each germanosilicide wire, three key parameters are recorded. First, we measure the critical temperature T_c, which provides an indirect measurement of the alloy's gap using the BCS formula in Eq. (7.7). Second, we measure the critical current I_c at base temperature. In wires with uniform geometry, a higher I_c suggests stronger superconducting pairing and better coherence within the film, potentially due to a higher density of Cooper pairs or fewer defects. Higher I_c values generally indicate that the film can sustain higher magnetic fields as well. Third, we measure the sheet resistance in the normal state R_N by heating the wires just above their T_c value. This resistance reflects the electron scattering processes within the

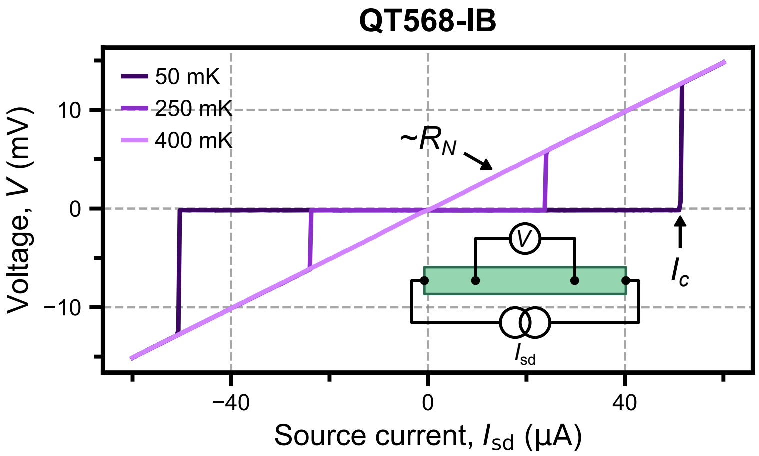

Figure 8.9: $I - V$ curves measured from a PtSiGe film at different cryostat temperatures. As the wire is heated to 400 mK, the critical current I_c decreases, and it transitions from the superconducting state to the normal state with resistance R_N.

material, where a lower R_N typically suggests fewer defects and grain boundaries, leading to better electron mobility.

By comparing T_c, I_c, and R_N across different alloys, we can draw conclusions about the structural properties and superconducting behavior of the alloys. For example, a film with a high T_c, high I_c, and low R_N would be inferred to be a high quality alloy, with fewer defects and strong superconducting properties. Additional insights can be gained by comparing measurements from nominally identical films. A wide spread of parameter values between different samples processed under the same conditions, or between different wires on the *same* sample, might indicate instability in the alloy formation process. All measured thin-film wires are 5 μm wide, with varying lengths of 10, 50, 100, and 200 μm. We do not notice any obvious correlation between wire length and T_c or I_c values in our experiments.

PtSiGe

In our transport measurements on PtSiGe samples, superconductivity is measured in 18 out of 22 tested wires. Figure 8.10 charts the superconductivity yield, broken down by annealing temperature [panel (a)] and BOE concentration [panel (b)]. Notably, the only PtSiGe wires which fail to superconduct are from samples processed with 20:1 BOE; those etched in 6:1

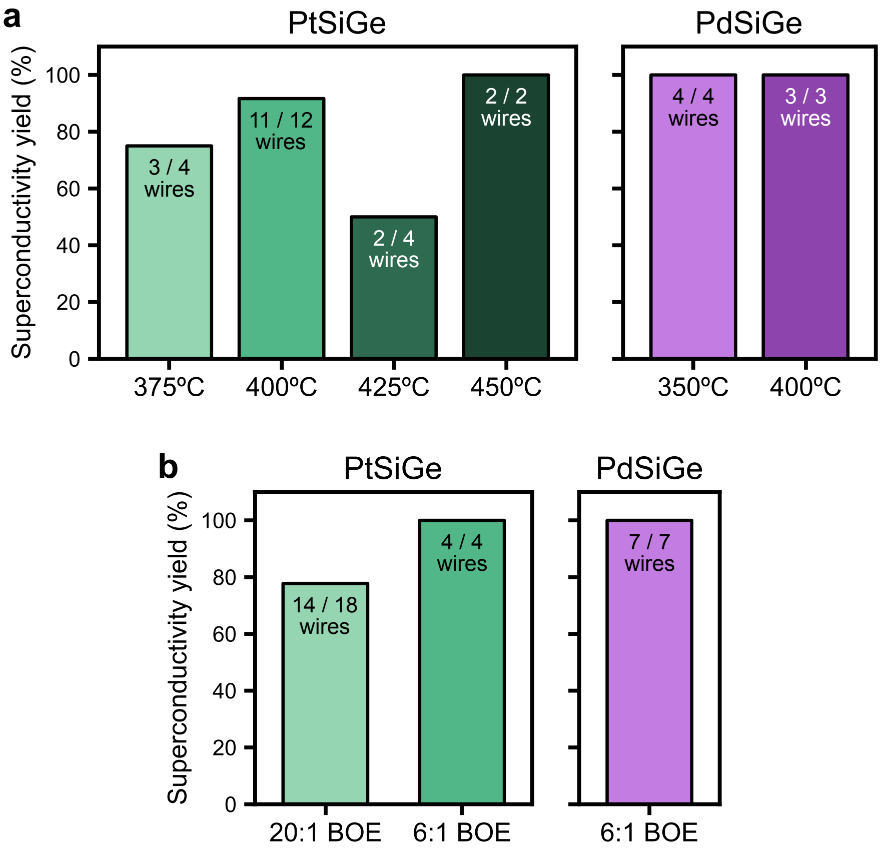

Figure 8.10: Superconductivity yield assessment of germanosilicide wires, broken down by: **(a)** sample annealing temperature; and **(b)** BOE concetration used for native oxide etching.

BOE have a perfect yeild. All four non-superconducting wires are found to have lateral unevenness in their alloys, with appearances similar to the left-side film in Fig. 8.5. This leads us to believe the unevenness of platinum in-diffusion creates discontinuities in the superconducting alloy along the wire.

Transport data from the PtSiGe alloys are plotted in Figs. 8.11(a) through (c) as a function of annealing temperature, with different markers representing each sample. There is significant variation in properties between different wires fabricated on the same sample. Furthermore, three films prepared identically with a 400°C annealing temperature display considerable sample-to-sample variance. The films' critical temperatures [Fig. 8.11(a)] range from $T_c \approx 390 - 540$ mK, showing a slight decline as the annealing temperature increases. The highest T_c values, indicative of the largest superconducting gap, are found in the sample

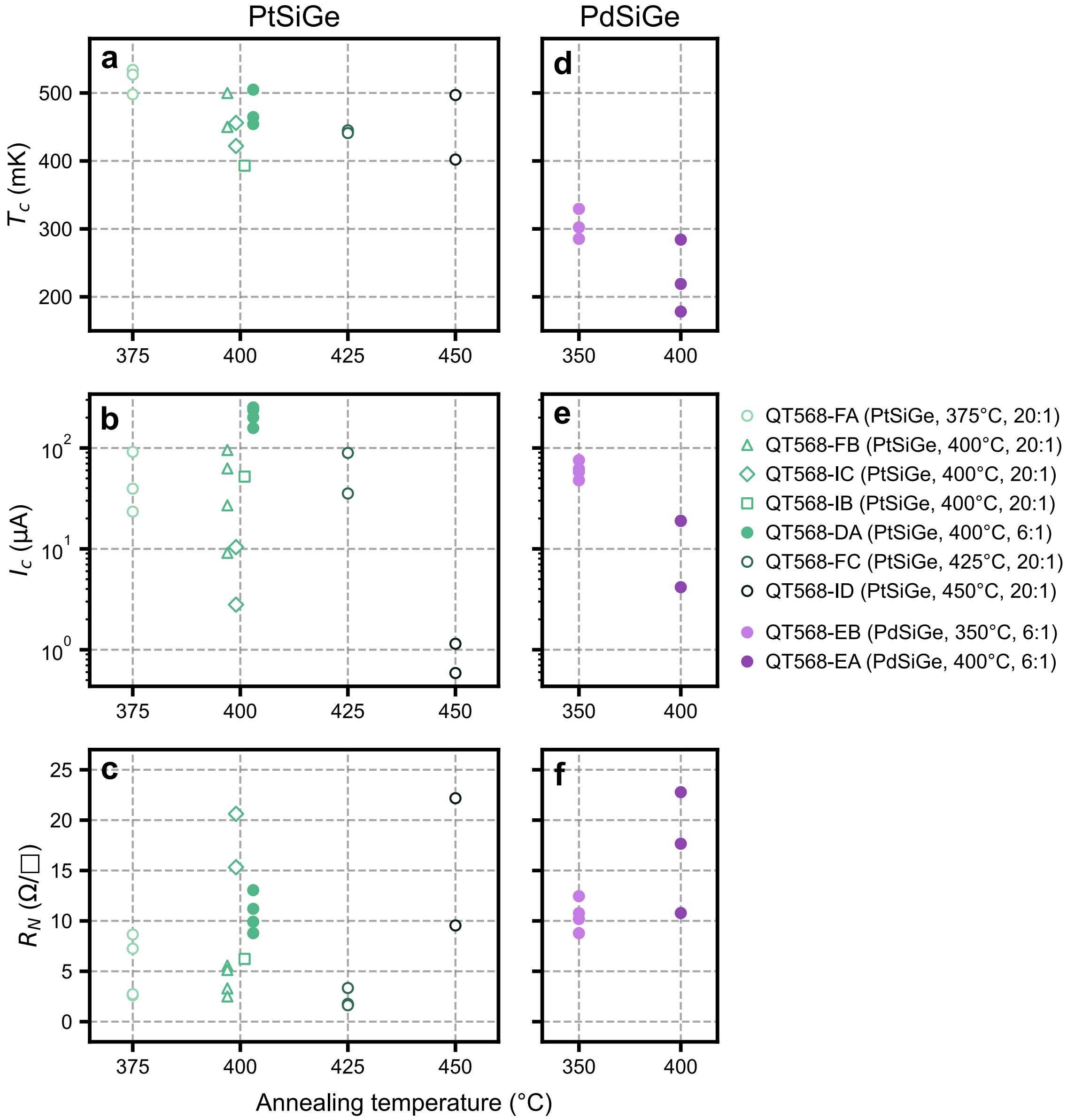

Figure 8.11: Superconducting properties of different germanosilicide alloys. For each wire, the critical temperature T_c, critical current I_c, and normal-state resistance R_N are measured. Data from samples processed with 6:1 and 20:1 BOE dips are shown with filled and unfilled markers, respectively. **(a-c)** Measurement data from PtSiGe wires. For clarity, data points from multiple samples annealed at 400°C are offset horizontally. **(d-f)** Measurement data from PdSiGe wires.

annealed at 375°C. The measured critical currents [Fig. 8.11(b)] have a particularly wide distribution, spanning multiple orders of magnitude with $I_c \sim 0.1 - 100$ μA. For the highest annealing temperature of 450°C, I_c drops significantly. The normal-state resistances

[Fig. 8.11(c)] are scattered around the $R_N \approx 1 - 22\ \Omega/\square$ range, with a trend toward higher resistance at increased annealing temperatures.

The data for samples processed with 6:1 and 20:1 BOE dips are differentiated in Fig. 8.11 by filled and unfilled markers, respectively. No substantial differences in T_c or R_N are observed between the 400°C PtSiGe wires preapred with different BOE treatments. It is, however, worth noting that the four wires from the sample etched with higher-concentration BOE have significantly higher I_c values than any other wire.

Overall, the transport data suggest that annealing PtSiGe films at 375°C or 400°C offers the best balance of high T_c, high I_c, and moderate R_N, making it the most promising condition for fabricating high-quality superconducting contacts. Conversely, raising the annealing temperature to 450°C appears to degrade the films' superconducting performance, likely due to increased defects or uneven alloy formation.

PdSiGe

Both PdSiGe samples were processed using 6:1 BOE, and superconductivity is measured in all seven wires tested, as Fig. 8.10 shows. A comparison of the PdSiGe alloys using the data in Figs. 8.11(d) through (f) reveals markedly better superconducting properties in the film annealed at 350°C, as well as less variability between wires. The critical temperatures for this alloy [Fig. 8.11(d)] range from $T_c \approx 280 - 330$ mK, while the alloy annealed at 400°C turns normal at $T_c \approx 180 - 280$ mK. The critical currents [Fig. 8.11(e)] are also higher for the 350°C alloy, with values of order $I_c \sim 10$ µA. The normal-state resistances vary from $R_N \approx 8 - 23\ \Omega/\square$, with the lower-annealing-temperature alloys less resistive, on average.

8.3.5 Discussion & Outlook

Our transport and microscopy studies on PtSiGe and PdSiGe alloys provide some useful insights into the challenges and opportunities of proximitizing germanium using the annealed alloy method. While our efforts have not led to a significant improvement in process stability or the superconducting gap beyond what has been previously reported, they have confirmed some important characteristics of these materials and highlighted areas for future improvement.

Our results indicate that while PtSiGe remains the most promising germanosilicide for proximitizing germanium, the incremental improvement in critical temperature achieved in our 375°C-annealed samples—slightly above the 500 mK T_c value reported by Tosato *et al.* in Ref. [292]—is not substantial enough to suggest a clear pathway for significantly enhancing the induced gap in germanium hybrid junctions. Separately, we have successfully established PdSiGe as a superconducting germanosilicide, marking (to my knowledge) the first recorded instance of its superconductivity. Unfortunately, though, the lower critical temperature of PdSiGe compared to PtSiGe makes it less viable for applications requiring a larger induced gap in germanium hybrid devices.

An important outcome from our studies is to underscore the importance of thoroughly removing the native oxide layer from the silicon cap prior to metal deposition. We have shown that incomplete oxide removal due to the use of low-concentration etchant can result in uneven metal diffusion and, consequently, reduced device yield. It may further lead to diminished superconducting coherence, as evidenced by lower critical currents in our PtSiGe films processed with 20:1 BOE. One challenge highlighted in our work is process instability when using the annealed alloy method to form superconducting contacts. The variability in crystallinity and superconducting performance observed across samples, even those annealed at modestly different temperatures, suggests that this fabrication approach introduces a level of instability that could pose significant challenges for achieving device uniformity at scale.

Moving forward, several improvements could enhance the robustness and reproducibility of our methodology. First, increasing the sample size would allow us to draw stronger conclusions about the tested alloys. Although we have prepared 10 samples and performed millikelvin characterization across 29 wires, it is still difficult to attribute different outcomes to specific changes in process conditions with high confidence due to the small sample size of our dataset. Further measurements are therefore needed to build up a statistical representation. Second, exploring a broader range of processing conditions would provide a more comprehensive understanding of the optimal parameters for alloy formation. For example, testing PtSiGe samples etched with 6:1 BOE and annealed at 375°C could reveal conditions that maximize both T_c and I_c. Investigating other processing parameters is also of interest, such as varying the deposited metal thickness, the annealing time, the SiGe spacer composition, or testing additional pre-deposition treatments. Unfortunately, a systematic characterization of each parameter requires a significant amount of time. Third, incorporating advanced TEM characterization techniques such as EDS, EELS, or HAADF-STEM could provide a clearer understanding of the elemental composition and crystal structure within the alloys, helping to explain the presence of amorphous layers or other unexpected features. Finally, while our focus has been on measuring continuous alloy films, future work should also include integrating these films into N-S junctions and JoFETs to directly asses the size, hardness, and magnetic field-compatibility of the gap they induce in germanium.

In conclusion, while our research has not identified a clear pathway for significantly improving the proximity effect of germanium, it lays a foundation for further exploration. The complexities and variability observed in the formation of superconducting germanosilicide alloys highlight the need for continued investigation into methods for achieving consistent and high-quality contacts. Future work will be essential in refining these processes and advancing the potential of germanium-based hybrid quantum devices.

Bibliography

[1] Richard P. Feynman. Simulating physics with computers. *International Journal of Theoretical Physics*, 21:467–488, 1982.

[2] Michael A. Neilsen and Isaac L. Chuang. *Quantum Computation and Quantum Information.* Cambridge University Press, Cambridge, 2010.

[3] David Deutsch, Adriano Barenco, and Artur Ekert. Universality in quantum computation. *Proceedings of the Royal Society of London. Series A: Mathematical, Physical and Engineering Sciences*, 449:669–677, 1995.

[4] Adriano Barenco, Charles H. Bennett, Richard Cleve, David P. DiVincenzo, Norman Margolus, Peter W. Shor, Tycho Sleator, John A. Smolin, and Harald Weinfurter. Elementary gates for quantum computation. *Physical Review A*, 52:3457–3467, 1995.

[5] Peter W. Shor. Algorithms for quantum computation: Discrete logarithms and factoring. In *Proceedings of the 35th Annual Symposium on Foundations of Computer Science (FOCS)*, pages 124–134. IEEE, 1994.

[6] Lov K. Grover. A fast quantum mechanical algorithm for database search. In *Proceedings of the 28th Annual ACM Symposium on Theory of Computing (STOC)*, pages 212–219. ACM, 1996.

[7] I. M. Georgescu, S. Ashhab, and F. Nori. Quantum simulation. *Reviews of Modern Physics*, 86(1):153–185, 2014.

[8] N. David Mermin. *Quantum Computer Science: An Introduction.* Cambridge University Press, Cambridge, 2007.

[9] David P. DiVincenzo. The Physical Implementation of Quantum Computation. *Fortschritte der Physik*, 48:771–783, 2000.

[10] Austin G. Fowler, Matteo Mariantoni, John M. Martinis, and Andrew N. Cleland. Surface codes: Towards practical large-scale quantum computation. *Physical Review A*, 86(3):032324, 2012.

[11] Jens Koch, Terri M. Yu, Jay Gambetta, A. A. Houck, D. I. Schuster, J. Majer, Alexandre Blais, M. H. Devoret, S. M. Girvin, and R. J. Schoelkopf. Charge-insensitive qubit design derived from the Cooper pair box. *Physical Review A*, 76:042319, 2007.

[12] J. A. Schreier, A. A. Houck, Jens Koch, D. I. Schuster, B. R. Johnson, J. M. Chow, J. M. Gambetta, J. Majer, L. Frunzio, M. H. Devoret, S. M. Girvin, and R. J. Schoelkopf. Suppressing charge noise decoherence in superconducting charge qubits. *Physical Review B*, 77:180502, 2008.

[13] Lieven M. K. Vandersypen and Mark A. Eriksson. Quantum computing with semiconductor spins. *Physics Today*, 72:38–45, 2019.

[14] B. J. Riel. An introduction to self-assembled quantum dots. *American Journal of Physics*, 76(8):750–757, 2008.

[15] Richard J. Warburton. Single spins in self-assembled quantum dots. *Nature Materials*, 12:483–493, 2013.

[16] Cherie R. Kagan, Efrat Lifshitz, Edward H. Sargent, and Dmitri V. Talapin. Building devices from colloidal quantum dots. *Science*, 353(6302):aac5523, 2016.

[17] Mengxia Liu, Nuri Yazdani, Maksym Yarema, Maximilian Jansen, Vanessa Wood, and Edward H. Sargent. Colloidal quantum dot electronics. *Nature Electronics*, 4:548–558, 2021.

[18] L. P. Kouwenhoven, D. G. Austing, and S. Tarucha. Few-electron quantum dots. *Reports on Progress in Physics*, 64(6):701–736, 2001.

[19] M. A. Reed. Molecular-scale electronics. *Proceedings of the IEEE*, 87(4):652–658, 1999.

[20] Juha T. Muhonen, Juan P. Dehollain, Arne Laucht, Fay E. Hudson, Rachpon Kalra, Takeharu Sekiguchi, Kohei M. Itoh, David N. Jamieson, Jeffrey C. McCallum, Andrew S. Dzurak, and Andrea Morello. Storing quantum information for 30 seconds in a nanoelectronic device. *Nature Nanotechnology*, 9:986–991, 2014.

[21] J. C. McCallum, B. C. Johnson, and T. Botzem. Donor-based qubits for quantum computing in silicon. *Applied Physics Reviews*, 8(3):031314, 2021.

[22] Leo P. Kouwenhoven, Charles M. Marcus, Paul L. McEuen, Seigo Tarucha, Robert M. Westervelt, and Ned S. Wingreen. Electron Transport in Quantum Dots. In *Mesoscopic Electron Transport*, volume 6, pages 105–214. Springer Netherlands, Dordrecht, 1997.

[23] W. G. van der Wiel, S. De Franceschi, J. M. Elzerman, T. Fujisawa, S. Tarucha, and L. P. Kouwenhoven. Electron transport through double quantum dots. *Reviews of Modern Physics*, 75(1):1–22, 2003.

[24] Guido Burkard, Thaddeus D. Ladd, Andrew Pan, John M. Nichol, and Jason R. Petta. Semiconductor spin qubits. *Reviews of Modern Physics*, 95(2):025003, 2023.

[25] T. Hayashi, T. Fujisawa, H. D. Cheong, Y. H. Jeong, and Y. Hirayama. Coherent Manipulation of Electronic States in a Double Quantum Dot. *Physical Review Letters*, 91:226804, 2003.

[26] Toshimasa Fujisawa, Toshiaki Hayashi, H. D. Cheong, Y. H. Jeong, and Yoshiro Hirayama. Rotation and phase-shift operations for a charge qubit in a double quantum dot. *Physica E: Low-dimensional Systems and Nanostructures*, 21(2):1046–1052, 2004.

[27] J. R. Petta, A. C. Johnson, J. M. Taylor, E. A. Laird, A. Yacoby, M. D. Lukin, C. M. Marcus, M. P. Hanson, and A. C. Gossard. Coherent Manipulation of Coupled Electron Spins in Semiconductor Quantum Dots. *Science*, 309(5744):2180–2184, 2005.

[28] R. Hanson, L. P. Kouwenhoven, J. R. Petta, S. Tarucha, and L. M. K. Vandersypen. Spins in few-electron quantum dots. *Reviews of Modern Physics*, 79(4):1217–1265, 2007.

[29] J. M. Taylor, J. R. Petta, A. C. Johnson, A. Yacoby, C. M. Marcus, and M. D. Lukin. Relaxation, dephasing, and quantum control of electron spins in double quantum dots. *Physical Review B*, 76:035315, 2007.

[30] Mark Friesen, Paul Rugheimer, Donald E. Savage, Max G. Lagally, Daniel W. van der Weide, Robert Joynt, and Mark A. Eriksson. Practical design and simulation of silicon-based quantum-dot qubits. *Physical Review B*, 67:121301, 2003.

[31] C. B. Simmons, Madhu Thalakulam, Nakul Shaji, Levente J. Klein, Hua Qin, R. H. Blick, D. E. Savage, M. G. Lagally, S. N. Coppersmith, and M. A. Eriksson. Single-electron quantum dot in Si/SiGe with integrated charge sensing. *Applied Physics Letters*, 91:1–3, 2007.

[32] Madhu Thalakulam, C. B. Simmons, B. M. Rosemeyer, D. E. Savage, M. G. Lagally, Mark Friesen, S. N. Coppersmith, and M. A. Eriksson. Fast tunnel rates in Si/SiGe one-electron single and double quantum dots. *Applied Physics Letters*, 96:183104, 2010.

[33] B. M. Maune, M. G. Borselli, B. Huang, T. D. Ladd, P. W. Deelman, K. S. Holabird, A. A. Kiselev, I. Alvarado-Rodriguez, R. S. Ross, A. E. Schmitz, M. Sokolich, C. A. Watson, M. F. Gyure, and A. T. Hunter. Coherent singlet-triplet oscillations in a silicon-based double quantum dot. *Nature*, 481:344–347, 2012.

[34] Floris A. Zwanenburg, Andrew S. Dzurak, Andrea Morello, Michelle Y. Simmons, Lloyd C. L. Hollenberg, Gerhard Klimeck, Sven Rogge, Susan N. Coppersmith, and Mark A. Eriksson. Silicon quantum electronics. *Reviews of Modern Physics*, 85:961–1019, 2013.

[35] E. Kawakami, P. Scarlino, D. R. Ward, F. R. Braakman, D. E. Savage, M. G. Lagally, Mark Friesen, S. N. Coppersmith, M. A. Eriksson, and L. M. K. Vandersypen. Electrical control of a long-lived spin qubit in a Si/SiGe quantum dot. *Nature Nanotechnology*, 9:666–670, 2014.

[36] M. Veldhorst, J. C. C. Hwang, C. H. Yang, A. W. Leenstra, B. de Ronde, J. P. Dehollain, J. T. Muhonen, F. E. Hudson, K. M. Itoh, A. Morello, and A. S. Dzurak. An addressable quantum dot qubit with fault-tolerant control-fidelity. *Nature Nanotechnology*, 9:981–985, 2014.

[37] M. Veldhorst, C. H. Yang, J. C. C. Hwang, W. Huang, J. P. Dehollain, J. T. Muhonen, S. Simmons, A. Laucht, F. E. Hudson, K. M. Itoh, A. Morello, and A. S. Dzurak. A two-qubit logic gate in silicon. *Nature*, 526:410–414, 2015.

[38] A. M. Tyryshkin, S. A. Lyon, A. V. Astashkin, and A. M. Raitsimring. Electron spin relaxation times of phosphorus donors in silicon. *Physical Review B*, 68:193207, 2003.

[39] Alexei M. Tyryshkin, Shinichi Tojo, John J. L. Morton, Helge Riemann, Nikolai V. Abrosimov, Peter Becker, Hans-Joachim Pohl, Thomas Schenkel, Michael L. W. Thewalt, Kohei M. Itoh, and S. A. Lyon. Electron spin coherence exceeding seconds in high-purity silicon. *Nature Materials*, 11:143–147, 2012.

[40] L. M. K. Vandersypen, H. Bluhm, J. S. Clarke, A. S. Dzurak, R. Ishihara, A. Morello, D. J. Reilly, L. R. Schreiber, and M. Veldhorst. Interfacing spin qubits in quantum dots and donors—hot, dense, and coherent. *npj Quantum Information*, 3(34), 2017.

[41] R. Li, N. I. Dumoulin Stuyck, S. Kubicek, J. Jussot, B. T. Chan, F. A. Mohiyaddin, A. Elsayed, M. Shehata, G. Simion, C. Godfrin, Y. Canvel, Ts. Ivanov, L. Goux, B. Govoreanu, and I. P. Radu. A flexible 300 mm integrated Si MOS platform for electron- and hole-spin qubits exploration. In *2020 IEEE International Electron Devices Meeting (IEDM)*, pages 38.3.1–38.3.4, 2020.

[42] A. M. J. Zwerver, T. Krähenmann, T. F. Watson, L. Lampert, H. C. George, R. Pillarisetty, S. A. Bojarski, P. Amin, S. V. Amitonov, J. M. Boter, R. Caudillo, D. Correas-Serrano, J. P. Dehollain, G. Droulers, E. M. Henry, R. Kotlyar, M. Lodari, F. Lüthi, D. J. Michalak, B. K. Mueller, S. Neyens, J. Roberts, N. Samkharadze, G. Zheng, O. K. Zietz, G. Scappucci, M. Veldhorst, L. M. K. Vandersypen, and J. S. Clarke. Qubits made by advanced semiconductor manufacturing. *Nature Electronics*, 5:184–190, 2022.

[43] Samuel Neyens, Otto K. Zietz, Thomas F. Watson, Florian Luthi, Aditi Nethwewala, Hubert C. George, Eric Henry, Mohammad Islam, Andrew J. Wagner, Felix Borjans, Elliot J. Connors, J. Corrigan, Matthew J. Curry, Daniel Keith, Roza Kotlyar, Lester F. Lampert, Mateusz T. Mądzik, Kent Millard, Fahd A. Mohiyaddin, Stefano Pellerano, Ravi Pillarisetty, Mick Ramsey, Rostyslav Savvystykh, Simon Schaal, Guoji Zheng, Joshua Ziegler, Nathaniel C. Bishop, Stephanie Bojarski, Jeanette Roberts, and James S. Clarke. Probing single electrons across 300-mm spin qubit wafers. *Nature*, 629:80–85, 2024.

[44] A. Elsayed, M. M. K. Shehata, C. Godfrin, S. Kubicek, S. Massar, Y. Canvel, J. Jussot, G. Simion, M. Mongillo, D. Wan, B. Govoreanu, I. P. Radu, R. Li, P. Van Dorpe, and K. De Greve. Low charge noise quantum dots with industrial CMOS manufacturing. *npj Quantum Information*, 10:70, 2024.

[45] Nard Dumoulin Stuyck, Andre Saraiva, Will Gilbert, Jesus Cifuentes Pardo, Ruoyu Li, Christopher C. Escott, Kristiaan De Greve, Sorin Voinigescu, David J. Reilly, and Andrew S. Dzurak. CMOS compatibility of semiconductor spin qubits. *arXiv:2409.03993*, 2024.

[46] X. Mi, T. M. Hazard, C. Payette, K. Wang, D. M. Zajac, J. V. Cady, and J. R. Petta. Magnetotransport studies of mobility limiting mechanisms in undoped Si/SiGe heterostructures. *Physical Review B*, 92:1–8, 2015.

[47] F. Schaffler, D. Tobben, H.-J. Herzog, G. Abstreiter, and B. Hollander. High-electron-mobility Si/SiGe heterostructures: influence of the relaxed SiGe buffer layer. *Semiconductor Science and Technology*, 7(2):260, 1992.

[48] Friedrich Schäffler. High-mobility Si and Ge structures. *Semiconductor Science and Technology*, 12:1515, 1997.

[49] T. M. Lu, D. C. Tsui, C.-H. Lee, and C. W. Liu. Observation of two-dimensional electron gas in a Si quantum well with mobility of 1.6 $\times 10^6$ cm^2/vs. *Applied Physics Letters*, 94:182102, 2009.

[50] D. Többen, F. Schäffler, A. Zrenner, and G. Abstreiter. Magnetotransport studies of remote doped Si/Si$_{1-x}$Ge$_x$ heterostructures grown on relaxed SiGe buffer layers. *Thin Solid Films*, 222(1):15–19, 1992.

[51] Thomas McJunkin. *Heterostructure Modifications, Fabrication Improvements, and Measurement Automation of Si/SiGe Quantum Dots for Quantum Computation*. PhD thesis, University of Wisconsin-Madison, 2021.

[52] John H. Davies. *The Physics of Low-Dimensional Semiconductors: An Introduction*. Cambridge University Press, Cambridge, first edition, 1998.

[53] D. M. Zajac, T. M. Hazard, X. Mi, E. Nielsen, and J. R. Petta. Scalable Gate Architecture for a One-Dimensional Array of Semiconductor Spin Qubits. *Physical Review Applied*, 6:054013, 2016.

[54] J. P. Dodson, Nathan Holman, Brandur Thorgrimsson, Samuel F. Neyens, E. R. MacQuarrie, Thomas McJunkin, Ryan H. Foote, L. F. Edge, S. N. Coppersmith, and M. A. Eriksson. Fabrication process and failure analysis for robust quantum dots in silicon. *Nanotechnology*, 31(50):505001, 2020.

[55] Wonill Ha, Sieu D. Ha, Maxwell D. Choi, Yan Tang, Adele E. Schmitz, Mark P. Levendorf, Kangmu Lee, James M. Chappell, Tower S. Adams, Daniel R. Hulbert, Edwin Acuna, Ramsey S. Noah, Justine W. Matten, Michael P. Jura, Jeffrey A. Wright, Matthew T. Rakher, and Matthew G. Borselli. A Flexible Design Platform for Si/SiGe Exchange-Only Qubits with Low Disorder. *Nano Letters*, 22(3):828–836, 2021.

[56] Ruoyu Li, Luca Petit, David P. Franke, Juan Pablo Dehollain, Jonas Helsen, Mark Steudtner, Nicole K. Thomas, Zachary R. Yoscovits, Kanwal J. Singh, Stephanie Wehner, Lieven M. K. Vandersypen, James S. Clarke, and Menno Veldhorst. A crossbar network for silicon quantum dot qubits. *Science Advances*, 4(7):eaar3960, 2018.

[57] J. M. Boter, J. P. Dehollain, J. P. G. van Dijk, T. Hensgens, R. Versluis, J. S. Clarke, M. Veldhorst, F. Sebastiano, and L. M. K. Vandersypen. A sparse spin qubit array with

integrated control electronics. In *2019 IEEE International Electron Devices Meeting (IEDM)*, pages 31.4.1–31.4.4, 2019.

[58] Aaron J. Weinstein, Matthew D. Reed, Aaron M. Jones, Reed W. Andrews, David Barnes, Jacob Z. Blumoff, Larken E. Euliss, Kevin Eng, Bryan H. Fong, Sieu D. Ha, Daniel R. Hulbert, Clayton A. C. Jackson, Michael Jura, Tyler E. Keating, Joseph Kerckhoff, Andrey A. Kiselev, Justine Matten, Golam Sabbir, Aaron Smith, Jeffrey Wright, Matthew T. Rakher, Thaddeus D. Ladd, and Matthew G. Borselli. Universal logic with encoded spin qubits in silicon. *Nature*, 615(7954):817–822, 2023.

[59] Francesco Borsoi, Nico W. Hendrickx, Valentin John, Marcel Meyer, Sayr Motz, Floor van Riggelen, Amir Sammak, Sander L. de Snoo, Giordano Scappucci, and Menno Veldhorst. Shared control of a 16 semiconductor quantum dot crossbar array. *Nature Nanotechnology*, 19:21–27, 2024.

[60] Chien-An Wang, Valentin John, Hanifa Tidjani, Cécile X. Yu, Alexander S. Ivlev, Corentin Déprez, Floor van Riggelen-Doelman, Benjamin D. Woods, Nico W. Hendrickx, William I. L. Lawrie, Lucas E. A. Stehouwer, Stefan D. Oosterhout, Amir Sammak, Mark Friesen, Giordano Scappucci, Sander L. de Snoo, Maximilian Rimbach-Russ, Francesco Borsoi, and Menno Veldhorst. Operating semiconductor quantum processors with hopping spins. *Science*, 385(6707):447–452, 2024.

[61] J.P. Dodson. *Overlapping Aluminum-Gate Quantum Dots for Valley-Orbit Based Qubits in Si/SiGe*. PhD thesis, University of Wisconsin-Madison, 2021.

[62] Nathan Holman. *Circuit Quantum Electrodynamics with Semiconductor Quantum Dots*. PhD thesis, University of Wisconsin-Madison, 2020.

[63] Yuli V. Nazarov and Yaroslav M. Blanter. *Quantum Transport: Introduction to Nanoscience*. Cambridge University Press, Cambridge, 2009.

[64] L. Petit, H. G. J. Eenink, M. Russ, W. I. L. Lawrie, N. W. Hendrickx, S. G. J. Philips, J. S. Clarke, L. M. K. Vandersypen, and M. Veldhorst. Universal quantum logic in hot silicon qubits. *Nature*, 580:355–359, 2020.

[65] C. H. Yang, R. C. C. Leon, J. C. C. Hwang, A. Saraiva, T. Tanttu, W. Huang, J. Camirand Lemyre, K. W. Chan, K. Y. Tan, F. E. Hudson, K. M. Itoh, A. Morello, M. Pioro-Ladrière, A. Laucht, and A. S. Dzurak. Operation of a silicon quantum processor unit cell above one kelvin. *Nature*, 580:350–354, 2020.

[66] Luca Petit, Maximilian Russ, Gertjan H. G. J. Eenink, William I. L. Lawrie, James S. Clarke, Lieven M. K. Vandersypen, and Menno Veldhorst. Design and integration of single-qubit rotations and two-qubit gates in silicon above one kelvin. *Communications Materials*, 3:82, 2022.

[67] Jonathan Y. Huang, Rocky Y. Su, Wee Han Lim, MengKe Feng, Barnaby van Straaten, Brandon Severin, Will Gilbert, Nard Dumoulin Stuyck, Tuomo Tanttu, Santiago Serrano, Jesus D. Cifuentes, Ingvild Hansen, Amanda E. Seedhouse, Ensar Vahapoglu,

Ross C. C. Leon, Nikolay V. Abrosimov, Hans-Joachim Pohl, Michael L. W. Thewalt, Fay E. Hudson, Christopher C. Escott, Natalia Ares, Stephen D. Bartlett, Andrea Morello, Andre Saraiva, Arne Laucht, Andrew S. Dzurak, and Chih Hwan Yang. High-fidelity spin qubit operation and algorithmic initialization above 1 K. *Nature*, 627:772–777, 2024.

[68] K. C. Nowack, M. Shafiei, M. Laforest, G. E. D. K. Prawiroatmodjo, L. R. Schreiber, C. Reichl, W. Wegscheider, and L. M. K. Vandersypen. Single-Shot Correlations and Two-Qubit Gate of Solid-State Spins. *Science*, 333(6047):1269–1272, 2011.

[69] T. Hensgens, T. Fujita, L. Janssen, Xiao Li, C. J. Van Diepen, C. Reichl, W. Wegscheider, S. Das Sarma, and L. M. K. Vandersypen. Quantum simulation of a Fermi–Hubbard model using a semiconductor quantum dot array. *Nature*, 548(7665):70–73, 2017.

[70] A. R. Mills, D. M. Zajac, M. J. Gullans, F. J. Schupp, T. M. Hazard, and J. R. Petta. Shuttling a single charge across a one-dimensional array of silicon quantum dots. *Nature Communications*, 10(1):1063, 2019.

[71] T.-K. Hsiao, C. J. van Diepen, U. Mukhopadhyay, C. Reichl, W. Wegscheider, and L. M. K. Vandersypen. Efficient Orthogonal Control of Tunnel Couplings in a Quantum Dot Array. *Physical Review Applied*, 13(5):054018, 2020.

[72] Haifeng Qiao, Yadav P. Kandel, Kuangyin Deng, Saeed Fallahi, Geoffrey C. Gardner, Michael J. Manfra, Edwin Barnes, and John M. Nichol. Coherent Multispin Exchange Coupling in a Quantum-Dot Spin Chain. *Physical Review X*, 10(3):031006, 2020.

[73] K. D. Petersson, J. R. Petta, H. Lu, and A. C. Gossard. Quantum Coherence in a One-Electron Semiconductor Charge Qubit. *Physical Review Letters*, 105(24):246804, 2010.

[74] Yoko Hada and Mikio Eto. Electronic states in silicon quantum dots: Multivalley artificial atoms. *Physical Review B*, 68:155322, 2003.

[75] H. Ekmel Ercan, S. N. Coppersmith, and Mark Friesen. Strong electron-electron interactions in Si/SiGe quantum dots. *Physical Review B*, 104:235302, 2021.

[76] C. B. Simmons, J. R. Prance, B. J. Van Bael, Teck Seng Koh, Zhan Shi, D. E. Savage, M. G. Lagally, R. Joynt, Mark Friesen, S. N. Coppersmith, and M. A. Eriksson. Tunable spin loading and T1 of a silicon spin qubit measured by single-shot readout. *Physical Review Letters*, 106:1–4, 2011.

[77] J. P. Dodson, H. Ekmel Ercan, J. Corrigan, Merritt P. Losert, Nathan Holman, Thomas McJunkin, L. F. Edge, Mark Friesen, S. N. Coppersmith, and M. A. Eriksson. How Valley-Orbit States in Silicon Quantum Dots Probe Quantum Well Interfaces. *Physical Review Letters*, 128(14):146802, 2022.

[78] Thomas McJunkin, Benjamin Harpt, Yi Feng, Merritt P. Losert, Rajib Rahman, J. P. Dodson, M. A. Wolfe, D. E. Savage, M. G. Lagally, S. N. Coppersmith, Mark Friesen, Robert Joynt, and M. A. Eriksson. SiGe quantum wells with oscillating Ge concentrations for quantum dot qubits. *Nature Communications*, 13(1):7777, 2022.

[79] Timothy B. Boykin, Gerhard Klimeck, M. A. Eriksson, Mark Friesen, S. N. Coppersmith, Paul Von Allmen, Fabiano Oyafuso, and Seungwon Lee. Valley splitting in strained silicon quantum wells. *Applied Physics Letters*, 84:115–117, 2004.

[80] Timothy B. Boykin, Gerhard Klimeck, Mark Friesen, S. N. Coppersmith, Paul von Allmen, Fabiano Oyafuso, and Seungwon Lee. Valley splitting in low-density quantum-confined heterostructures studied using tight-binding models. *Physical Review B*, 70:165325, 2004.

[81] Mark Friesen, Sucismita Chutia, Charles Tahan, and S. N. Coppersmith. Valley splitting theory of SiGe/Si/SiGe quantum wells. *Physical Review B*, 75:115318, 2007.

[82] M. G. Borselli, R. S. Ross, A. A. Kiselev, E. T. Croke, K. S. Holabird, P. W. Deelman, L. D. Warren, I. Alvarado-Rodriguez, I. Milosavljevic, F. C. Ku, W. S. Wong, A. E. Schmitz, M. Sokolich, M. F. Gyure, and A. T. Hunter. Measurement of valley splitting in high-symmetry Si/SiGe quantum dots. *Applied Physics Letters*, 98:123118, 2011.

[83] Joshua S. Schoenfield, Blake M. Freeman, and HongWen Jiang. Coherent manipulation of valley states at multiple charge configurations of a silicon quantum dot device. *Nature Communications*, 8:64, 2017.

[84] Edward H. Chen, Kate Raach, Andrew Pan, Andrey A. Kiselev, Edwin Acuna, Jacob Z. Blumoff, Teresa Brecht, Maxwell D. Choi, Wonill Ha, Daniel R. Hulbert, Michael P. Jura, Tyler E. Keating, Ramsey Noah, Bo Sun, Bryan J. Thomas, Matthew G. Borselli, C. A. C. Jackson, Matthew T. Rakher, and Richard S. Ross. Detuning Axis Pulsed Spectroscopy of Valley-Orbital States in Si/SiGe Quantum Dots. *Physical Review Applied*, 15:044033, 2021.

[85] Mats Volmer, Tom Struck, Arnau Sala, Bingjie Chen, Max Oberländer, Tobias Offermann, Ran Xue, Lino Visser, Jhih-Sian Tu, Stefan Trellenkamp, Łukasz Cywiński, Hendrik Bluhm, and Lars R. Schreiber. Mapping of valley splitting by conveyor-mode spin-coherent electron shuttling. *npj Quantum Information*, 10:61, 2024.

[86] C. H. Yang, A. Rossi, R. Ruskov, N. S. Lai, F. A. Mohiyaddin, S. Lee, C. Tahan, G. Klimeck, A. Morello, and A. S. Dzurak. Spin-valley lifetimes in a silicon quantum dot with tunable valley splitting. *Nature Communications*, 4:2069, 2013.

[87] Peihao Huang and Xuedong Hu. Spin relaxation in a Si quantum dot due to spin-valley mixing. *Physical Review B*, 90:235315, 2014.

[88] Xin Zhang, Rui-Zi Hu, Hai-Ou Li, Fang-Ming Jing, Yuan Zhou, Rong-Long Ma, Ming Ni, Gang Luo, Gang Cao, Gui-Lei Wang, Xuedong Hu, Hong-Wen Jiang, Guang-Can Guo, and Guo-Ping Guo. Giant Anisotropy of Spin Relaxation and Spin-Valley Mixing in a Silicon Quantum Dot. *Physical Review Letters*, 124:257701, 2020.

[89] Nicholas E. Penthorn, Joshua S. Schoenfield, Lisa F. Edge, and HongWen Jiang. Direct Measurement of Electron Intervalley Relaxation in a Si/SiGe Quantum Dot. *Physical Review Applied*, 14:054015, 2020.

[90] Samuel F. Neyens, Ryan H. Foote, Brandur Thorgrimsson, T. J. Knapp, Thomas McJunkin, L. M. K. Vandersypen, Payam Amin, Nicole K. Thomas, James S. Clarke, D. E. Savage, M. G. Lagally, Mark Friesen, S. N. Coppersmith, and M. A. Eriksson. The critical role of substrate disorder in valley splitting in Si quantum wells. *Applied Physics Letters*, 112:1–5, 2018.

[91] Brian Paquelet Wuetz, Merritt P. Losert, Sebastian Koelling, Lucas E. A. Stehouwer, Anne-Marije J. Zwerver, Stephan G. J. Philips, Mateusz T. Mądzik, Xiao Xue, Guoji Zheng, Mario Lodari, Sergey V. Amitonov, Nodar Samkharadze, Amir Sammak, Lieven M. K. Vandersypen, Rajib Rahman, Susan N. Coppersmith, Oussama Moutanabbir, Mark Friesen, and Giordano Scappucci. Atomic fluctuations lifting the energy degeneracy in Si/SiGe quantum dots. *Nature Communications*, 13:7730, 2022.

[92] Merritt P. Losert, M. A. Eriksson, Robert Joynt, Rajib Rahman, Giordano Scappucci, Susan N. Coppersmith, and Mark Friesen. Practical strategies for enhancing the valley splitting in Si/SiGe quantum wells. *Physical Review B*, 108:125405, 2023.

[93] Thomas McJunkin, E. R. Macquarrie, Leah Tom, S. F. Neyens, J. P. Dodson, Brandur Thorgrimsson, J. Corrigan, H. Ekmel Ercan, D. E. Savage, M. G. Lagally, Robert Joynt, S. N. Coppersmith, Mark Friesen, and M. A. Eriksson. Valley splittings in Si/SiGe quantum dots with a germanium spike in the silicon well. *Physcial Review B*, 104:1–11, 2021.

[94] Yi Feng and Robert Joynt. Enhanced valley splitting in si layers with oscillatory Ge concentration. *Physical Review B*, 106:085304, 2022.

[95] Benjamin D. Woods, Hudaiba Soomro, E. S. Joseph, Collin C. D. Frink, Robert Joynt, M. A. Eriksson, and Mark Friesen. Coupling conduction-band valleys in SiGe heterostructures via shear strain and Ge concentration oscillations. *npj Quantum Information*, 10:54, 2024.

[96] J. Corrigan, J. P. Dodson, H. Ekmel Ercan, J. C. Abadillo-Uriel, Brandur Thorgrimsson, T. J. Knapp, Nathan Holman, Thomas McJunkin, Samuel F. Neyens, E. R. Macquarrie, Ryan H. Foote, L. F. Edge, Mark Friesen, S. N. Coppersmith, and M. A. Eriksson. Coherent Control and Spectroscopy of a Semiconductor Quantum Dot Wigner Molecule. *Physical Review Letters*, 127:127701, 2021.

[97] J. Gorman, D. G. Hasko, and D. A. Williams. Charge-Qubit Operation of an Isolated Double Quantum Dot. *Physical Review Letters*, 95:090502, 2005.

[98] Daniel Loss and David P. DiVincenzo. Quantum computation with quantum dots. *Physical Review A*, 57:120–126, 1998.

[99] Zhan Shi, C. B. Simmons, Daniel R. Ward, J. R. Prance, Xian Wu, Teck Seng Koh, John King Gamble, D. E. Savage, M. G. Lagally, Mark Friesen, S. N. Coppersmith, and M. A. Eriksson. Fast coherent manipulation of three-electron states in a double quantum dot. *Nature Communications*, 5:3020, 2013.

[100] Dohun Kim, D. R. Ward, C. B. Simmons, John King Gamble, Robin Blume-Kohout, Erik Nielsen, D. E. Savage, M. G. Lagally, Mark Friesen, S. N. Coppersmith, and M. A. Eriksson. Microwave-driven coherent operation of a semiconductor quantum dot charge qubit. *Nature Nanotechnology*, 10(3):243–247, 2015.

[101] Dohun Kim, Daniel R. Ward, Christie B. Simmons, Don E. Savage, Max G. Lagally, Mark Friesen, Susan N. Coppersmith, and Mark A. Eriksson. High-fidelity resonant gating of a silicon-based quantum dot hybrid qubit. *npj Quantum Information*, 1:15004, 2015.

[102] M. D. Reed, B. M. Maune, R. W. Andrews, M. G. Borselli, K. Eng, M. P. Jura, A. A. Kiselev, T. D. Ladd, S. T. Merkel, I. Milosavljevic, E. J. Pritchett, M. T. Rakher, R. S. Ross, A. E. Schmitz, A. Smith, J. A. Wright, M. F. Gyure, and A. T. Hunter. Reduced Sensitivity to Charge Noise in Semiconductor Spin Qubits via Symmetric Operation. *Physical Review Letters*, 116(11):110402, 2016.

[103] Reed W. Andrews, Cody Jones, Matthew D. Reed, Aaron M. Jones, Sieu D. Ha, Michael P. Jura, Joseph Kerckhoff, Mark Levendorf, Seán Meenehan, Seth T. Merkel, Aaron Smith, Bo Sun, Aaron J. Weinstein, Matthew T. Rakher, Thaddeus D. Ladd, and Matthew G. Borselli. Quantifying error and leakage in an encoded Si/SiGe triple-dot qubit. *Nature Nanotechnology*, 14:747–750, 2019.

[104] F. H. L. Koppens, C. Buizert, K. J. Tielrooij, I. T. Vink, K. C. Nowack, T. Meunier, L. P. Kouwenhoven, and L. M. K. Vandersypen. Driven coherent oscillations of a single electron spin in a quantum dot. *Nature*, 442(7104):766–771, 2006.

[105] M. Pioro-Ladrière, T. Obata, Y. Tokura, Y.-S. Shin, T. Kubo, K. Yoshida, T. Taniyama, and S. Tarucha. Electrically driven single-electron spin resonance in a slanting Zeeman field. *Nature Physics*, 4:776–779, 2008.

[106] J. M. Elzerman, R. Hanson, L. H. Willems van Beveren, B. Witkamp, L. M. K. Vandersypen, and L. P. Kouwenhoven. Single-shot read-out of an individual electron spin in a quantum dot. *Nature*, 430:431–435, 2004.

[107] J. R. Petta, A. C. Johnson, A. Yacoby, C. M. Marcus, M. P. Hanson, and A. C. Gossard. Pulsed-gate measurements of the singlet-triplet relaxation time in a two-electron double quantum dot. *Physical Review B*, 72:161301, 2005.

[108] Peter Stano and Daniel Loss. Review of performance metrics of spin qubits in gated semiconducting nanostructures. *Nature Reviews Physics*, 4:672–688, 2022.

[109] John J. L. Morton, Dane R. McCamey, Mark A. Eriksson, and Stephen A. Lyon. Embracing the quantum limit in silicon computing. *Nature*, 479:345–353, 2011.

[110] Will Gilbert, Tuomo Tanttu, Wee Han Lim, MengKe Feng, Jonathan Y. Huang, Jesus D. Cifuentes, Santiago Serrano, Philip Y. Mai, Ross C. C. Leon, Christopher C. Escott, Kohei M. Itoh, Nikolay V. Abrosimov, Hans-Joachim Pohl, Michael L. W. Thewalt, Fay E. Hudson, Andrea Morello, Arne Laucht, Chih Hwan Yang, Andre Saraiva, and Andrew S. Dzurak. On-demand electrical control of spin qubits. *Nature Nanotechnology*, 18:131–136, 2023.

[111] Tuomo Tanttu, Wee Han Lim, Jonathan Y. Huang, Nard Dumoulin Stuyck, Will Gilbert, Rocky Y. Su, MengKe Feng, Jesus D. Cifuentes, Amanda E. Seedhouse, Stefan K. Seritan, Corey I. Ostrove, Kenneth M. Rudinger, Ross C. C. Leon, Wister Huang, Christopher C. Escott, Kohei M. Itoh, Nikolay V. Abrosimov, Hans-Joachim Pohl, Michael L. W. Thewalt, Fay E. Hudson, Robin Blume-Kohout, Stephen D. Bartlett, Andrea Morello, Arne Laucht, Chih Hwan Yang, Andre Saraiva, and Andrew S. Dzurak. Assessment of the errors of high-fidelity two-qubit gates in silicon quantum dots. *Nature Physics*, 2024.

[112] Irina Heinz, Felix Borjans, Matthew Curry, Roza Kotlyar, Florian Luthi, Mateusz T. Mądzik, Fahd A. Mohiyaddin, Nathaniel Bishop, and Guido Burkard. Fast quantum gates for exchange-only qubits using simultaneous exchange pulses. *arXiv*, 2024.

[113] Intel Corporation. Intel's New Quantum Chip 'Tunnel Falls' to Advance Quantum Research. Intel Newsroom, June 2023. Accessed: 2024-10-01.

[114] M. Field, C. G. Smith, M. Pepper, D. A. Ritchie, J. E. F. Frost, G. A. C. Jones, and D. G. Hasko. Measurements of Coulomb blockade with a noninvasive voltage probe. *Physical Review Letters*, 70:1311–1314, 1993.

[115] D. P. DiVincenzo, D. Bacon, J. Kempe, G. Burkard, and K. B. Whaley. Universal quantum computation with the exchange interaction. *Nature*, 408:339–342, 2000.

[116] J. Kempe, D. Bacon, D. A. Lidar, and K. B. Whaley. Theory of decoherence-free fault-tolerant universal quantum computation. *Physical Review A*, 63:042307, 2001.

[117] Maximilian Russ and Guido Burkard. Three-electron spin qubits. *Journal of Physics: Condensed Matter*, 29(39):393001, 2017.

[118] Jacob Z. Blumoff, Andrew S. Pan, Tyler E. Keating, Reed W. Andrews, David W. Barnes, Teresa L. Brecht, Edward T. Croke, Larken E. Euliss, Jacob A. Fast, Clayton A.C. Jackson, Aaron M. Jones, Joseph Kerckhoff, Robert K. Lanza, Kate Raach, Bryan J. Thomas, Roland Velunta, Aaron J. Weinstein, Thaddeus D. Ladd, Kevin Eng, Matthew G. Borselli, Andrew T. Hunter, and Matthew T. Rakher. Fast and High-Fidelity State Preparation and Measurement in Triple-Quantum-Dot Spin Qubits. *PRX Quantum*, 3(1):010352, 2022.

[119] K. Ono, D. G. Austing, Y. Tokura, and S. Tarucha. Current Rectification by Pauli Exclusion in a Weakly Coupled Double Quantum Dot System. *Science*, 297(5585):1313–1317, 2002.

[120] J. Medford, J. Beil, J. M. Taylor, S. D. Bartlett, A. C. Doherty, E. I. Rashba, D. P. DiVincenzo, H. Lu, A. C. Gossard, and C. M. Marcus. Self-consistent measurement and state tomography of an exchange-only spin qubit. *Nature Nanotechnology*, 8(9):654–659, 2013.

[121] Brennan Undseth, Oriol Pietx-Casas, Eline Raymenants, Mohammad Mehmandoost, Mateusz T. Mądzik, Stephan G. J. Philips, Sander L. de Snoo, David J. Michalak, Sergey V. Amitonov, Larysa Tryputen, Brian Paquelet Wuetz, Viviana Fezzi, Davide Degli Esposti, Amir Sammak, Giordano Scappucci, and Lieven M. K. Vandersypen. Hotter is Easier: Unexpected Temperature Dependence of Spin Qubit Frequencies. *Physical Review X*, 13:041015, 2023.

[122] Brennan Undseth, Xiao Xue, Mohammad Mehmandoost, Maximilian Rimbach-Russ, Pieter T. Eendebak, Nodar Samkharadze, Amir Sammak, Viatcheslav V. Dobrovitski, Giordano Scappucci, and Lieven M.K. Vandersypen. Nonlinear Response and Crosstalk of Electrically Driven Silicon Spin Qubits. *Physical Review Applied*, 19:044078, 2023.

[123] Yun-Pil Shim and Charles Tahan. Charge-noise-insensitive gate operations for always-on, exchange-only qubits. *Physical Review B*, 93:121410, 2016.

[124] E. A. Laird, J. M. Taylor, D. P. DiVincenzo, C. M. Marcus, M. P. Hanson, and A. C. Gossard. Coherent spin manipulation in an exchange-only qubit. *Physical Review B*, 82(7):075403, 2010.

[125] Frederico Martins, Filip K. Malinowski, Peter D. Nissen, Edwin Barnes, Saeed Fallahi, Geoffrey C. Gardner, Michael J. Manfra, Charles M. Marcus, and Ferdinand Kuemmeth. Noise Suppression Using Symmetric Exchange Gates in Spin Qubits. *Physical Review Letters*, 116:116801, 2016.

[126] Elliot Connors. *Advancement of silicon-based spin qubits: Fast readout, noise spectroscopy, and coherent control in Si/SiGe quantum dots.* PhD thesis, University of Rochester, 2022.

[127] Bryan H. Fong and Stephen M. Wandzura. Universal quantum computation and leakage reduction in the 3-qubit decoherence free subsystem. *Quantum Information & Computation*, 11(11–12):1003–1018, 2011.

[128] Daniel Zeuch, R. Cipri, and N. E. Bonesteel. Analytic pulse-sequence construction for exchange-only quantum computation. *Physical Review B*, 90:045306, 2014.

[129] Daniel Zeuch and N. E. Bonesteel. Simple derivation of the Fong-Wandzura pulse sequence. *Physical Review A*, 93:010303, 2016.

[130] Violeta N. Ivanova-Rohling, Niklas Rohling, and Guido Burkard. Discovery of an exchange-only gate sequence for CNOT with record-low gate time using reinforcement learning. *arXiv*, 2024.

[131] Edwin Acuna, Joseph D. Broz, Kaushal Shyamsundar, Antonio B. Mei, Colin P. Feeney, Valerie Smetanka, Tiffany Davis, Kangmu Lee, Maxwell D. Choi, Brydon Boyd, June Suh, Wonill D. Ha, Cameron Jennings, Andrew S. Pan, Daniel S. Sanchez, Matthew D. Reed, and Jason R. Petta. Coherent control of a triangular exchange-only spin qubit. *arXiv*, 2024.

[132] E. Knill, D. Leibfried, R. Reichle, J. Britton, R.B. Blakestad, J.D. Jost, C. Langer, R. Ozeri, S. Seidelin, and D.J. Wineland. Randomized benchmarking of quantum gates. *Physical Review A*, 77(1):012307, 2008.

[133] Joseph Emerson, Robert Alicki, and Karol Zyczkowski. Scalable noise estimation with random unitary operators. *Journal of Optics B: Quantum and Semiclassical Optics*, 7(10):S347–S352, 2005.

[134] Scott Aaronson. And yet quantum computing continues to progress. Shtetl-Optimized, April 2024. Accessed: 2024-10-11.

[135] Samuel F. Neyens, E. R. MacQuarrie, J. P. Dodson, J. Corrigan, Nathan Holman, Brandur Thorgrimsson, M. Palma, Thomas McJunkin, L. F. Edge, Mark Friesen, S. N. Coppersmith, and M. A. Eriksson. Measurements of Capacitive Coupling Within a Quadruple-Quantum-Dot Array. *Physical Review Applied*, 12:064049, 2019.

[136] J. M. Raimond, M. Brune, and S. Haroche. Manipulating quantum entanglement with atoms and photons in a cavity. *Reviews of Modern Physics*, 73:565–582, 2001.

[137] H. Mabuchi and A. C. Doherty. Cavity Quantum Electrodynamics: Coherence in Context. *Science*, 298(5597):1372–1377, 2002.

[138] Herbert Walther, Benjamin T. H. Varcoe, Berthold-Georg Englert, and Thomas Becker. Cavity quantum electrodynamics. *Reports on Progress in Physics*, 69(5):1325, 2006.

[139] Alexandre Blais, Ren-Shou Huang, Andreas Wallraff, S. M. Girvin, and R. J. Schoelkopf. Cavity quantum electrodynamics for superconducting electrical circuits: An architecture for quantum computation. *Physical Review A*, 69(6):062320, 2004.

[140] P. Krantz, M. Kjaergaard, F. Yan, T. P. Orlando, S. Gustavsson, and W. D. Oliver. A quantum engineer's guide to superconducting qubits. *Applied Physics Reviews*, 6(2):021318, 2019.

[141] Alexandre Blais, Arne L. Grimsmo, S. M. Girvin, and Andreas Wallraff. Circuit quantum electrodynamics. *Reviews of Modern Physics*, 93:025005, 2021.

[142] J. G. Kroll, W. Uilhoorn, K. L. van der Enden, D. de Jong, K. Watanabe, T. Taniguchi, S. Goswami, M. C. Cassidy, and L. P. Kouwenhoven. Magnetic field compatible circuit quantum electrodynamics with graphene josephson junctions. *Nature Communications*, 9:4615, 2018.

[143] M. Hays, G. de Lange, K. Serniak, D. J. van Woerkom, D. Bouman, P. Krogstrup, J. Nygård, A. Geresdi, and M. H. Devoret. Direct Microwave Measurement of Andreev-Bound-State Dynamics in a Semiconductor-Nanowire Josephson Junction. *Physical Review Letters*, 121(4):047001, 2018.

[144] Guido Burkard, Michael J. Gullans, Xiao Mi, and Jason R. Petta. Superconductor–semiconductor hybrid-circuit quantum electrodynamics. *Nature Reviews Physics*, 2(3):129–140, 2020.

[145] Matthias Mergenthaler, Ani Nersisyan, Andrew Patterson, Martina Esposito, Andreas Baumgartner, Christian Schönenberger, G. Andrew D. Briggs, Edward A. Laird, and Peter J. Leek. Circuit Quantum Electrodynamics with Carbon-Nanotube-Based Superconducting Quantum Circuits. *Physical Review Applied*, 15:064050, 2021.

[146] A. A. Houck, D. I. Schuster, J. M. Gambetta, J. A. Schreier, B. R. Johnson, J. M. Chow, L. Frunzio, J. Majer, M. H. Devoret, S. M. Girvin, and R. J. Schoelkopf. Generating single microwave photons in a circuit. *Nature*, 449(7160):328–331, 2007.

[147] Max Hays. *Realizing an Andreev Spin Qubit: Exploring Sub-gap Structure in Josephson Nanowires Using Circuit QED*. PhD thesis, Yale University, 2021.

[148] David M. Pozar. *Microwave Engineering*. John Wiley & Sons, Inc., Hoboken, fourth edition, 2012.

[149] E. T. Jaynes and F. W. Cummings. Comparison of quantum and semiclassical radiation theories with application to the beam maser. *Proceedings of the IEEE*, 51(1):89–109, 1963.

[150] X. Mi, J. V. Cady, D. M. Zajac, P. W. Deelman, and J. R. Petta. Strong coupling of a single electron in silicon to a microwave photon. *Science*, 355:156–158, 2017.

[151] A. Wallraff, A. Stockklauser, T. Ihn, J. R. Petta, and A. Blais. Comment on "Vacuum Rabi Splitting in a Semiconductor Circuit QED System". *Physical Review Letters*, 111:249701, 2013.

[152] Xiao Mi. *Circuit Quantum Electrodynamics with Silicon Charge and Spin Qubits*. PhD thesis, Princeton University, 2018.

[153] E. M. Purcell. Spontaneous emission probabilities at radio frequencies. *Physical Review*, 69:681, 1946.

[154] A. A. Houck, J. A. Schreier, B. R. Johnson, J. M. Chow, Jens Koch, J. M. Gambetta, D. I. Schuster, L. Frunzio, M. H. Devoret, S. M. Girvin, and R. J. Schoelkopf. Controlling the Spontaneous Emission of a Superconducting Transmon Qubit. *Physical Review Letters*, 101(8):080502, 2008.

[155] A. Bienfait, J. J. Pla, Y. Kubo, X. Zhou, M. Stern, C. C. Lo, C. D. Weis, T. Schenkel, D. Vion, D. Esteve, J. J. L. Morton, and P. Bertet. Controlling spin relaxation with a cavity. *Nature*, 531(7592):74–77, 2016.

[156] J. R. Schrieffer and P. A. Wolff. Relation between the Anderson and Kondo Hamiltonians. *Physical Review*, 149:491–492, 1966.

[157] Jurgen Dijkema, Xiao Xue, Patrick Harvey-Collard, Maximilian Rimbach-Russ, Sander L. de Snoo, Guoji Zheng, Amir Sammak, Giordano Scappucci, and Lieven M. K Vandersypen. Two-qubit logic between distant spins in silicon. *arXiv*, 2023.

[158] Mark Friesen, Joydip Ghosh, M. A. Eriksson, and S. N. Coppersmith. A decoherence-free subspace in a charge quadrupole qubit. *Nature Communications*, 8:15923, 2017.

[159] J. V. Koski, A. J. Landig, M. Russ, J. C. Abadillo-Uriel, P. Scarlino, B. Kratochwil, C. Reichl, W. Wegscheider, Guido Burkard, Mark Friesen, S. N. Coppersmith, A. Wallraff, K. Ensslin, and T. Ihn. Strong photon coupling to the quadrupole moment of an electron in a solid-state qubit. *Nature Physics*, 16:642–646, 2020.

[160] L. Childress, A. S. Sørensen, and M. D. Lukin. Mesoscopic cavity quantum electrodynamics with quantum dots. *Physical Review A*, 69(4):042302, 2004.

[161] R. Amsüss, Ch. Koller, T. Nöbauer, S. Putz, S. Rotter, K. Sandner, S. Schneider, M. Schramböck, G. Steinhauser, H. Ritsch, J. Schmiedmayer, and J. Majer. Cavity QED with Magnetically Coupled Collective Spin States. *Physical Review Letters*, 107:060502, 2011.

[162] C. Eichler, A. J. Sigillito, S. A. Lyon, and J. R. Petta. Electron Spin Resonance at the Level of 10^4 Spins Using Low Impedance Superconducting Resonators. *Physical Review Letters*, 118:037701, 2017.

[163] S. Probst, A. Bienfait, P. Campagne-Ibarcq, J. J. Pla, B. Albanese, J. F. Da Silva Barbosa, T. Schenkel, D. Vion, D. Esteve, K. Mølmer, J. J. L. Morton, R. Heeres, and P. Bertet. Inductive-detection electron-spin resonance spectroscopy with 65 spins/$\sqrt{\mathrm{Hz}}$ sensitivity. *Applied Physics Letters*, 111:202604, 2017.

[164] A. J. Landig, J. V. Koski, P. Scarlino, U. C. Mendes, A. Blais, C. Reichl, W. Wegscheider, A. Wallraff, K. Ensslin, and T. Ihn. Coherent spin–photon coupling using a resonant exchange qubit. *Nature*, 560(7717):179–184, 2018.

[165] Cécile X. Yu, Simon Zihlmann, José C. Abadillo-Uriel, Vincent P. Michal, Nils Rambal, Heimanu Niebojewski, Thomas Bedecarrats, Maud Vinet, Étienne Dumur, Michele Filippone, Benoit Bertrand, Silvano De Franceschi, Yann-Michel Niquet, and Romain Maurand. Strong coupling between a photon and a hole spin in silicon. *Nature Nanotechnology*, 18:741–746, 2023.

[166] J. H. Ungerer, A. Pally, A. Kononov, S. Lehmann, J. Ridderbos, P. P. Potts, C. Thelander, K. A. Dick, V. F. Maisi, P. Scarlino, A. Baumgartner, and C. Schönenberger. Strong coupling between a microwave photon and a singlet-triplet qubit. *Nature Communications*, 15:1068, 2024.

[167] X. Mi, M. Benito, S. Putz, D. M. Zajac, J. M. Taylor, Guido Burkard, and J. R. Petta. A coherent spin–photon interface in silicon. *Nature*, 555:599–603, 3 2018.

[168] N. Samkharadze, G. Zheng, N. Kalhor, D. Brousse, A. Sammak, U. C. Mendes, A. Blais, G. Scappucci, and L. M. K. Vandersypen. Strong spin-photon coupling in silicon. *Science*, 359(6380):1123–1127, 2018.

[169] Patrick Harvey-Collard, Jurgen Dijkema, Guoji Zheng, Amir Sammak, Giordano Scappucci, and Lieven M. K. Vandersypen. Coherent Spin-Spin Coupling Mediated by Virtual Microwave Photons. *Physical Review X*, 12(2):021026, 2022.

[170] N. Samkharadze, A. Bruno, P. Scarlino, G. Zheng, D. P. DiVincenzo, L. DiCarlo, and L. M. K. Vandersypen. High-Kinetic-Inductance Superconducting Nanowire Resonators for Circuit QED in a Magnetic Field. *Physical Review Applied*, 5:044004, 2016.

[171] A. Stockklauser, P. Scarlino, J. V. Koski, S. Gasparinetti, C. K. Andersen, C. Reichl, W. Wegscheider, T. Ihn, K. Ensslin, and A. Wallraff. Strong Coupling Cavity QED with Gate-Defined Double Quantum Dots Enabled by a High Impedance Resonator. *Physical Review X*, page 011030, 2017.

[172] Nathan Holman, J. P. Dodson, L. F. Edge, S. N. Coppersmith, Mark Friesen, R. McDermott, and M. A. Eriksson. Microwave engineering for semiconductor quantum dots in a cQED architecture. *Applied Physics Letters*, 117(8):083502, 2020.

[173] Patrick Harvey-Collard, Guoji Zheng, Jurgen Dijkema, Nodar Samkharadze, Amir Sammak, Giordano Scappucci, and Lieven M. K. Vandersypen. On-Chip Microwave Filters for High-Impedance Resonators with Gate-Defined Quantum Dots. *Physical Review Applied*, 14:034025, 2020.

[174] Nathan Holman, D. Rosenberg, D. Yost, J. L. Yoder, R. Das, William D. Oliver, R. McDermott, and M. A. Eriksson. 3D integration and measurement of a semiconductor double quantum dot with a high-impedance TiN resonator. *npj Quantum Information*, 7:137, 2021.

[175] T. Frey, P. J. Leek, M. Beck, A. Blais, T. Ihn, K. Ensslin, and A. Wallraff. Dipole Coupling of a Double Quantum Dot to a Microwave Resonator. *Physical Review Letters*, 108(4):046807, 2011.

[176] T. Frey, P. J. Leek, M. Beck, J. Faist, A. Wallraff, K. Ensslin, T. Ihn, and M. Büttiker. Quantum dot admittance probed at microwave frequencies with an on-chip resonator. *Physical Review B*, 86(11):115303, 2012.

[177] A. Wallraff, D. I. Schuster, A. Blais, L. Frunzio, J. Majer, M. H. Devoret, S. M. Girvin, and R. J. Schoelkopf. Approaching Unit Visibility for Control of a Superconducting Qubit with Dispersive Readout. *Physical Review Letters*, 95:060501, 2005.

[178] J. Majer, J. M. Chow, J. M. Gambetta, Jens Koch, B. R. Johnson, J. A. Schreier, L. Frunzio, D. I. Schuster, A. A. Houck, A. Wallraff, A. Blais, M. H. Devoret, S. M. Girvin, and R. J. Schoelkopf. Coupling superconducting qubits via a cavity bus. *Nature*, 449(7161):443–447, 2007.

[179] Michael Tavis and Frederick W. Cummings. Exact Solution for an N-Molecule—Radiation-Field Hamiltonian. *Physical Review*, 170:379–384, 1968.

[180] F. Borjans, X. G. Croot, X. Mi, M. J. Gullans, and J. R. Petta. Resonant microwave-mediated interactions between distant electron spins. *Nature*, 577(7789):195–198, 2020.

[181] Norbert Schuch and Jens Siewert. Natural two-qubit gate for quantum computation using the XY interaction. *Physical Review A*, 67:032301, 2003.

[182] J. M. Taylor, H.-A. Engel, W. Dür, A. Yacoby, C. M. Marcus, P. Zoller, and M. D. Lukin. Fault-tolerant architecture for quantum computation using electrically controlled semiconductor spins. *Nature Physics*, 1:177–183, 2005.

[183] T. Fujita, T. A. Baart, C. Reichl, W. Wegscheider, and L. M. K. Vandersypen. Coherent shuttle of electron–spin states. *npj Quantum Information*, 3:22, 2017.

[184] T. Seidler, T. Struck, R. Xue, N. Focke, S. Trellenkamp, H. Bluhm, and L. R. Schreiber. Conveyor-mode single-electron shuttling in Si/SiGe for a scalable quantum computing architecture. *npj Quantum Information*, 8:100, 2022.

[185] A. Noiri, K. Takeda, T. Nakajima, T. Kobayashi, A. Sammak, G. Scappucci, and S. Tarucha. A shuttling-based two-qubit logic gate for linking distant silicon quantum processors. *Nature Communications*, 14:5740, 2023.

[186] R. Xue, M. Beer, I. Seidler, S. Humpohl, J.-S. Tu, S. Trellenkamp, T. Struck, H. Bluhm, and L. R. Schreiber. Si/SiGe QuBus for single electron information-processing devices with memory and micron-scale connectivity function. *Nature Communications*, 15:2296, 2024.

[187] Floor van Riggelen-Doelman, Chien-An Wang, Sander L. de Snoo, William I. L. Lawrie, Nico W. Hendrickx, Maximilian Rimbach-Russ, Amir Sammak, Giordano Scappucci, Corentin Déprez, and Menno Veldhorst. Coherent spin qubit shuttling through germanium quantum dots. *Nature Communications*, 15:5716, 2024.

[188] Andrew J. Kerman. Quantum information processing using quasiclassical electromagnetic interactions between qubits and electrical resonators. *New Journal of Physics*, 15, 2013.

[189] Nicolas Didier, Jérôme Bourassa, and Alexandre Blais. Fast Quantum Nondemolition Readout by Parametric Modulation of Longitudinal Qubit-Oscillator Interaction. *Physical Review Letters*, 115:1–5, 2015.

[190] Rusko Ruskov and Charles Tahan. Quantum-limited measurement of spin qubits via curvature couplings to a cavity. *Physical Review B*, 99:245306, 2019.

[191] D. H. Slichter, R. Vijay, S. J. Weber, S. Boutin, M. Boissonneault, J. M. Gambetta, A. Blais, and I. Siddiqi. Measurement-Induced Qubit State Mixing in Circuit QED from Up-Converted Dephasing Noise. *Physical Review Letters*, 109(15):153601, 2012.

[192] J. Ikonen, J. Goetz, J. Ilves, A. Keränen, A. M. Gunyho, M. Partanen, K. Y. Tan, D. Hazra, L. Grönberg, V. Vesterinen, S. Simbierowicz, J. Hassel, and M. Möttönen. Qubit Measurement by Multichannel Driving. *Physical Review Letters*, 122(8):80503, 2019.

[193] Baptiste Royer, Arne L. Grimsmo, Nicolas Didier, and Alexandre Blais. Fast and high-fidelity entangling gate through parametrically modulated longitudinal coupling. *Quantum*, 1:11, 2017.

[194] Rusko Ruskov and Charles Tahan. Modulated longitudinal gates on encoded spin qubits via curvature couplings to a superconducting cavity. *Physical Review B*, 103:035301, 2021.

[195] S. E. Nigg, A. Fuhrer, and D. Loss. Superconducting Grid-Bus Surface Code Architecture for Hole-Spin Qubits. *Physical Review Letters*, 118:147701, Apr 2017.

[196] K. D. Petersson, L. W. McFaul, M. D. Schroer, M. Jung, J. M. Taylor, A. A. Houck, and J. R. Petta. Circuit quantum electrodynamics with a spin qubit. *Nature*, 490(7420):380–383, 2012.

[197] M. Kjaergaard, M. E. Schwartz, J. Braumüller, P. Krantz, J. I.-J. Wang, S. Gustavsson, and W. D. Oliver. Superconducting Qubits: Current State of Play. *Annual Review of Condensed Matter Physics*, 11(1):369–395, 2020.

[198] F. Beaudoin, D. Lachance-Quirion, W. A. Coish, and M. Pioro-Ladrière. Coupling a single electron spin to a microwave resonator: Controlling transverse and longitudinal couplings. *Nanotechnology*, 27(46):464003, 2016.

[199] C. Eichler and J. R. Petta. Realizing a Circuit Analog of an Optomechanical System with Longitudinally Coupled Superconducting Resonators. *Physical Review Letters*, 120(22):227702, 2018.

[200] R. Dassonneville, T. Ramos, V. Milchakov, L. Planat, É. Dumur, F. Foroughi, J. Puertas, S. Leger, K. Bharadwaj, J. Delaforce, C. Naud, W. Hasch-Guichard, J. J. García-Ripoll, N. Roch, and O. Buisson. Fast High-Fidelity Quantum Nondemolition Qubit Readout via a Nonperturbative Cross-Kerr Coupling. *Physical Review X*, 10:11045, 2020.

[201] S. Hazra, K. V. Salunkhe, A. Bhattacharjee, G. Bothara, S. Kundu, T. Roy, M. P. Patankar, and R. Vijay. Engineering cross resonance interaction in multi-modal quantum circuits. *Applied Physics Letters*, 116:152601, 2020.

[202] H. Toida, T. Ohrai, Y. Matsuzaki, K. Kakuyanagi, and S. Saito. Control of the transition frequency of a superconducting flux qubit by longitudinal coupling to the photon number degree of freedom in a resonator. *Physical Review B*, 102(9):94502, 2020.

[203] S. Touzard, A. Kou, N. E. Frattini, V. V. Sivak, S. Puri, A. Grimm, L. Frunzio, S. Shankar, and M. H. Devoret. Gated Conditional Displacement Readout of Superconducting Qubits. *Physical Review Letters*, 122(8):80502, 2019.

[204] C. G. L. Bøttcher, S. P. Harvey, S. Fallahi, G. C. Gardner, M. J. Manfra, U. Vool, S. D. Bartlett, and A. Yacoby. Parametric longitudinal coupling between a high-impedance superconducting resonator and a semiconductor quantum dot singlet-triplet spin qubit. *Nature Communications*, 13:4773, 2022.

[205] D. K. C. MacDonald. *Noise and Fluctuations: An Introduction.* Wiley, New York, 1962.

[206] Zhan Shi, C. B. Simmons, J. R. Prance, John King Gamble, Teck Seng Koh, Yun-Pil Shim, Xuedong Hu, D. E. Savage, M. G. Lagally, M. A. Eriksson, Mark Friesen, and S. N. Coppersmith. Fast Hybrid Silicon Double-Quantum-Dot Qubit. *Physical Review Letters*, 108(14):140503, 2012.

[207] Dohun Kim, Zhan Shi, C. B. Simmons, D. R. Ward, J. R. Prance, Teck Seng Koh, John King Gamble, D. E. Savage, M. G. Lagally, Mark Friesen, S. N. Coppersmith, and Mark A. Eriksson. Quantum control and process tomography of a semiconductor quantum dot hybrid qubit. *Nature*, 511:70–74, 2014.

[208] Teck Seng Koh, John King Gamble, Mark Friesen, M. A. Eriksson, and S. N. Coppersmith. Pulse-Gated Quantum-Dot Hybrid Qubit. *Physical Review Letters*, 109(25):250503, 2012.

[209] J. Gabelli, G. Feve, J.-M. Berroir, B. Placais, A. Cavanna, B. Etienne, Y. Jin, and D. C. Glattli. Violation of Kirchhoff's Laws for a Coherent RC Circuit. *Science*, 313(5786):499–502, 2006.

[210] Faustin W. Carter, Trupti Khaire, Clarence Chang, and Valentyn Novosad. Low-loss single-photon NbN microwave resonators on Si. *Applied Physics Letters*, 115(9):092602, 2019.

[211] J. Corrigan, Benjamin Harpt, Nathan Holman, Rusko Ruskov, Piotr Marciniec, D. Rosenberg, D. Yost, R. Das, William D. Oliver, R. McDermott, Charles Tahan, Mark Friesen, and M.A. Eriksson. Longitudinal coupling between a $\mathrm{Si}/\mathrm{Si}_{1-x}\mathrm{Ge}_x$ double quantum dot and an off-chip TiN resonator. *Physical Review Applied*, 20(6):064005, 2023.

[212] Victor Champain, Simon Zihlmann, Alessandro Chessari, Benoit Bertrand, Heimanu Niebojewski, Etienne Dumur, Xavier Jehl, Vivien Schmitt, Boris Brun, Clemens Winkelmann, Yann-Michel Niquet, Michele Filippone, Silvano De Franceschi, and Romain Maurand. Parametric longitudinal coupling of a semiconductor charge qubit and a RF resonator. *arXiv*, 2024.

[213] Gang Cao, Hai-Ou Li, Guo-Dong Yu, Bao-Chuan Wang, Bao-Bao Chen, Xiang-Xiang Song, Ming Xiao, Guang-Can Guo, Hong-Wen Jiang, Xuedong Hu, and Guo-Ping

Guo. Tunable Hybrid Qubit in a GaAs Double Quantum Dot. *Physical Review Letters*, 116:086801, 2016.

[214] Brandur Thorgrimsson, Dohun Kim, Yuan-Chi Yang, L. W. Smith, C. B. Simmons, Daniel R. Ward, Ryan H. Foote, J. Corrigan, D. E. Savage, M. G. Lagally, Mark Friesen, S. N. Coppersmith, and M. A. Eriksson. Extending the coherence of a quantum dot hybrid qubit. *npj Quantum Information*, 3:32, 2017.

[215] Wonjin Jang, Min-Kyun Cho, Hyeongyu Jang, Jehyun Kim, Jaemin Park, Gyeonghun Kim, Byoungwoo Kang, Hwanchul Jung, Vladimir Umansky, and Dohun Kim. Single-Shot Readout of a Driven Hybrid Qubit in a GaAs Double Quantum Dot. *Nano Letters*, 21(12):4999, 2021.

[216] Sanghyeok Park, Jared Benson, J. Corrigan, J. P. Dodson, S. N. Coppersmith, Mark Friesen, and M. A. Eriksson. Single-shot latched readout of a quantum dot qubit using barrier gate pulsing. *arXiv*, 2024.

[217] J. M. Elzerman, R. Hanson, L. H. Willems Van Beveren, L. M.K. Vandersypen, and L. P. Kouwenhoven. Excited-state spectroscopy on a nearly closed quantum dot via charge detection. *Applied Physics Letters*, 84:4617–4619, 2004.

[218] Kevin S. Guo, MengKe Feng, Jonathan Y. Huang, Will Gilbert, Kohei M. Itoh, Fay E. Hudson, Kok Wai Chan, Wee Han Lim, Andrew S. Dzurak, and Andre Saraiva. Methods for transverse and longitudinal spin-photon coupling in silicon quantum dots with intrinsic spin-orbit effect. *arXiv*, 2023.

[219] J. R. Petta, H. Lu, and A. C. Gossard. A Coherent Beam Splitter for Electronic Spin States. *Science*, 327(5966):669–672, 2010.

[220] X. Mi, Csaba G. Péterfalvi, Guido Burkard, and J. R. Petta. High-Resolution Valley Spectroscopy of Si Quantum Dots. *Physical Review Letters*, 119:1–5, 2017.

[221] X. Croot, X. Mi, S. Putz, M. Benito, F. Borjans, G. Burkard, and J. R. Petta. Flopping-mode electric dipole spin resonance. *Physical Review Research*, 2(1):012006, 2020.

[222] Rusko Ruskov and Charles Tahan. Longitudinal (curvature) couplings of an N-level qudit to a superconducting resonator at the adiabatic limit and beyond. *Physical Review B*, 109:245303, 2024.

[223] H. Kamerlingh Onnes. Further experiments with liquid helium. C. On the change of electric resistance of pure metals at very low temperatures etc. IV. The resistance of pure mercury at helium temperatures. In *Koninklijke Nederlandse Akademie van Wetenschappen, Proceedings*, volume 13, pages 1274–1276, 1911.

[224] Walther Meissner and Robert Ochsenfeld. Ein neuer Effekt bei eintritt der Supraleitfähigkeit. *Naturwissenschaften*, 21(44):787–788, 1933.

[225] Fritz London and Heinz London. The electromagnetic equations of the supraconductor. *Proceedings of the Royal Society of London. Series A: Mathematical and Physical Sciences*, 149(866):71–88, 1935.

[226] Vitaly L. Ginzburg and Lev D. Landau. On the theory of superconductivity. *Zhurnal Eksperimental'noi i Teoreticheskoi Fiziki*, 20:1064–1082, 1950.

[227] John Bardeen, Leon N. Cooper, and Robert Schrieffer. Theory of superconductivity. *Physical Review*, 108(5):1175–1204, 1957.

[228] Michael Tinkham. *Introduction to Superconductivity*. McGraw-Hill, New York, second edition, 1996.

[229] Leon N. Cooper. Bound Electron Pairs in a Degenerate Fermi Gas. *Physical Review*, 104:1189–1190, 1956.

[230] N. N. Bogoljubov. On a new method in the theory of superconductivity. *Il Nuovo Cimento*, 7:794–805, 1958.

[231] A. F. Andreev. The thermal conductivity of the intermediate state in superconductors. *Journal of Experimental and Theoretical Physics (U.S.S.R.)*, 19(5):1228–1231, 1964.

[232] G. E. Blonder, M. Tinkham, and T. M. Klapwijk. Transition from metallic to tunneling regimes in superconducting microconstrictions: Excess current, charge imbalance, and supercurrent conversion. *Physical Review B*, 25(7):4515–4532, 1982.

[233] P. A. M. Benistant, A. P. van Gelder, H. van Kempen, and P. Wyder. Angular relation and energy dependence of Andreev reflection. *Physical Review B*, 32(5):3351, 1985.

[234] T. M. Klapwijk. Proximity Effect From an Andreev Perspective. *Journal of Superconductivity*, 17(5):593–611, 2004.

[235] P. G. de Gennes. Boundary Effects in Superconductors. *Reviews of Modern Physics*, 36:225–237, 1964.

[236] Gert Eilenberger. Transformation of Gorkov's equation for type II superconductors into transport-like equations. *Zeitschrift für Physik A Hadrons and nuclei*, 214:195–213, 1968.

[237] Klaus D. Usadel. Generalized Diffusion Equation for Superconducting Alloys. *Physical Reiew Letters*, 25:507–509, 1970.

[238] C. W. J. Beenakker and H. Van Houten. Josephson Current through a Superconducting Quantum Point Contact Shorter than the Coherence Length. *Physical Review Letters*, 66(23):3056, 1991.

[239] Akira Furusaki and Masaru Tsukada. Current-carrying states in josephson junctions. *Physical Review B*, 43(13):10164, 1991.

[240] J-D. Pillet, C. H. L. Quay, P. Morfin, C. Bena, A. Levy Yeyati, and P. Joyez. Andreev bound states in supercurrent-carrying carbon nanotubes revealed. *Nature Physics*, 6(12):965–969, 2010.

[241] B. D. Josephson. Possible new effects in superconductive tunnelling. *Physics Letters*, 1(7):251–253, 1962.

[242] R. Landauer. Spatial Variation of Currents and Fields Due to Localized Scatterers in Metallic Conduction. *IBM Journal of Research and Development*, 1(3):223–231, 1957.

[243] T. D. Clark. PhD thesis, University of London, 1971. Unpublished.

[244] Tatsushi Akazaki, Hideaki Takayanagi, Junsaku Nitta, and Takatomo Enoki. A Josephson field effect transistor using an InAs-inserted-channel $In_{0.52}Al_{0.48}As/In_{0.53}Ga_{0.47}As$ inverted modulation-doped structure. *Applied Physics Letters*, 68(3):418–420, 1996.

[245] Yong-Joo Doh, Jorden A. van Dam, Aarnoud L. Roest, Erik P. A. M. Bakkers, Leo P. Kouwenhoven, and Silvano De Franceschi. Tunable supercurrent through semiconductor nanowires. *Science*, 309(5732):272–275, 2005.

[246] Pablo Jarillo-Herrero, Jorden A. Van Dam, and Leo P. Kouwenhoven. Quantum supercurrent transistors in carbon nanotubes. *Nature*, 439(7079):953–956, 2006.

[247] Hubert B. Heersche, Pablo Jarillo-Herrero, Jeroen B. Oostinga, Lieven M. K. Vandersypen, and Alberto F. Morpurgo. Bipolar supercurrent in graphene. *Nature*, 446(7131):56–59, 2007.

[248] T. D. Clark, R. J. Prance, and A. D. C. Grassie. Feasibility of hybrid Josephson field effect transistors. *Journal of Applied Physics*, 51(5):2736–2743, 1980.

[249] Tom Doekle Vethaak. *Silicide-based Josephson field effect transistors for superconducting qubits*. PhD thesis, Université Grenoble Alpes, 2021.

[250] Anatoly F. Volkov and Hideaki Takayanagi. Effect of gate voltage on critical current in controllable superconductor–normal-metal–superconductor Josephson junctions. *Physical Review B*, 53(22):15162, 1996.

[251] J. Shabani, M. Kjaergaard, H. J. Suominen, Younghyun Kim, F. Nichele, K. Pakrouski, T. Stankevic, R. M. Lutchyn, P. Krogstrup, R. Feidenhans'l, S. Kraemer, C. Nayak, M. Troyer, C. M. Marcus, and C. J. Palmstrøm. Two-dimensional epitaxial superconductor-semiconductor heterostructures: A platform for topological superconducting networks. *Physical Review B*, 93:155402, 2016.

[252] Thorvald Wadum Larsen, Karl David Petersson, Ferdinand Kuemmeth, Thomas Sand Jespersen, Peter Krogstrup, Jesper Nygård, and Charles M. Marcus. Semiconductor-nanowire-based superconducting qubit. *Physical Review Letters*, 115(12):127001, 2015.

[253] G. De Lange, B. Van Heck, A. Bruno, D. J. Van Woerkom, A. Geresdi, S. R. Plissard, E. P. A. M. Bakkers, A. R. Akhmerov, and L. DiCarlo. Realization of microwave quantum circuits using hybrid superconducting-semiconducting nanowire Josephson elements. *Physical Review Letters*, 115(12):127002, 2015.

[254] Lucas Casparis, Malcolm R. Connolly, Morten Kjaergaard, Natalie J. Pearson, Anders Kringhøj, Thorvald W. Larsen, Ferdinand Kuemmeth, Tiantian Wang, Candice Thomas, Sergei Gronin, Geoffrey C. Gardner, Michael J. Manfra, Charles M. Marcus, and Karl D. Petersson. Superconducting gatemon qubit based on a proximitized two-dimensional electron gas. *Nature Nanotechnology*, 13:915–919, 2018.

[255] C. Janvier, L. Tosi, L. Bretheau, Ç. Ö. Girit, M. Stern, P. Bertet, P. Joyez, D. Vion, D. Esteve, M. F. Goffman, H. Pothier, and C. Urbina. Coherent manipulation of Andreev states in superconducting atomic contacts. *Science*, 349(6253):1199–1202, 2015.

[256] C. Padurariu and Yu. V. Nazarov. Theoretical proposal for superconducting spin qubits. *Physical Review B*, 81:144519, 2010.

[257] M. Hays, V. Fatemi, D. Bouman, J. Cerrillo, S. Diamond, K. Serniak, T. Connolly, P. Krogstrup, J. Nygård, A. Levy Yeyati, A. Geresdi, and M. H. Devoret. Coherent manipulation of an Andreev spin qubit. *Science*, 373(6553):430–433, 2021.

[258] Ettore Majorana. Teoria simmetrica dell'elettrone e del positrone. *Il Nuovo Cimento*, 14:171–184, 1937.

[259] Ville T. Lahtinen and Jiannis K. Pachos. A short introduction to topological quantum computation. *SciPost Physics*, 3:021, 2017.

[260] A.Yu. Kitaev. Fault-tolerant quantum computation by anyons. *Annals of Physics*, 303(1):2–30, 2003.

[261] Benjamin David Woods. *Majorana Nanostructures and Their Electrostatic Environment*. PhD thesis, West Virginia University, 2021.

[262] A Yu Kitaev. Unpaired Majorana fermions in quantum wires. *Physics-Uspekhi*, 44:131–136, 2001.

[263] Roman M. Lutchyn, Jay D. Sau, and S. Das Sarma. Majorana Fermions and a Topological Phase Transition in Semiconductor-Superconductor Heterostructures. *Physical Review Letters*, 105:077001, 2010.

[264] Yuval Oreg, Gil Refael, and Felix von Oppen. Helical Liquids and Majorana Bound States in Quantum Wires. *Physical Review Letters*, 105:177002, 2010.

[265] Falko Pientka, Anna Keselman, Erez Berg, Amir Yacoby, Ady Stern, and Bertrand I. Halperin. Topological Superconductivity in a Planar Josephson Junction. *Physical Review X*, 7:021032, 2017.

[266] Michael Hell, Karsten Flensberg, and Martin Leijnse. Coupling and braiding Majorana bound states in networks defined in two-dimensional electron gases with proximity-induced superconductivity. *Physical Review B*, 96:035444, 2017.

[267] R. M. Lutchyn, E. P. A. M. Bakkers, L. P. Kouwenhoven, P. Krogstrup, C. M. Marcus, and Y. Oreg. Majorana zero modes in superconductor–semiconductor heterostructures. *Nature Reviews Materials*, 3:52–68, 2018.

[268] Karsten Flensberg, Felix von Oppen, and Ady Stern. Engineered platforms for topological superconductivity and Majorana zero modes. *Nature Reviews Materials*, 6(10):944–958, 2021.

[269] V. Mourik, K. Zuo, S. M. Frolov, S. R. Plissard, E. P. A. M. Bakkers, and L. P. Kouwenhoven. Signatures of Majorana Fermions in Hybrid Superconductor-Semiconductor Nanowire Devices. *Science*, 336:1003–1007, 2012.

[270] Anindya Das, Yuval Ronen, Yonatan Most, Yuval Oreg, Moty Heiblum, and Hadas Shtrikman. Zero-bias peaks and splitting in an Al–InAs nanowire topological superconductor as a signature of Majorana fermions. *Nature Physics*, 8(12):887–895, 2012.

[271] M. T. Deng, S. Vaitiekėnas, E. B. Hansen, J. Danon, M. Leijnse, K. Flensberg, J. Nygård, P. Krogstrup, and C. M. Marcus. Majorana bound state in a coupled quantum-dot hybrid-nanowire system. *Science*, 354(6319):1557–1562, 2016.

[272] S. M. Albrecht, A. P. Higginbotham, M. Madsen, F. Kuemmeth, T. S. Jespersen, J. Nygård, P. Krogstrup, and C. M. Marcus. Exponential protection of zero modes in Majorana islands. *Nature*, 531(7593):206–209, 2016.

[273] Dominique Laroche, Daniël Bouman, David J. van Woerkom, Alex Proutski, Chaitanya Murthy, Dmitry I. Pikulin, Chetan Nayak, Ruben J. J. van Gulik, Jesper Nygård, Peter Krogstrup, Leo P. Kouwenhoven, and Attila Geresdi. Observation of the 4π-periodic Josephson effect in indium arsenide nanowires. *Nature Communications*, 10:1–7, 2017.

[274] Önder Gül, Hao Zhang, Jouri D. S. Bommer, Michiel W. A. de Moor, Diana Car, Sébastien R. Plissard, Erik P. A. M. Bakkers, Attila Geresdi, Kenji Watanabe, Takashi Taniguchi, and Leo P. Kouwenhoven. Ballistic Majorana nanowire devices. *Nature Nanotechnology*, 13(3):192–197, 2018.

[275] Antonio Fornieri, Alexander M. Whiticar, F. Setiawan, Elías Portolés, Asbjørn C.C. Drachmann, Anna Keselman, Sergei Gronin, Candice Thomas, Tian Wang, Ray Kallaher, Geoffrey C. Gardner, Erez Berg, Michael J. Manfra, Ady Stern, Charles M. Marcus, and Fabrizio Nichele. Evidence of topological superconductivity in planar Josephson junctions. *Nature*, 569:89–92, 2019.

[276] Hechen Ren, Falko Pientka, Sean Hart, Andrew T. Pierce, Michael Kosowsky, Lukas Lunczer, Raimund Schlereth, Benedikt Scharf, Ewelina M. Hankiewicz, Laurens W. Molenkamp, Bertrand I. Halperin, and Amir Yacoby. Topological superconductivity in a phase-controlled Josephson junction. *Nature*, 569:93–98, 2019.

[277] S. Vaitiekėnas, G. W. Winkler, B. van Heck, T. Karzig, M.-T. Deng, K. Flensberg, L. I. Glazman, C. Nayak, P. Krogstrup, R. M. Lutchyn, and C. M. Marcus. Flux-induced topological superconductivity in full-shell nanowires. *Science*, 367(6485):eaav3392, 2020.

[278] A. Banerjee, O. Lesser, M. A. Rahman, H.-R. Wang, M.-R. Li, A. Kringhøj, A. M. Whiticar, A. C. C. Drachmann, C. Thomas, T. Wang, M. J. Manfra, E. Berg, Y. Oreg, Ady Stern, and C. M. Marcus. Signatures of a topological phase transition in a planar Josephson junction. *Physical Review B*, 107:245304, 2023.

[279] Leo Kouwenhoven. Perspective on Majorana bound-states in hybrid superconductor-semiconductor nanowires. *arXiv*, 2024.

[280] Dmitry I. Pikulin, Bernard van Heck, Torsten Karzig, Esteban A. Martinez, Bas Nijholt, Tom Laeven, Georg W. Winkler, John D. Watson, Sebastian Heedt, Mine Temurhan, Vicky Svidenko, Roman M. Lutchyn, Mason Thomas, Gijs de Lange, Lucas Casparis, and Chetan Nayak. Protocol to identify a topological superconducting phase in a three-terminal device. *arXiv*, 2021.

[281] Morteza Aghaee, Arun Akkala, Zulfi Alam, Rizwan Ali, Alejandro Alcaraz Ramirez, Mariusz Andrzejczuk, Andrey E. Antipov, Pavel Aseev, Mikhail Astafev, Bela Bauer, Jonathan Becker, Srini Boddapati, Frenk Boekhout, Jouri Bommer, Tom Bosma, Leo Bourdet, Samuel Boutin, Philippe Caroff, Lucas Casparis, Maja Cassidy, Sohail Chatoor, Anna Wulf Christensen, Noah Clay, William S. Cole, Fabiano Corsetti, Ajuan Cui, Paschalis Dalampiras, Anand Dokania, Gijs de Lange, Michiel de Moor, Juan Carlos Estrada Saldaña, Saeed Fallahi, Zahra Heidarnia Fathabad, John Gamble, Geoff Gardner, Deshan Govender, Flavio Griggio, Ruben Grigoryan, Sergei Gronin, Jan Gukelberger, Esben Bork Hansen, Sebastian Heedt, Jesús Herranz Zamorano, Samantha Ho, Ulrik Laurens Holgaard, Henrik Ingerslev, Linda Johansson, Jeffrey Jones, Ray Kallaher, Farhad Karimi, Torsten Karzig, Evelyn King, Maren Elisabeth Kloster, Christina Knapp, Dariusz Kocon, Jonne Koski, Pasi Kostamo, Peter Krogstrup, Mahesh Kumar, Tom Laeven, Thorvald Larsen, Kongyi Li, Tyler Lindemann, Julie Love, Roman Lutchyn, Morten Hannibal Madsen, Michael Manfra, Signe Markussen, Esteban Martinez, Robert McNeil, Elvedin Memisevic, Trevor Morgan, Andrew Mullally, Chetan Nayak, Jens Nielsen, William Hvidtfelt Padkær Nielsen, Bas Nijholt, Anne Nurmohamed, Eoin O'Farrell, Keita Otani, Sebastian Pauka, Karl Petersson, Luca Petit, Dmitry I. Pikulin, Frank Preiss, Marina Quintero-Perez, Mohana Rajpalke, Katrine Rasmussen, Davydas Razmadze, Outi Reentila, David Reilly, Richard Rouse, Ivan Sadovskyy, Lauri Sainiemi, Sydney Schreppler, Vadim Sidorkin, Amrita Singh, Shilpi Singh, Sarat Sinha, Patrick Sohr, Toma š Stankevič, Lieuwe Stek, Henri Suominen, Judith Suter, Vicky Svidenko, Sam Teicher, Mine Temuerhan, Nivetha Thiyagarajah, Raj Tholapi, Mason Thomas, Emily Toomey, Shivendra Upadhyay, Ivan Urban, Saulius Vaitiekėnas, Kevin Van Hoogdalem, David Van Woerkom, Dmitrii V. Viazmitinov, Dominik Vogel, Steven Waddy, John Watson, Joseph Weston, Georg W. Winkler, Chung Kai Yang, Sean Yau, Daniel Yi, Emrah Yucelen, Alex Webster, Roland Zeisel,

and Ruichen Zhao. InAs-Al hybrid devices passing the topological gap protocol. *Physical Review B*, 107:245423, 2023.

[282] Jay D. Sau and S. Das Sarma. Realizing a robust practical Majorana chain in a quantum-dot-superconductor linear array. *Nature Communications*, 3, 2012.

[283] Tom Dvir, Guanzhong Wang, Nick van Loo, Chun-Xiao Liu, Grzegorz P. Mazur, Alberto Bordin, Sebastiaan L. D. ten Haaf, Ji-Yin Wang, David van Driel, Francesco Zatelli, Xiang Li, Filip K. Malinowski, Sasa Gazibegovic, Ghada Badawy, Erik P. A. M. Bakkers, Michael Wimmer, and Leo P. Kouwenhoven. Realization of a minimal Kitaev chain in coupled quantum dots. *Nature*, 614(7948):445–450, 2023.

[284] Sebastiaan L. D. ten Haaf, Qingzhen Wang, A. Mert Bozkurt, Chun-Xiao Liu, Ivan Kulesh, Philip Kim, Di Xiao, Candice Thomas, Michael J. Manfra, Tom Dvir, Michael Wimmer, and Srijit Goswami. A two-site Kitaev chain in a two-dimensional electron gas. *Nature*, 630(8016):329–334, 2024.

[285] Martin Leijnse and Karsten Flensberg. Parity qubits and poor man's Majorana bound states in double quantum dots. *Physical Review B*, 86(13):134528, 2012.

[286] Athanasios Tsintzis, Rubén Seoane Souto, Karsten Flensberg, Jeroen Danon, and Martin Leijnse. Majorana Qubits and Non-Abelian Physics in Quantum Dot–Based Minimal Kitaev Chains. *PRX Quantum*, 5:010323, 2024.

[287] Manfred Robert Schroeder. *Fractals, Chaos, Power Laws: Minutes from an Infinite Paradise.* W. H. Freeman, New York, 1991.

[288] Qingzhen Wang, Sebastiaan L. D. ten Haaf, Ivan Kulesh, Di Xiao, Candice Thomas, Michael J. Manfra, and Srijit Goswami. Triplet correlations in Cooper pair splitters realized in a two-dimensional electron gas. *Nature Communications*, 14(1):4876, 2023.

[289] Joseph O'Connell Yuan, Kaushini S. Wickramasinghe, William M. Strickland, Matthieu C. Dartiailh, Kasra Sardashti, Mehdi Hatefipour, and Javad Shabani. Epitaxial superconductor-semiconductor two-dimensional systems for superconducting quantum circuits. *Journal of Vacuum Science & Technology A*, 39(3), 2021.

[290] Marta Pita-Vidal, Arno Bargerbos, Rok Žitko, Lukas J. Splitthoff, Lukas Grünhaupt, Jaap J. Wesdorp, Yu Liu, Leo P. Kouwenhoven, Ramón Aguado, Bernard van Heck, Angela Kou, and Christian Kraglund Andersen. Direct manipulation of a superconducting spin qubit strongly coupled to a transmon qubit. *Nature Physics*, 19(8):1110–1115, 2023.

[291] Amir Sammak, Diego Sabbagh, Nico W. Hendrickx, Mario Lodari, Brian Paquelet Wuetz, Alberto Tosato, LaReine Yeoh, Monica Bollani, Michele Virgilio, Markus Andreas Schubert, Peter Zaumseil, Giovanni Capellini, Menno Veldhorst, and Giordano Scappucci. Shallow and Undoped Germanium Quantum Wells: A Playground for Spin and Hybrid Quantum Technology. *Advanced Functional Materials*, 29:1807613, 4 2019.

[292] Alberto Tosato, Vukan Levajac, Ji-Yin Wang, Casper J. Boor, Francesco Borsoi, Marc Botifoll, Carla N. Borja, Sara Martí-Sánchez, Jordi Arbiol, Amir Sammak, Menno Veldhorst, and Giordano Scappucci. Hard superconducting gap in germanium. *Communications Materials*, 4(1):23, 2023.

[293] M. Lodari, O. Kong, M. Rendell, A. Tosato, A. Sammak, M. Veldhorst, A. R. Hamilton, and G. Scappucci. Lightly strained germanium quantum wells with hole mobility exceeding one million. *Applied Physics Letters*, 120(12), 2022.

[294] Giordano Scappucci, Christoph Kloeffel, Floris A. Zwanenburg, Daniel Loss, Maksym Myronov, Jian-Jun Zhang, Silvano De Franceschi, Georgios Katsaros, and Menno Veldhorst. The germanium quantum information route. *Nature Reviews Materials*, 6(10):926–943, 2021.

[295] Kohei Itoh, W. L. Hansen, E. E. Haller, J. W. Farmer, V. I. Ozhogin, A. Rudnev, and A. Tikhomirov. High purity isotopically enriched ^{70}Ge and ^{74}Ge single crystals: Isotope separation, growth, and properties. *Journal of Materials Research*, 8(6):1341–1347, 1993.

[296] A. J. Sigillito, R. M. Jock, A. M. Tyryshkin, J. W. Beeman, E. E. Haller, K. M. Itoh, and S. A. Lyon. Electron Spin Coherence of Shallow Donors in Natural and Isotopically Enriched Germanium. *Physical Review Letters*, 115:247601, 2015.

[297] Jonathan H. Prechtel, Andreas V. Kuhlmann, Julien Houel, Arne Ludwig, Sascha R. Valentin, Andreas D. Wieck, and Richard J. Warburton. Decoupling a hole spin qubit from the nuclear spins. *Nature Materials*, 15:981–986, 2016.

[298] Franco De Palma, Fabian Oppliger, Wonjin Jang, Stefano Bosco, Marián Janík, Stefano Calcaterra, Georgios Katsaros, Giovanni Isella, Daniel Loss, and Pasquale Scarlino. Strong hole–photon coupling in planar ge: probing the charge degree and wigner molecule states. *arXiv:2310.20661*, 2023.

[299] Marco Valentini, Oliver Sagi, Levon Baghumyan, Thijs de Gijsel, Jason Jung, Stefano Calcaterra, Andrea Ballabio, Juan Aguilera Servin, Kushagra Aggarwal, Marian Janik, et al. Parity-conserving Cooper-pair transport and ideal superconducting diode in planar germanium. *Nature Communications*, 15(1):169, 2024.

[300] Yuan Kang, Zong-Hu Li, Zhen-Zhen Kong, Fang-Ge Li, Tian-Yue Hao, Ze-Cheng Wei, Song-Yan Deng, Bao-Chuan Wang, Hai-Ou Li, Gui-Lei Wang, Guang-Can Guo, Gang Cao, and Guo-Ping Guo. Coupling of a hole double quantum dot in planar germanium to a microwave cavity. *Physical Review Applied*, 22:024054, Aug 2024.

[301] N. W. Hendrickx, W. I. L. Lawrie, L. Petit, A. Sammak, G. Scappucci, and M. Veldhorst. A single-hole spin qubit. *Nature Communications*, 11(1):3478, 2020.

[302] N. W. Hendrickx, D. P. Franke, A. Sammak, G. Scappucci, and M. Veldhorst. Fast two-qubit logic with holes in germanium. *Nature*, 577:487–491, 2020.

[303] Nico W. Hendrickx, William I. L. Lawrie, Maximilian Russ, Floor van Riggelen, Sander L. de Snoo, Raymond N. Schouten, Amir Sammak, Giordano Scappucci, and Menno Veldhorst. A four-qubit germanium quantum processor. *Nature*, 591:580–585, 2021.

[304] R. Mizokuchi, R. Maurand, F. Vigneau, M. Myronov, and S. De Franceschi. Ballistic One-Dimensional Holes with Strong g-Factor Anisotropy in Germanium. *Nano Letters*, 18:4861–4865, 2018.

[305] Melina Luethi, Katharina Laubscher, Stefano Bosco, Daniel Loss, and Jelena Klinovaja. Planar josephson junctions in germanium: Effect of cubic spin-orbit interaction. *Physical Review B*, 107:035435, 2023.

[306] Katharina Laubscher, Jay D. Sau, and Sankar Das Sarma. Majorana zero modes in gate-defined germanium hole nanowires. *Physical Review B*, 109:035433, 2024.

[307] Katharina Laubscher, Jay D. Sau, and Sankar Das Sarma. Germanium-based hybrid semiconductor-superconductor topological quantum computing platforms: Disorder effects. *arXiv:2404.16285*, 2024.

[308] Benjamin D. Woods and Mark Friesen. Realizing Majorana Kramers pairs in two-channel InAs-Al nanowires with highly misaligned electric fields. *Physical Review B*, 108:155142, 2023.

[309] Melina Luethi, Henry F. Legg, Katharina Laubscher, Daniel Loss, and Jelena Klinovaja. Majorana bound states in germanium Josephson junctions via phase control. *Physical Review B*, 108:195406, 2023.

[310] Jie Xiang, Andy Vidan, Michael Tinkham, Robert M. Westervelt, and Charles M. Lieber. Ge/Si nanowire mesoscopic Josephson junctions. *Nature Nanotechnology*, 1(3):208–213, 2006.

[311] N. W. Hendrickx, D. P. Franke, A. Sammak, M. Kouwenhoven, D. Sabbagh, L. Yeoh, R. Li, M. L. V. Tagliaferri, M. Virgilio, G. Capellini, G. Scappucci, and M. Veldhorst. Gate-controlled quantum dots and superconductivity in planar germanium. *Nature Communications*, 9:2835, 2018.

[312] Florian Vigneau, Raisei Mizokuchi, Dante Colao Zanuz, Xuhai Huang, Susheng Tan, Romain Maurand, Sergey Frolov, Amir Sammak, Giordano Scappucci, Francois Lefloch, and Silvano De Franceschi. Germanium quantum-well Josephson field-effect transistors and interferometers. *Nano Letters*, 19:1023–1027, 2019.

[313] N. W. Hendrickx, M. L. V. Tagliaferri, M. Kouwenhoven, R. Li, D. P. Franke, A. Sammak, A. Brinkman, G. Scappucci, and M. Veldhorst. Ballistic supercurrent discretization and micrometer-long Josephson coupling in germanium. *Physical Review B*, 99:075435, 2019.

[314] Kushagra Aggarwal, Andrea Hofmann, Daniel Jirovec, Ivan Prieto, Amir Sammak, Marc Botifoll, Sara Martí-Sánchez, Menno Veldhorst, Jordi Arbiol, Giordano Scappucci, et al. Enhancement of proximity-induced superconductivity in a planar Ge hole gas. *Physical Review Research*, 3(2):L022005, 2021.

[315] M. Hinderling, S. C. ten Kate, M. Coraiola, D. Z. Haxell, M. Stiefel, M. Mergenthaler, S. Paredes, S. W. Bedell, D. Sabonis, and F. Nichele. Direct microwave spectroscopy of Andreev bound states in planar Ge Josephson junctions. *arXiv*, 2024.

[316] Axel Leblanc, Chotivut Tangchingchai, Zahra Sadre Momtaz, Elyjah Kiyooka, Jean-Michel Hartmann, Gonzalo Troncoso Fernandez-Bada, Boris Brun-Barriere, Vivien Schmitt, Simon Zihlmann, Romain Maurand, Étienne Dumur, Silvano De Franceschi, and François Lefloch. From nonreciprocal to charge-4e supercurrents in Ge-based Josephson devices with tunable harmonic content. *arXiv*, 2023.

[317] Axel Leblanc, Chotivut Tangchingchai, Zahra Sadre Momtaz, Elyjah Kiyooka, Jean-Michel Hartmann, Frédéric Gustavo, Jean-Luc Thomassin, Boris Brun, Vivien Schmitt, Simon Zihlmann, Romain Maurand, Étienne Dumur, Silvano De Franceschi, and François Lefloch. Gate- and flux-tunable $\sin(2\varphi)$ Josephson element in proximitized junctions. *arXiv*, 2024.

[318] Oliver Sagi, Alessandro Crippa, Marco Valentini, Marian Janik, Levon Baghumyan, Giorgio Fabris, Lucky Kapoor, Farid Hassani, Johannes Fink, Stefano Calcaterra, Daniel Chrastina, Giovanni Isella, and Georgios Katsaros. A gate tunable transmon qubit in planar Ge. *Nature Communications*, 15(1):6400, 2024.

[319] Lazar Lakic, William I. L. Lawrie, David van Driel, Lucas E. A. Stehouwer, Menno Veldhorst, Giordano Scappucci, Ferdinand Kuemmeth, and Anasua Chatterjee. A proximitized quantum dot in germanium. *arXiv*, 2024.

[320] J. A. Kittl, K. Opsomer, C. Torregiani, C. Demeurisse, S. Mertens, D. P. Brunco, M. J. H. Van Dal, and A. Lauwers. Silicides and germanides for nano-CMOS applications. *Materials Science and Engineering: B*, 154:144–154, 2008.

[321] George F. Hardy and John K. Hulm. Superconducting Silicides and Germanides. *Physical Review*, 89(4):884–884, 1953.

[322] Ch. J. Raub, W. H. Zachariasen, T. H. Geballe, and B. T. Matthias. Superconductivity of some new Pt-metal compounds. *Journal of Physics and Chemistry of Solids*, 24(9):1093–1100, 1963.

[323] J. R. Gavaler. Superconductivity in Nb–Ge films above 22 K. *Applied Physics Letters*, 23(8):480–482, 1973.

[324] Ch. J. Raub. Superconductivity of the platinum metals and their alloys. *Materials & Design*, 5(3):129–136, 1984.

[325] S. Gaudet, C. Detavernier, A. J. Kellock, P. Desjardins, and C. Lavoie. Thin film reaction of transition metals with germanium. *Journal of Vacuum Science & Technology A: Vacuum, Surfaces, and Films*, 24(3):474–485, 2006.